198(3), 2024

COMBUSTION ENGINES

Politechnika Poznańska

Wydział Inżynierii Lądowej i Transportu
Wydział Technologii Chemicznej

ul. Piotrowo 3; 60-965 Poznań

Studia Podyplomowe

Inżynieria systemów zasilania wodorem

II edycja

H2.put.poznan.pl

Due to the dynamic development of machine and vehicle powertrains, the "Combustion Engines" scientific journal, while retaining its historical title, currently publishes works related not only to internal combustion engines, but also other powertrains, including hybrid drives, electric drives and fuel cells.

PTNSS Supporting Members
Członkowie wspierający PTNSS

BOSMAL Automotive Research and Development Institute Ltd
Instytut Badań i Rozwoju Motoryzacji BOSMAL Sp. z o.o

Motor Transport Institute
Instytut Transportu Samochodowego

Institute of Aviation
Sieć Badawcza Łukasiewicz – Instytut Lotnictwa

Automotive Industry Institute
Sieć Badawcza Łukasiewicz – Przemysłowy Instytut Motoryzacji

Sieć Badawcza Łukasiewicz – Poznański Instytut Technologiczny

AVL List GmbH

Air Force Institute of Technology
Instytut Techniczny Wojsk Lotniczych

Military Institute of Armoured & Automotive Technology
Wojskowy Instytut Techniki Pancernej i Samochodowej

Toyota Motor Poland Ltd. Sp. z o.o.

RADWAG Balances and Scales
RADWAG Wagi Elektroniczne

MS Mechatronic Solutions Group

FOGO Sp. z o.o.

Horus Energia Sp. z o.o.

COMBUSTION ENGINES
A Scientific Magazine

2024, 198(3)

Year LXIII

PL ISSN 2300-9896
PL eISSN 2658-1442

Publisher:
Polish Scientific Society of Combustion Engines
60-965 Poznan, pl. M. Skłodowskiej-Curie 5, Poland
tel.: +48 61 6475966, fax: +48 61 6652204
E-mail: sekretariat@ptnss.pl
WebSite: http://www.ptnss.pl
Papers available on-line: http://combustion-engines.eu

Contents

Publisher:

Polish Scientific Society of Combustion Engines
60-965 Poznan, pl. M. Sklodowskiej-Curie 5, Poland
tel.: +48 61 6475966, fax: +48 61 6652204
E-mail: sekretariat@ptnss.pl
WebSite: http://www.ptnss.pl

Subscriptions
Send subscription requests to the Publisher's address.
Cost of a single issue PLN 100.

Preparation for print
ARS NOVA Publishing House
60-782 Poznan, ul. Grunwaldzka 17/10A

Circulation: 60 copies

Printing and binding

Zakład Poligraficzny Moś i Łuczak, sp. j.,
Poznań, ul. Piwna 1

The journal is under the patronage of the Transport Committee and the Machine Building Committee of the Polish Academy of Sciences

The journal is registered and listed in the Polish and international database

Papers published in the
Combustion Engines
quarterly receive 70 points as stated by the Notification of the Minister of Science dated 5 January 2024.

Declaration of the original version
The original version of the Combustion Engines journal is the printed version.

Cover
I – 6.6-litre V8 Hennesse Venom F5 engine *(www.autoevolution.com)*; background *(Glowing abstract yellow orange and black wave – 123freevectors.com)*
IV – Porsche 911 Carrera GTS – Electric turbocharger *(press.porsche.com)*

Article citation info:
Chojnowski J, Karczewski M, Szamrej GA. Dual-fuel engines using hydrogen-enriched fuels as an ecological source of energy for transport, industry and power engineering. Combustion Engines. 2024;198(3):3-12. https://doi.org/10.19206/CE-176800

Janusz CHOJNOWSKI
Mirosław KARCZEWSKI
Grzegorz Aleksander SZAMREJ

Combustion Engines
Polish Scientific Society of Combustion Engines

Dual-fuel engines using hydrogen-enriched fuels as an ecological source of energy for transport, industry and power engineering

ARTICLE INFO

Received: 31 May 2023
Revised: 10 December 2023
Accepted: 11 December 2023
Available online: 19 January 2024

Displacing internal combustion engines (ICE) from the passenger car sector does not mean displacing it from all industries and specific applications. Thanks to the analysis of data on compression ignition (CI) engines used in the world, it is possible to prepare ready-made solutions for the most common engines in selected industries or for those whose greenhouse gas emissions will be the largest and most expensive for their owners in the coming years. The basic solution presented in this article gives the possibility of powering the engines with the most ecological currently known alternative engine fuels and using the already existing methane transmission infrastructure around the world. Their greatest advantage is their availability and low carbon content, which allows to minimize carbon dioxide emissions, both by burning hydrogen-enriched fuels and by increasing the efficiency of the engines modified by dual fuel supply system. Properly made external dual-fuel installation allows to improve the thermal efficiency of the CI engine. Work on this issue may help in the development of, for example, high-efficiency flex fuel power generators, which, as the current situation in Ukraine shows, are worthy. Thanks to the diversification of power sources for power generators, the countries is able to increase the reliability and security of energy supplies even in difficult conditions, such as armed conflict or natural disasters.

Key words: *dual-fuel, alternative fuels, hydrogen-enriched fuels, industrial engine*

1. Introduction

1.1. Global CO_2 emissions and energy sources in the world

Improving the protection of the natural environment, reducing the emission of harmful exhaust components and greenhouse gases is a path of development that is of interest to the general public. The idea of using the current technological achievements in the form of Dual Fuel (DF) and Reactivity controlled compression ignition (RCCI) engines proposed in this article, together with the use of ecological fuels blended with hydrogen, is part of the trend of reducing CO_2 emissions into the atmosphere, because it covers all the most emission-intensive economic sectors, which have been marked in the Fig. 1.

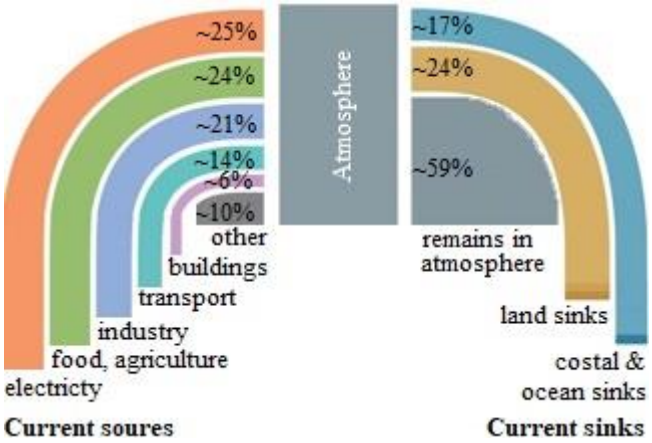

Fig. 1. Sources of CO_2 emissions to the atmosphere in the world [52]

The largest CO_2 emitters use mainly natural gas (NG), coal and oil to generate energy (Fig. 2).

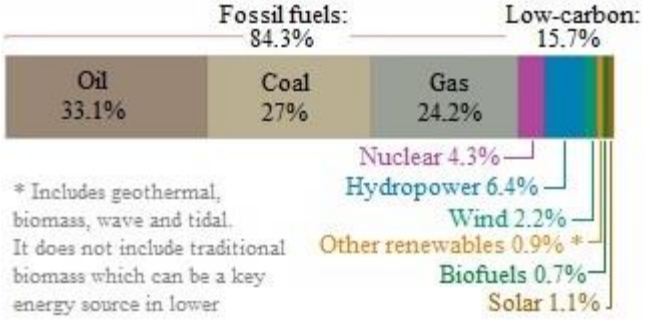

Fig. 2. Total world energy mix (electricity, transport & heat) [3, 52]

The idea presented in this article, which will make it possible to replace them with hydrogen in internal combustion engines, can reduce the consumption of two of these fuels.

1.2. Worldwide use of ICE in industrial applications

The use of combustion engines in power systems plays a key role in maintaining system continuity in various emergency situations, including armed conflicts, natural disasters and weather anomalies. These engines serve as backup power sources and ensure reliable electricity generation in the event of failure of the basic power infrastructure and will important in stabilizing electricity grids with a large share of uncontrollable renewable energy sources [9, 19].

In times of armed conflict or war, the electrical network may become the target of disruption or destruction. In such scenarios, internal combustion engines provide power con-

tinuity. These engines can be integrated with stand-alone power generators or connected to the grid through synchronized operation with existing power plants [9, 19].

In the event of natural disasters such as earthquakes, hurricanes or floods, the electrical infrastructure is exposed to severe damage, leading to power outages. Combustion engines, equipped with suitable generators, can be quickly deployed to affected areas to restore electricity. Their mobility and flexibility allow them to be stationed near critical facilities such as hospitals, emergency response centers or communication networks, ensuring that essential services continue to function [9, 19].

Weather anomalies such as extreme heat waves, periods of frost or storms can also stress the power grid and potentially cause blackouts. During such events, internal combustion engines may be run as peak power plants to meet the increased demand. These engines can quickly increase energy production and stabilize the grid, compensating for fluctuating renewable energy sources or reduced efficiency of conventional power plants affected by extreme conditions. Figure 3 shows the process of stabilizing the power system in New England USA at the beginning of 2023 [10, 51, 53].

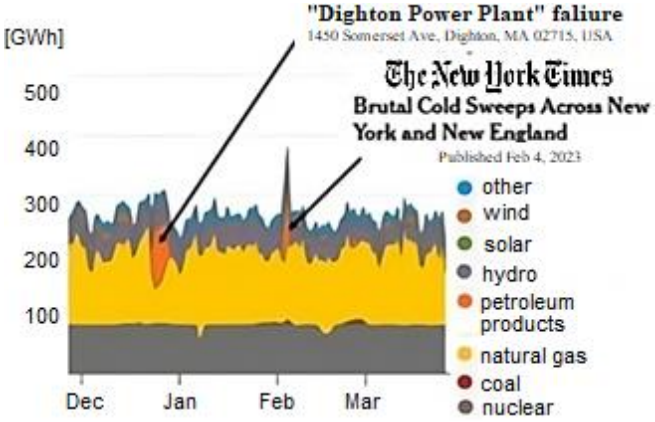

Fig. 3. Graph of the use of electrical energy sources for New England, USA in the period from 12.2022 to 4.2023, with marked anomalies where it was necessary to use emergency generators using ICE [10, 51]

The chart above showing the daily production of electricity by energy source shows two crises in which internal combustion engines were used as an intervention, which in the event of a failure of the Dighton natural gas power plant, and later during severe frosts in New England, over 5 GW of power installed in power generators was launched [51, 53].

In addition, the availability of fuel storage facilities for internal combustion engines allows them to operate independently of external power sources for extended periods of time. This self-sufficiency becomes invaluable in situations where the primary power supply is cut off for various reasons, such as damaged transmission lines or disruptions in fuel supplies. To increase the resilience of power systems in emergency situations, it is essential to have a well-maintained fleet of ICE with regular fuel supply and maintenance procedures. Proper training and preparedness are critical to the successful deployment and operation of these engines in emergency situations. However, it should be noted that while internal combustion engines provide a reliable backup power solution, they come with emissions and environmental concerns. To mitigate these problems, efforts must be made to minimize their use and shift to cleaner and more sustainable alternatives such as renewables, energy storage systems and microgrids. Nevertheless, in the context of maintaining the continuity of the system in emergency situations, internal combustion engines continue to play an important role until more sustainable solutions become commonplace and available.

In total, there are 34,937 electricity generation installations installed in the world. Diesel oil and derived fuels are used in 3626 power plants with a total installed capacity of approximately 250 GW, including approximately 800 of these installations also running on natural gas, and additionally 3697 power plants with natural gas turbine engines with a capacity of max. 1.2 TW. For comparison, 127 GW of capacity is installed in pumped storage power plants around the world [11, 12, 56]. This shows how important the internal combustion engines play in the power system.

As far as industry and heavy industry are concerned, the authors of this article are currently unable to find data on the global use of internal combustion engines, however, legislative changes in the United States (US) and European Union (EU) will lead to a reduction in CO_2 emissions from these engines in the near future and will force entities using them to disclosure.

1.3. Worldwide use of ICE in transport

Combustion engines also continue to play a key role in transport. There are currently around 350 million [16, 55] diesel engines in goods transport vehicles. There are a total of 450 million cars with such engines on land, and about 50,000 heavy transport ships (over 1000 tons of load capacity) and a total of over 2 million various types of ships and ships powered by diesel engines [32]. In 2018, 8×10^{18} Joules of energy contained in the fuel were needed to power marine transport with diesel fuels and its derivatives, and in total it is already 10×10^{18} joules of energy when adding this value with the demand for natural gas as shown in Fig. 4 [21, 32].

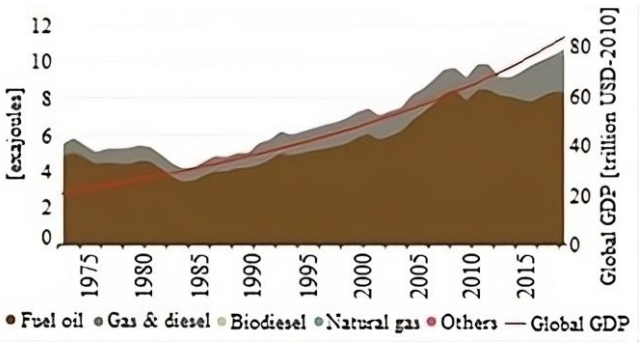

Fig. 4. Estimated energy demand contained in water transport fuel in the world [21]

In the case of road vehicles, the possibility of reducing carbon dioxide emissions is even higher than in the case of energy, industry or water transport, due to the possibility of additionally increasing the efficiency of the engine operating on two fuels and reducing the emission of harmful ex-

haust components. Carbon dioxide emissions in road transport are more than 2.5 times higher than in sea transport and account for nearly 30% of all carbon dioxide emissions from transport [40]. Despite legislative efforts and the hard work of constructors and engineers building motor vehicles, due to, among others, consumption, they did not ultimately contribute to drastic decreases in emissions, as shown in the Fig. 5. Consider here is the best-executed scenario of actions, i.e. the effect of reforms in the EU. In the European Union, the trend of reducing carbon dioxide emissions is the strongest compared to other countries in the world. As you can see in the graph in Fig. 5, emissions in the last decade began to decrease (very slightly, and the decrease in 2020 was the result of the pandemic), which, however, is not yet the effect that could be achieved by using alternative fuels proposed by our team, which, as mentioned , can significantly exceed the 35% reduction compared to diesel emissions, thanks also to the increase in efficiency of the engine operating in dual-fuel mode [8, 40].

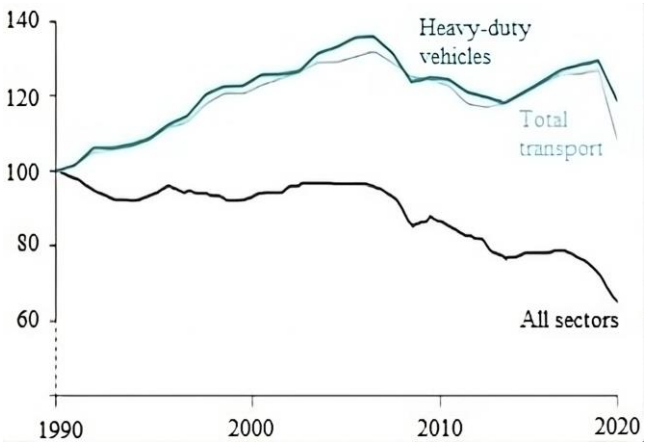

Fig. 5. Relative CO_2 emissions from transport since 1990 in EU [8]

2. Material and methods

2.1. Hydrogen enriched fuels

Hydrogen-enriched fuels may be the key to reducing carbon dioxide emissions generated in the combustion process in internal combustion engines. Their current development has been very intensive for several years, and after the EU decision to limit the sale of combustion cars by 2035 [7, 46], work on low- and zero-emission fuels has accelerated even further. Their production may allow the operation of new cars with ICE powered only by those fuels which total greenhouse gas (GHG) emissions over the entire use cycle will be zero. Many car manufacturers believe that they can determine the future of automotive development, the aviation and maritime industries already treat them as the only source of energy to maintain their transport fleet in the future in the form of zero-emission means of transport [18]. The lack of real alternatives means that industries that need large energy resources invest in this technology in a way that is not only declarative – like the automotive industry – but also fully real, already implementing a huge number of investments related to their use [15, 23, 57]. The existing research methodology still mainly takes into account how many substances the engine actually emits in the place where it is used. In addition to carbon dioxide and water, each of the other substances that affect the natural environment can be neutralized in the exhaust gas catalytic reactor, which is why carbon dioxide, which is the basic greenhouse gas produced in the combustion process, is the focus of reducing emissions in internal combustion engines. The currently used fuels are able to reduce the level of carbon dioxide emissions. Its complete elimination can be done using pure hydrogen or substances binding it with elements other than carbon dioxide, such as ammonia. The use of pure hydrogen or ammonia is currently used, but in a very limited form [47], and it is easier to introduce fuels that can directly replace fuels distributed in the current infrastructure, such as Hydrogen enriched Compressed Natural Gas (HCNG) also in configuration with fully renewable biomethane – replace fossil Compressed Natural Gas (CNG), or Hydro-treated Vegetable Oil (HVO) – replacing diesel, and methanol – replacing gasoline. The possibility of their hydrogenation translates directly into the level of carbon dioxide emissions during their combustion. In addition, both of these fuels come from renewable energy sources such as biogas for HCNG and vegetable oil for HVO. Their total carbon footprint is very low, it can be practically zero when hydrogen is obtained from green energy sources. The methods of obtaining hydrogen are varied and, depending on the energy source used for its production, it may be characterized by a different degree of GHG emissions.

For the purposes of our considerations, green hydrogen should be taken into account, because the EU directs its industry and energy sector to the production of such hydrogen. Green hydrogen is hydrogen whose total carbon footprint does not exceed 2 kg of CO_2 equivalent per kg of hydrogen produced. Hydrogen produced from renewable energy sources has a zero-carbon footprint, and combining it with biogas we get a fuel whose carbon footprint will be practically zero – HCNG is a mixture of natural gas and hydrogen with proportions set by the manufacturer of this fuel, with limitations resulting primarily from the technical capabilities of the system distribution of this fuel. The distribution of natural gas is easier than the distribution of hydrogen and its high content in this fuel causes a number of changes in its properties, making it impossible to distribute it through the natural gas distribution system [42]. However, the hydrogen content can reach up to 50% of the mixture volume, which is a noticeable share of hydrogen in this fuel and allows to reduce carbon dioxide emissions to the atmosphere during its combustion compared to pure natural gas or methane [38].

HVO, on the other hand, reduces carbon dioxide emissions both by reducing the chemical share of carbon in this fuel in favor of hydrogen and by using plant substances in the process of its production, thanks to which practically all carbon dioxide emitted to the atmosphere was previously absorbed by the plants from which this fuel was created [4].

The situation is similar with methanol, which, although it is not an additionally hydrogenated fuel, its production is based primarily on agricultural production from plants that quantitatively absorb most of the carbon dioxide that is emitted in the process of burning this fuel [35].

In another article by the authors of this publication entitled "A review of low-CO_2 emission fuels for a dual-fuel RCCI engine" [25] a list was developed, which selected fuels with the lowest potential for carbon dioxide emissions into the atmosphere, and on its basis, those with the greatest potential to reduce CO_2 emissions from internal combustion engines in the future were selected. It clearly shows that the emission for HCNG is the lowest of all fuels, and its decrease is proportional to the hydrogen content in this fuel. Further opportunities to increase the concentration of hydrogen in the mixture will increase along with the development of distribution technology and the development of hydrogen networks, which will allow for a gradual transition to pure hydrogen in such installations in the future, which will be related to the EU "FIT for 55" assumptions [50]. Table 1 below shows part of the developed table.

However, only two hydrogen-enriched fuels, HCNG and HVO, were selected for the purpose of this work. This is due to the analysis carried out by the authors in a number of their articles [25, 48, 49] in which we presented the concept of using dual-fuel engines in the future, whose overall efficiency exceeds both conventional CI and Spark Ignition (SI) engines, and the flexibility of fuel use is practically unlimited. These engines require both high-octane and high-cetane fuels at the same time, which means that two fuels with diametrically opposed properties must be used. The selection of two fuels with the lowest carbon dioxide emissions allows you to determine how low carbon dioxide emissions will be possible in the future for ICE, the use of which in the power industry and heavy industry will not be phased out in Europe by 2050 [25, 48].

2.2. Principle of operation and advantages of a dual-fuel engine

To ignite the mixture of air and high-octane fuel, a dual-fuel engine uses high-cetane fuel injected directly into the combustion chamber just before its self-ignition, causing further combustion of the entire mixture located in the space above the piston. In a variant of the dual-fuel engine, called the RCCI engine (Reactivity Controlled Compression Ignition), the self-ignition of the high-cetane fuel, in this case the high-reactive fuel, causes the auto-ignition of a homogeneous mixture of the high-octane fuel, called the low-reactive fuel, with air. The RCCI engine is a DF engine variant of the Homogeneous Charge Compression Ignition (HCCI) engine, which is characterized by higher thermal efficiency than a classic dual-fuel engine or a standard CI diesel engine. Figure 6 below shows the view of the combustion process in the chamber operation of the Gasoline, Diesel, HCCI and RCCI dual fuel engine.

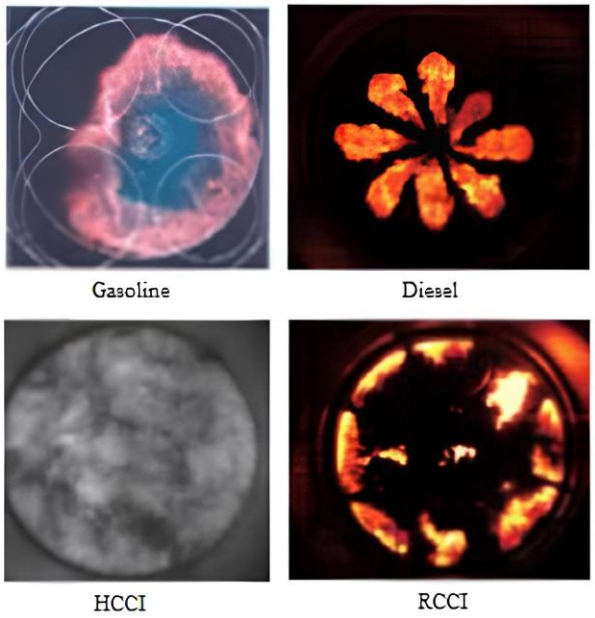

Fig. 6. A view of the combustion process in the chamber during operation of the Gasoline, Diesel, HCCI and RCCI dual fuel engine [22]

In industry, maritime transport and energy, DF engines have been the main source of propulsion for years. This is due to the possibility of using cheaper and less emission-intensive fuels such as CNG, Liquefied Natural Gas (LNG) or bio-CNG/LNG. Their use in SI engines is less economical due to the lower efficiency of these engines compared to dual-fuel engines. Engines on an industrial scale usually work only with necessary breaks, so the higher efficiency of a given solution translates directly into the economy of operation of a given engine and this indicator is crucial in this type of application. DF engines, especially RCCI engines, achieve higher efficiency thanks to a very even temperature distribution in the combustion chamber and a lower maximum combustion temperature. The following Fig. 7 shows an example of the temperature distribution in an RCCI engine and a classic CI engine.

Table 1. Selected fuels properties (full table available at [25])

		Petrol	Diesel	HVO	M100	CNG	HCNG15	HCNG30	HCNG50
C/H ratio	% of weight	9	7.26/6.73	5.49	3	3	2.77	2.52	2.15
	molecular	~3:4	~3:5	0.46	1:4	1:4	0.23/0.24	0.21/0.22	0.18/0.19
Hydrogen weight content [%]		10	12/(12.96)	15.4	12.5	25	26.5 (25.75)	28.39 (26.5)	31.75 (27.5)
Carbon weight content [%]		69–70	69–74	~70	~70	56.1–55.35	55–54.3	53.56–52.85	51.05–50.37
CH_4 emission potential		Low	Low	Low	Low	Very high	High	High	Medium/ high
N_2O emission potential		Very high	Medium	Low	High	Medium	Low	Low	low
Mainly emission potential		HC, CO, CO_2, NO_2, NO_x	HC, CO, CO_2, NO_2, NO_x	HC, CO, NO_2, NO_x	HC, NO_2, NO_x	CH_4, NO_2, NO_x	CH_4, NO_2, NO_x	CH_4, NO_2, NO_x	NO_2, NO_x

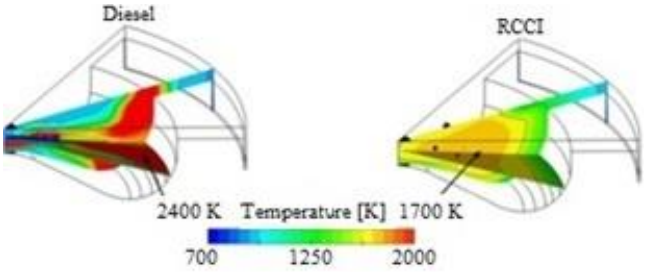

Fig. 7. Temperature distribution in the combustion chamber for diesel only and RCCI [45]

The high efficiency of these engines also results from the possibility of using the entire space above the piston as a combustion chamber, which in a classic CI engine is limited to a small combustion chamber located in the piston. The time needed for a good mixing of low-reactive fuel with air is provided by indirectly supplying this fuel to the intake manifold, or a series of high-pressure injections directly into the combustion chamber in various phases of engine operation called Direct Dual Fuel Stratification (DDFS) [5, 17].

This strategy is used in more advanced solutions, and both methods of powering the dual-fuel engine can also be mixed to improve the results.

Dual-fuel engines are also characterized by extraordinary fuel flexibility – they can be used with all fuels that can be used in classic SI and CI engines. This allows for an emergency change of the fuel used in the engines in the event of difficulties with the supply of the standard power source, and it is also easy to adapt the engine to burn more ecological fuels when they become widely available. among others for this reason, HCNG is such a good example of a fuel evolving towards an ecological fuel of the future, from which it will be easy to switch to clean, green hydrogen, and the highly reactive fuel, which in our considerations is HVO [4, 14], in the future may be a zero-emission e-fuel that can be used in these engines with only minimal or zero emission fuels and use them with higher efficiency than SI engines and in some cases also fuel cells [16].

3. Potential and reasons for the use of dual-fuel engines using hydrogen-enriched fuels

It should be remembered that the engines used in the power industry, maritime transport or industry have a much higher efficiency than high-speed SI and CI engines. The most efficient engines already achieve an efficiency of 54.6% [30, 31, 44, 54]. Overall efficiency of up to 55% in low-speed engines is no longer uncommon, and designers predict that thanks to RCCI technology in engines of this type it will be possible to achieve values of 60% [44]. Such performance makes engines of this type an attractive alternative to turbine engines, fuel cells or batteries that allow the development of electromobility. Hydrogen, which is not only a fuel, but also a storage of energy generated from electricity sources, combusted in internal combustion engines, allows for the recovery of this energy when it is needed. The graph below in Fig. 8 below shows the electricity production in the power system, which shows the scenarios for different capacities of installed PV installations.

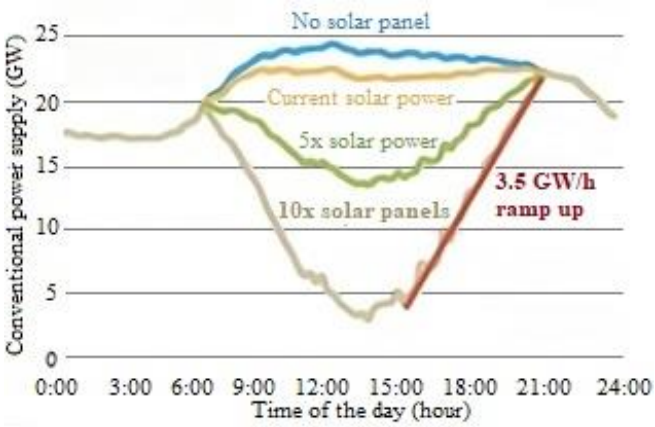

Fig. 8. Scenarios of electricity production using PV in the energy mix (based on [26])

The figure above shows how the power of the installed photovoltaic installations in the power grid affects production during the day. The visible decrease in production from conventional sources around noon is problematic for the system operators and for this reason the need to store the energy produced during this period will increase. A network constructed in this way will require energy to be delivered in the period when Renewable Energy Source (RES) does not operate with high power and its storage in the period when it is operating. One of the methods of energy storage is the production of hydrogen and its subsequent use, e.g. in internal combustion engines. Thanks to the possibility of using the existing natural gas distribution network, it is possible to distribute hydrogen to the target customer in the form of HCNG fuel. In combustion engines, the use of liquid fuels also allows the combustion of green hydrogen, because fuels enriched with it, such as HVO, can use for this process green hydrogen produced during the surplus of electricity production from RES. Due to the possibilities offered by DF ICE in the use of green energy sources, simulations have been developed showing the level of carbon dioxide emissions depending on the hydrogen content in HCNG, at various degrees of replacement [5] of high-reactivity fuel with low-reactivity fuel. The graph below in Fig. 9 shows the effect of the hydrogen content on the carbon dioxide emissions during complete combustion of HCNG.

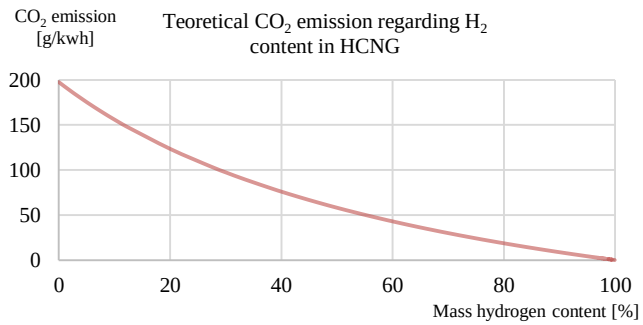

Fig. 9. Impact of hydrogen content on CO_2 emissions from HCNG combustion

The influence of hydrogen content on carbon dioxide emissions visible in the graph in Fig. 9 clearly shows that with the initial increase in hydrogen content at low concentrations, carbon dioxide emission decreases more intensively than with high hydrogen content in the mixture. This shows how important it may be to add methane, even with a small amount of hydrogen, to improve the ecological parameters of this fuel.

The chart on the Fig. 10 below shows the level of carbon dioxide emissions for various types of ICE and the fuels used in them, with the assumed values of overall efficiency of SI engines fueled with gasoline at the level of 36.4% [54], SI fueled with CNG at the level of 39% [27, 37], CI fueled with oil or HVO of 44% [37], DF of 45% [37], and RCCI of 46% [43].

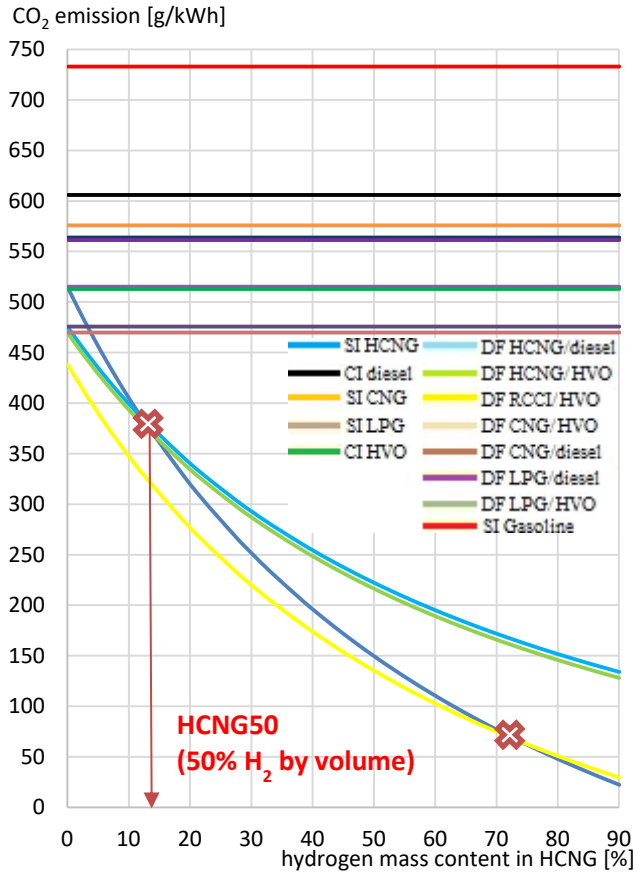

Fig. 10. Carbon dioxide emission intensity for different types of engines and different types of fuels used as a function of hydrogen content in HCNG fuel with maximal fuel replacement in DF mode at the 80% level for CNG & HCNG fuel and 35% for LPG

The graph above clearly shows the impact of the hydrogen content in HCNG on carbon dioxide emissions and shows the advantage of DF engines in the range where the hydrogen concentration in the HCNG mixture does not exceed 50% of the volume content in the mixture (~12% of the mass content). This is the limit value at which hydrogen can be mixed with NG without serious consequences related to the safety and impact of this fuel on the corrosiveness of steel [34] and other serious problems with combustion and distribution [1, 2, 13, 14, 20, 24, 29, 33, 36, 39, 41]. These hydrogen contents in HCNG constitute a mixture that can be effectively used in combustion engines, as determined in many tests [14, 20, 24]. To better understand the advantages of using two different types of engines in specific operating conditions, three additional simulations, presented in the charts below were presented and analyzed. Figure 11 and 12 represent engine used in transport, Fig. 13 represent the same type of engines but used in power engineering or industry.

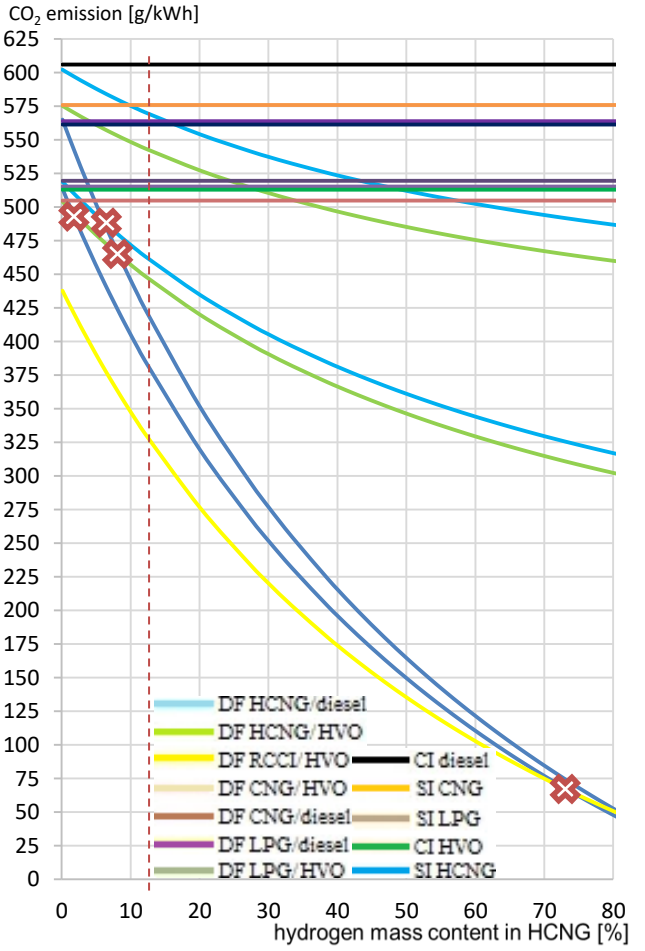

Fig. 11. Carbon dioxide emission intensity for different types of engines and different types of fuels used as a function of hydrogen content in HCNG fuel with maximal fuel replacement in DF mode at the 80% level and 50% level for CNG & HCNG fuel and 35% for LPG and different efficiency for engines using HCNG fuel

Lines of the same color symbolize the range in which an engine of a given type can operate when powered by a specific fuel. The line with the lowest achieved CO_2 emissions symbolizes the optimal operating point at which the engine operates, at which the assumed replacement rate is 80% and the maximum efficiency, as written earlier, is 45%. The line of the same color with the higher emission value shows the engine operating condition in which the maximum efficiency is reduced by 10%, which in this case results from the reduction of the engine speed, while the degree of replacement decreases in the square of its maximum value, i.e. for the maximum replacement of 50% it drops to 25%, and for 80% it drops to 64%. These values correspond to the values achieved on two types of gas in-

stallations that are most often used in DF engines. Lower replacement values allow the engine to operate at low load without the risk of knocking combustion. Both of these factors are taken into account in the emissions calculation for the line representing the maximum emissions during normal operation of the described engine. Dotted line shows the HCNG50 level.

Figure 11 shows that only when operating optimally (with high efficiency and degree of replacement), a DF engine is able to produce lower CO_2 emissions than an SI engine using HCNG fuel with a low H_2 content (< 50% V/V). The low replacement degree, which is characteristic of low-advanced and inexpensive gas installations, means that the use of SI engines actually becomes a more ecological solution, despite their lower overall efficiency. The graphs below (Fig. 12) show the CO_2 emissions with maximum replacement of a DF engine of 50% and 80%. The emission crossover points for the SI & DF engines show the H_2 content of HCNG at which CO_2 emissions are equal.

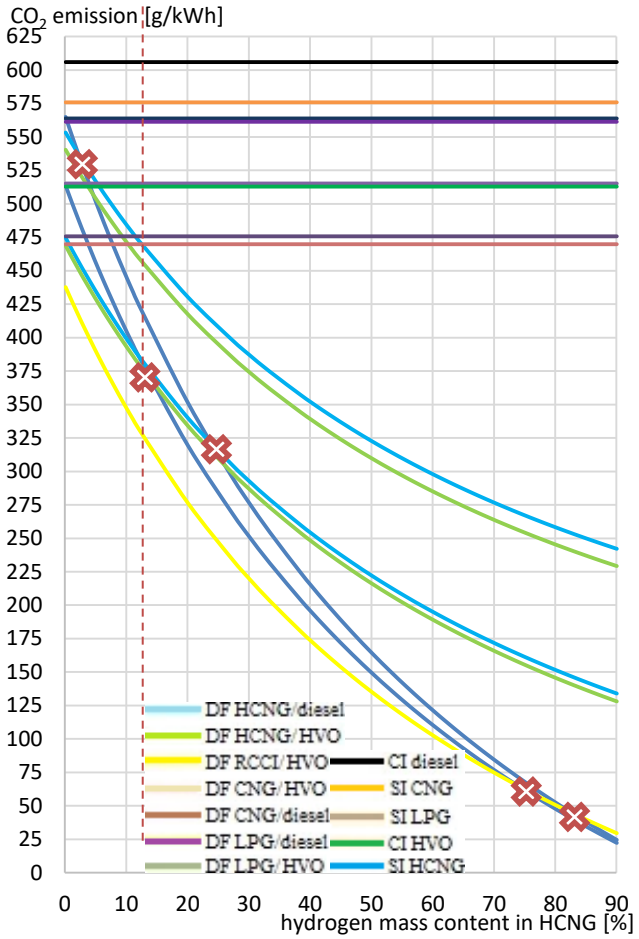

Fig. 12. Carbon dioxide emission intensity for different types of engines and different types of fuels used as a function of hydrogen content in HCNG fuel with maximal fuel replacement in DF mode at the 80% level for CNG & HCNG fuel and 35% for LPG

This clearly shows what type of engine is worth to use when HCNG fuel with a bit higher H_2 content is available. We can clearly see the contents, which SI engines prepared for gas fuel are a less emission-intensive option than DF engines. Even the use of HVO does not significantly change this situation and only when operating at the highest efficiency similar CO_2 emission values for both engine types are achieved. The level at which the RCCI engine is more emissive than the SI engine is a value very close to using pure H_2 with an admixture of NG, not NG with an admixture of H_2, and is beyond the reach of the currently used transmission infrastructure.

For the HCNG fuel at the level of hydrogen mass content around 5% (~20% V/V) the CO_2 emission is similar in DF HCNG fueled engines and SI HCNG engines. HCNG with a low H_2 content between 5–20% V/V is the popular option for the nearest future, what stands DF engines as the more ecological than SI engines, fueled by that kind of HCNG fuel mix.

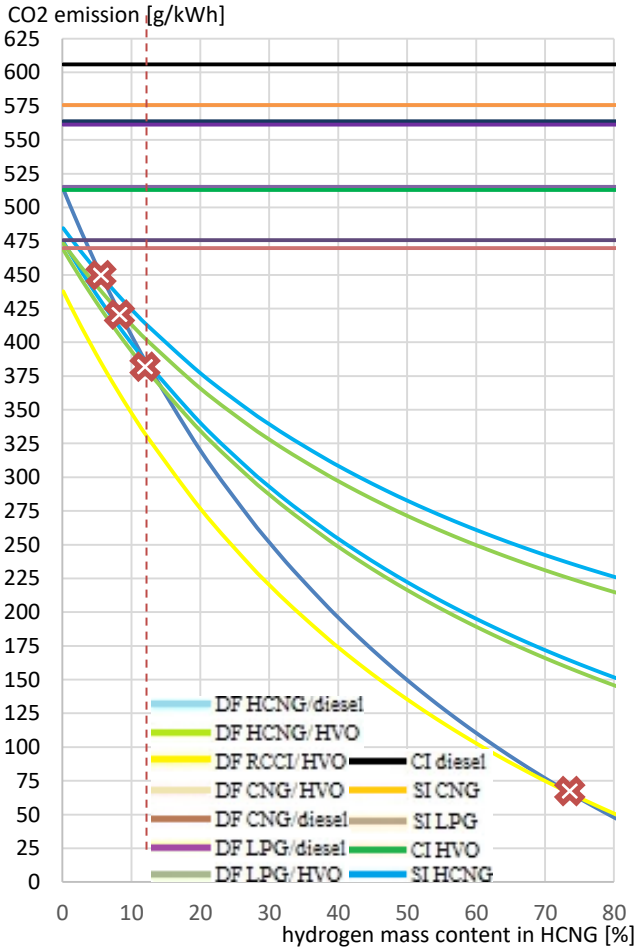

Fig. 13. Carbon dioxide emission intensity for different types of engines and different types of fuels used as a function of hydrogen content in HCNG fuel with maximal fuel replacement in DF mode at the 80% level and 50% level for CNG & HCNG fuel and 35% for LPG

The third graph shows a stationary engine operating at constant speed but with different loads. In the scope of operation of this engine, only the impact of changing the degree of fuel replacement was taken into account, and it was assumed that a higher generation gas installation was used, allowing for achieving high degrees of replacement, which in continuous operation as a power generator has its economic justification. A smaller range of CO_2 emissions in which the engine operates is visible. This allows to see

more clearly when such an engine is emitting a similar amount of CO_2 as an equivalent SI engine where their emissions levels are crossing. For HCNG with H_2 mass content below 10%, it can be seen that even in the least optimal operating range, DF engines have a similar emission level to SI engines. The impact of the use of HVO is also more clearly visible here, which, with a reduced degree of replacement, significantly reduces the level of CO_2 emissions.

This proves that until the infrastructure for supplying hydrogen to end users is in place, dual-fuel engines will have an advantage over SI engines. When pure hydrogen can be distributed and burned in engines as the only fuel, or with highly reactive fuel, which is completely zero-emission.

4. Conclusions

In industrial engines, low-emission fuels will be of great importance due to their common occurrence in the power plants, industry and maritime transport, and the amount of fuel they consume. The cost-critical nature of these industries adds to the importance of the efficiency of the engines used in these industries. Therefore, our simulations allow us to determine the limits according to which we can be guided in the application of given types of engines, where dual-fuel engines should be used when using HCNG 0–50 fuel, while in cases where ammonia or pure hydrogen would be used, it would be more favorable for environmental reasons would be the use of CI engines.

Summing up, the presented solution can provide:

- reduction of CO_2 emissions in operating installations using internal combustion engines by over 35%
- lowering the operating costs of enterprises; flexibility in the use of different fuels
- increasing the operational reliability of the power system
- improving the structure of the energy mix
- increasing the potential for further development of green energy sources in the existing energy infrastructure
- extending the lifetime of internal combustion engines already produced and the existing power generation structure
- the use of a gas installation in DF engines, which allows for low levels of fuel substitution, leads to performance that is uncompetitive compared to SI engines in terms of CO_2 emissions
- stationary engines whose speed is constant and the load is always high enough to ensure that these engines operate with relatively high overall efficiency make their use justified at any available HCNG concentration
- the RCCI engines allows a reduction in CO_2 emissions practically over the entire range of H_2 content in HCNG compared to SI engines. When RCCI engines become widely available, the use of hydrogen-enriched fuels in fueling should become the standard.

Acknowledgements

This work was financed by Military University of Technology under University Research Grant UGB 22-833/2023.

Nomenclature

CI	compression ignition
CNG	compressed natural gas
CO_2	carbon dioxide
DDFS	direct dual fuel stratification
DF	dual fuel
EU	European Union
ICE	internal combusiton engines
GHG	greenhouse gas
HCCI	homogeneous charge compression ignition
HCNG	hydrogen enriched compressed natural gas
HVO	hydro-treated vegetable oil
H_2	hydrogen
LNG	liquefied natural gas
NG	natural gas
PV	photovoltaics
RES	renewable energy source
RCCI	reactivity controlled compression ignition
SI	spark ignition
UGB	university research grant
US	United States

Bibliography

[1] Albayrak B. Use of hydrogen-methane blends in internal combustion engines. InTech 2012. https:/doi.org/10.5772/50597

[2] Alrazen HA, Ahmad KA. HCNG fueled spark-ignition (SI) engine with its effects on performance and emissions. Renew Sust Energ Rev. 2018;82:324-342. https:/doi.org/10.1016/j.rser.2017.09.035

[3] Costain. Blue or green hydrogen: what colour will the fuel of the future be? https://www.costain.com/news/insights/blue-or-green-hydrogen-what-colour-will-the-fuel-of-the-future-be/ (accessed on May 20, 2023).

[4] Cummins. Hydrotreated vegetable oil (HVO) explained. https://www.cummins.com/news/2022/07/01/hydrotreated-vegetable-oil-hvo-explained (accessed on May 21, 2023).

[5] Direct injection for dual fuel stratification (DDFS): Improving the control of heat release in advanced IC engine combustion strategies. ERC Wisconsin. https://erc.wisc.edu/publications/direct-injection-for-dual-fuel-stratification-ddfs-improving-the-control-of-heat-release-in-advanced-ic-engine-combustion-strategies/ (accessed on May 24, 2023).

[6] Dual-fuel engines. Southwest Research Institute. https://www.swri.org/dual-fuel-engines (accessed on May 27, 2023)

[7] Euronews. In win for Germany, EU agrees to exempt e-fuels from 2035 ban on new sales of combustion engines. https://www.euronews.com/my-europe/2023/03/28/in-win-for-germany-eu-agrees-to-exempt-e-fuels-from-2035-ban-on-new-sales-of-combustion-en (accessed on May 18, 2023).

[8] European Environment Agency. CO_2 emissions of new heavy-duty vehicles in Europe. https://www.eea.europa.eu/publications/co2-emissions https://scied.ucar.edu/activity/solving-carbon-dioxide-problem (accessed on May 21, 2023).
[9] Forbes. Emergency electrical generators. https://www.forbes.com/home-improvement/contractor/emergency-electrical-generators/ (accessed on May 11, 2023).
[10] Gemma Power Systems. Dighton Power Project. https://www.gemmapower.com/portfolio/dighton-power-project/ (accessed on May 16, 2023).
[11] Global Energy Observatory. Power Plants – Gas. http://globalenergyobservatory.org/list.php?db=PowerPlants&type=Gas (accessed on May 17, 2023).
[12] Global Energy Observatory. Power Plants – Oil. http://ec2-184-73-254-120.compute-1.amazonaws.com/list.php?db=PowerPlants&type=Oil (accessed on May 16, 2023).
[13] Grabner P, Wimmer A, Gerbig F, Krohmer A. Hydrogen as a fuel for internal combustion engines - properties, problems and chances. 5th International Colloquium Fuels. 2005, 3-13.
[14] Haghighi K, McTaggart-Cowan GP. Modelling the impacts of hydrogen–methane blend fuels on a stationary power generation engine. Energies. 2023;16:2420. https:/doi.org/10.3390/en16052420
[15] Haldor Topsøe. Sustainable aviation fuel. https://www.topsoe.com/sustainable-aviation-fuel?gclid=EAIaIQobChMIjejEvMWN_wIVCLwYCh1OvApGEAAYBCAAEgLmWfD_BwE (accessed on May 31, 2023).
[16] Heywood JB. Internal combustion engine fundamentals. 2nd Edition. New York: McGraw-Hill Education 2018.
[17] Huang G, Li Z, Zhao W, Zhang Y, Li J, He Z, Qian Y, Zhu L, Lu X: Effects of fuel injection strategies on combustion and emissions of intelligent charge compression ignition (IC-CI) mode fueled with methanol and biodiesel. https://doi.org/10.1016/j.fuel.2020.117851.
[18] IAV. E-fuels: power of the future. https://www.iav.com/en/what-moves-us/e-fuels-power-of-the-future/ (accessed on May 19, 2023).
[19] Ilyushin PV, Pazderin AV. Approaches to organization of emergency control at isolated operation of energy areas with distributed generation. In: 2018 International Ural Conference on Green Energy (UralCon). Chelyabinsk, Russia; 2018:149-155. https:/doi.org/10.1109/URALCON.2018.8544361
[20] Ingo C, Tuuf J, Björklund-Sänkiaho M. Impact of hydrogen on natural gas compositions to meet engine gas quality requirements. Energies. 2022;15:7990. https:/doi.org/10.3390/en15217990
[21] International Renewable Energy Agency (IRENA). Decarbonising shipping: a pathway to decarbonise the shipping sector by 2050. 2021.
[22] International Research Association. A comparative study of lean NO_x emission prediction techniques for combustion engines. International Research Journal of Engineering and Technology (IRJET). 2016;3(7):1231-1234. http://www.pubs.iscience.in/journal/index.php/ira/article/view/758
[23] International Transport Forum (ITF). Potential of e-fuels to decarbonise ships and aircraft. https://www.itf-oecd.org/sites/default/files/docs/potential-efuels-decarbonise-ships-aircraft.pdf (accessed on May 19, 2023).
[24] Jamrozik A, Tutak W, Grab-Rogaliński K. An experimental study on the performance and emission of the diesel/CNG dual-fuel combustion mode in a stationary CI engine. Energies. 2019;12:3857. https:/doi.org/10.3390/en12203857
[25] Karczewski M, Chojnowski J, Szamrej G. A review of low-CO2 emission fuels for a dual-fuel RCCI engine. Energies. 2021;14(2):383. https:/doi.org/10.3390/en14020383
[26] Klimstra J, Hotakainen M. Smart power generation – The future of electricity production. Vaasa, Helsinki, Finland: Publisher 2021.
[27] Kuiken K. Gas- and dual-fuel engines: for ship propulsion, power plants and cogeneration: from 0 to 100,000 kW; target global energy training. Onnen, The Netherlands 2016.
[28] Luo S, Ma F, Mehra R, Huang Z. Deep insights of HCNG engine research in China. Fuel. 2019;263:116612. https:/doi.org/10.1016/j.fuel.2019.116612
[29] Ma F, Mehra RK. Study of quasi-dimensional combustion model of hydrogen- enriched compressed natural gas (HCNG) engines. IntechOpen 2016. https:/doi.org/10.5772/65753
[30] MAN Diesel. MAN B&W G95ME-C9.2-TII Project Guide. May 2014. p. 16. https://man-es.com/applications/projectguides/2stroke/content/printed/G95ME-C9_2.pdf (accessed on May 27, 2023).
[31] MAN Diesel. MAN B&W S80ME-C9.4-TII Project Guide. May 2014. https://man-es.com/applications/projectguides/2stroke/content/printed/S80ME-C9_4.pdf (accessed on May 31, 2023).
[32] Maritime News. Top 15 Shipowning Countries. http://infomaritime.eu/index.php/2021/08/22/top-15-shipowning-countries/ (accessed on May 12, 2023).
[33] Mehra RK, Duan H, Luo S, Rao A, Ma F. Experimental and artificial neural network (ANN) study of hydrogen enriched compressed natural gas (HCNG) engine under various ignition timings and excess air ratios. Appl Energ. 2018;228: 736-754. https:/doi.org/10.1016/j.apenergy.2018.06.085
[34] Melaina MW, Antonia O, Penev M. Blending hydrogen into natural gas pipeline networks: a review of key issues. NREL Report, USA 2013. https://www.nrel.gov/docs/fy13osti/51995.pdf
[35] Methanol Institute. Renewable methanol. https://www.methanol.org/renewable/ (accessed on May 22, 2023).
[36] Mitianiec W. Factors determing ignition and efficient combus-tion in modern engines operating on gaseous fuels. IntechOpen 2012. https:/doi.org/10.5772/48306
[37] Natural gas engines for heavy-duty applications. DieselNet Technology Guide. https://dieselnet.com/tech/engine_natural-gas_heavy-duty.php (accessed on May 27, 2023).
[38] Natural Petroleum Council. Hydrogen enriched compressed natural gas (HCNG). https://www.npc.org/FTF_Topic_papers/25-HCNG.pdf (accessed on May 20, 2023).
[39] Oni BA, Sanni SE, Ibegbu AJ, Aduojo AA. Experimental optimization of engine performance of a dual-fuel compression-ignition engine operating on hydrogen-compressed natural gas and Moringa biodiesel. Energy Reports. 2021;7: 607-619. https:/doi.org/10.1016/j.egyr.2021.01.019
[40] Our world in data. CO_2 emissions from transport. https://ourworldindata.org/co2-emissions-from-transport (accessed on May 17, 2023).
[41] Pandey V, Badruddin IA, Khan TMY. Effect of H_2 blends with compressed natural gas on emissions of SI engine having modified ignition timings. Fuel. 2022;321:123930. https:/doi.org/10.1016/j.fuel.2022.123930

[42] PDPU. Hydrogen-compressed natural gas. https://www.pdpu.ac.in/downloads/3%20Hydrogen-Compressed-Natural-Gas.pdf (accessed on May 20, 2023).
[43] Pilot test report: Argonon. LNG Binnenvaart. https://lngbinnenvaart.eu/wp-content/uploads/2020/09/pilot-test-report-argonon.pdf#page=13&zoom=auto,-202,21 (accessed on May 28, 2023).
[44] RCCI engine operation towards 60% thermal efficiency. https://www.researchgate.net/publication/267927464_RCCI_Engine_Operation_Towards_60_Thermal_Efficiency (accessed on May 31, 2023).
[45] Reitz DR, Duraisamy G. Review of high efficiency and clean reactivity controlled compression ignition (RCCI) combustion in internal combustion engines. Prog Energ Combust. 2015;46:12-71. https:/doi.org/10.1016/j.pecs.2014.10.003
[46] Reuters. EU, German deal maps legal path for e-fuel cars after 2035. https://www.reuters.com/business/autos-transportation/eu-german-deal-maps-legal-path-e-fuel-cars-after-2035-document-2023-03-27/ (accessed on May 18, 2023).
[47] Surygała J. Wodór jako paliwo. Wydawnictwa Naukowo-Techniczne. Warsaw 2008.
[48] Szamrej G. Homogeneous mixture CI engines as a key to the further development of IC piston engines. Biuletyn Wojskowej Akademii Technicznej. 2021;70(4):15-58. https:/doi.org/10.5604/01.3001.0016.0535
[49] Szamrej G, Karczewski M, Chojnowski J. A review of technical solutions for RCCI engines. Combustion Engines. 2022;189(2):36-46. https://doi.org/10.19206/CE-142551
[50] Taylor Wessing. Q&A energy and infrastructure: Fit for 55. 2022. https://www.taylorwessing.com/en/insights-and-events/insights/2022/01/q-and-a-energy-and-infrastructure-fit-for-55 (accessed on May 22, 2023).
[51] The New York Times. Cold Arctic Blast Weather Updates. https://www.nytimes.com/live/2023/02/04/nyregion/cold-arctic-blast-weather (accessed on May 15, 2023).
[52] UCAR Center for science education. Solving the carbon dioxide problem. https://scied.ucar.edu/activity/solving-carbon-dioxide-problem (accessed on May 10, 2023).
[53] U.S. Energy information administration. New England Dash-board – Electricity. https://www.eia.gov/dashboard/newengland/electricity (accessed on May 14, 2023).
[54] Wikipedia. Brake-specific fuel consumption. https://en.wikipedia.org/wiki/Brake-specific_fuel_consumption (accessed on May 26, 2023).
[55] Wikipedia. Motor vehicles. https://en.wikipedia.org/wiki/Motor_vehicles (accessed on May 14, 2023)
[56] World Resources Institute. Global Power Plant Database. https://datasets.wri.org/dataset/globalpowerplantdatabase (accessed on May 16, 2023).
[57] World Shipping Council. Fuel EU maritime: Can do more. https://www.worldshipping.org/news/fueleu-maritime-can-do-more (accessed on May 19, 2023).

Janusz Chojnowski, MEng. – Faculty of Mechanical Engineering, Military University of Technology in Warsaw, Poland.
e-mail: *janusz.chojnowski@wat.edu.pl*

Grzegorz Aleksander Szamrej, MEng. – Faculty of Mechanical Engineering, Military University of Technology in Warsaw, Poland.
e-mail: *grzegorz.szamrej@wat.edu.pl*

Mirosław Karczewski, DEng. – Faculty of Mechanical Engineering, Military University of Technology in Warsaw, Poland.
e-mail: *miroslaw karczewski@wat.edu.pl*

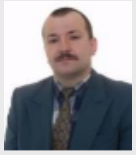

Article citation info:
Laskowski P, Zimakowska-Laskowska M. The problem of emission of total particulate matter and heavy metals from tribological systems in vehicles. Combustion Engines. 2024;198(3):13-19. https://doi.org/10.19206/CE-183121

Piotr LASKOWSKI
Magdalena ZIMAKOWSKA-LASKOWSKA

Combustion Engines
Polish Scientific Society of Combustion Engines

The problem of emission of total particulate matter and heavy metals from tribological systems in vehicles

ARTICLE INFO

Received: 5 September 2023
Revised: 20 January 2024
Accepted: 25 January 2024
Available online: 13 April 2024

The article presents the problem of particulate matter and heavy metal emissions from the tribological systems (road abrasion, brake and tyre wear) road of cars equipped with internal combustion engines (ICEs), battery electric vehicles (BEVs), hybrids and plug-in vehicles (PHEVs). The results of mathematical modelling carried out for obtaining of the emissions of particulate matter and heavy metals, such as As, Cd, Cr, Cu, Ni, Pb, Se and Zn, resulting from road abrasion, brakes and tyre wear, are presented. Emissions are shown depending on the average speed and type of traffic (traffic in the city (urban), outside the city (rural) and on the highway) and the type of vehicle.

Key words: *BEV, ICE, heavy metals, particulate matters, emission*

1. Introduction

According to the source, the particles emitted due to the automobile's operation can be divided into spent traffic-related particles and unused traffic-related particles emitted due to the incomplete combustion of fuel and lubricants during combustion. trial. They are either generated from unused traffic-related sources or exist as materials already deposited in the environment, only to be disturbed again by traffic-induced turbulence. Particulate matter emissions have been well studied and characterized, and technological improvements have led to significant emission reductions [4, 5, 17]. On the other hand, decommissioning processes are still insufficiently studied and several questions remain unanswered regarding the physicochemical properties, emission factors and harmful health effects of wear particles [4, 5, 17]. The most important wear processes leading to direct particulate matter (PM) and heavy metals emissions are tire, brake, clutch and road wear. Other potential causes include engine wear, worn wheel bearings, corrosion of other vehicle parts, street furniture and fences [4, 5, 17].

Airborne particles are generated when the tyres of a car interact with the road and when the brakes are used to reduce the speed. The main factor responsible for this is the shear forces created by the friction between the surfaces. Additionally, when the surfaces become hot due to contact, the evaporation of material from the surfaces can also contribute to particle production [13].

Tyre wear

Vehicle tyres carry the load of the vehicle and passengers, provide traction and steering, and absorb changes in the road surface, improving the ride quality. The tyre consists of a complex rubber mixture, though the precise ingredients used in commercially available tyres are usually not made publicly available for commercial reasons. According to a study by Camatini et al. [2], the typical composition of passenger car tyres is 75% styrene butadiene rubber, 15% natural rubber, and 10% polybutadiene. Different types of elements are blended into the mixture to achieve the desired characteristics during the manufacturing process and to ensure the expected road conditions. One of the most important additives is zinc oxide (ZnO), which acts as a vulcanizer. According to Smolders and Degryse [16], the typical concentration of ZnO in the tyre tread ranges from 1.2% (passenger cars) to 2.1% (trucks) [13].

The friction created between the tyre tread and the road surface is the source of complex physical and chemical process that affect the wear of the tyre. As a result, the particles released from the tyre and those on the road surface are connected, and wear particles on the road surface are inextricably linked [13].

The amount your tyres wear down is based on a various parameter like what type of tyres you have, where they're located, what they're made of, their condition and age, the weight of your vehicle and its frame, the way of driving (speeding, starting and stopping, taking corners), what the road surface type is like, and meteorological conditions, mainly the air temperature and moisture. The way you drive affects how quickly your car wears down. Even when the car is going at a steady speed, the tyre still has a tiny amount of slipping on the road – this is what gives it a grip. As the driving dynamics increase (cornering, braking, acceleration) in response to greater forces generated at the surface-tyre interface, slippage occurs, which may cause additional wear of both the tyre and the road surface. Therefore, 'smooth' driving extends the life of the tyre and *vice versa*. The tyre's lifetime decreases as the intensity of intense or transient vehicle operation increases [13].

Brake wear

Currently, two brake system designs are being employed: disc brakes, in which flat brake pads press against a spinning metal disc, and drum brakes, in which curved pads press against the interior of a spinning cylinder. Disc brakes are typically installed in more diminutive vehicles (passenger cars and motorcycles) as well as the front wheels of light trucks. Drum brakes, which have been in use for a longer period of time, are more common in larger vehicles, though disc brakes are becoming more prevalent in newer heavy-duty vehicles.

Currently are used the two main brake system configurations: disc brakes, where flat brake pads are pressed against a rotating metal disc, and drum brakes, where curved pads are pressed against the inside surface of a rotating cylinder. Disc brakes are typically used on smaller vehicles (cars and motorcycles) and the front wheels of light trucks. Traditionally, the drum brakes are used on heavier vehicles, although disc brakes are increasingly used on newer heavy-duty vehicles [3, 13].

The components of brake linings consist of binders, fibers, fillers, and friction modifiers which can all be thermoresistant. The binders are modified phenol-formaldehyde resins and the fibers come in metallic, mineral, ceramic, and aramid varieties like steel, copper, brass, potassium titanate, glass, asbestos, organic material, or Kevlar. Fillers are usually inexpensive materials such as barium and antimony sulphate, kaolinite clays, magnesium and chromium oxides, or metal powders. Friction modifiers can be organic, inorganic, or metallic and graphite is the most commonly used modifier, but cashew dust, ground rubber, and soot are also used. Asbestos fibers were once used in brake pads, but have been completely banned in the European fleet [14].

The brake wear material's chemical composition depends on the manufacturer, the application used (car, truck, etc.), and the targeted properties of the brake pads. Studies from Legret and Pagotto [11] and Hildemann et al. [7] suggest the pads are generally composed of primarily metals coupled with silicon composites. Iron typically contributes up to 46%, copper up to 14%, organic material around 13%, and then a few other metals such as lead (~4%), zinc (~2%), calcium, and barium [15].

The abrasion of tyres and brakes leads to the emission of particulate matter (PM) and heavy metals, such as arsenic (As), cadmium (Cd), chromium (Cr), copper (Cu), nickel (Ni), lead (Pb), selenium (Sn) and zinc (Zn). This article, in particular, focuses on the air quality assessment of particulate matter, lead, arsenic, cadmium and nickel, since there are national regulations and EU directives that set limits for such substances to ensure human and plant health is protected.

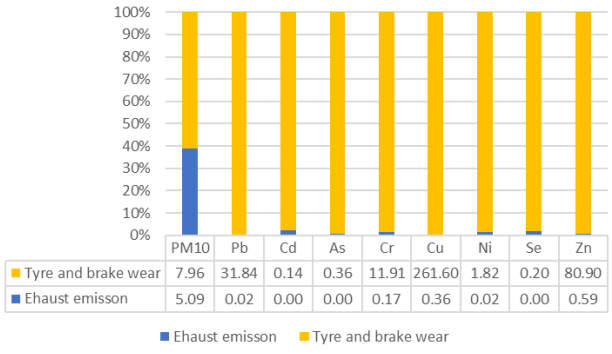

	PM10	Pb	Cd	As	Cr	Cu	Ni	Se	Zn
Tyre and brake wear	7.96	31.84	0.14	0.36	11.91	261.60	1.82	0.20	80.90
Ehaust emisson	5.09	0.02	0.00	0.00	0.17	0.36	0.02	0.00	0.59

Fig. 1. Percentage of emissions from tyre and brake wear (as a sum) and exhaust system

For road traffic, it is expected to assume that most primary particulates are emitted from exhaust gases and that most coarse particles originate from sources other than exhaust gases. This is not accurate, as there is much evidence to suggest that non-exhaust particles contribute to both fine and coarse PM10. While there are a number of studies that report that the contribution of exhaust and non-exhaust sources to total traffic-related PM10 emissions is roughly equal, it is expected that the contribution of non-exhaust sources will increase in the future due to continued reductions in emissions [4, 5, 17]. The National Centre for Emissions Management (KOBiZE) [12] has estimated that the emission of particulate matter and heavy metals from abrasion in 2021 was greater than that from exhaust systems, which is illustrated in Fig. 1.

2. Materials and methods

For modelling purposes, COPERT software was used for implementing the Tier 3 methodology [13]. COPERT is a software tool, coordinated by the EEA, and widely used for the mathematical modelling of air pollutant emissions from mobile sources.

The COPERT model was utilized for the mathematical air emissions estimation by employing the EMEP Guidebook [13] recommendations. This general equation was used for separate calculations of the emissions from tyre wear and brake wear:

$$T_E = \sum_j N_j \times M_j \times EF_{TSP,s,j} \times f_{s,i} \times S_s(V) \qquad (1)$$

where: T_E – the total amount of emissions released within a certain time period and geographical area [g], N_j – the number of cars in category j within the specified region, M_j – the distance in kilometres that each vehicle of category j travelled during the pre-designated time frame, $EF_{TSP,s,j}$ – the mass emission factor for total suspended particulates (TSP) for vehicles in category j [g/km], $F_{s,I}$ – mass fraction of TSP that can be attributed to particle size class i, $S_s(V)$ – the adjustment needed for an average vehicle travelling at speed V.

The index j is associated with the type of vehicle, while the index s indicates where the particulate matter (PM) originated from, either tyre (T) or brake (B) wear. The particle size classes i include TSP, PM10, PM2.5, PM1 and PM0.1.

For their math modelling, the authors employed the COPERT software to calculate emissions. They followed the directions in the EMEP Guidebook 2019 [13] which is a standard of air pollutant emission inventories.

Based on the applied methodology, driving is split into three types due to the most frequent driving conditions: urban, rural, and highway.

In this section, the authors used COPERT (Computer Programme to Calculate Emissions from Road Traffic), a complex modelling software tool for calculating air pollutant emissions from road transport. The applied methodology followed d the EMEP (European Monitoring and Evaluation Programme) Guidebook 2019 [13] guidelines.

Using the COPERT model made estimating emissions following international and EU law requirements possible. Road transport emissions estimates were based on the following:

– fuel consumption
– engine size
– number of vehicles per category

– vehicle weight
– emissions control technology
– mileage per vehicle class
– share per road class (urban, rural, and highway)
– average speed per vehicle type and per road class
– monthly temperature (minimum and maximum)
– fuel characteristics.

In the case of the simulation presented in the article, the most important input data are the vehicle mass, mileage per vehicle class, share per road class (urban, rural, and highway); average speed per vehicle type and road class.

The mathematical approach included in the COPERT software is classified as a "Tier 3" approach for quantitative emissions assessment. It should be emphasized that all of the emissions factors included in the COPERT model were determined based on laboratory testing under the WLTP driving cycle [13, 20].

The estimations were conducted based on the following basic assumptions: the estimates were made assuming that one vehicle travelled 10,000 km. Equal shares of vehicle traffic in the urban, rural and highway were assumed. It was also assumed that cars drive at average speeds type of traffic: urban, rural and highway of 31.5 km/h, 70 km/h and 120 km/h, respectively.

Based on the mathematical modelling, the authors want to check the following dependencies:

– the influence of the type of vehicles on tyre and brake wear particulate matter and heavy metals emissions; to simulation only passenger cars were used for the simulation (internal combustion engines (ICE) with various types of fuel, hybrid, plug-in (PHEV) and battery electric vehicles (BEV)) on emissions
– the influence of the type of traffic (urban, rural and highway) on the on tyre and brake wear particulate matter and heavy metals emission
– the influence of the average velocity on tyre and brake wear particulate matter and heavy metals emissions.

Simulations were carried out for two types of emissions: brake wear and tyre wear.

3. Results

This method enabled the simulations depicted in Fig. 2 through 9, which demonstrate the effect of the vehicle type on tyre and brake wear emissions. In the simulations, only passenger cars such as internal combustion engine, hybrid, plug-in, and battery electric vehicles were utilized for tyre and brake wear emissions.

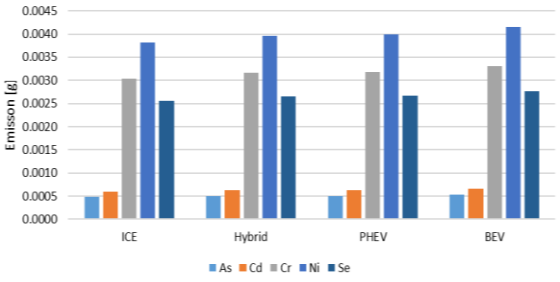

Fig. 2. The influence of vehicle type on tyre wear heavy metals (arsenic, cadmium, chromium, nickel and selenium) emissions

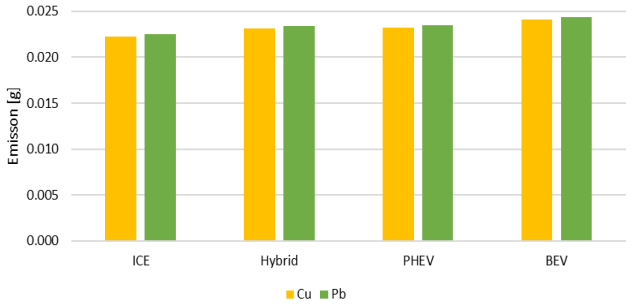

Fig. 3. The influence of vehicle type on tyre wear heavy metals (copper, lead) emissions

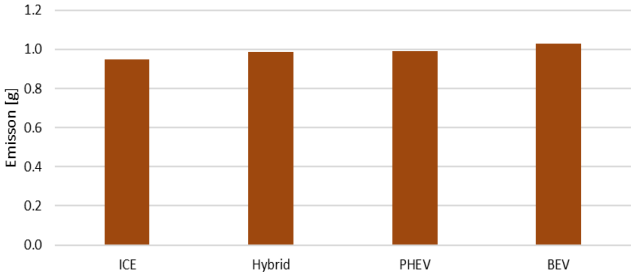

Fig. 4. The influence of vehicle type on tyre wear heavy metals (zinc) emissions

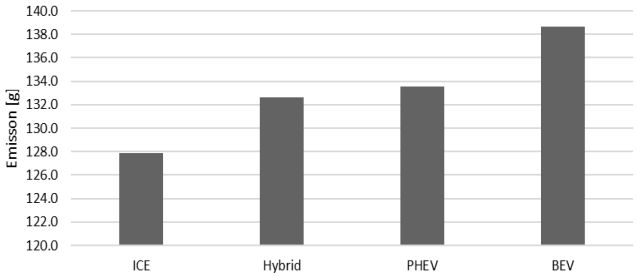

Fig. 5. The influence of vehicle type on tyre wear particulate matter emissions

The Fig. 2–5 shows that the emission of heavy metals particulate matter from tyre wear, the emission from BEV is the highest, and in the case of ICEV – the lowest. There is a slight difference in emissions from Hybrid and PHEV for the heavy metals emission simulated. The weight of the vehicles most likely causes this relationship; BEVs are the heaviest of the vehicles tested.

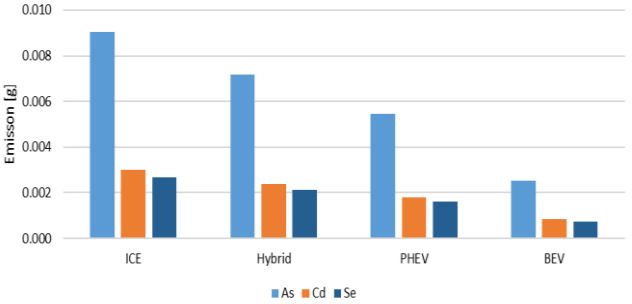

Fig. 6. The influence of vehicle brake wear on tyre wear heavy metals (arsenic, cadmium, selenium) emissions

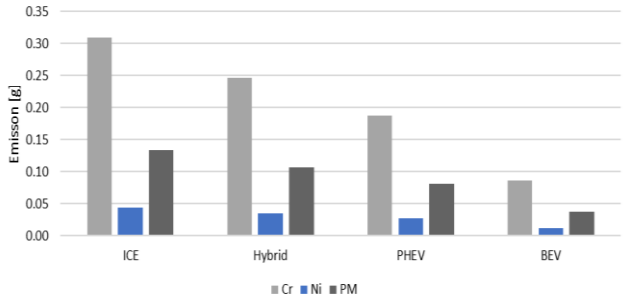

Fig. 7. The influence of vehicle brake wear on tyre wear heavy metals (chromium, nickel) and particulate matter emissions

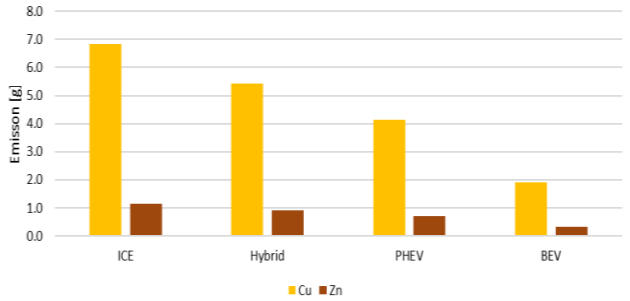

Fig. 8. The influence of vehicle brake wear on tyre wear heavy metals (copper, zinc) emissions

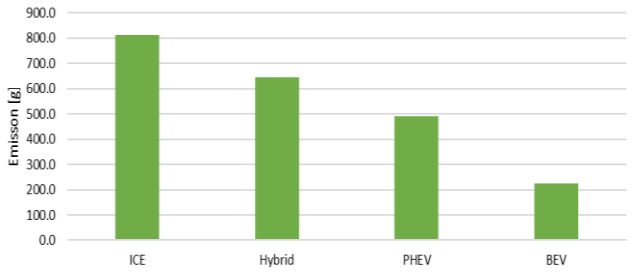

Fig. 9. The influence of vehicle brake wear on tyre wear heavy metals (lead) emissions

In contrary to the case of emissions from tyre abrasion, emissions from brake abrasion are the highest for ICE cars and the lowest for BEVs. There is also a noticeable difference in particulate matter and heavy metal emissions for hybrid and PHEV, with lower emissions for PHEV. The lower emissions for BEV, PHEV and hybrid than for ICEv are due to the use of regenerative braking in electric and hybrid vehicles (Fig. 6–9).

The particulate matter emissions from tyre wear shown in Fig. 5 are higher for BEVs, with significantly lower emissions for ICE cars. In the case of heavy metals (Fig. 2 and 9), there is no significant difference in tyre abrasion emissions, but there is a noticeable relationship that these emissions are higher for BEV.

On the other hand, the relationship is reversed in the case of brake wear. For BEV, attrition emissions for all pollutants tested are lower than for ICE, hybrid and plug-in (Fig. 6–9).

Figures 10 to 18 show the influence of the type of traffic (urban, rural and highway) on the tyre and brake wear emission.

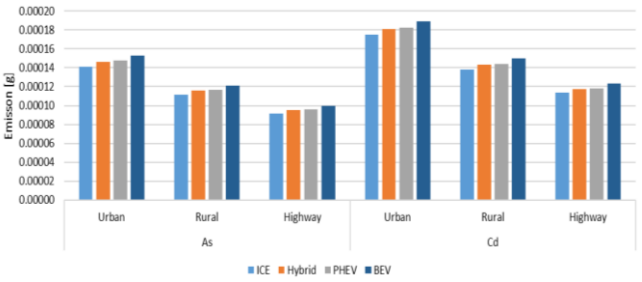

Fig. 10. The influence of the type of traffic (urban, rural and highway) on the tyre wear heavy metals (arsenic, cadmium) emission

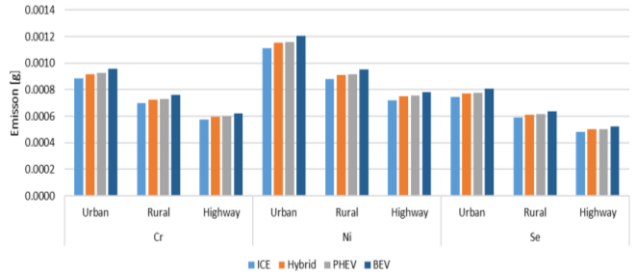

Fig. 11. The influence of the type of traffic (urban, rural and highway) on the tyre wear heavy metals (chromium, nickel, selenium) emission

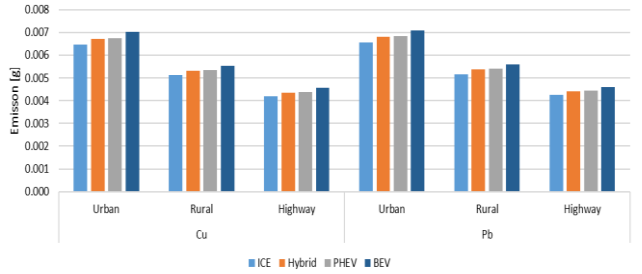

Fig. 12. The influence of the type of traffic (urban, rural and highway) on the tyre wear heavy metals (copper, lead) emission

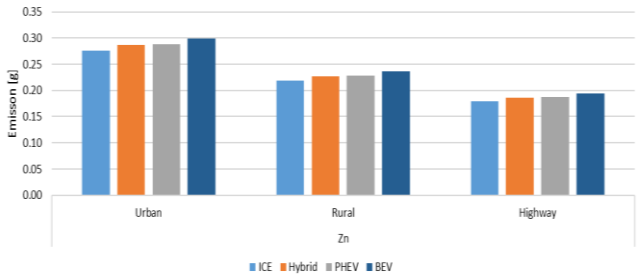

Fig. 13. The influence of the type of traffic (urban, rural and highway) on the tyre wear heavy metals (zinc) emission

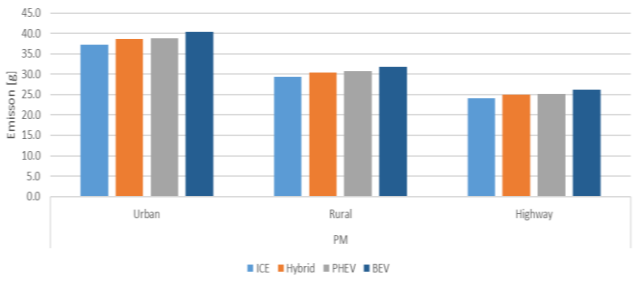

Fig. 14. The influence of the type of traffic (urban, rural and highway) on the tyre wear particulate matter emission

There is a visible dependency that emissions from tyre abrasion are highest in cities, where vehicles constantly brake while driving in traffic congestion, which causes higher abrasion.

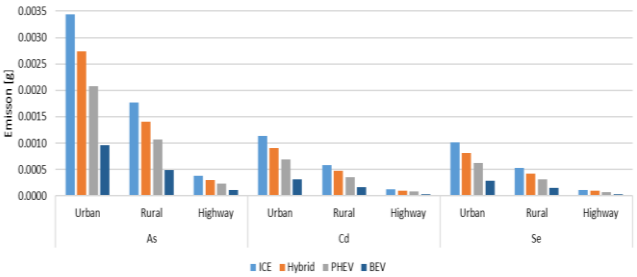

Fig. 15. The influence of the type of traffic (urban, rural and highway) on the brake wear heavy metals (arsenic, cadmium, selenium) emission

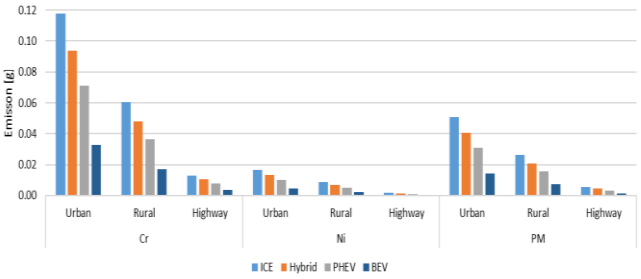

Fig. 16. The influence of the type of traffic (urban, rural and highway) on the brake wear heavy metals (chromium, nickel) and particulate matter emission

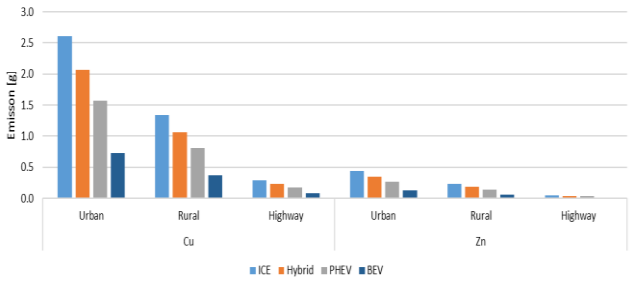

Fig. 17. The influence of the type of traffic (urban, rural and highway) on the brake wear heavy metals (copper, zinc) emission

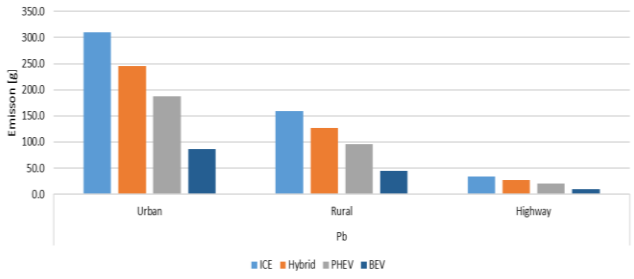

Fig. 18. The influence of the type of traffic (urban, rural and highway) on the brake wear heavy metals (lead) emission

Figures 10 to 18 show a noticeable relationship between higher emissions from abrasion of tyres and brake wear in urban areas and significantly lower highway emissions. In the case of this simulation, there also occurs a dependency between higher emissions from tyre wear for BEV compared to other types of drive and lower emissions from brake wear for this type of vehicle.

Figures 19 to 22 show the influence of the average velocity on the tyre and brake wear emissions.

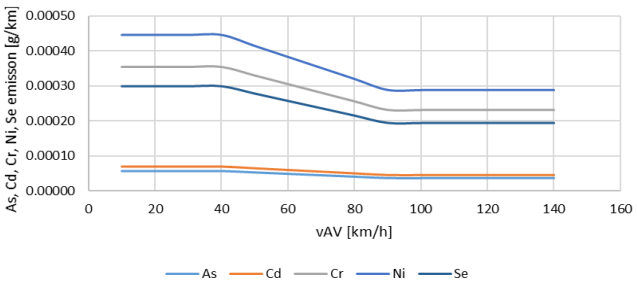

Fig. 19. The influence of the average velocity on the tyre heavy metals (arsenic, cadmium, chromium, nickel, selenium) emissions

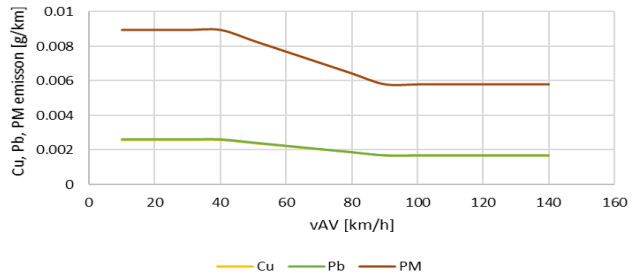

Fig. 20. The influence of the average velocity on the tyre heavy metals (chromium, lead) and particulate matter emissions

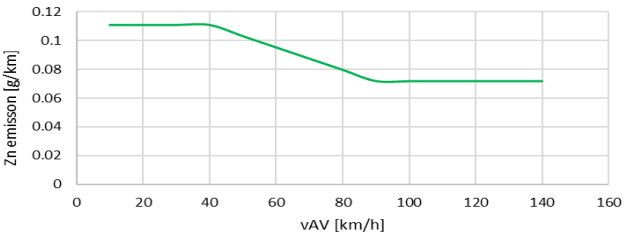

Fig. 21. The influence of the average velocity on the tyre heavy metals (zinc) emissions

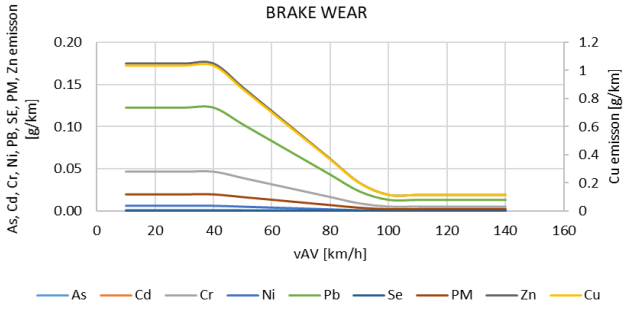

Fig. 22. The influence of the average velocity on the break wear heavy metals (arsenic, cadmium, chromium, copper, nickel, lead, selenium and zinc) and particulate matter emissions

Similarly, to the simulations presented in Fig. 10 to 18, and in Fig. 19 to 22, it can be seen that the higher the speed, the lower the emission of heavy metals and particulate matter from tyre and brake abrasion.

4. Discussion

The weight of a BEV is greater than that of an ICE vehicle, resulting in an impact on tyre wear. Figures 2 to 9 illustrate that BEVs, hybrids, and plug-ins all have higher emissions for all pollutants. This finding is supported by other studies, such as by Timmers and Achten [19], which found that electric vehicles are 24% heavier than their non-electric counterparts, weighing an additional 280 kg.

Beddows and Harrison [1] recently conducted a study that compared battery electric and combustion engine vehicles based on power output. On average, electric cars had a weight increase of 258 kg and 314 kg in comparison to petrol and diesel cars, resulting in an increase of 7–10% for PM10 and PM2.5 emissions from tyre wear.

The studies by Beddows & Harrison [1], and by Liu et al. [11] both indicated a similar rise in tyre wear. The study [11] also revealed the differences between small, medium and large internal combustion engine vehicles, with an average of 10–20% variation between the segments. Woo et al. [21] analysed that a 20% increase in vehicle weight would lead to a 15–20% growth in tyre wear emissions. Tests conducted by the Emissions Analytics in real-world conditions demonstrated that for a 500kg increase in vehicle weight, tyre wear emissions increased by 21%. Lastly, Oroumiyeh and Zhu [14] measured the tyre wear of small, medium and large vehicles, finding that the tyre wear was proportional to the vehicle weight.

It has been observed that the correlation between tyre abrasion and emissions is not observable for emissions from brake wear. This has been corroborated in various studies, including by Beddows & Harrison [1], which demonstrated that a heavier vehicle weight in electric vehicles leads to a 10–15% increase in brake wear, and consequently, non-exhaust emissions.

The research [20] resulted in the same conclusion about the influence of body mass on brake wear emissions. They discovered that a 20% rise in the weight of a vehicle caused a 15–20% increase in emissions. The research resulted in the same conclusion about the influence of body mass on brake wear emissions. Moreover, they discovered that a 20% rise in the mass of a vehicle caused a 15–20% increase in emissions.

The findings showed that there was a 9–17% reduction in the emission rates of PM10 and PM2.5 from brakes when the weight of the battery electric vehicle was increased. It is also worth noticing that electric vehicles typically come with regenerative braking which is a system that takes the energy from braking and turns it into electricity, which can then be used to power the vehicle and aid in acceleration.

More research is necessary to understand the emission reduction potential of brakes [12]. However, preliminary measurements by Hagino et al. [6], Stanard et al. [18], and Koupal et al. [8] suggest that the brakes can reduce emissions significantly.

5. Conclusion

It is expected that vehicles will brake more frequently in congested areas, leading to higher emissions from abrasion. This fact is supported by mathematical modelling, which is illustrated in Fig. 10 to 18. Emissions from tyres and brake wear in urban areas are significantly higher than on the highways.

As demonstrated by Fig. 19 to 22, the faster average driving speed, the less the tyre wear, likely due to the fact that city driving usually involves more braking and turning than highway driving does.

It is anticipated that decarbonizing and advocating for BEV will result in the elimination of emissions from exhaust systems. However, this may create further issues with particulate matter and heavy metal emissions due to tyre and brake abrasion. This may lead to people inhaling heavy metal dust, which can result in future severe health consequences.

Acknowledgements

This work was supported by the Faculty of Automotive and Construction Machinery Engineering Warsaw University of Technology.

Nomenclature

As	arsenic
BEV	battery electric vehicle
Cd	cadmium
Cr	chrome
Cu	copper
ICE	internal combustion engine
Ni	nickel
Pb	lead
PHEV	plug-in
PM	particulate matter
Se	selenium
Zn	zinc

Bibliography

[1] Beddows DCS, Harrison RM. PM10 and PM2.5 emission factors for non-exhaust particles from road vehicles: dependence upon vehicle mass and implications for battery electric vehicles. Atmos Environ. 2021;244:117886. https://doi.org/10.1016/j.atmosenv.2020.117886

[2] Camatini M, Crosta GF, Dolukhanyan T, Sung C, Giuliani G, Corbetta GM et al. Microcharacterization and identification of tyre debris in heterogeneous laboratory and environmental specimens. Mater Charact. 2001;46:271-283. https://doi.org/10.1016/S1044-5803(00)00098-X

[3] CEPMEIP, 2003. Co-ordinated European Programme on Particulate Matter Emission Inventories, Projections and Guidance. http://www.air.sk/tno/cepmeip/ (accessed on 19 July 2019).

[4] Dimopoulos Eggenschwiler P, Schreiber D, Habersatter J. Brake particle PN and PM emissions of a hybrid light duty vehicle measured on the chassis dynamometer. Atmosphere. 2023;14(5):784. https://doi.org/10.3390/atmos14050784

[5] Grigoratos T, Martini G. Brake wear particle emissions: a review. Environ Sci Pollut. 2015;22:2491-2504. https://doi.org/10.1007/s11356-014-3696-8
[6] Hagino H. Sensitivity and reproducibility of brake wear particle emission measurements using JARI system. PMP 50th Meeting. 2019.
[7] Hildemann LM, Markowski GR, Cass GR. Chemical composition of emissions from urban sources of fine organic aerosol. Envir Sci Tech. 1991;25:744-759. https://doi.org/10.1021/es00016a021
[8] Koupal J, Denbleyker A, Kishan S, Vedula R, Agudelo C. Brake wear particulate matter emissions modelling. Eastern Research Group, Inc., LINK Engineering Company 2021. CA21-3232. https://rosap.ntl.bts.gov/view/dot/60273
[9] Laskowski PP, Zimakowska-Laskowska M, Zasina D, Wiatrak M. Comparative analysis of the emissions of carbon dioxide and toxic substances emitted by vehicles with ICE compared to the equivalent emissions of BEV. Combustion Engines. 2021;187(4):102-105. https://doi.org/10.19206/CE-141739
[10] Legret M, Pagotto C. Evaluation of pollutant loadings in the runoff waters from a major rural highway. Sci Total Environ. 1999;235:143-150. https://doi.org/10.1016/s0048-9697(99)00207-7
[11] Liu Y, Chen H, Gao J, Li Y, Dave K, Chen J et al. Comparative analysis of non-exhaust airborne particles from electric and internal combustion engine vehicles. J Hazard Mater. 2021;420:126626. https://doi.org/10.1016/j.jhazmat.2021.126626
[12] Ministry of Climate and Environment. 2023. Poland's Informative Inventory Report. Submission under the UNECE CLRTAP and NEC Directive. https://cdr.eionet.europa.eu/pl/eu/nec_revised/iir/envyei5sq/
[13] Ntziachristos L, Boulter P. Road transport. In: EMEP/EEA – 1.A.3.b.vi-vii Road tyre and brake wear. 2019. https://www.eea.europa.eu/publications/emep-eea-guidebook-2019/part-b-sectoral-guidance-chapters/1-energy/1-a-combustion/1-a-3-b-vi/view
[14] Oroumiyeh F, Zhu Y. Brake and tire particles measured from on-road vehicles: effects of vehicle mass and braking intensity. Atmos Environ. 2021;12:100121. https://doi.org/10.1016/j.aeaoa.2021.100121
[15] Rauterberg-Wulff A. Determination of emission factors for tire wear particles by tunnel measurements. 8th International Symposium 'Transport and Air Pollution'. 1999. Graz.
[16] Smolders E, Degryse F. Fate and effect of zinc from tire debris in soil. Envir Sci Tech. 2002;36:3706-3710. https://doi.org/10.1021/es025567p
[17] Sommer F, Dietze V, Baum A, Sauer J, Gilge S, Maschowski C et al. Tire abrasion as a major source of microplastics in the environment. Aerosol Air Qual. 2018;18: 2014-2028. https://doi.org/10.4209/aaqr.2018.03.0099
[18] Stanard A, Tim D, Palacios C, Kishan S. Brake and tire wear emissions. Report for CARB Project 17RD016. 2021. https://ww2.arb.ca.gov/sites/default/files/2021-04/17RD016.pdf
[19] Timmers VRJH, Achten PAJ. Non-exhaust PM emissions from electric vehicles. Atmos Environ. 2016;134:10-17. https://doi.org/10.1016/j.atmosenv.2016.03.017
[20] Wiśniowski P, Gis M. Representativeness of emissions of toxic substances in bench tests reflecting the road traffic conditions of a vehicle. Combustion Engines. 2019;177(2): 88-90. https://doi.org/10.19206/CE-2019-215
[21] Woo SH, Jang H, Lee SB, Lee S. Comparison of total PM emissions emitted from electric and internal combustion engine vehicles: an experimental analysis. Sci Total Environ. 2022;842:156961. https://doi.org/10.1016/j.scitotenv.2022.156961

Piotr Laskowski, DEng. – Faculty of Automotive and Construction Machinery Engineering, Warsaw University of Technology, Poland.
e-mail: *piotr.laskowski@pw.edu.pl*

Magdalena Zimakowska-Laskowska, DEng. – Environment Protection Centre, Motor Transport Institute, Poland.
e-mail: *magdalena.zimakowska-laskowska@its.waw.pl*

Article citation info:
Bebkiewicz K, Szczepański K, Chłopek Z. Simulation studies of pollutant emissions from road vehicles using models for inventories of pollutant emissions. Combustion Engines. 2024;198(3):20-26. https://doi.org/10.19206/CE-184051

Katarzyna BEBKIEWICZ
Krystian SZCZEPAŃSKI
Zdzisław CHŁOPEK

Combustion Engines
Polish Scientific Society of Combustion Engines

Simulation studies of pollutant emissions from road vehicles using models for inventories of pollutant emissions

ARTICLE INFO

Received: 30 November 2023
Revised: 15 January 2024
Accepted: 12 February 2024
Available online: 4 May 2024

Countries are obliged by international regulations to conduct annual pollutant emissions inventories. Road transport is one of the sectors for which an inventory of pollutant emissions is carried out. Determining pollutant emissions from road transport is possible only by modeling these emissions – that is why unified emission models are used. In this work, the COPERT and HBEFA INFRAS software are used to determine pollutant emissions characteristics for various vehicle traffic models. The article presents the principles of modeling pollutant emissions from road vehicles. The rules for qualifying road vehicles into elementary and cumulative categories have been systematized. Models of road vehicle traffic and ways of taking them into account in modeling pollutant emissions are presented. The following emissions of pollutants harmful to the health and life of living organisms are considered: carbon monoxide, non-methane volatile organic compounds, nitrogen oxides and total suspended particles. The trends of the national annual emissions of the tested pollutants for the years 2000–2020 and the results of simulation tests of pollutant emissions models are presented.

Key words: *road transport, air pollutant emissions inventory, emission modeling*

1. Introduction

The aim of the work is to use the procedures applied in the official pollutant emissions inventory from sector of road transport to study the model of this emission. The operating states of combustion engines, that determine emissions of pollutants from combustion engines are [6]:

– engine speed process
– torque process
– thermal state of the combustion engine.

The quantities determining pollutant emissions from road vehicles are [6]:

– vehicle velocity process
– vehicle movement resistance
– thermal state of the combustion engine.

Therefore, in the pollutant emissions inventory from road vehicles, vehicle traffic models are adopted.

Road transport emission inventories are currently performed in every developed country. The inventory of pollutant emissions from mobile sources is compiled using dedicated models of emissions. This is due to the fact that it is not possible to estimate the total emissions from mobile sources using empirical methods, unlike stationary sources. For this reason, it is necessary to use standardized procedures for comparative purposes. In the pollutant emissions inventory, procedures are used in accordance with the guidebook for the national inventories prepared by the Convention's Task Force on Emission Inventories and Projection (TFEIP) and the European Environmental Agency (EEA) [1–3, 10, 18]. To estimate emissions of air pollutants from vehicles, COPERT software is used [13, 14, 19]. This model was developed at Aristotle University of Thessaloniki in cooperation, among others, with the creators of the HBEFA INFRAS AG software [8, 20].

Activities connected to modeling pollutant emissions from road vehicles were also part of the CORINAIR program [15]. Moreover, the European programs COST 319 „Estimation of pollutant emission from transport" [16, 21] and MEET [23] played an important role.

The article aims to use the procedures applied in the official inventory of pollutant emissions from road vehicles to study the model of this emission due to the input data and model parameters:

– the input data characterizes the configuration of road vehicles in relation to the number and intensity of their use in the elementary category
– the model parameters concern the nature of road vehicle movement.

2. Objectives of modeling emissions from road vehicles

The most important objectives of modeling emissions connected with road transport are [3, 26, 27]:

– preparing inventory of pollutant emissions associated with the use of road vehicles in time as well as space, depending on their types and the conditions of use
– examining the influence of road vehicles configuration and operating conditions on road transport pollutant emissions
– assessing the environmental effects of pollutants emitted from road vehicles.

The Polish Air Pollutant Emission Inventory is performed by the National Centre for Emission Management (KOBiZE) at the Institute of Environmental Protection – National Research Institute (IOŚ-PIB). Following Poland's international obligations, reports with the results [24, 25] are provided to the European Union as a result of Directive (EU) 2016/2284 of the European Parliament and the Council of 14 December 2016 on the reduction of national emissions of certain atmospheric pollutants [12, 17] and to the United Nations Economic Commission for Europe under the Convention on Long-Range Transboundary Air Pollution [12].

As a result of KOBiZE's activities in the field of pollution emission inventory, many articles were published, including [3–7, 26, 27].

The paper [3] presents the results of an inventory of pollutants hazardous to the health of living organisms emitted by road transport in Poland between 1990 and 2017. The following substances were analysed: carbon monoxide, non-methane volatile organic compounds, nitrogen oxides and size fractions of particulate matter. The results showed that between 1990 and 2017, annual emissions from road vehicles in Poland had an increasing trend for TSP (74%), PM10 (64%), PM2.5 (52%) and NO_x (25%), while emissions of CO (–117%) and NMLZO (–85%) had a decreasing trend.

The paper [26] presents the results of an inventory of pollutant emissions from road transport in Poland for the period 1990–2020. The energy intensity of road vehicles of the cumulative categories was also studied. Analysis of the energy emission factor of pollutants clearly shows that it is decreasing, except ammonia, which is linked to the use of catalytic reduction systems for nitrogen oxides.

The article [27] analysed the changes in annual national emissions of selected pollutants due to the contribution of these emissions from the cumulative category of road vehicles to total national annual emissions from transport. Road transport has the dominant share in national emissions, and significant progress in reducing emissions can be attributed to significant technical improvements in the internal combustion engines of road vehicles.

The paper [4] investigated the environmental risks posed by particulates generated by road transport. Areas with characteristic traffic conditions were used for the study: within and outside cities, as well as highways and expressways. The obtained results showed that technical progress in the automotive sector contributed largely to reducing the emission of particulate matter contained in exhaust gases, but had a small impact on the emission of particulate matter from tribological processes.

Article [5] presents the results of research on pollutant emissions from road vehicles in cumulative categories depending on traffic conditions: in cities, outside cities, as well as on highways and expressways. Large differences were found in the shares of individual pollutants from vehicles in the tested traffic conditions. This is particularly visible in the case of nitrogen oxides, which have the largest share of emissions outside cities, unlike other substances with the largest share of emissions in cities with heavy traffic.

Paper [6] presents the results of research on the impact of the thermal state of vehicle combustion engines on pollutant emissions in the years 1990–2017. The results show that during engine warm-up, carbon monoxide emissions constitute the largest share (up to 50%) in the national annual total emissions. Next in order are volatile organic compounds, and the lowest is share of nitrogen oxides (less than 5%).

Paper [7] presents the results of the inventory of pollutant emissions from motor vehicles in Poland using COPERT 5 software. The relative increase in emissions of carbon monoxide and non-methane volatile organic compounds is less than 10%, that of nitrogen oxides and particulate matter is less than 15%, and that of carbon dioxide is approximately 14%.

The article [27] included an inventory of pollutant emissions in Poland from various transport categories in the years 1990–2020. The shares of the national annual emission of the tested pollutants from each examined transport category in the total national annual emission from transport were assessed.

Research on the inventory of pollutant emissions from anthropogenic sources is also carried out in other countries

For example, [9] presents the results of an inventory of pollutant emissions from road transport in China. The results of testing the intensity of pollutant emissions in a grid with a high resolution of 0.5° × 0.5° made it possible to determine the distribution of their concentrations using models of the spread of pollutants.

Paper [22] presents the results of an inventory of pollution from various sectors, including road transport, in Jakarta in 2005–2015. To determine the intensity of pollutant emissions, pollutant emission averaged factors for the cumulated categories of road vehicles were used. In the road transport sector, heavy duty vehicles had the largest share in pollutant emissions.

3. Methodology

The following physical quantities are used in modeling emissions associated with road transport activities for the inventory purposes [11]:

- Specific distance emission of pollutants – b_m – that is, the derived emission of pollutants – m, relative to the length of road travelled by the road vehicle – s.

$$b_m = \frac{dm}{ds} \tag{1}$$

- Pollutant emissions intensity – E_m – derivative of pollutant emissions concerning time – t.

$$E_m = \frac{dm}{dt} \tag{2}$$

National annual emission of pollutants, defined as the intensity of national emissions averaged over one calendar year – E_a.

The methodology for simulation studies of road vehicles emissions using emission inventory models includes the following tasks:

1. Systematizing the problems of:
   - modeling pollutant emissions from road transport
   - identification of the model of emissions related with road vehicles.
2. Modeling the nature of road vehicle traffic under given conditions:
   - in urban congestion – Cg
   - in urban with no congestion – U
   - rural – R
   - motorways and highways – H.
3. Simulation studies on the model of pollutant emissions arising from road traffic considering a variety of model inputs in Poland between 2000 and 2020:
   - number of vehicles in individual cumulative categories

– use intensity of road vehicles of cumulative categories
– model parameters.

4. Sensitivity studies of the road vehicles emission model on different vehicle traffic conditions.

The substance pollutants considered in this work, and whose emissions are inventoried are as follows:

– carbon monoxide – CO
– non-methane volatile organic compounds – NMVOC
– nitrogen oxides – NO_x
– total suspended particulate matter – TSP.

Specific distance emissions in the case of road transport are modeled as a function of the average value of the vehicle speed process.

Data for modeling pollutant emissions from road transport in Poland were adopted following official data used in the pollutant emission inventory [24, 25].

4. Modeling the structure of road vehicles

The classification of road vehicles is defined in so-called categories [8, 9]. In general, a category is a set of entities that share certain attributes and are interrelated. The elementary category comprises those vehicles that have the same criterion characteristics. The cumulative category comprises those vehicles, which do not have the same criterion characteristics.

The criterion characteristics for elementary categories [13, 14] are as follows:

– purpose of a road vehicle
– conventional size of the road vehicle
– ecological category due to pollutant emissions
– engine circulation
– fuel type
– type of engine and drive system.

The cumulative categories due to the use of a road vehicle [13, 14] are as follows:

– passenger cars
– light commercial vehicles
– heavy duty trucks
– city buses
– coaches
– L-category road vehicles.

5. Simulation studies on the model of pollutant emissions from road vehicles

5.1. Types of simulation studies

The simulation studies on the pollutant emission model from road vehicles was carried out in accordance with the following program:

– simulation studies of emissions from passenger cars in 2020 based on the HBEFA INFRAS model [20]
– simulation studies of emissions from individual cumulative categories of vehicles between 2000 and 2020 based on the COPERT model [13, 14]
– simulation studies of emissions from passenger cars due to model vehicle traffic conditions based on the HBEFA INFRAS model [20].

5.2. Example results of the emission model simulation studies for passenger cars in 2020

Figures 1–4 show the characteristics of the specific distance emissions from the cumulative category of passenger cars as a function of the average speed.

Specific distance emission are determined for traffic in model conditions (available in the HBEFA INFRA software): urban traffic congestion, urban traffic with no congestion, rural, motorways and highways.

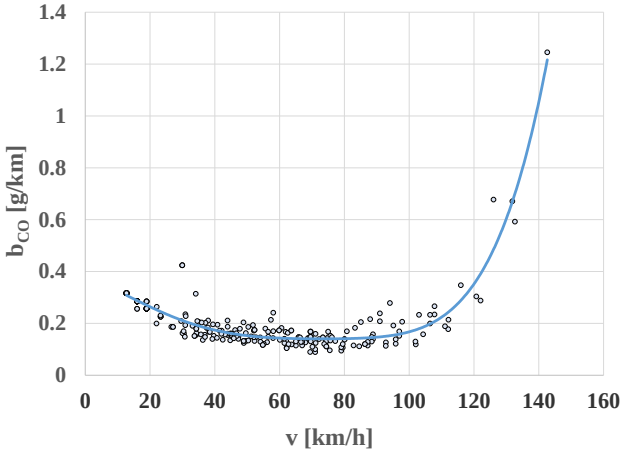

Fig. 1. Characteristics of the specific distance CO emission – b_{CO} depending on the average speed – v of passenger cars

There is a clear increase in specific distance emission of CO as the average speed of the vehicle increases, which results in an increase in engine load.

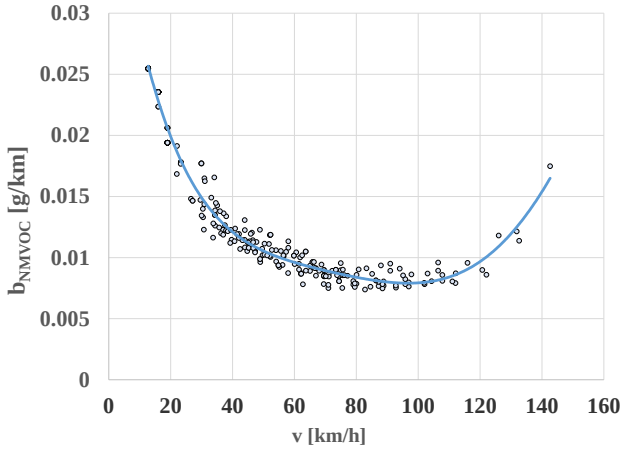

Fig. 2. Characteristics of the specific distance NMVOC emission – b_{NMVOC} depending on the average speed – v of passenger cars

The high value of specific distance NMVOC emissions for low average vehicle speed results from the large share of engine operating time at idle speed and at low loads in these traffic models. The increase in specific distance emission of NMVOC at a high average speed of the vehicle corresponds to a high engine load.

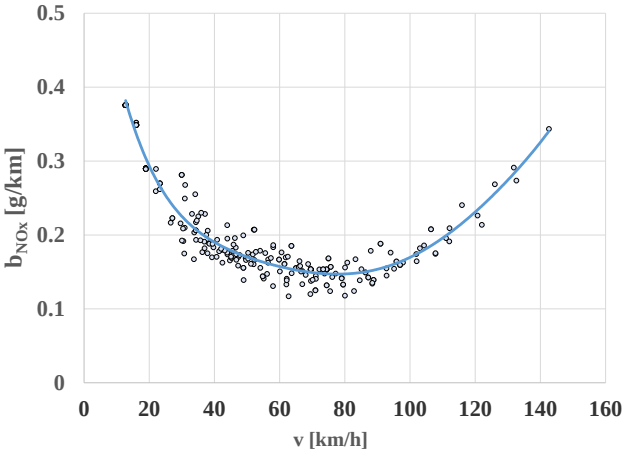

Fig. 3. Characteristics of the specific distance NO_x emission – b_{NOx} depending on the average speed – v of passenger cars

The high value of specific distance emissions of NO_x for a low average vehicle speed results from high traffic instability – frequent braking and acceleration. The increase at high vehicle speed results from the increasing engine load.

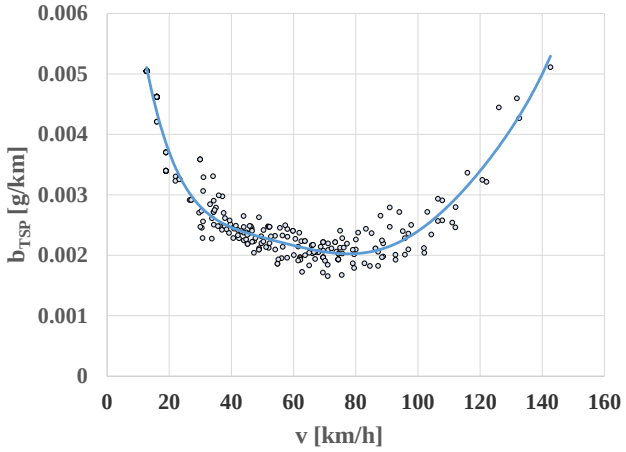

Fig. 4. Characteristics of the specific distance TSP r – b_{TSP} depending on the average speed – v of passenger cars

The correlation of the specific distance TSP emission with the average speed of the vehicle is similar to the pattern of specific distance NO_x emission.

Despite some differences in specific distance pollutant emissions for traffic models with a similar value of average vehicle velocity, the dependence of these emissions on average velocity shows a clear regularity.

The characteristics of the specific distance emissions for all traffic conditions enable the approximation of the dependence on the average velocity in a regular form.

5.3. Example results of the emissions model simulation studies for road transport between 2000 and 2020

In the Figures 5–8 are shown examples of national annual emissions of selected pollutants in the years 2000–2020 from selected cumulative categories of road vehicles in model traffic conditions: urban congestion, urban outside traffic congestion, rural, highways and motorways, and the total emission of pollutants.

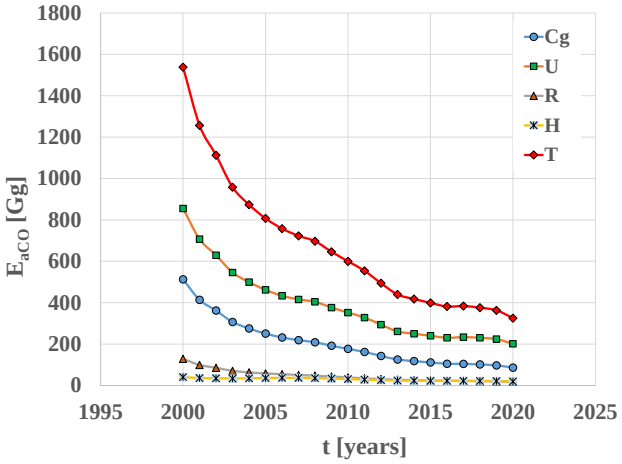

Fig. 5. National annual CO emission – E_{aCO} from passenger cars in years 2000–2020 in model traffic conditions: Cg – urban congestion, U – urban outside traffic congestion, R – rural, H – highways and motorways and T – the total CO emission

There is a general dependence on the decrease in the CO emission from passenger cars in subsequent balancing years in all model traffic conditions, despite the significant intensification of vehicle use. This environmentally beneficial trend results from the technological progress of introduced vehicles.

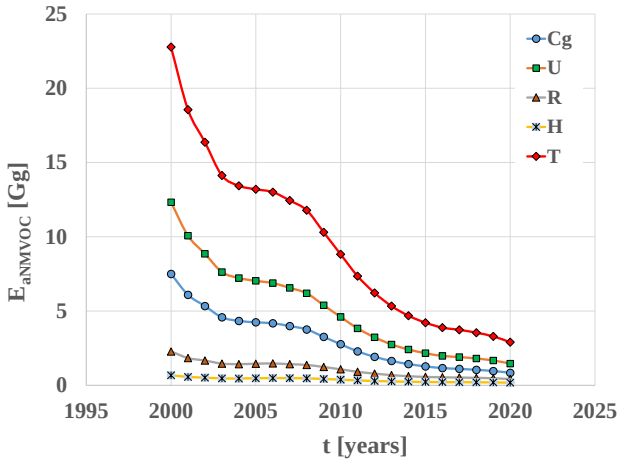

Fig. 6. National annual NMVOC emission – E_{aVMVOC} from light commercial vehicles in years 2000–2020 in model traffic conditions: Cg – urban congestion, U – urban outside traffic congestion, R – rural, H – highways and motorways and T – the total NMVOC emission

The trend in the NMVOC emission from light commercial vehicles is similar to the trend of CO emission.

The trend of the NO_x emission is different than for the emission of CO and NMVOC. Initially – until 2009 – NO_x emission increased as a result of the significant intensification of the use of heavy duty trucks, which is linked to the economic progress in that period. Only in recent years, the value of NO_x emissions has been determined by increasing the effectiveness of catalytic nitrogen oxide reduction systems.

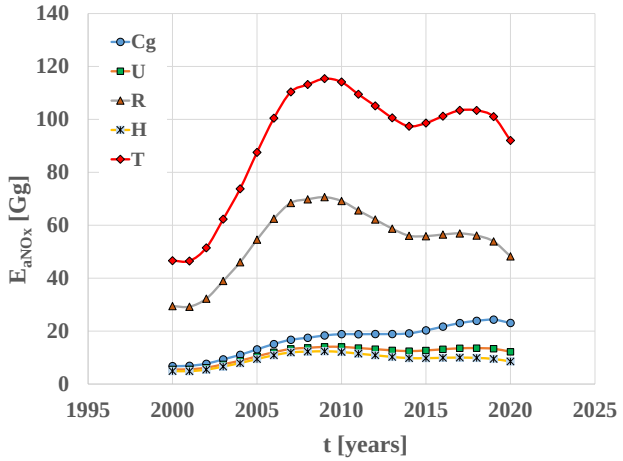

Fig. 7. National annual NO_x emission – E_{aNOx} from heavy duty trucks in years 2000–2020 in model traffic conditions: Cg – urban congestion, U – urban outside traffic congestion, R – rural, H – highways and motorways and T – the total NO_x emission

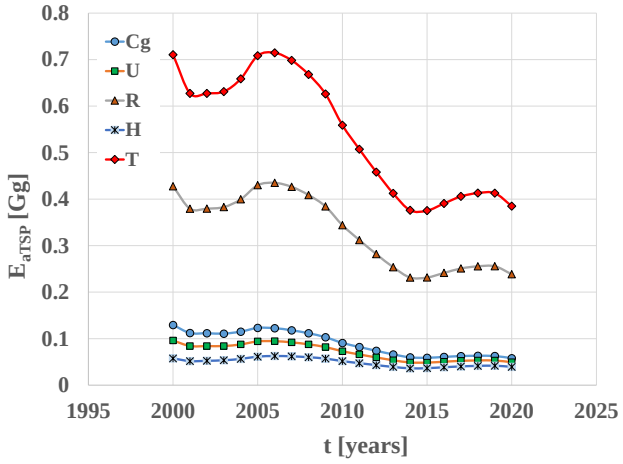

Fig. 8. National annual TSP emission – E_{aTSP} from coaches in years 2000–2020 in model traffic conditions: Cg – urban congestion, U – urban outside traffic congestion, R – rural, H – highways and motorways and T – the total TSP emission

TSP emission from coaches has a general tendency to decrease (the exception is the period from 2002 to 2006 and from 2015 to 2019). This is due to significant progress in the technical vehicles properties.

The dependency between annual national emissions in the years 2000–2020 for various categories of road vehicles and various pollutants varies. In general, despite the significant intensification of the use of vehicles (their number and annual mileage), CO and NMVOC emissions have a clear downward trend. Progress in technology, particularly in the area of emissions reduction, has contributed to this. For NO_x and TSP emissions, there is no such clear dependency. In this case, there is a more difficult way to reduce pollutant emissions – this trend occurs after 2006–2009.

5.4. Emissions model simulation studies for passenger cars due to model vehicle traffic conditions

Simulation studies on the emission model for passenger cars due to model vehicle traffic conditions was carried out in order to test the sensitivity of road emissions in model traffic conditions differing in average driving velocity.

Table 1 presents the simulation program for the model of emissions from passenger cars in terms of their average speed in model traffic conditions.

Table 1. Simulation program for the model of pollutant emissions from passenger cars in terms of their average speed in model traffic conditions

Simulation number		1	2	3	4	5
Model traffic conditions	Average speed [km/h]					
Urban congestion	v_{Cg}	4	5	6	7	8
Urban outside traffic congestion	v_U	30	35	40	45	50
Rural	v_R	60	65	70	75	80
Highways and motorways	v_H	100	105	110	115	120

In the Figures 9–12 are shown the dependencies of specific distance emission from passenger cars in model traffic conditions on average velocity.

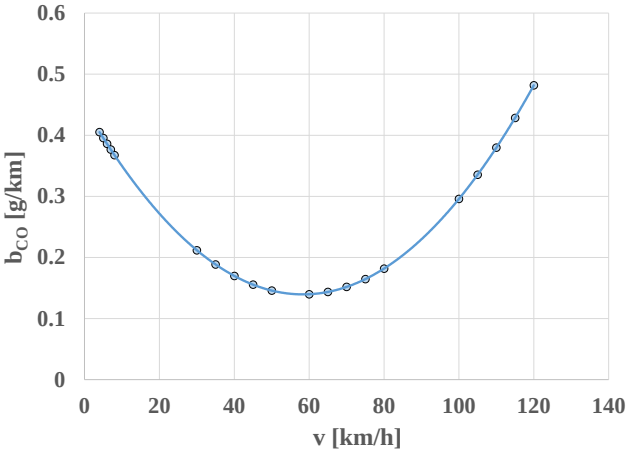

Fig. 9. Dependency of specific distance CO emission from passenger cars in model traffic conditions – b_{CO} on average speed – v

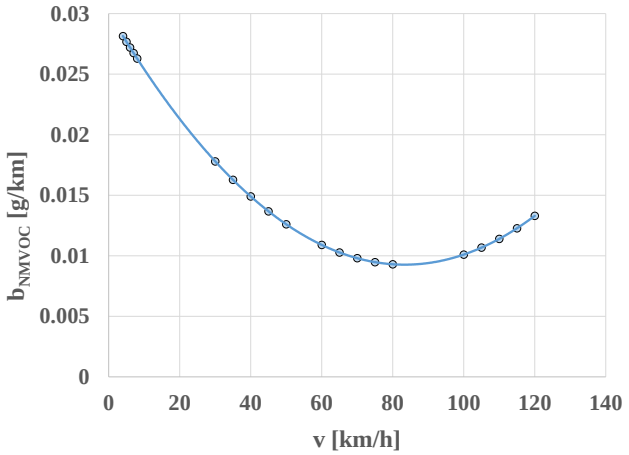

Fig. 10. Dependency of specific distance NMVOC emission from passenger cars in model traffic conditions – b_{NMVOC} on average speed – v

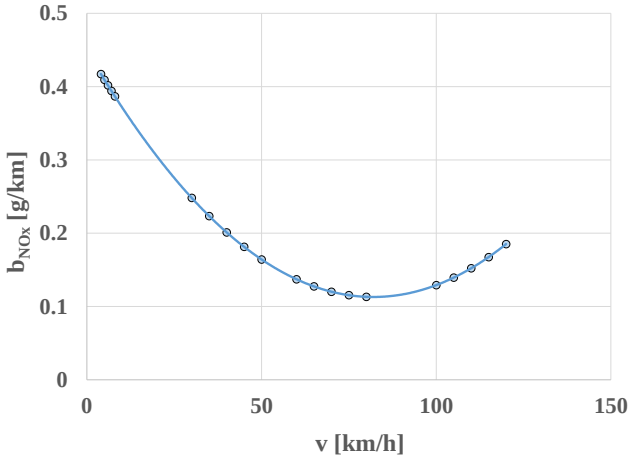

Fig. 11. Dependency of specific distance NO_x emission from passenger cars in model traffic conditions – b_{NOx} on average speed – v

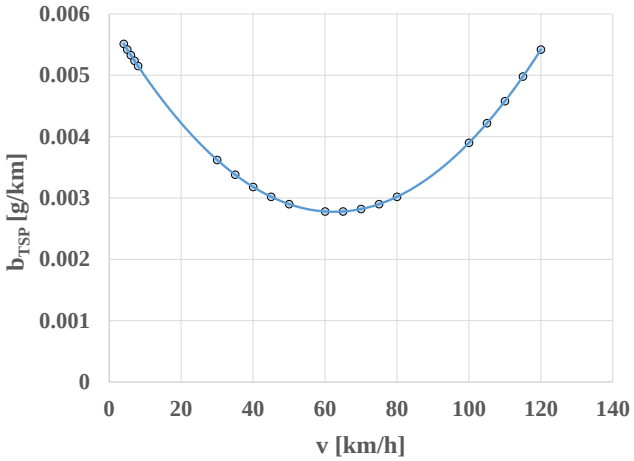

Fig. 12. Dependency of specific distance TSP emission from passenger cars in model traffic conditions – b_{TSP} on average speed – v

The regularity of specific distance pollutant emissions from passenger cars in model traffic conditions for various average velocity values is clearly visible. The figures show that it is possible to approximate specific distance emission depending on the average vehicle speed.

It is characteristic that for the vehicle movement in model of traffic congestion, specific distance emissions decrease as the average velocity increases. The situation is similar for the urban vehicle traffic model outside congestion. For the traffic model in rural areas, specific distance emissions increase as the average velocity increases. This dependence is even stronger for traffic on highways and motorways.

6. Conclusions

Based on the presented analyses and simulation studies results, the following conclusions can be formulated:

1. Modeling is the only possible way to determine the total pollutant emissions from mobile sources.
2. It is possible to use the procedures used for the official air pollutant emission inventories from road vehicles to study the model of this emission due to the input data and model parameters characterizing the structure, intensity and method of use of road vehicles.
3. The average vehicle speed is an effective zero-dimensional characteristic for assessing the nature of vehicle movement in the task of inventorying pollutant emissions from road vehicles.
4. The dependence between specific distance emissions and the average speed of vehicles of elementary categories is used for modeling pollutant emissions from road transport. This dependency is determined based on the empirical research results.
5. Despite the significant intensification of the use of road vehicles between 2000 and 2020, the total national annual emissions have a clear downward trend. This is the effect of a change in the structure of road vehicles due to their ecological properties – pollutant emissions.
6. The most visible tendency is to reduce the annual national CO and NMVOC emissions. The tendency to decrease the national annual NO_x and TSP emissions is less visible.

Nomenclature

b	specific distance emission
Cg	urban congestion
CO	carbon monoxide
Ea	national annual emission
H	highways and motorways
NMVOC	non-methane volatile organic compounds
NO_x	nitrogen oxides
R	rural
TSP	total suspended particulate matter
U	urban outside traffic congestion
V	average vehicle velocity

Bibliography

[1] 2006 IPCC Guidelines for National Greenhouse Gas Inventories.

[2] André M. The ARTEMIS European driving cycles for measuring car pollutant emissions. Sci Total Environ. 2004; 334-335:73-84. https://doi.org/10.1016/j.scitotenv.2004.04.070

[3] Bebkiewicz K, Chłopek Z, Lasocki J, Szczepański K, Zimakowska-Laskowska M. The inventory of pollutants hazardous to the health of living organisms, emitted by road transport in Poland between 1990 and 2017. Sustainability. 2020;12:5387. https://doi.org/10.3390/su12135387

[4] Bebkiewicz K, Chłopek Z, Sar H, Szczepański K, Zimakowska-Laskowska M. Assessment of environmental risks of particulate matter emissions from road transport based on the emission inventory. Appl Sci. 2021;11(13):6123. https://doi.org/10.3390/app11136123

[5] Bebkiewicz K, Chłopek Z, Sar H, Szczepański K, Zimakowska-Laskowska M. Assessment of impact of vehicle traffic conditions: urban, rural and highway, on the results of pollu-

tant emissions inventory. Archives of Transport. 2021;60(4): 57-69. https://doi.org/10.5604/01.3001.0015.5477
[6] Bebkiewicz K, Chłopek Z, Sar H, Szczepański K, Zimakowska-Laskowska M. Influence of the thermal state of vehicle combustion engines on the results of the national inventory of pollutant emissions. Appl Sci. 2021;11(19):9084. https://doi.org/10.3390/app11199084.
[7] Bebkiewicz K, Chłopek Z, Lasocki J, Szczepański K, Zimakowska-Laskowska M. Inventory of pollutant emission from motor vehicles in Poland using the COPERT 5 software. Combustion Engines. 2019;178(3):150-154. https://doi.org/10.19206/CE-2019-326
[8] BUWAL (Bundesamt für Umwelt, Wald und Landschaft), INFRAS AG (Infrastruktur-, Umwelt- und Wirtschaftsberatung). Luftschadstoffemissionen des Strassenverkehrs 1950–2010, BUWAL-Bericht 1995;255.
[9] Cao GL, Zhang XY, Gong SL, An XQ, Wang YQ. Emission inventories of primary particles and pollutant gases for China. Atmos Sci. 2011;56:781-788. https://doi.org/10.1007/s11434-011-4373-7
[10] Chłopek Z, Dębski B, Szczepański K. Theory and practice of inventory pollutant emission from civilization-related sources: share of the emission harmful to health from road transport. The Archives of Automotive Engineering – Archiwum Motoryzacji. 2018;79(1):5-22. https://doi.org/10.14669/AM.VOL.79.ART1
[11] Chłopek Z. Modelowanie procesów emisji spalin w warunkach eksploatacji trakcyjnej silników spalinowych (in Polish). Prace Naukowe. Seria „Mechanika" z. 173. Oficyna Wydawnicza Politechniki Warszawskiej. Warszawa 1999.
[12] Convention on Long-Range Transboundary Air Pollution.
[13] COPERT | EMISIA SA. (accessed on 2023.11.25).
[14] COPERT Training 5. COPERT 5 vs COPERT 4. European Environment Agency. 2016.
[15] Corinair – European Environment Agency (europa.eu). (accessed on 2023.11.25).
[16] COST 319 – Publications Office of the EU (europa.eu). (accessed on 2023.11.25).
[17] Directive (EU) 2016/2284 of the European Parliament and of the Council of 14 December 2016 on the reduction of national emissions of certain atmospheric pollutants, amending Directive 2003/35/EC and repealing Directive 2001/81/EC.
[18] EEA/EMEP Emission Inventory Guidebook 2019.
[19] Gkatzoflias D, Kouridis C, Ntziachristosand L, Samaras Z. COPERT 4 Computer programme to calculate emissions from road transport. User manual (version 9.0).
[20] INFRAS AG: Handbuch für Emissionsfaktoren des Strassenverkehrs; Version 3.2. Bern 2022.
[21] Joumard R. Methods of estimation of atmospheric emissions from transport: European scientist network and scientific state-of-the-art. Action COST 319. Final INRETS report N° LTE 9901. 1999.
[22] Lestari P, Damayanti S, Arrohman MK. Emission inventory of pollutants (CO, SO_2, PM2.5 and NO_x) in Jakarta Indonesia. IOP Conf Ser: Earth Environ Sci. 2020;489(1):012014. https://doi.org/10.1088/1755-1315/489/1/012014
[23] Methodology for Calculating Transport Emissions and Energy Consumption | TRIMIS (europa.eu). (accessed on 2023.11.25).
[24] Poland's Informative Inventory Report 2021, Air pollutant emissions in Poland 1990–2019. Submission under the UN ECE Convention on Long-range Transboundary Air Pollution and Directive (EU) 2016/2284. Warszawa 2021.
[25] Poland's Informative Inventory Report 2022. Air pollutant emissions in Poland 1990–2020. Submission under the UN ECE Convention on Long-range Transboundary Air Pollution and Directive (EU) 2016/2284. Warszawa 2022.
[26] Szczepański K, Bebkiewicz K, Chłopek Z, Sar H, Zakrzewska D. Analysis of the national annual emission of pollutants from road transport in Poland in the years 1990–2020. Energies. 2023;16(10):4083. https://doi.org/10.3390/en16104083
[27] Szczepański K, Chłopek Z, Sar H, Zimakowska-Laskowska M. Assessment of pollutant emission in Poland from various categories of transport. Environmental Protection and Natural Resources Ochrona Środowiska i Zasobów Naturalnych. 2022;33:1-6. https://doi.org/10.2478/oszn-2022-0004

Katarzyna Bebkiewicz, MEng. – Institute of Environmental Protection – National Research Institute, Poland.
e-mail: *katarzyna.bebkiewicz@kobize.pl*

Krystian Szczepański, DSc., DEng. – Professor of IOS-PIB – Institute of Environmental Protection – National Research Institute, Poland.
e-mail: *krystian.szczepanski@ios.edu.pl*

Prof. Zdzisław Chłopek, DSc., DEng. – Institute of Environmental Protection – National Research Institute, Poland.
e-mail: *zdzislaw.chlopek@kobize.pl*

Article citation info:
Murzyński D. Evaluation of the effects of the application of Ti−C:H DLC coatings obtained by PVD techniques in the kinematic pairs of internal combustion engines and powertrain systems. Combustion Engines. 2024;198(3):27-33. https://doi.org/10.19206/CE-184217

Dawid MURZYŃSKI

Combustion Engines
Polish Scientific Society of Combustion Engines

Evaluation of the effects of the application of Ti−C:H DLC coatings obtained by PVD techniques in the kinematic pairs of internal combustion engines and powertrain systems

ARTICLE INFO

Received: 15 December 2023
Revised: 10 February 2024
Accepted: 18 February 2024
Available online: 12 May 2024

The article attempts to analyze the possible effects of using Ti−C:H DLC carbon coatings produced by pulsed magnetron sputtering (PVD) to reduce friction coefficient and wear in kinematic pairs found in internal combustion engines and powertrain systems used in automotive vehicles. The aim of such action is primarily to reduce internal losses in the aforementioned units. The coatings were deposited on heat-treated bearing steel 100Cr6, and examined using a scanning electron microscope FEI Quanta 200 Mark II with the chemical analyzer EDS EDAX Genesis XM 2i, tribotester T−01M examining the friction coefficient in the ball-disc correlation and Hommel Werke T8000 profilometers, additionally, in order to check the coating thickness, studies were carried out using the Calotest method. The results obtained indicate that both the friction coefficient and wear are drastically reduced concerning samples on which no DLC coatings were applied.

Key words: *pulsed magnetron sputtering, diamond-like carbon, friction coefficient, wear rate*

1. Introduction

Air pollution [17], and the associated threats to human life, have become an urgent problem to be solved, as it is a cause of premature deaths in the EU [1, 12, 23]. In addition, road transport is one of the main factors that contribute to emissions of pollutants.

For several decades, steps have been taken to create a more "green" transport, for this purpose a several regulations and legal regulations have been introduced that define the requirements that vehicles must meet [10, 13, 21, 24, 28, 32, 33, 39].

It is expected that new, increasingly stringent emission standards will influence vehicle manufacturers to design and implement increasingly sophisticated and effective exhaust cleaning systems [6]. Taking into account that many issues regarding "zero emission" transport are still unresolved (e.g. related to the availability and distribution of CO_2-free electricity, charging infrastructure for electric vehicles in cities, sourcing of raw materials for battery production), vehicles using combustion engines will continue to be produced and sold in the form of hybrid drive systems, which consume less fuel and therefore have lower emissions of pollutants into the atmosphere [6, 31].

The energy and material losses resulting from friction processes and increased wear are a major economic and environmental burden for the entire world [14]. Considering that passenger cars in the world consume 350 million tons of oil annually to overcome friction, which also has an impact on CO_2 emissions and increased costs resulting from the regeneration and replacement of worn parts, the pursuit of minimizing friction and wear becomes a necessity [14]. Many authors support this opinion, arguing further that the automotive industry is moving not only towards increased efficiency, lower fuel consumption, improved reliability, and more environmentally friendly products, but also towards less lubricants [5, 18, 25].

The automotive industry is one of the most important users of modern surface technologies, which improve the materials and products used, making it possible to introduce new and innovative solutions based on the special properties of thin coatings. The use of appropriate coatings makes it possible to change the surface properties in the context of [3]:

- mechanical (frictional wear, frictional resistance)
- chemical (corrosion)
- electrical (conductivity)
- optical (transmittance, reflection, absorption, aesthetic effect).

Examples of attempts to use coatings for mechanical purposes in the automotive industry are primarily:

- Piston rings – coated with chrome galvanically, chromium nitride, titanium nitride in PVD techniques [3, 18, 36, 38, 40]
- Cylinders in engine blocks (carbon steel reinforced with ceramics – thermal spraying) [3]
- Crankshaft bearings – Al−Sn, Al−Sn−Bi alloys [3]
- Ball pivots – plasma nitriding, oxidation [3, 38]
- Injector needles in gasoline engines – carbon DLC coatings – PVD [3, 35, 38]
- Piston pins – carbon DLC coatings – PVD [3]
- Pushrods – carbon DLC coatings – PVD [3, 18]
- Camshaft journals and camshafts – carbon DLC coatings – PVD [3, 18, 22]
- Valves – carbon DLC coatings – PVD [3, 22]
- Gearboxes – carbon DLC coatings – PVD [3, 18, 19, 22, 38].

Continuous research is being conducted, in which attempts are being made to create thin-film coatings for automotive applications, for example based on metal-doped DLC (diamond-like carbon) coatings, or boron carbide [16, 26, 34, 43, 44]. However, an aspect that is increasingly being paid attention to is the cooperation of the proposed

thin-film coatings with currently used lubricants and their additives in order to minimize friction [5, 16, 19, 25, 27, 34, 40, 41]. Lubricants have been developed and optimized for the cooperation of metallic surfaces in kinematic pairs used in the automotive industry, while solutions considering "improved surfaces" through applied thin-film coatings are not yet commercialized [25, 34].

Engineers often treat thin-film coating technology as a backup tool, not optimized for design. It happens that this solution is applied to unsuitable substrates (e.g. too low substrate hardness), which results in lesser use of the potential of the applied coating [18]. This technology should be already included in the design phase, so that it becomes a design tool, and it is possible to optimize its use, to achieve maximum benefits [18].

Over the past few decades, many coatings have been developed for thin-film technologies, used both to reduce frictional wear, and losses associated with friction, or to improve corrosion resistance. Metal coatings are used (e.g. based on elements such as Cr, Ni, and Ti), as well as those based on metal nitrides (e.g. CrN, TiN, and TiAlN AlN), metal carbides (e.g. TiC, WC), as well as metal carbonitrides (e.g. TiCN, TiAlCN). Another group that has found application is diamond-like carbon coatings (DLC), which are characterized by high wear resistance and hardness and a low friction coefficient [29].

DLC coating is a type of amorphous carbon coating, whose properties are determined by the content of sp^3 bonds (similar to diamonds) and sp^2 bonds (similar to graphite) and the content of hydrogen [3, 25, 29]. DLC coatings can be divided into those without hydrogen (ta−C, a−C), coatings with hydrogen (ta−C:H, a−C:H) and doped with both metals (a−C:H:M), and non-metallic elements (a−C:H:X) [3, 25, 29].

In automotive engineering, due to their properties, a−C:H and a−C:H:M coatings are most commonly used [25]. a−C:H coatings, despite their high hardness and wear resistance, are characterized by high internal stresses, which can cause problems with obtaining adequate adhesion to the substrate [4]. In the case of metal-doped coatings (a−C:H:M), internal stresses are reduced due to the decrease in coating hardness, thus reducing the problem with adhesion to the substrate. They still show a small friction coefficient, but their wear resistance decreases [4]. The disadvantages of DLC coatings include changing wear and tribological properties with increasing temperature. From a temperature of 100°C, these properties begin to deteriorate, and in the range of high temperatures, hydrogen begins to be released from the DLC matrix [15, 25, 37]. Therefore, the use of such coatings in conditions where high operating temperature dominates is problematic [25]. It should also be mentioned that the technology for producing DLC coatings is expensive, and it is crucial to develop a method in which high repeatability, efficiency and reliability are achieved at the lowest possible cost [20].

Taking into account the excellent tribological and wear resistant properties of DLC coatings and the possibility of modifying these properties by changing the parameters of the layer deposition process and using additives in the form of metals and non-metals, the adaptability of such a solution is high, however, it is necessary to optimize the coating for specific applications.

2. Experimental details

To analyze the possibilities and effects of using DLC coatings in kinematic pairs used in internal combustion engines and vehicle systems, an attempt was made to investigate how these coatings would affect the change in tribological properties in kinematic pairs made of bearing steel 100Cr6 after heat treatment under dry friction conditions.

For research purposes, a a−C:H:M coating was planned, in which the metal used to modify the DLC coating was titanium (Ti−C:H). These studies aimed to determine the parametric properties of the applied coatings and to verify how they would affect the change in the friction coefficient and wear in a kinematic pair made of 100Cr6 steel.

It was assumed that the Ti−C:H coating would be applied to both elements (sample and counter-sample) and only to the sample, while the counter-sample would remain unchanged. The deposition temperature was limited to 200°C in order not to cause structural changes in the base material and a target coating thickness of about 1μm was planned. Lower deposition temperature of the coating may affect its adhesion to the substrate and deteriorate its properties. Therefore, the study aims to investigate the properties of the coating obtained at a lower deposition temperature.

2.1. The technology of applying Ti-C:H coatings

The substrates on which the coatings were applied were made of 100Cr6 steel after heat treatment (hardening and tempering). They were cylindrical plates with a diameter of 28 mm and balls with a diameter of 10 mm. The samples were polished to achieve a roughness of Ra < 0.02 mm. The substrate preparation process also required washing in an alkaline bath and deionized water using ultrasonic cleaners.

Table 1. Composition of 100Cr6 (wt.%) [2]

Fe	C	Cr	Mn	Si	Cu	Ni	Mo	Al
Bal.	0.97	1.38	0.28	0.28	0.21	0.18	0.06	0.04

Prepared samples were placed in a vacuum chamber on a rotating table, in planetary rotation holders at a distance of 10 cm from the source. The coatings were applied by reactive magnetron sputtering using a titanium target. The chamber was initially pumped down to a pressure of 2×10^{-3} Pa to remove oxygen, then the pressure was increased by controlled introduction of argon, until a working pressure of 0.3 Pa was reached.

The first step in the coating deposition process is ion cleaning, which is used to remove oxides and prepare the substrates for coating. The process parameters are: working pressure of 0.5 Pa, substrate polarization voltage of −600 V, arc discharge current of 85 A, and duration of 8 minutes. During the deposition of the target coating, the substrate polarization voltage was maintained at −90 V, and the sputtering power on the titanium target was 1500 W. The process temperature was 150°C, acetylene flow was 18 SCCM, and the duration was 75 minutes.

2.2. Characterization methods

The thickness of the coatings was determined using the Calotest method, i.e. the spherical grinding method according to DIN EN 1071-2:2003.

The adhesion of the obtained coatings was checked using the scratch method on a Revetest Scratch Tester device.

The surface roughness of the obtained coatings was investigated using a Hommel Werke T8000 profilometer, repeating the measurement five times for each sample.

The surface morphology and composition analysis were performed on a FEI Quanta 200 Mark II scanning electron microscope with an EDAX Genesis XM 2i chemical analyzer.

The verification of the microhardness of the obtained coatings was checked using a Fischerscope HM 2000 microhardness tester according to ISO 14577.

The tribological tests were carried out on a T-01M device in a ball-disc combination according to ASTM G 99 and DIN 50324. The following parameters were adopted:

- Load: 20 N
- Speed: 0.2 m/s
- Distance: 1000 m
- Wear radius: 0.01–0.013 m
- Number of revolutions: 12243–15915
- Test duration: 5000 s
- Ball diameter: 0.01 m.

2.3. Results and discussion

Morphological studies of the surface conducted on a scanning electron microscope showed that no defects such as cracks, local delaminations, or chips were present in the applied coatings (Fig. 1). The presence of microdroplets was also observed on the surface of the applied coatings, which can lead to a deterioration of tribological properties [8, 14]. The size of these microdroplets is variable, with diameters of up to several micrometers being recorded.

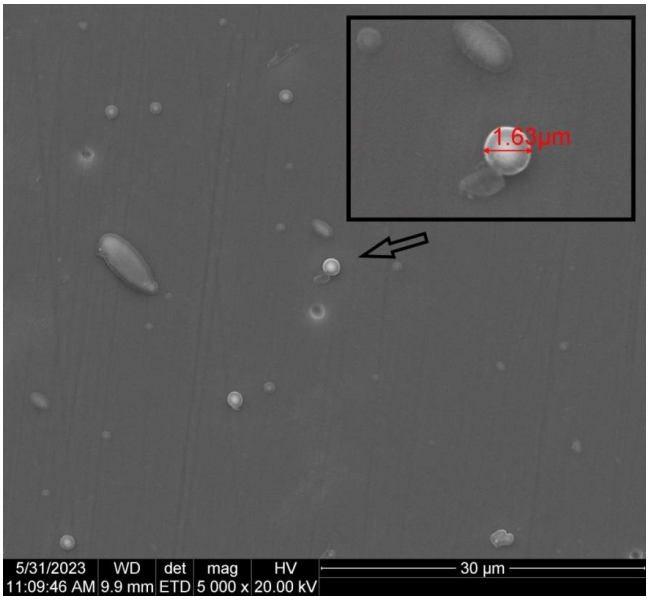

Fig. 1. SEM image of the surface of a 100Cr6 steel sample with a Ti−C:H coating

Chemical composition analysis (EDS) showed that the Ti−C:H coating consists of titanium and carbon, however, it was observed that the microdroplets have a different atomic ratio of carbon and titanium than the coating itself (Fig. 2). In the coating, 77.57 at. % of carbon and 22.43 at. % of titanium were recorded, while in the microdroplet 89.48 at. % of carbon and 10.42 at. % of titanium were recorded. It is to be supposed that the coating will have different tribological properties than microdroplets. They may have a particular impact in the first phase of the tribological test, because in the first phase of the running-in process, the detachment of microdroplets from the substrate can occur, which can introduce disturbances in the operation of the kinematic pair [8].

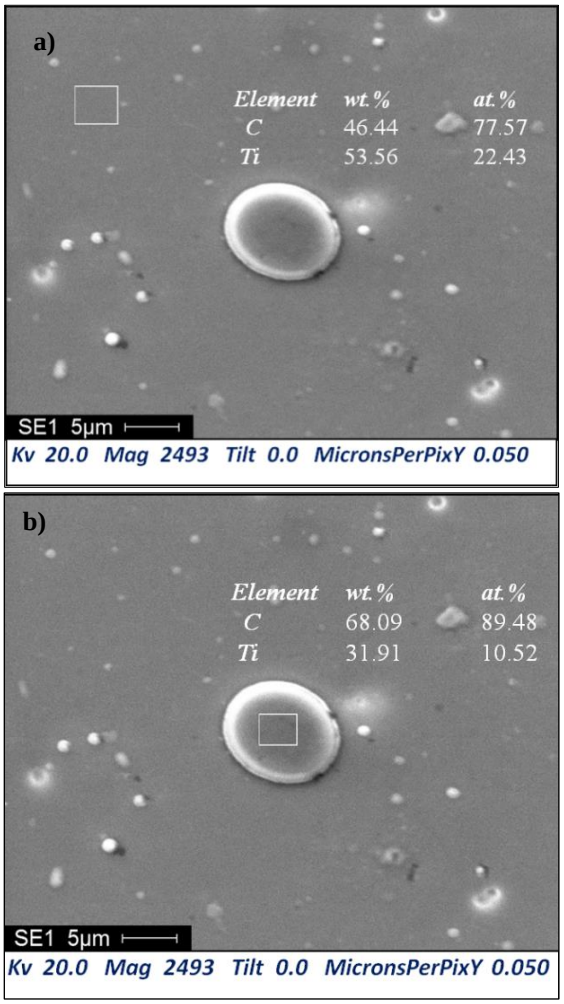

Fig. 2. EDS analysis of a Ti−C:H coating. a) coating, b) microdroplets

Thickness measurements performed using the Calotest method showed that the Ti−C:H coating deposited on 100Cr6 steel samples has an average thickness of 1.035 ±0.021 µm, so the process time was well chosen, since the assumption was to obtain a coating with a thickness close to 1 µm.

Roughness measurements showed that the roughness parameters increase after the Ti−C:H coating process, as shown in Table 2. The deterioration of these parameters is related to the presence of microdroplets on the surface of

the coating, which were formed as a result of the coating process. These results confirm the conclusions of the observations made on the scanning electron microscope.

Table 2. Roughness parameters of uncoated samples and samples with a Ti−C:H coating

		Samples before the coating process	Samples after the DLC coating process
R_a	[nm]	5.3 ±0.57	6.3 ±0.57
R_z	[nm]	29 ±6.5	70 ±11
R_{max}	[nm]	48 ±29	85 ±17

Adhesion tests performed using the scratch test method on samples with applied Ti−C:H coatings showed that the first coating damage (L_{c1}) was recorded at a pressing force of 9 N, coating damage and tearing (L_{c2}) at a force of 16.32 N, and complete detachment of the coating from the substrate (L_{c3}) was recorded at a pressure of 40.15 N. The adhesion of the coating depends on, among other things, the process parameters of the coating deposition, stresses in the coating, its thickness, the hardness of the coating, and in the case of a-C:H coatings, the degree of hydrogenation [9, 11, 30]. The results of adhesion tests are shown in Fig. 3.

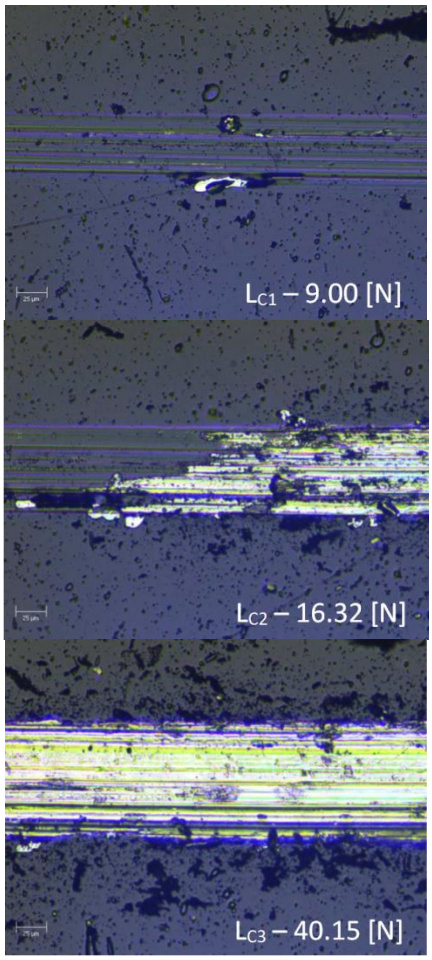

Fig. 3. Scratch test results of the Ti–C:H coating applied to a 100Cr6 steel substrate

Microhardness tests performed on a Fischerscope HM 2000 microhardness tester showed that the Ti−C:H coating applied to a 100Cr6 steel substrate has a higher hardness than the substrate, with a recorded value of 776.82 ±48.81 HV, and the substrate hardness is 58.93 ±0.6 HRC (~674 HV). This test was performed with a Vickers indenter depth of 0.25 μm to eliminate the influence of the substrate on the coating hardness measurements. The obtained hardness is due to the high degree of hydrogenation, since with its increase, the hardness of the produced coating decreases [11].

Tribological tests in a ball-on-disc configuration were carried out under dry friction conditions at ambient temperature. The tests were carried out for three kinematic pair variants. In the first variant, the Ti−C:H coating was applied to both the sample (disc) and the counter-sample (ball) made of 100Cr6 steel. The second variant is a sample coated with DLC and a counter-sample made of bearing steel without coating. In the third combination, samples made of steel were tested without the applied Ti−C:H coatings.

The recorded friction coefficient for all three kinematic pair variants indicates that the Ti−C:H coating significantly reduces the above-mentioned coefficient (Fig. 4), which is consistent with the data contained in the literature on DLC coatings [3, 5, 7, 25, 27, 38].

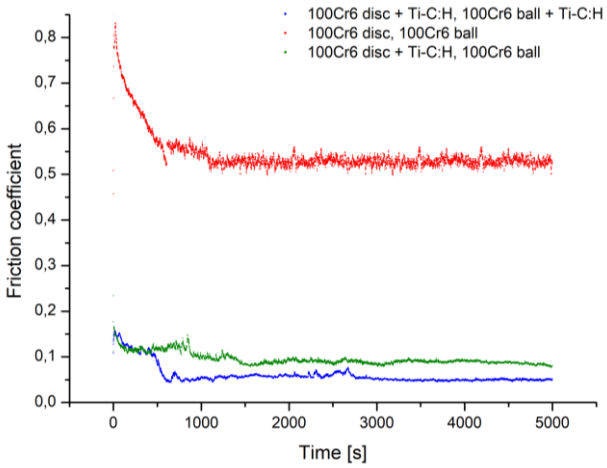

Fig. 4. Comparison of the recorded friction coefficient over time for all studied samples

In the first phase of the tribotest, the running-in process takes place in the kinematic pair, and then the recorded friction coefficient stabilizes. The calculated average value after 3000 s for each test indicates that the lowest friction coefficient was obtained for samples coated with Ti−C:H. The calculated values are presented in Table 3.

Table 3. Calculated friction coefficient after the break-in period of all studied samples

Sample	Friction coefficient
disk 100Cr6 + Ti−C:H, ball 100Cr6 + Ti−C:H	0.049 ±0.0014
disc 100Cr6 + Ti−C:H, ball 100Cr6	0.088 ±0.0035
disc 100Cr6, ball 100Cr6	0.540 ±0.0196

In the running-in period, in the case of the kinematic pair under study on which the Ti−C:H coating was applied, the recorded friction coefficient decreases (~500 s), which may be associated with the detachment and fall-off of microdroplets formed during the coating process, which is consistent with data found in the literature [8]. After the running-in period, the recorded friction coefficient decreases to a value close to 0.05. In the case of the kinematic pair in which only the disc was coated with the Ti−C:H coating, this process occurs more gently, and a sharp decrease in the friction coefficient resulting from the process of detachment of microdroplets from the coating was not observed.

Tribological tests have shown that the Ti−C:H doped DLC coating applied to both the sample and the counter-sample reduces the friction coefficient by eleven times compared to samples without coatings in dry friction conditions (0.049 vs 0.540). In the case of 100Cr6 steel samples with Ti−C:H coating and a counter-sample (ball) made of 100Cr6 steel, a friction coefficient six times lower than in the study on samples without coatings was recorded, and twice as high as in the case of the study for samples and counter-samples with DLC coatings.

The calculated wear rate of the sample and counter-sample (k_{vc}, k_{vb}) based on the conducted tests indicates that the lowest wear was recorded in the case of the pair on which the Ti−C:H coating was applied (Table 4).

Table 4. Wear rate of the sample and counter-sample after tribological testing

	Wear rate	
	Sample (disc)	Counter-sample (ball)
Sample	k_{vc} [mm^3/(N·m)]	k_{vb} [mm^3/(N·m)]
disc 100Cr6 + Ti−C:H, ball 100Cr6 + Ti−C:H	$1.86 \cdot 10^{-7} \pm 6.29 \cdot 10^{-8}$	$3.03 \cdot 10^{-11} \pm 7.3 \cdot 10^{-12}$
disc 100Cr6 + Ti−C:H, ball 100Cr6	$5.26 \cdot 10^{-7} \pm 5.16 \cdot 10^{-8}$	$8.25 \cdot 10^{-9} \pm 2.7 \cdot 10^{-9}$
disc 100Cr6, ball 100Cr6	$1.08 \cdot 10^{-5} \pm 1.09 \cdot 10^{-6}$	$1.11 \cdot 10^{-5} \pm 1.1 \cdot 10^{-7}$

The application of the Ti−C:H coating significantly reduces wear in the kinematic pair under study made of 100Cr6 steel compared to samples without coatings. In the case of the kinematic pair on which the Ti−C:H coating was applied only to the disc, it was observed that the wear is three times greater than in the case of the pair on which the coating was applied to both elements. The greatest changes in the case of the degree of wear were observed for the counter-sample (ball). It should be concluded that coating one element will effectively reduce the friction coefficient and wear of the sample under dry friction conditions, however, it is most effective to coat both elements in the kinematic pair.

The application of Ti–C:H coating can reduce the friction coefficient and wear rate, which allows for lower resistance and longer service life of kinematic pairs. However, their application is problematic due to limitations resulting from operation at elevated temperatures. Therefore, in order to reduce losses, it can be proposed to use them in every kinematic pair in internal combustion engines and drive systems, provided that they do not operate at elevated temperatures (above 100°C). An additional advantage is also the increased wear resistance in case of loss of lubrication due to failure or in boundary lubrication conditions.

3. Conclusions

Based on the conducted research, in which it was checked how the applied Ti−C:H coating would affect the reduction of the degree of wear and the friction coefficient, which is responsible for losses in the kinematic pair, the following conclusions were drawn:

- morphology studies of the surface performed on a scanning electron microscope showed that the coatings applied to the steel substrate did not show any defects (cracks, delamination, discontinuities, cracks), the only observation was the occurrence of microdroplets with of a size of several micrometers
- tribological testing showed that coatings applied to both the sample and the counter-sample reduced the friction coefficient by eleven times compared to samples without coatings under dry friction conditions (0.049 vs 0.540)
- analysis of the wear coefficients (k_{vc}, k_{vb}) of the sample and the counter-sample showed that DLC Ti−C:H coatings reduce wear by 58 times compared to samples without coating (k_{vc}), while in the case of the counter-sample (steel ball), the wear coefficient is several orders of magnitude smaller
- tribological tests performed on a sample made of 100Cr6 steel with a Ti−C:H coating and a counter-sample (ball) made of 100Cr6 steel, show a 6-fold lower friction coefficient than in the test on samples without coatings, and 2 times higher than in the case of the test for samples and counter-samples with DLC coatings
- coating one element with a Ti−C:H coating effectively reduces the friction coefficient and wear of samples in a kinematic pair under dry friction conditions, however, coating both elements in the kinematic pair is most effective
- the use of Ti−C:H coatings in kinematic pairs used in internal combustion engines and powertrains can reduce friction, especially in boundary lubrication or complete lack of lubrication (failure). This translates into reduced losses and wear, which is important in the search for solutions to reduce emissions of harmful compounds into the atmosphere, as well as to reduce fuel consumption
- taking into account the working conditions in the kinematic pairs of internal combustion engines and powertrains used in vehicles, the key is to select the right coatings, optimize them, and also seek solutions that primarily take into account the cooperation of the deposited coatings with lubricants
- to minimize losses generated in internal combustion engines and powertrains, it is essential to create a system in which individual kinematic pairs will have a reduced friction coefficient as a result of the methods of surface improvement used, strictly adapted to the conditions of their operation.

To find the most optimal solutions that lead to reduced losses, the continuation of research is planned:

– studies of kinematic pairs in which different PVD coatings will be applied to individual elements, and their optimization
– the influence of the lubricants used on the proposed PVD coatings that reduce wear and friction in kinematic pairs
– the influence of temperature on the generated friction coefficient in kinematic pairs coated with PVD coatings.

Acknowledgements

The author would like to express his gratitude to Ms. Karolina Kminikowska from the Mechanical Department of the Koszalin University of Technology for conducting surface morphology studies and composition analysis using a scanning electron microscope.

Bibliography

[1] Anenberg SC, Miller J, Henze DK, Minjares R, Achakulwisut P. The global burden of transportation tailpipe emissions on air pollution-related mortality in 2010 and 2015. Environ Res Lett. 2019;14(9):094012. https://doi.org/10.1088/1748-9326/ab35fc

[2] Barrow ATW, Kang J-H, Rivera-Díaz-del-Castillo PEJ. The $\epsilon \rightarrow \eta \rightarrow \theta$ transition in 100Cr6 and its effect on mechanical properties. Acta Mater. 2012;60(6-7):2805-2815. https://doi.org/10.1016/j.actamat.2012.01.046

[3] Bewilogua K, Bräuer G, Dietz A, Gäbler J, Goch G, Karpuschewski B et al. Surface technology for automotive engineering. CIRP Ann – Manuf Techn. 2009;58:608-627. https://doi.org/10.1016/j.cirp.2009.09.001

[4] Bewilogua K, Wittorf R, Thomsen H, Weber M. DLC based coatings prepared by reactive d.c. magnetron sputtering. Thin Solid Films. 2004;447-448:142-147. https://doi.org/10.1016/S0040-6090(03)01088-5

[5] Bobzin K, Bagcivan N, Goebbels N, Yilmaz K, Hoehn B-R, Michaelis K et al. Lubricated PVD CrAlN and WC/C coatings for automotive applications. Surf Coat Tech. 2009;204:1097-1101. https://doi.org/10.1016/j.surfcoat.2009.07.045

[6] Boger T, Rose D, He S, Joshi A. Developments for future EU7 regulations and the path to zero impact emissions – a catalyst substrate and filter supplier's perspective. Transport Eng. 2022;10:100129. https://doi.org/10.1016/j.treng.2022.100129

[7] Bouabibsa I, Lamri S, Sanchette F, Structure, mechanical and tribological properties of Me-doped diamond-like carbon (DLC) (Me = Al, Ti, or Nb) hydrogenated amorphous carbon coatings. Coatings. 2018;8:370. https://doi.org/10.3390/coatings8100370

[8] Carlsson P, Olsson M. PVD coatings for sheet metal forming processes – a tribological evaluation. Surf Coat Tech. 2006;200(14-15):4654-4663. https://doi.org/10.1016/j.surfcoat.2004.10.127

[9] Wei C, Yen J-Y. Effect of film thickness and interlayer on the adhesion strength of diamond like carbon films on different substrates. Diam Relat Mater. 2007;16(4-7):1325-1330. https://doi.org/10.1016/j.diamond.2007.02.003

[10] Commission Regulation (EU) 2016/646 of 20 April 2016 amending Regulation (EC) No 692/2008 as regards emissions from light passenger and commercial vehicles (Euro 6) (Text with EEA relevance). European Commission. http://data.europa.eu/eli/reg/2016/646/oj

[11] Czyzniewski A. Preparation and characterisation of a-C and a-C:H coatings deposited by pulsed magnetron sputtering. Surf Coat Tech. 2009;203(8):1027-1033. https://doi.org/10.1016/j.surfcoat.2008.09.027

[12] EEA, Air quality in Europe 2021. https://www.eea.europa.eu/publications/air-quality-in-europe-2021/

[13] Egerstrom N, Mulholland E, Dornoff J, Miller J, Rodríguez F. Emission reductions and public health benefits from timely Euro 7 standards, 2023 International Council on Clean Transportation 2023. https://theicct.org/wp-content/uploads/2023/09/Euro-7-premature-deaths.pdf

[14] Erdemir A, Eryilmaz O. Achieving superlubricity in DLC films by controlling bulk, surface, and tribochemistry. Friction. 2014;2:140-155. https://doi.org/10.1007/s40544-014-0055-1

[15] Erdemir A, Fenske GR. Tribological performance of diamond and diamondlike carbon films at elevated temperatures. Tribol T. 1996;39(4):787-794. https://doi.org/10.1080/10402009608983596

[16] Evaristo M, Fernandes F, Cavaleiro A. Influence of the alloying elements on the tribological performance of DLC coatings in different sliding conditions. Wear. 2023;526-527:204880. https://doi.org/10.1016/j.wear.2023.204880

[17] Florides GA, Christodoulides P. Global warming and carbon dioxide through sciences. Environ Int. 2009;35(2):390-401. https://doi.org/10.1016/j.envint.2008.07.007

[18] Gåhlin R, Larsson M, Hedenqvist P. ME-C:H coatings in motor vehicles. Wear. 2001;249:302-309. https://doi.org/10.1016/S0043-1648(01)00565-8

[19] Gondár E, Bošanský M, Rusnák J, Tóth F, Repková J. The application of DLC coating on convex-concave (C-C) gearings. Manufacturing Technology. 2019;19(6):930-935. https://doi.org/10.21062/ujep/398.2019/a/1213-2489/MT/19/6/930

[20] Hans M, Büchel R, Grischke M, Hobi R, Zäch M. High-volume PVD coating of precision components of large volumes at low process costs. Surf Coat Tech. 2000;123:288-293. https://doi.org/10.1016/S0257-8972(99)00477-6

[21] Kmieć M, Weber M, Romijn M, Matews D. Application of automotive safety design methodologies to the development of Euro 7 emission control systems including on board monitoring. Combustion Engines. 2020;188(1):75-82. https://doi.org/10.19206/CE-141291

[22] Kolk van der GJ. Wear resistance of amorphous dlc and metal containing DLC in industrial applications. In: Donnet C, Erdemir A. (eds). Tribology of diamond-like carbon films. Springer, Boston 2008. https://doi.org/10.1007/978-0-387-49891-1_19

[23] Mulholland E, Miller J, Bernard Y, Lee K, Rodríguez F. The role of NO_x emission reductions in Euro 7/VII vehicle emission standards to reduce adverse health impacts in the EU27 through 2050. Transport Eng. 2022;9:100133. https://doi.org/10.1016/j.treng.2022.100133

[24] Mulholland E, Miller J, Braun C, Jin L, Rodríguez F. Quantifying the long-term air quality and health benefits from Euro 7/VII standards in Europe. International Council on Clean Transportation. Washington 2021. https://theicct.org/publication/quantifying-the-long-term-air-quality-and-health-benefits-from-euro-7-vii-standards-in-europe/

[25] Neville A, Morina A, Haque T, Voong M. Compatibility between tribological surfaces and lubricant additives – how friction and wear reduction can be controlled by surface/lube synergies. Tribol Int. 2007;40:1680-1695. https://doi.org/10.1016/j.triboint.2007.01.019
[26] Olofsson U, Sjöström H, Sjödin U. Increased wear resistance of roller bearings using Me–C:H coated rollers. J Tribol. 2000;122(4):682-688. https://doi.org/10.1115/1.1310559
[27] Podgornik B, Sedlaček M, Vižintin J. Compatibility of DLC coatings with formulated oils. Tribol Int. 2008;41:564-570. https://doi.org/10.1016/j.triboint.2007.12.004
[28] Regulation of the European Parliament and of the Council on type-approval of motor vehicles and engines and of systems, components and separate technical units intended for such vehicles, with respect to their emissions and battery durability (Euro 7) and repealing Regulations (EC) No 715/2007 and (EC) No 595/2009. https://eur-lex.europa.eu/legal-content/EN/TXT/?uri=CELEX%3A52022PC0586
[29] Sedlaček M, Podgornik B, Vižintin J. Tribological properties of DLC coatings and comparison with test results: Development of a database. Mater Charact. 2008;59(2):151-161. https://doi.org/10.1016/j.matchar.2006.12.008
[30] Sheeja D, Tay BK, Lau SP, Shi X. Tribological properties and adhesive strength of DLC coatings prepared under different substrate bias voltages. Wear. 2001;249(5-6):433-439. https://doi.org/10.1016/S0043-1648(01)00541-5
[31] Skuza A, Szumska E, Jurecki R. Fuel consumption and CO_2 emission analysis of hybrid and conventional vehicles in urban conditions. Combustion Engines. 2023;195(4):48-55. https://doi.org/10.19206/CE-169569
[32] Szramowiat M, Szałek A. Analysis of the operation of the hybrid drive system in the light of the proposed Euro 7 standard. Combustion Engines. 2021;187(4):65-8. https://doi.org/10.19206/CE-141263
[33] Szymański P, Ciuffo B, Fontaras G, Martini G, Pekar F. The future of road transport in Europe. Environmental implications of automated, connected and low-carbon mobility. Combustion Engines. 2021;186(3):3-10. https://doi.org/10.19206/CE-141605
[34] Tamura Y, Zhao H, Wang C, Morina A, Neville A. Interaction of DLC and B4C coatings with fully formulated oils in boundary lubrication conditions. Tribol Int. 2016;93:666-680. https://doi.org/10.1016/j.triboint.2015.02.029
[35] Treutler CPO. Industrial use of plasma-deposited coatings for components of automotive fuel injection systems. Surf Coat Tech. 2005;200(5-6):1969-1975. https://doi.org/10.1016/j.surfcoat.2005.08.012
[36] Tung SC, McMillan ML. Automotive tribology overview of current advances and challenges for the future. Tribol Int. 2004;37:517-536. https://doi.org/10.1016/j.triboint.2004.01.013
[37] Vanhulsel A, Blanpain B, Celis J-P, Roos J, Dekempeneer E, Smeets J. Study of the wear behaviour of diamond-like coatings at elevated temperatures. Surf Coat Tech. 1998; 98(1-3):1047-1052. https://doi.org/10.1016/S0257-8972(97)00227-2
[38] Vetter J, Barbezat G, Crummenauer J, Avissar J. Surface treatment selections for automotive applications. Surf Coat Tech. 2005;200:1962-1968, https://doi.org/10.1016/j.surfcoat.2005.08.011
[39] Vestreng V, Ntziachristos L, Semb A, Reis S, Isaksen ISA, Tarrasón L. Evolution of NO_x emissions in Europe with focus on road transport control measures. Atmos Chem Phys. 2009;9(4):1503-1520. https://doi.org/10.5194/acp-9-1503-2009
[40] Wróblewski P. Analysis of torque waveforms in two-cylinder engines for ultralight aircraft propulsion operating on 0W-8 and 0W-16 Oils at high thermal loads using the diamond-like carbon composite coating. SAE Int J Engines. 2022;15(1):129-146. https://doi.org/10.4271/03-15-01-0005
[41] Wróblewski P, Kachel S. The concept of the contact angle in the process of oil film formation in internal combustion piston engines. Sci Rep. 2023;13:20715. https://doi.org/10.1038/s41598-023-47763-9
[42] Wróblewski P, Koszalka G. An experimental study on frictional losses of coated piston rings with symmetric and asymmetric geometry. SAE Int J Engines. 2021;14(6):853-866. https://doi.org/10.4271/03-14-06-0051
[43] Wróblewski P, Rogólski R. Experimental analysis of the influence of the application of TiN, TiAlN, CrN and DLC1 coatings on the friction losses in an aviation internal combustion engine intended for the propulsion of ultralight aircraft. Materials. 2021;14:6839. https://doi.org/10.3390/ma14226839
[44] Yakabe F, Jinbo Y, Kumagai M, Horiuchi T, Kuwahara H, Ochiai S. Excellent durability of DLC film on carburized steel (JISSCr420) under a stress of 3.0 GPa. J Phys: Conf Ser. 2008;100:082049. https://doi.org/10.1088/1742-6596/100/8/082049

Dawid Murzyński, DEng. – Faculty of Mechanical Engineering, Department of Transport Engineering, University of Technology, Koszalin, Poland.
e-mail: *dawid.murzynski@tu.koszalin.pl*

Article citation info:
Orliński P, Sikora M, Bednarski M, Laskowski P, Gis M, Wiśniowski P. Evaluation of selected combustion parameters in a compression-ignition engine powered by hydrogenated vegetable oil (HVO). Combustion Engines. 2024;198(3):34-40. https://doi.org/10.19206/CE-184222

Piotr ORLIŃSKI
Mieczysław SIKORA
Mateusz BEDNARSKI
Piotr LASKOWSKI
Maciej GIS
Piotr WIŚNIOWSKI

Combustion Engines
Polish Scientific Society of Combustion Engines

Evaluation of selected combustion parameters in a compression-ignition engine powered by hydrogenated vegetable oil (HVO)

ARTICLE INFO

Received: 30 November 2023
Revised: 12 February 2024
Accepted: 18 February 2024
Available online: 13 April 2024

The article carries out a detailed analysis and evaluation of indicators related to the combustion process (pressure and temperature in the engine combustion chamber, heat release rate, heat release fraction) in a JCB 444 TA4i compression-ignition engine fuelled with diesel and hydrogenated vegetable oil (HVO). During the empirical tests, the operation of the exhaust gas recirculation (EGR) system was stopped, and no other changes were made to the engine settings (factory settings were used). In the first stage, the empirical tests were carried out on the speed characteristics of an engine dynamometer. Then, an experiment was carried out at the engine crankshaft speed corresponding to the maximum torque - which consisted of determining the indicators related to the combustion process at a constant mass flow of fuel: diesel and HVO fuel. This provided information on the effect of hydrogenated vegetable oil on the combustion process in relation to the diesel engine feed. The conclusions drawn from the empirical study can be used to develop guidelines to change the operating map of a compression-ignition engine when it is fed with hydrogenated vegetable oil.

Keywords: *combustion process, compression-ignition engine, hydrogenated vegetable oil*

1. Introduction

Due to the targets set by the EU institutions regarding standards for emissions of toxic components from exhaust gases, the automotive industry will be forced to undergo a decarbonization process. Unfortunately, the time given by EU regulations to carry out this process is very short. This will, of course, force companies and enterprises to make rapid changes in organization and management. The problem is that if the entire process of training, testing, implementation, budgeting, and purchasing in the automotive market is to be carried out reliably, this process takes years. Many companies have fleets of vehicles and are looking for solutions to reduce CO_2 emissions [2, 18, 23]. At the same time, these companies would not want to change the composition of their fleets from internal combustion engine vehicles to electric motor vehicles. One solution could be to fuel internal combustion engines with fuels with similar physical and chemical properties to diesel [4, 6]. Such fuels include those derived from biomass, i.e., from vegetable oils, animal fats, and waste oils. All these components can be used as raw materials for alternative fuels. The group of alternative fuels includes higher fatty acid methyl esters (FAME) [10, 11]. These are fuels produced from oilseed crops such as linseed, rapeseed, or soybeans by transesterification [12, 18]. FAME fuels have several advantages over diesel, such as reduced emissions of hydrocarbons (HC), carbon monoxide (CO), and particulate matter (PM) and better ignition [20]. However, FAME fuel applications also come with limitations. FAME fuel can cause corrosion of storage tanks and also has a higher viscosity, which negatively affects fuel injection [4]. An alternative to FAME fuel can be hydrotreated vegetable oil (HVO). It is a synthetic liquid biofuel free of aromatics, oxygen, and sulfur [22]. In terms of chemical structure, it consists of straight-chain paraffinic hydrocarbons. The fuel is produced by hydrotreating vegetable oils, animal fats, or waste oils [17, 24]. Advantages of HVO fuel over FAME fuel include high heating value and cetane value, lower turbidity temperature, and lower viscosity [5, 16]. With fewer unsaturated compounds in its chemical composition, HVO shows better oxidation stability than FAME [1]. HVO fuel consists of straight-chain alkanes, which have a lower activation energy than the aromatic ring-shaped hydrocarbons of which diesel fuel is composed [24]. Therefore, the ignition delay for HVO fuel is shorter than diesel fuel's. This results in an earlier onset of combustion and reduced HC, CO, and PM emissions compared to diesel [15]. This shows that hydrotreated vegetable oil can be the fuel that can allow to plan and manage the reduction of carbon footprint and toxic emissions in the fleet in a professional manner [13]. However, studies are needed to show the effect of feeding an internal combustion engine with HVO fuel compared to diesel fuel on engine performance, power, torque, fuel consumption, efficiency, pressures, HRR, fuel dose burn rate, and combustion chamber temperature.

2. Materials and methods

The main objective of this research is to compare the effects of HVO fuel relative to diesel fuel on the combustion and performance of a JCB 444 TA4i-81 compression-ignition engine located on an engine dynamometer in the Combustion Engine Laboratory at the Institute of Vehicles and Working Machines at Warsaw University of Technology without interfering with the engine's design and control system.

2.1. Fuel

Two fuels were considered in the present study. Tests were performed for hydrotreated HVO vegetable oil and, comparatively, for diesel fuel. Table 1 summarizes the key physical and chemical parameters of the fuels along with the methods of determination. Table 1 shows the basic physical and chemical properties of the two fuels and provides the basis for the hypothesis that HVO fuel can be used as a replacement fuel for diesel fuel.

Table 1. Selected properties of HVO and diesel oil [8, 9, 20, 23]

Properties	Method	Unit	HVO	Diesel fuel
Density at 15°C	–	kg/m^3	777.8	830.6
Kinematic viscosity	–	mm^2/s	2.646	2.969
Dynamic viscosity	–	Pa·s	$2.06 \cdot 10^{-3}$	$2.47 \cdot 10^{-3}$
Cetane number	ASTM D613	–	79.6	54.6
Pour point	ISO 3016	°C	−58	−39
Flash point	ISO 2719	°C	66.3	70.5
Cold filter plugging point	EN 116	°C	−44	−22
Monoaromatic	–	%v/v	0.50	20.1
Polyaromatic	–	%v/v	0	3.0
Total aromatic	–	%v/v	0	23.1
Flammability	–	°C	60.5	74.0
Lower Heating Value	–	MJ/kg	44.35	42.65
Hydrogen	–	%m/m	15.00	13.72
Carbon	–	%m/m	85.00	85.67
Oxygen	–	%m/m	0	0.61
Sulphur	–	%m/m	0.53	6.50
Ash content	EN ISO 6245	%v/v	0.002	0.014
FAME	–	%v/v	0.05	5.00
Approx. formula	–	–	$C_{13}H_{28}$	$C_{13}H_{24}O_{0.06}$

Hydrogenated vegetable oil is a high-quality diesel product made entirely from renewable raw materials, i.e., vegetable oils and fat waste. HVO is a second-generation biofuel [14]. Hydrotreated vegetable oils are mixtures of paraffin hydrocarbons [3]. These fuels are free of any sulfur and aromatic compounds. As for the physicochemical properties of HVO fuel, special attention should be paid to the lower density value of HVO fuel compared to diesel fuel and the higher cetane number value of HVO fuel compared to ordinary diesel fuel. The main advantages of HVO fuel over diesel fuel are the just-mentioned high cetane number, high energy density, and the absence of oxygen in the molecule of the resulting fuel. An important advantage of HVO fuel is the pour point, which can be as low as –58°C. This, in turn, makes HVO suitable for use in very cold winters and at different geographic latitudes. Importantly, the production and use of HVO is largely climate-neutral if only renewable energy sources are used. HVO is obtained from waste cooking oils, fats, and fat residues, waste fats, and vegetable oil. One solution that will consider the goal of environmental protection and, at the same time, will not make it necessary to reorganize the operations of companies and ordinary households very quickly is to use biofuel as a substitute for diesel. Such a fuel is hydrotreated vegetable oil.

2.2. The engine test

Empirical tests were carried out on an engine dynamometer located at the Faculty of Automotive and Construction Machinery Engineering at the Warsaw University of Technology. The bench was based on a 4-cylinder JCB compression-ignition engine. The engine operates in a four-stroke cycle and has 16 valves (two intake and exhaust valves per cylinder. The crankshaft also drives a high-pressure fuel pump via gears. The pump is part of an electronically controlled common rail fuel injection system. The test engine was installed on a bench equipped with measuring instruments to record engine torque based on the SCHENCK brake (accuracy ±2 Nm), fuel consumption (accuracy 1%) and engine crankshaft speed. The AVL IndiSmart system was used to determine the engine's operating gas pressure. The engine specifications are shown in Table 2.

Table 2. Technical data of JCB engine [27]

Description	Unit	JCB SH Engine
Engine variants	–	Turbocharged with intercooler
Emission compliance	–	US-EPA Tier 4i, EU Stage IIIB
Rated speed	rpm	2200
Weight (dry)	kg	496
Number of cylinders	–	4
Nominal bore size	mm	103
Stroke	mm	132
Cylinder arrangement	–	In line
Combustion cycle	–	4-stroke
Firing order	–	1-3-4-2
Compression ratio	–	16.7:1
Direction of rotation (viewed from front {crankshaft pulley} end)	–	Clockwise
Valves	–	4 per cylinder
Valve clearances measured at the tappet end of the rockers (measured cold)		
– Inlet	mm	0.04–0.23
– Exhaust	mm	0.04–0.6
Lubricating oil pressure (dependent on engine temperature and speed)	MPa	0.16–0.65
Filter type	–	Screw-on canister (with drain facility)
Pressure to open by-pass valve	MPa	0.16
Oil pressure relief valve setting	MPa	0.6
Oil pressure switch setting	MPa	0.06 (falling)
Oil pump	–	Integral unit with relief valve
Combustion system	–	Common rail direct injection
High pressure fuel pump	–	High pressure with electron cally controlled fuel metering

The engine dynamometer stand is based on a JCB engine. The main internal and external components of the JCB engine assembly are shown below. The structure of the JCB engine is shown in Fig. 1–3.

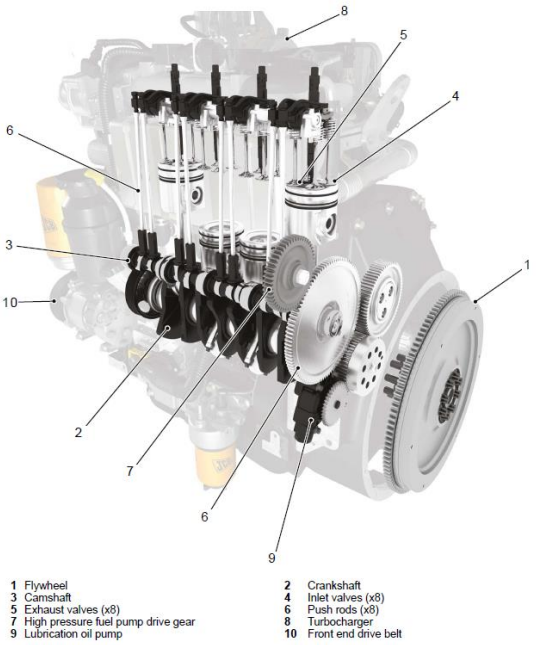

Fig. 1. JCB engine design [27]

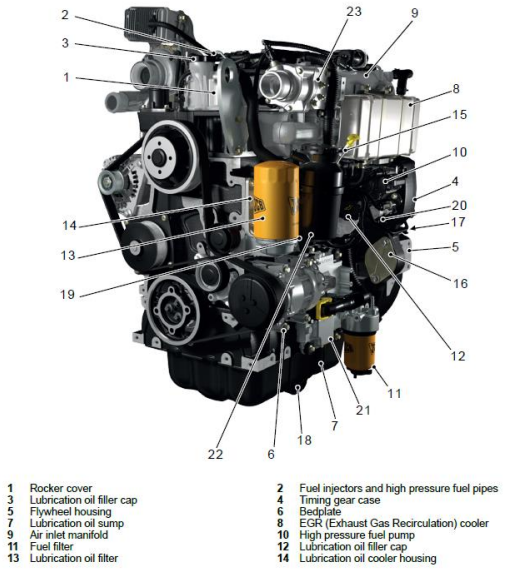

Fig. 2. JCB engine design [27]

2.3 Methods

The empirical tests on the JCB engine were planned so that during their implementation, the exhaust gas recirculation (EGR) system was not operating, and, in addition, no other changes were made to the engine settings (factory settings were used). In the first stage, empirical research was carried out on the speed characteristics. Then, an experiment was performed at the rotational speed of the engine crankshaft corresponding to the maximum torque – consisting of determining indicators related to the combustion process at a constant mass flow of fuels [kg/h]: diesel fuel (DF) and hydrogenated vegetable oil (HVO). In this way, information can be obtained about the impact of HVO on the combustion process in relation to the power supply of the DF engine.

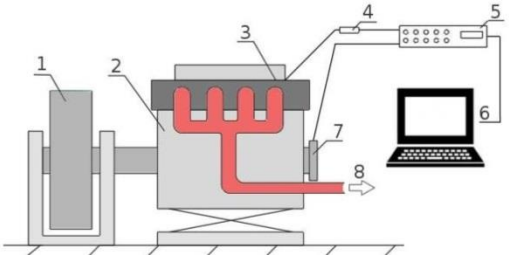

Fig. 3. Test stand: 1 – Schenck eddy current engine brake, 2 – JCB engine, 3 – pressure sensor, 4 – signal amplifier, 5 – AVL Indismart, 6 – computer for acquisition data, 7 – crankshaft position sensor, 8 – exhaust gases

The research engine was installed on a stand equipped with measuring instruments enabling the registration of engine torque based on the SCHENCK eddy current brake, fuel consumption, and engine crankshaft rotation speed. The AVL IndiSmart data acquisition system was used to determine the operating gas pressure in the engine cylinder. Relative error the gas pressure in the combustion chamber of the tested engine is $\delta = 0.25\%$ (measuring range 0–25 MPa). The test stand was built in accordance with the standards BN74/1340-12 and PN-88/S-02005.

One of the main characteristics of the fuel combustion process in an CI engine is the characteristic of the relative amount of heat released. Thanks to it, we can present the amount and rate of release of the relative amount of heat in the combustion process [10]. The rate of heat release based on data recorded in cylinder pressure was analysed as a function of crankshaft rotation angle at a crankshaft speed of 1400 rpm (speed corresponding to maximum torque). The heat release rate (HRR), can be calculated using the following formula [10]:

$$\mathrm{HRR} = \frac{\kappa}{\kappa-1} p \frac{dV}{d\varphi} + \frac{1}{\kappa-1} V \frac{dp}{d\varphi} \quad \text{[J/CAD]} \tag{1}$$

where $\frac{c_p}{c_v} = \kappa$.

The temperature can be determined from the ideal gas equation of state when the pressure and volume are known, and the mass is assumed to be constant at a given point in the characteristic.

The specific fuel consumption (SFC) was determined based on the hourly fuel consumption (HFC) measured during the experiment and the determined effective power (EP) at a given engine operating point:

$$\mathrm{SFC} = \frac{\mathrm{HFC}}{\mathrm{EP}} \cdot 1000 \ \text{[g/(kW·h)]} \tag{2}$$

$$\mathrm{HFC} = \frac{m_f}{t} \ \text{[g/h]} \tag{3}$$

where: m_f – fuel mass [g], t – fuel mass consumption time [h].

The useful power was determined on the basis of the torque (T) and angular speed of the crankshaft (ω):

$$\mathrm{EP} = \frac{T \cdot \omega}{1000} \ \text{[kW]} \tag{4}$$

where: T – torque crankshaft torque [Nm], ω – angular speed of the crankshaft [rad/s].

3. Results

This chapter presents the waveforms of torque and effective power. The following figures show the specific fuel consumption curves in the conditions described in section 2.3. The chapter ends with drawings regarding the combustion process, including the pressure and temperature of the working medium, heat release rate, and heat release factor. All of them were concerned with powering the engine with two HVO fuels and diesel fuel.

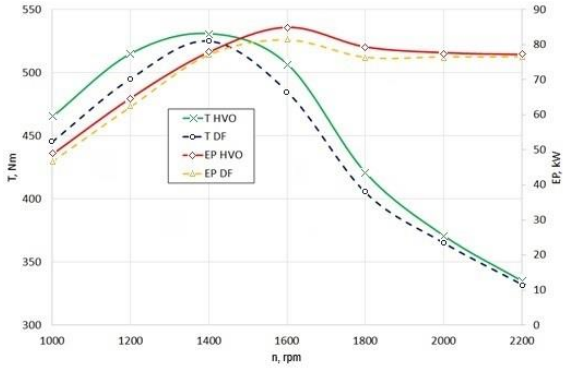

Fig. 4. Speed characteristics. Curves of the effective power and torque of the engine crankshaft as a function of the crankshaft rotation angle when the engine is powered by two fuels: diesel fuel (DF) and hydrogenated vegetable oil (HVO)

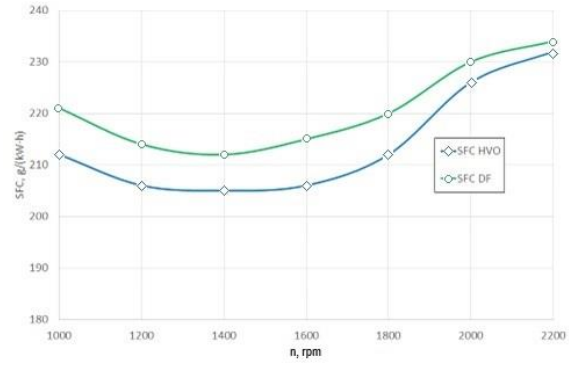

Fig. 5. Speed characteristics. Specific fuel consumption (SFC) curves as a function of the crankshaft rotation angle when the engine is powered by two fuels: diesel fuel (DF) and hydrogenated vegetable oil (HVO)

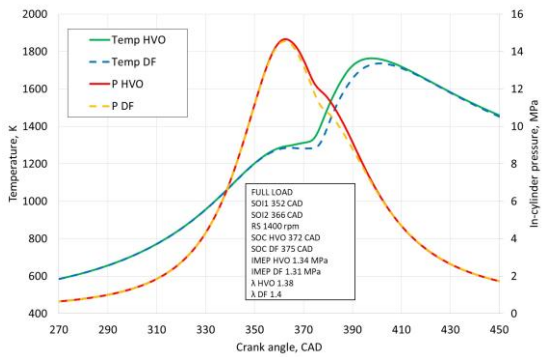

Fig. 6. Curves of pressure and temperature of the working medium in the combustion chamber as a function of the crankshaft rotation angle. Measurement made at maximum load and engine crankshaft speed of 1400 rpm

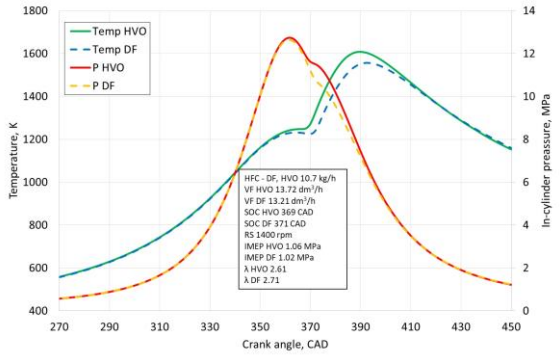

Fig. 7. Curves of pressure and temperature of the working medium in the combustion chamber as a function of the crankshaft rotation angle. Measurement made at a constant fuel mass flow of 10.7 kg/h and at an engine crankshaft speed of 1400 rpm

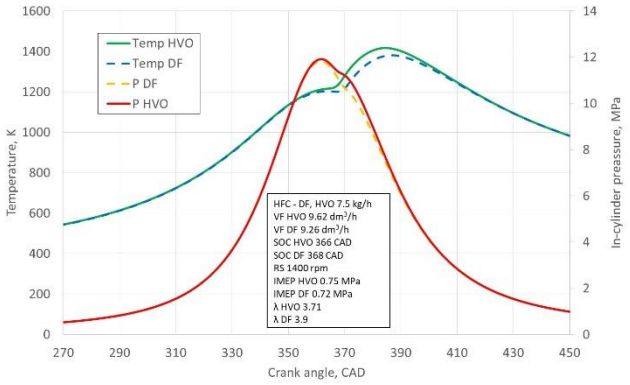

Fig. 8. Curves of pressure and temperature of the working medium in the combustion chamber as a function of the crankshaft rotation angle. Measurement made at a constant fuel mass flow of 7.5 kg/h and at an engine crankshaft speed of 1400 rpm

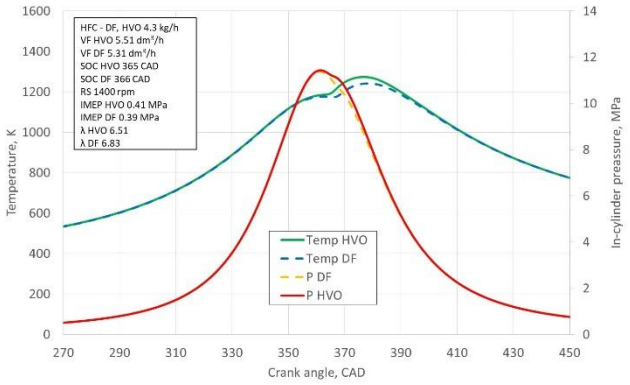

Fig. 9. Curves of pressure and temperature of the working medium in the combustion chamber as a function of the crankshaft rotation angle. Measurement made at a constant fuel mass flow of 4.3 kg/h and at an engine crankshaft speed of 1400 rpm

4. Conclusions and summary

Conclusions from the drawings presented in chapter 3:

1. The speed characteristics at the maximum volumetric fuel dose HVO (in the entire engine crankshaft rotational speed range) result in higher engine crankshaft torques and effective powers. Up to a maximum of 5% (Fig. 4).

2. Based on the speed characteristics at the maximum volumetric fuel dose, specific fuel consumption was reduced by up to 4% in the entire crankshaft speed range of the engine fueled with HVO fuel (Fig. 5).

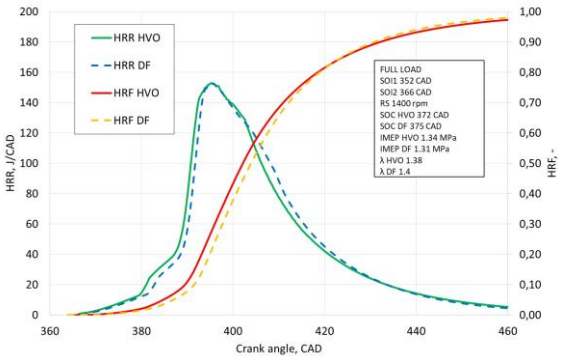

Fig. 10. Heat release rate (HRR) and heat release fraction (HRF) as a function of the crankshaft rotation angle. Values determined at maximum load and engine crankshaft speed of 1400 rpm

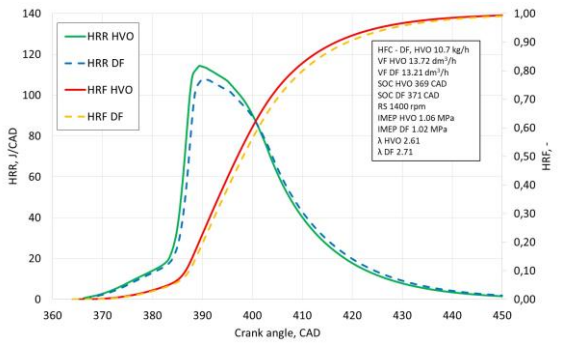

Fig. 11. Heat release rate (HRR) and heat release fraction (HRF) as a function of the crankshaft rotation angle. Values determined at a constant fuel mass flow of 10.7 kg/h and at an engine crankshaft rotation speed of 1400 rpm

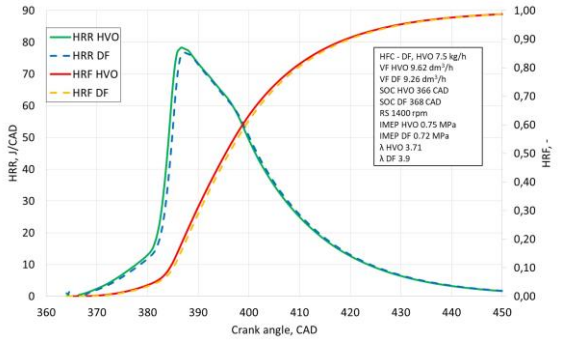

Fig. 12. Heat release rate (HRR) and heat release fraction (HRF) as a function of the crankshaft rotation angle. Values were determined at a constant fuel mass flow of 7.5 kg/h and at an engine crankshaft speed of 1400 rpm

3. Analyzing the course of pressure and temperature of the working medium in the combustion chamber as a function of the crankshaft rotation angle, one can notice in the case of the engine fueled with HVO fuel:
   - earlier start of the combustion process by 3 degrees CA, resulting in an increase in the maximum temperature in the combustion chamber by approximately 40 K and maintaining a similar level of maximum pressure at the engine operating point corresponding to the maximum load and crankshaft rotation speed of 1400 rpm (Fig. 6).

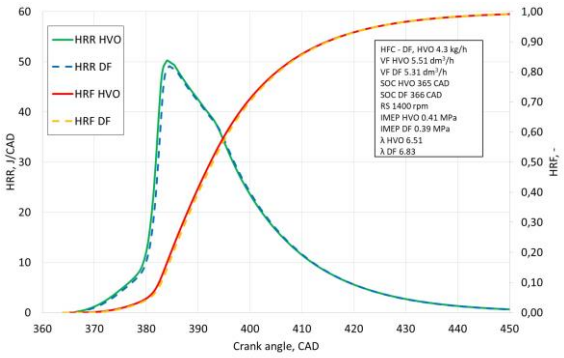

Fig. 13. Heat release rate (HRR) and heat release fraction (HRF) as a function of the crankshaft rotation angle. Values determined at a constant fuel mass flow of 4.3 kg/h and at an engine crankshaft speed of 1400 rpm

   - earlier start of the combustion process by 2 degrees CA, resulting in an increase in the maximum temperature in the combustion chamber by approximately 45 K and maintaining a similar level of maximum pressure at the engine operating point with a constant fuel mass flow of 10.7 kg/h for the tested fuels and at the crankshaft rotation speed engine speed of 1400 rpm (Fig. 7).
   - earlier start of the combustion process by 2 degrees CA, resulting in an increase in the maximum temperature in the combustion chamber by approximately 35 K and maintaining a similar level of maximum pressure at the engine operating point with a constant fuel mass flow of 7.5 kg/h for the tested fuels and at the crankshaft rotation speed engine speed of 1400 rpm (Fig. 8).
   - earlier start of the combustion process by 1 degree CA, resulting in an increase in the maximum temperature in the combustion chamber by approximately 10 K and maintaining a similar level of maximum pressure at the engine operating point with a constant fuel mass flow of 4.3 kg/h for the tested fuels and at the crankshaft rotation speed engine speed of 1400 rpm (Fig. 9).
4. Analyzing the heat release rate (HRR) and heat release fraction (HRF) as a function of the crankshaft rotation angle, it can be seen that in the case of fueling the engine with HVO fuel, one can notice an earlier start of the combustion process, higher maximum HRR values and the completion of the combustion process in a shorter time. The same crankshaft rotation angle.

In all measurement cases, the engine powered by HVO fuel showed increased IMEP. The indicated mean effective pressure in a compressor ignition engine is determined by various factors related to the combustion process. In all research cases, the average temperature in the combustion

chamber was higher (on HVO fuel). According to point 3 from chapter 4 – the earlier start of combustion – lower ignition delay can increase IMEP value. The increase of IMEP may result from better fuel atomization. The lower kinematic viscosity of the HVO fuel and the lower ignition temperature may improve the combustion process, which is noticeable by increasing IMEP. Lambda's value for HVO fuel was higher than that of diesel fuel. Due to the higher temperature and pressure in the combustion chamber, the kinetic energy of the exhaust gases increases. This may cause an increase in the amount of air forced into the engine by the turbocharger and, therefore, increase the excess air ratio.

The differences in combustion process indicators noticed during the tests result mainly from different physicochemical properties of the tested fuels. The most important of them are fuel calorific value, fuel density, and cetane number. HVO fuel has a higher cetane number compared to diesel fuel, which results in a shorter auto-ignition delay period and an earlier start of the fuel combustion process. Moreover, HVO fuel has a higher calorific value compared to diesel oil, which has a significant impact on the engine operating parameters. In the case of fueling the JCB engine with HVO fuel, no significant differences were noticed in the engine operating parameters or the combustion process. Therefore, according to the authors, the fuel can be a replacement for diesel oil even without major modifications or changes to engine settings. Based on the results and literature analysis, modern compression-ignition engines can use mixtures of HVO and diesel fuel in various concentrations without loss of engine performance. Thanks to modern fuel injectors with a fuel injection start sensor, the engine management units are able to correct the settings regarding the fuel injection process to eliminate differences in the physicochemical properties of the tested fuels. Thanks to the method of obtaining HVO fuel, it is possible to reduce CO_2 production by up to 90%, which is a particularly important parameter that may contribute to the popularization of this fuel, especially in heavy transport.

Acknowledgements

This paper was co-financed under the research grant of the Warsaw University of Technology supporting the scientific activity in the discipline of Civil Engineering, Geodesy and Transport (No. 15/ILGiT/2023).

Nomenclature

EP	effective power
DF	diesel fuel
FAME	fatty acid methyl esters
HRF	heat release fraction
HRR	heat release rate
HVO	hydrogenated vegetable oil
RS, n	engine crankshaft rotation speed
SFC	specific fuel consumption
SOC	start of combustion
T	engine crankshaft torque
VF	volume flow

Bibliography

[1] Ambat I, Srivastava V, Sillanpää M. Recent advancement in biodiesel production methodologies using various feedstock: a review. Renew Sust Energ Rev. 2018;90:356-69. https://doi.org/10.1016/j.rser.2018.03.069

[2] Andrych-Zalewska M. Research of pollutant emissions from automotive internal combustion engines in conditions corresponding to the actual use of vehicles. Combustion Engines. 2023;193:64-70. https://doi.org/10.19206/CE-162621

[3] Bortel I, Vávra J, Takáts M. Effect of HVO fuel mixtures on emissions and performance of a passenger car size diesel engine. Renew Energ. 2019;140:680-691. https://doi.org/10.1016/j.renene.2019.03.067

[4] da Costa RBR, Roque LFA, de Souza TAZ, Coronado CJR, Pinto GM, Cintra AJA et al. Experimental assessment of renewable diesel fuels (HVO/Farnesane) and bioethanol on dual-fuel mode. Energ Convers Manage. 2022;258:115554. https://doi.org/10.1016/j.enconman.2022.115554

[5] d'Ambrosio S, Mancarella A, Manelli A. Utilization of Hydrotreated Vegetable Oil (HVO) in a Euro 6 dual-loop EGR diesel engine: Behavior as a drop-in fuel and potentialities along calibration parameter sweeps. Energies. 2022;15:7202. https://doi.org/10.3390/en15197202

[6] Grzelak P, Żółtowski A. Environmental assessment of the exploitation of diesel engines powered by biofuels. Combustion Engines. 2020;180:31-35. https://doi.org/10.19206/CE-2020-105

[7] Hunicz J, Krzaczek P, Gęca M, Rybak A, Mikulski M. Comparative study of combustion and emissions of diesel engine fuelled with FAME and HVO. Combustion Engines. 2021;184:72-78. https://doi.org/10.19206/CE-135066

[8] Karavalakis G, Jiang Y, Yang J, Durbin T, Nuottimäki J, Lehto K. Emissions and fuel economy evaluation from two current technology heavy-duty trucks operated on HVO and FAME blends. SAE Int J Fuels Lubr. 2016;9:177-190. https://doi.org/10.4271/2016-01-0876

[9] Ko J, Jin D, Jang W, Myung CL, Kwon S, Park S. Comparative investigation of NO_x emission characteristics from a Euro 6-compliant diesel passenger car over the NEDC and WLTC at various ambient temperatures. Appl Energ. 2017;187:652-662. https://doi.org/10.1016/j.apenergy.2016.11.105

[10] Kruczyński SW, Orliński P. Combustion of methyl esters of various origins in the agricultural engine. Indian J Eng Mater S. 2013;20:483-491.

[11] Kruczyński SW, Orliński P, Biernat K. Camelina oil as a biofuel for diesel engines. Przem Chem. 2012;91(1):111-114.

[12] Kurczynski D, Wcisło G, Łagowski P. Experimental study of fuel consumption and exhaust gas composition of a diesel engine powered by biodiesel from waste of animal origin. Energies. 2021;14:3472. https://doi.org/10.3390/en14123472

[13] Lorenzi G, Baptista P, Venezia B, Silva C, Santarelli M. Use of waste vegetable oil for hydrotreated vegetable oil production with high-temperature electrolysis as hydrogen source. Fuel. 2020;278:117991. https://doi.org/10.1016/j.fuel.2020.117991

[14] Murtonen T, Aakko-Saksa P, Kuronen M, Mikkonen S, Lehtoranta K. Emissions with heavy-duty diesel engines and vehicles using FAME, HVO and GTL fuels with and without DOC+POC aftertreatment. SAE Int J Fuels Lubr. 2010; 2:147-166. https://doi.org/10.4271/2009-01-2693

[15] Parravicini M, Barro C, Boulouchos K. Experimental characterization of GTL, HVO, and OME based alternative fuels for diesel engines. Fuel. 2021;292:120177. https://doi.org/10.1016/j.fuel.2021.120177

[16] Permpool N, Gheewala SH. Environmental and energy assessment of alternative fuels for diesel in Thailand. J Clean Prod. 2017;142:1176-1182. https://doi.org/10.1016/j.jclepro.2016.08.081

[17] Pinto GM, da Costa RBR, de Souza TAZ, Rosa AJAC, Raats OO, Roque LFA, et al. Experimental investigation of performance and emissions of a CI engine operating with HVO and farnesane in dual-fuel mode with natural gas and biogas. Energy. 2023;277:127648. https://doi.org/10.1016/j.energy.2023.127648

[18] Pryciński P, Wawryszczuk R, Korzeb J, Pielecha P, Murawski J. Selected vehicle emissivity assessment issues in passenger transport services. Combustion Engines. 2023; 195:14-22. https://doi.org/10.19206/CE-169806

[19] Shepel O, Matijošius J, Rimkus A, Orynycz O, Tucki K, Świć A. Combustion, ecological, and energetic indicators for mixtures of hydrotreated vegetable oil (HVO) with duck fat applied as fuel in a compression ignition engine. Energies. 2022;15:7892. https://doi.org/10.3390/en15217892

[20] Sikora M, Orliński P, Matej J. Hydro-treated vegetable oil as a potential biofuel for self-ignition engines. Transport Samochodowy. 2022;1:14-20. https://doi.org/10.5604/01.3001.0015.8709

[21] Soam S, Hillman K. Factors influencing the environmental sustainability and growth of hydrotreated vegetable oil (HVO) in Sweden. Bioresource Technol Rep. 2019;7: 100244. https://doi.org/10.1016/j.biteb.2019.100244

[22] Stępień Z. Synthetic automotive fuels. Combustion Engines. 2023;192(1):78-90. https://doi.org/10.19206/CE-152526

[23] Szpica D, Czaban J, Banaszuk P, Weresa E. The diesel and the vegetable oil properties assessment in terms of pumping capability and cooperation with internal combustion engine fuelling system. Acta Mechanica et Automatica. 2015;9:14-18. https://doi.org/10.1515/ama-2015-0003

[24] Zeman P, Hönig V, Kotek M, Táborský J, Obergruber M, Mařík J et al. Hydrotreated vegetable oil as a fuel from waste materials. Catalysts. 2019;9(4):337. https://doi.org/10.3390/catal9040337

[25] Zhang Z, Lu Y, Roskilly AP, Yu X, Wang Y, Smallbone A. Investigation of the macroscopic characteristics of hydrotreated vegetable oil (HVO) spray using CFD method. Fuel. 2019;237:28-39. https://doi.org/10.1016/j.fuel.2018.09.141

[26] Žvirblis T, Hunicz J, Matijošius J, Rimkus A, Kilikevičius A, Gęca M. Improving diesel engine reliability using an optimal prognostic model to predict diesel engine emissions and performance using pure diesel and hydrogenated vegetable oil. Eksploat Niezawodn. 2023;25(4):174358. https://doi.org/10.17531/ein/174358

[27] JCB T4i 448 elec engine (4 cyl) service repair manual. https://issuu.com/xiangjixian32/docs/jcb_t4i_448_elec_engine__4_cyl__service_repair_man#google_vignette

Prof. Piotr Orliński, DSc., DEng. – Faculty of Automotive and Construction Machinery Engineering, Warsaw University of Technology, Poland.
e-mail: *piotr.orlinski@pw.edu.pl*

Piotr Laskowski DSc., DEng. – Faculty of Automotive and Construction Machinery Engineering, Warsaw University of Technology, Poland.
e-mail: *piotr.laskowski@pw.edu.pl*

Mieczysław Sikora, MEng. – Faculty of Automotive and Construction Machinery Engineering, Warsaw University of Technology, Poland.
e-mail: *mieczyslaw.sikora@pw.edu.pl*

Maciej Gis, DEng. – Motor Transport Institute, Environmental Protection Center, Poland.
e-mail: *maciej.gis@its.waw.pl*

Mateusz Bednarski, MEng. – Faculty of Automotive and Construction Machinery Engineering, Warsaw University of Technology, Poland.
e-mail: *mateusz.bednarski@pw.edu.pl*

Piotr Wiśniowski, DEng. – Motor Transport Institute, Environmental Protection Center, Poland.
e-mail: *piotr.wisniowski@its.waw.pl*

Article citation info:
Grzelak P, Chłopek Z, Szczepański K. Properties of substitute motor fuels produced from ethanol in biorefineries. Combustion Engines. 2024;198(3):41-47. https://doi.org/10.19206/CE-184488

Paulina GRZELAK
Zdzisław CHŁOPEK
Krystian SZCZEPAŃSKI

Combustion Engines
Polish Scientific Society of Combustion Engines

Properties of substitute motor fuels produced from ethanol in biorefineries

ARTICLE INFO

Received: 30 November 2023
Revised: 22 January 2024
Accepted: 20 February 2024
Available online: 6 April 2024

The article presents the definition of bioindustry, in particular biorefinery. The technology for obtaining synthetic fuel EtG (Ethanol to Gasoline) in a plant using bioethanol from food waste was presented. The physicochemical properties of EtG fuel were presented. EtG fuel stands out due to its limited content of benzene and sulfur and a low content of mechanical impurities and heavy metals. EtG fuel can be considered a replacement fuel for motor gasoline. The results of exhaust emissions tests from vehicles with spark-ignition engines in the WLTC test on a hot and cold engine were presented. It was found that EtG fuel is characterized by lower specific distance emissions of CO, NO_x, and CH_4 and slightly higher specific distance emissions of NMHC when starting a cold engine compared to gasoline, while the specific distance emission of CO_2 for both fuels were very similar

Key words: *biorefinery, substitute motor fuels, bioethanol, ethanol to gasoline*

1. Introduction

Due to the increasingly intense expectation to develop rationalization of the use of available energy carriers and raw materials to meet the needs of societies while ensuring the needs of the environment, new production methods are being sought. This role is played by the so-called bioindustry. An integrated bioindustry is an industry that uses a spectrum of techniques to obtain products such as chemicals, bio-based fuels, food, feed ingredients, biomaterials, and usable energy, taking into account the three pillars of sustainability: environment, economy, and society.

There are many possibilities for using types of biologically derived raw materials [1–4, 6–9, 13–17, 19–23, 25].

The article [1] reviews the current state of knowledge about algae biofuel as a renewable energy source.

Article [2] describes current challenges and opportunities to sustainably increase biomass production and highlights future technologies to further improve the production of biofuels directly from sunlight. It was postulated that in order to objectively assess the environmental impact of the use of fuels of biological origin, it is necessary to conduct LCA tests.

Publications [3, 25] present a comprehensive review of the catalytic conversion of bioethanol to hydrocarbons – gasoline components. A great potential of this technology was found.

The studies [4, 22, 23] present the Global Biorefinery Status Report (GBRSR), published by the IEA Bioenergy Task 42 Biorefinery. The report provides an overview of the latest developments in biorefinery. The report compiles data and information reported by representatives of partner countries and member states in the National Reports of Task 42 Biorefinery.

The publication [7] contains systematic information on the biorefinery system as a basic element of sustainable civilization development.

Articles [6, 14, 16, 17] are dedicated to future technologies aimed at further improving the production of fuels of biological origin directly from sunlight – the so-called "synthetic biology". Particularly, great hopes are associated with the use of microorganisms for this purpose. The current progress in hybrid technologies (biomass production, wastewater treatment, reduction of greenhouse gas emissions) enables the effective production of first-class products, such as, above all, renewable fuels.

Article [21] provides an overview of techniques developed to valorize biomass for the production of platform chemicals in a biorefinery and the status of commercialization. Biomass is treated as a way to constantly deplete limited fossil resources, the use of which is attributed to an adverse impact on the environment.

The article [8] analyzed the problems of biorefinery systems according to the criteria: technology, raw materials, and products. Attention was paid to the possibility of obtaining products with versatile uses in biorefineries, e.g. not only renewable fuels, but also animal feed.

The study [13] presents an existing biorefinery in Venice, created as a result of the transformation of a conventional oil refinery in which HVO fuel (Hydrotreated Vegetable Oil) is produced. The article also presents the parameters of this new biofuel and compares them with the parameters of other fuels used to power compression-ignition engines, such as FAME (Fatty Acid Methyl Esters) and diesel oil, and discusses the prospects for the development of HVO fuels in Europe.

The publication [20] presents the balance of fuel consumption in the United States of America. It has been found that in the last few decades, the consumption of transport fuels corresponds to about 1/3 of all energy consumed, of which about 90% comes from fossil sources, which is a serious ecological problem.

The paper [19] presents basic information on the metabolic engineering of microorganisms for the production of fourth-generation biofuels. The fourth-generation fuel production technology is presented as a fundamental pro-ecological contrast to earlier technologies.

Monograph [9] is dedicated to the use of methane fuels to power the internal combustion engines of city buses. The work presents a systematic classification of methane fuels, distinguishing renewable fuels produced from biogas.

The article [15] highlighted the great possibilities of using bioethanol as an oxygen component for conventional gasoline to power spark-ignition engines. It was found that in modern spark-ignition engines, it is possible to use gasoline with the addition of ethanol up to 30% V/V as a fuel treated as a substitute fuel, thus not requiring changes in the design, materials used, and control algorithms of combustion engines.

The use of biofuels of biological origin is the subject of many publications [2, 9–12, 15, 18, 26]. In most cases, significant ecological benefits related to pollutant emissions were found.

The publication [9] describes the results of research on pollutant emissions from spark-ignition engines powered by methane fuels intended to power city buses. The tests were performed on an engine dynamometer in static and dynamic homologation tests. A significant reduction in emissions of carbon monoxide, hydrocarbons and nitrogen oxides was found, and – obviously in relation to compression-ignition engines originally used to power city buses – a particularly significant reduction in particulate matter emissions.

Paper [10] presents the results of research on the combustion process in a compression-ignition engine powered by diesel oil and methyl esters of rapeseed oil with summer and winter additives. The aim of the research was to assess whether, due to the properties of the combustion process, it is justified to treat rapeseed oil methyl esters as substitute fuels for diesel oil. It was found that the tested biological fuels meet these requirements, especially fuel with summer additives.

In publication [11], the emission of pollutants from a compression-ignition engine used in a passenger car was examined in driving tests. The sensitivity of pollutant emissions to the concentration of rapeseed oil methyl esters in the mixture with diesel oil was tested. A significant reduction in road emissions of carbon monoxide, hydrocarbons and, especially, particulate matter was found thanks to the use of rapeseed oil methyl esters.

The publication [12] presents the results of tests on pollutant emissions from combustion engines powered by bioethanol fuels: E95 for compression-ignition engines and E85 for spark-ignition engines. It was found that the use of bioethanol fuels compared to conventional fuels reduces emissions of carbon monoxide, hydrocarbons and nitrogen oxides, and in the case of compression-ignition engines – an additional significant reduction in particulate matter emissions.

The study [15] examined the emission of pollutants from internal combustion engines powered by mixtures of gasoline and ethanol in driving tests starting with a cold engine. A beneficial effect of the use of ethanol on pollutant emissions when starting a cold engine was found.

The publication [18] examines the emission of pollutants from compression-ignition engines powered by mixtures of diesel oil with esters of biological oils and esters of biological oils and bioethanol. Confirming the beneficial effect of bio-additives on the emission of pollutants harmful to the health and life of living organisms, the authors focus mainly on reducing fossil carbon dioxide emissions.

Paper [2] presents the results of tests on a spark ignition engine powered by gasoline with a mixture of biological additives. The tests were performed on an engine dynamometer in static conditions. The beneficial effect of the use of oxygen additives on pollutant emissions has been confirmed.

Publication [26] presents the results of empirical research and tests of the developed mathematical model of a marine engine powered by a mixture of diesel oil and n-butanol. Benefits in terms of pollutant emissions were found when using biological additives to power the engine. The results of empirical research confirmed the adequacy of the developed mathematical model.

Perspectives of advanced biofuels development, including using ethanol as a raw material, were described in Global biorefinery status report 2022 by IEA Bioenergy [4, 22].

One of the products of the bio-industry used to power internal combustion engines is fuel called EtG (Ethanol to Gasoline), which is a substitute fuel for gasoline for spark ignition engines.

The results of empirical research on the use of biological additives to conventional fuels confirm the benefits in terms of the emission of pollutants harmful to the health and life of living organisms and – which is obvious – a reduction in bituminous carbon dioxide emissions.

There are relatively few publications on the use of biologically derived fuels as substitute fuels to power internal combustion engines. Such fuel for spark-ignition engines is EtG fuel, which is a hydrocarbon fuel made from bioethanol. For these reasons, this study deals with comparative studies of pollutant emissions from the engine of a passenger car fuelled with commercial gasoline and EtG synthetic fuel.

2. EtG fuel (Ethanol to Gasoline)

EtG is a fuel produced from renewable sources, which has functional properties corresponding to those of motor gasoline. EtG fuel meets the quality requirements specified in the Regulation of the Minister of Economy of December 17, 2010 and can be added to gasoline as a biocomponent intended for the fuels used in spark-ignition engines.

The most important advantages of producing and using EtG fuel are as follows:

- EtG fuel is produced from renewable sources. The biomass used in the bioethanol production process comes from waste raw materials (i.a. waste bread). The production and use of EtG fuel enables the achievement of the National Indicative Target and the National Reduction Target in gasoline fuels at the level provided for by EU directives for 2020–2030 or even higher. EtG fuel therefore meets the criteria of sustainable development.
- The EtG fuel production process does not require a large amount of energy from external sources. This is facilitated by the possibility of using raw (unpurified) alcohol in the production process of EtG fuel. The low energy consumption of the EtG fuel production process results in reduced greenhouse gas emissions.

Table 1 shows the parameters of the EtG fuel.

Table 1. Parameters of EtG fuel

Parameter	Unit	Result
Density at the temperature 15°C	kg/m^3	761.1
Appearance	–	bright and transparent
Vapour pressure (dry vapour pressure equivalent)	kPa	57.0
N-paraffins	% V/V	11.44
I-paraffins	% V/V	32.59
Olefins	% V/V	1.95
Naphthenes	% V/V	7.60
Aromatic hydrocarbons	% V/V	41.84
Polycyclic hydrocarbons	% V/V	0.31
Not specified	% V/V	4.27
Oxygen derivatives	% V/V	0.00
Oxygen	% m/m	0.00
Benzene	% V/V	0.30

3. Research methodology

Empirical tests of the effects of using EtG fuel were carried out on a chassis dynamometer in accordance with the WLTP type 3 [5, 24].

The research equipment used in the tests met the formal requirements of the approval procedures.

The object of the research was a passenger car – a Hyundai i30 with a spark-ignition engine (Euro 6AP level). The vehicle was fuelled by motor gasoline and EtG fuel. Tests were performed to start a cold and hot engine.

4. Results of empirical research

The specific distance emissions of CO, NMHC, CH_4, NO_x, CO_2, and operational fuel consumption are presented in Fig. 1–12.

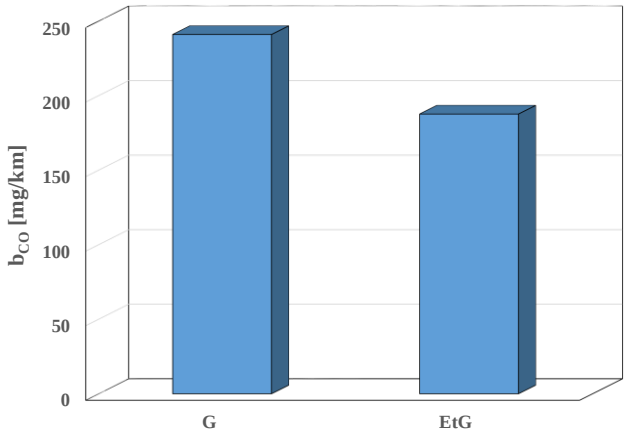

Fig. 1. The CO specific distance emission – b_{CO} when the vehicle is fuelled with gasoline – G and EtG for cold start

Specific distance emission of CO in the cold start is lower for EtG (187.7 mg/km) than for motor gasoline (241 mg/km). The difference in road carbon monoxide emissions is over 50 mg/km (Fig. 1).

The situation is similar for starting a hot engine: when powered by petrol, specific distance emissions of CO is over 73.4 mg/km, and when powered by EtG fuel – about 46.6 mg/km. The absolute difference is over 26 mg/km, but the relative difference is larger when the engine is hot (Fig. 2).

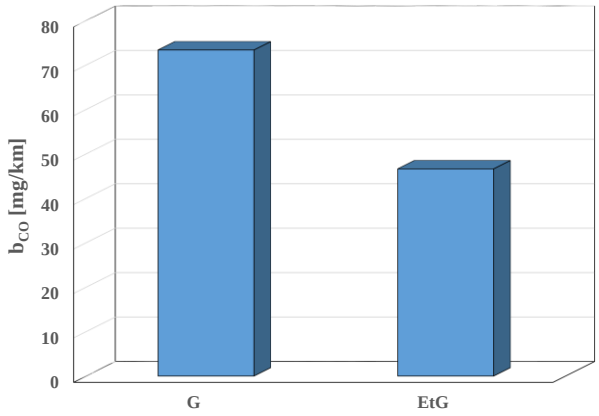

Fig. 2. The CO specific distance emission – b_{CO} when the vehicle is fuelled with gasoline – G and EtG for hot start

The impact of the thermal condition of the engine at start-up on carbon monoxide emissions is very significant.

In the case of emissions of organic compounds, the emissions of non-methane hydrocarbons and methane are examined.

For NMHC specific distance emissions in the cold start test (29.6 mg/km) are higher when the engine is fuelled with EtG fuel (39.0 mg/km). The difference is significant – almost 10 mg/km (Fig. 3).

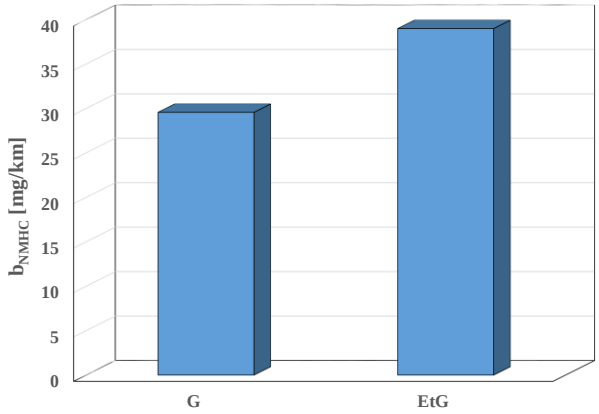

Fig. 3. The NMHC specific distance emission – b_{NMHC} in the WLTC test when the vehicle is fuelled with gasoline – G and EtG for cold start

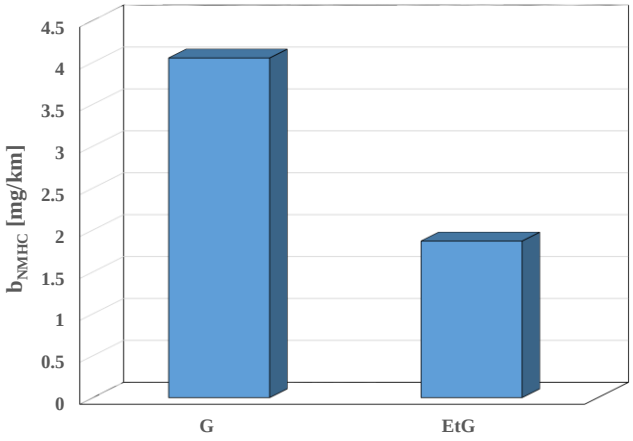

Fig. 4. The NMHC specific distance emission – b_{NMHC} when the vehicle is fuelled with gasoline – G and EtG for hot start

It is different for the hot start of the engine – the specific distance emission of non-methane hydrocarbons for motor gasoline is 4.1 mg/km, and EtG fuel is 1.9 mg/km. In this case the difference is over 2 mg/km (Fig. 4). The thermal condition of the engine during its start-up has a very large influence on the test results, more than in the event of carbon monoxide emissions. The thermal condition of the engine during its start-up in the event of EtG fuel has a particularly remarkable influence on the test result.

Specific distance emissions of CH_4 in the cold engine start test (6.2 mg/km) are much lower for EtG fuel (2.2 mg/km). The difference is approximately 4 mg/km (Fig. 5).

The dissimilarity in specific distance emission of CH_4 in the test with a hot engine start is even greater. For motor gasoline, this emission is almost 4.5 mg/km, and for EtG fuel – about 0.2 mg/km (Fig. 6).

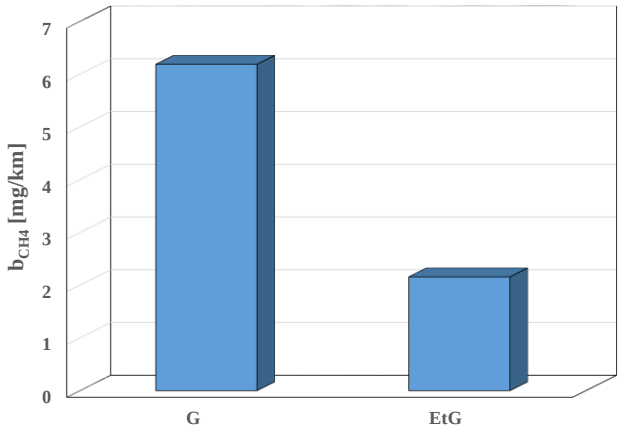

Fig. 5. The CH_4 specific distance emission – b_{CH4} when the vehicle is fuelled with gasoline – G and EtG for cold start.

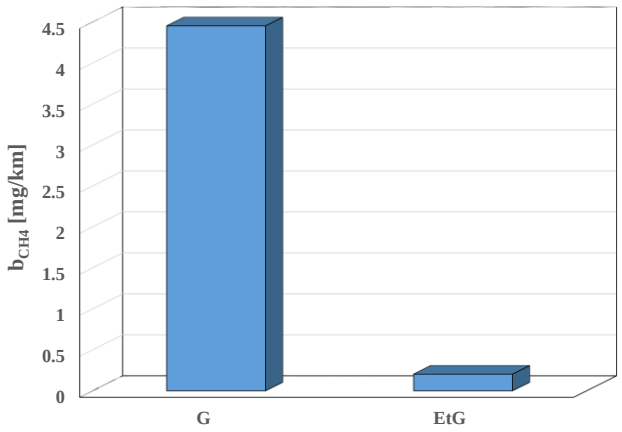

Fig. 6. The CH_4 specific distance emission of methane – b_{CH4} when the vehicle is fuelled with gasoline – G and EtG for hot start

The influence of the thermal condition of the engine during its start-up is much greater for specific distance emission of CH_4 when the engine is fuelled with EtG fuel. In general, the influence of the thermal condition of the engine during its start-up on specific distance emission of organic compounds is greater for non-methane hydrocarbons than for methane.

The specific distance emission of NO_x in the cold start test is about 1.5 mg/km higher for motor gasoline (13.1 mg/km) than for EtG fuel (11.7 mg/km), so the difference is small (Fig. 7).

The difference in specific distance emission of NO_x during hot star-up is even smaller – this difference can be assessed as insignificant: 5.2 mg/km for motor gasoline and 5.0 mg/km for EtG fuel (Fig. 8).

The influence of the thermal condition of the engine at start-up on specific distance emission of nitrogen oxides is much smaller than in the event of CO, especially biocompounds.

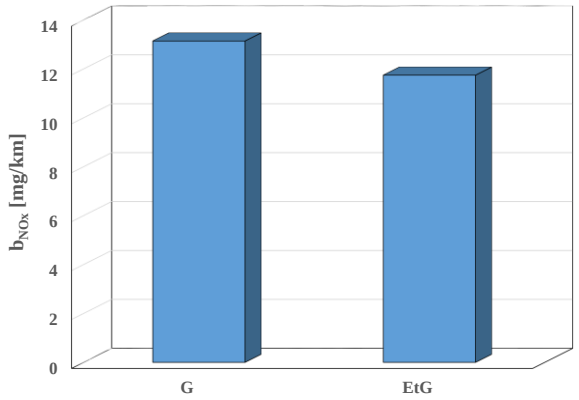

Fig. 7. The NO_x specific distance emission of nitrogen oxides – b_{NOx} when the vehicle is fuelled with gasoline – G and EtG for cold start

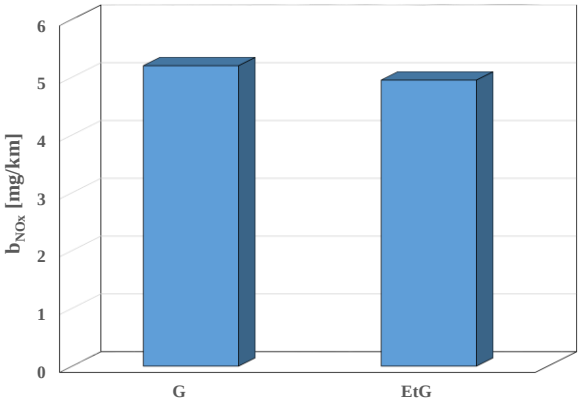

Fig. 8. The NO_x specific distance emission – b_{NOx} when the vehicle is fuelled with gasoline – G and EtG for hot start

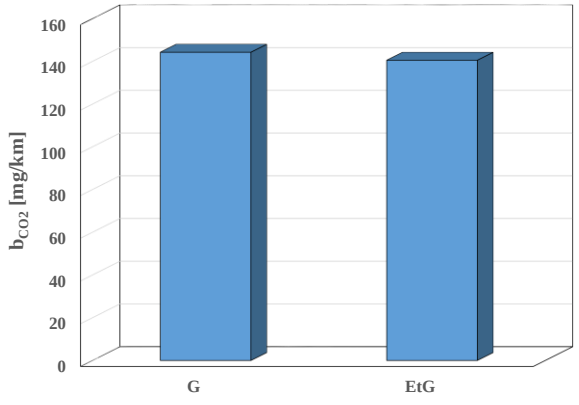

Fig. 9. The CO_2 specific distance emission – b_{CO2} when the vehicle is fuelled with gasoline – G and EtG for cold start

The specific distance emission of CO_2 when starting a cold engine is slightly higher for motor gasoline (Fig. 9).

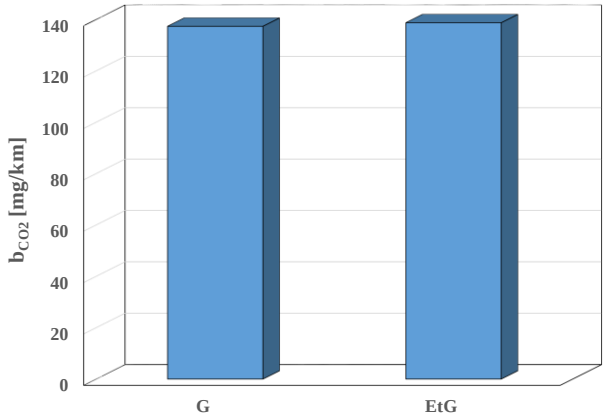

Fig. 10. The CO_2 specific distance emission of carbon dioxide – b_{CO2} in the WLTC test when the vehicle is fuelled with gasoline – G and EtG for hot start

In the case of a hot start-up, it can be estimated that the specific distance emission of CO_2 is similar for both tested fuels (Fig. 10).

The engine's thermal condition at the start of the engine has a very small influence on the specific distance of CO_2 emission.

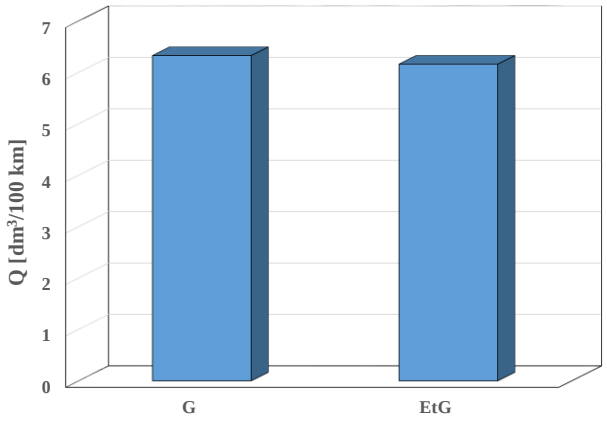

Fig. 11. The operational fuel consumption – Q when the vehicle is fuelled with gasoline – G and EtG for cold start

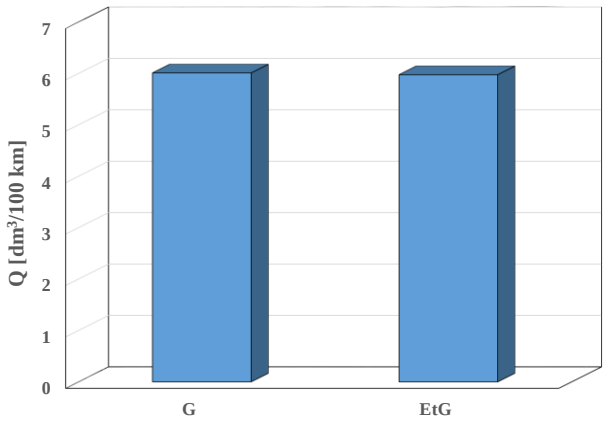

Fig. 12. The operational fuel consumption – Q when the vehicle is fuelled with gasoline – G and EtG for hot start

The dependence for operational fuel consumption is practically identical to those for specific distance emission of CO_2 (Fig. 11, 12).

The relative decrease of the value of physical quantity "w" for the use of EtG fuel in relation to the value for the use of gasoline is defined as follows:

$$\delta = -2 \cdot \frac{w_{EtG} - w_G}{W_{EtG} + w_G} \quad (1)$$

Based on the empirical research conducted, the conclusions are as follows:

1. The use of EtG fuel causes a relative reduction in specific distance emissions of the following pollutants for could start-up compared to the use of motor gasoline:
   – carbon monoxide 24.9%
   – methane 96.6%
   – nitrogen oxides 11.2%
   – carbon dioxide 2.6%
   – and operational fuel consumption 2.7%.
2. The use of EtG fuel causes a relative increase in specific distance emission of NMHC for hot start compared to the use of gasoline by 27.5%.
3. The use of EtG fuel causes a relative reduction in specific distance emissions of the following pollutants for hot start compared to the use of gasoline:
   – carbon monoxide 44.6%
   – non-methane hydrocarbons 73.8%
   – methane 182.5%
   – nitrogen oxides 4.9%
   – carbon dioxide –1.0%
   – and operational fuel consumption 0.6%.
4. The use of EtG fuel causes a slight relative increase in specific distance emission of CO_2 with hot start-up compared to the use of gasoline by approximately 1%.
5. The greatest impact on pollutant emissions is caused a cold engine start for NMHC, CH_4, CO, and NO_x. The relative change in specific distance emissions is for:
   – non-methane hydrocarbons for EtG fuel about 180%
   – non-methane hydrocarbons for gasoline about 150%
   – methane for EtG fuel over 170%
   – for carbon monoxide for both fuels over 100%
   – for nitrogen oxides for both fuels almost 100%.

   In general, it can be stated that the use of bioethanol fuel instead of gasoline to power a spark ignition engine brings ecological benefits in terms of emissions of pollutants harmful to health and fossil carbon dioxide emissions.

5. Summary

In the summary of the article, the conclusions are as follows:

1. The production of non-petroleum fuels in biorefineries is an important element of energy safety. There is also an important aspect of protecting natural resources.
2. An important benefit is that biorefinery fuels are produced from waste products that pose a serious threat to the environment.
3. The production of fuels in biorefineries is characterized by low energy consumption – this is an economic bene-

fit, and it also results in a reduction in greenhouse gas emissions.

4. In general, it can be stated that the use of EtG instead of gasoline to power a spark ignition engine brings ecological benefits in terms of pollutants and fossil carbon dioxide emissions.
5. EtG fuel is characterized by extremely low content of benzene, sulfur, and nitrogen, mechanical impurities, and the content of heavy metals is below the limit of the test method determination. This has significant environmental impacts related to eutrophication and acidification.
6. EtG fuel is not the only product of the biorefinery installation. This process also produces biopropane and biobutane, which can be used as biocomponents or self-contained biofuels.

Further directions of planned research on the properties of ethanol fuels include:

– tests in real vehicle driving conditions, including: in RDE tests,
– tests in model vehicle traffic conditions, significantly different in nature, typical for driving: in traffic jams, in cities outside traffic jams, on roads outside cities and on highways and expressways,
– tests in various engine operating states, both static and dynamic.

Nomenclature

b	specific distance emission
CH_4	methane
CO	carbon monoxide
CO_2	carbon dioxide
EtG	Ethanol to Gasoline
NMHC	non-methane hydrocarbons
NO_x	nitrogen oxides
Q	operational fuel consumption
w	value of physical quantity
WLTC	Worldwide harmonized Light vehicles Test Cycle
WLTP	Worldwide harmonized Light vehicles Test Procedure
δ	relative reduction

Bibliography

[1] Alam F, Mobin S, Chowdhury H. Third generation biofuel from algae. Procedia Engineer. 2015;105:763-768. https://doi.org/10.1016/j.proeng.2015.05.068

[2] Andrych-Zalewska M, Sitnik L, Sroka Z, Mihaylov V. Fuel with a higher content of bio components in greenhouse effect aspects. Combustion Engines. 2023;192(1):36-42. https://doi.org/10.19206/CE-147741

[3] Anekwe IMS, Isa YM, Oboirien B. Bioethanol as a potential eco-friendlier feedstock for catalytic production of fuels and petrochemicals. J Chem Technol Biot. 2023;98:2077-2094. https://doi.org/10.1002/jctb.7399

[4] Annevelink B, Chavez LG, van Ree R, Gursel IV. Global biorefinery status report 2022. In IEA Bioenergy: Task 42 Biorefining in a Circular Economy. IEA Bioenergy. https://www.ieabioenergy.com/wp-content/uploads/2022/09/IEA-Bioenergy-Task-42-Global-biorefinery-status-report-2022-220712.pdf (accessed on 24.08.2023).

[5] Annex XXI to Commission Regulation (EU) 2017/1151 as last amended by Commission Regulation (EU) 2018/1832. https://www.legislation.gov.uk/eur/2018/1832/adopted

[6] Aro EM. From first generation biofuels to advanced solar biofuels. Ambio. 2016;45:24-31. https://doi.org/10.1007/s13280-015-0730-0

[7] Biernat K, Grzelak P. Biorefinery systems as an element of sustainable development, biofuels – status and perspective. InTech. 2015. https://doi.org/10.5772/60448

[8] Cherubini F, Jungmeier G, Wellisch M, Willke T, Skiadas I, Van Ree R et al. Toward a common classification approach for biorefinery systems. Biofuel Bioprod Bior. 2009;3(5): 534-546. https://doi.org/10.1002/bbb.172

[9] Chłopek Z, Gis W, Menes E, Waśkiewicz J. The study of the use biomethane to the supply city buses in Poland. Motor Transport Institute. Warszawa 2013.

[10] Chłopek Z, Jagiełło S, Juwa S, Zakrzewska D. Examination of the combustion process in a compression ignition engine fuelled with diesel oil and rape methyl esters. The Archives of Automotive Engineering – Archiwum Motoryzacji. 2017;76(2):17-35. https://doi.org/10.14669/AM.VOL.76.ART1

[11] Chłopek Z, Grzelak P, Zakrzewska D. Evaluation of the influence of car engine power supply with rapeseed oil esters on emission of pollutants in dynamic conditions. Machine Dynamics Research. 2018;47(4):55-71.

[12] Chłopek Z. Ecological aspects of using bioethanol fuel to power combustion engines. Eksploat Niezawodn. 2007;35: 65-69. https://archive.ein.org.pl/2007-03

[13] Grzelak PL, Żółtowski A. Environmental assessment of the exploitation of diesel engines powered by biofuels. Combustion Engines. 2020;180(1):31-35. https://doi.org/10.19206/CE-2020-105

[14] Ho S-H, Ye X, Hasunuma T, Chang J-S, Kondo A. Perspectives on engineering strategies for improving biofuel production from microalgae: A critical review. Biotechnol Adv. 2014;32(8):1448-1459. https://doi.org/10.1016/j.biotechadv.2014.09.002

[15] Iodice P, Langella G, Amoresano A. Ethanol in gasoline fuel blends: Effect on fuel consumption and engine out emissions of SI engines in cold operating conditions. Appl Therm Eng. 2018;130:1081-1089. https://doi.org/10.1016/j.applthermaleng.2017.11.090

[16] Jungmeier G, Hingsamer M, van Ree R. Biofuel-driven biorefineries. A selection of the most promising biorefinery concepts to produce large volumes of road transportation biofuels by 2025. IEA Bioenergy – Task 42 Biorefinery, February 2013. https://task42.ieabioenergy.com/publications/biofuel-driven-biorefineries/

[17] Maity JP, Bundschuh J, Chen C-Y, Bhattacharya P. Microalgae for third generation biofuel production, mitigation of greenhouse gas emissions and wastewater treatment: present and future perspectives: a mini review. Energy. 2014;78: 104-113. https://doi.org/10.1016/j.energy.2014.04.003

[18] Mofijur M, Rasul MG, Hyde J, Azad AK, Mamat R, Bhuiya MMK. Role of biofuel and their binary (diesel-biodiesel) and ternary (ethanol-biodiesel-diesel) blends on internal combustion. Renew Sust Energ Rev. 2016;53:265-278. https://doi.org/10.1016/j.rser.2015.08.046

19] Moravvej Z, Makarem MA, Rahimpur MR. The fourth generation of biofuel (Chapter 20). Second and Third Generation of Feedstocks. The Evolution of Biofuels. 2019;557-597. https://doi.org/10.1016/B978-0-12-815162-4.00020-3

[20] Rosentrater KA. Production and use of evolving corn-based fuel ethanol coproducts in the U.S. Biofuels – Status and Perspective. InTech. 2015. https://doi.org/10.5772/59951

[21] Takkellapati S, Li T, Gonzalez MA. An overview of biorefinery-derived platform chemicals from a cellulose and hemicellulose biorefinery. Clean Technol Envir. 2018;20:1615-1630. https://doi.org/10.1007/s10098-018-1568-5

[22] Van Dyk S, Su J, McMillan JD, Saddles JN. Drop-in biofuels: The key role that co-processing will play in its production. IEA Bioenergy. Task 39. 2019. https://www.ieabioenergy.com/wp-content/uploads/2019/09/Task-39-Drop-in-Biofuels-Full-Report-January-2019.pdf (accessed on 15.12.2022).

[23] Van Ree R, Annevelink E. Status Report Biorefinery 2007. November 2007. http://www.wur.nl (accessed on 31.10. 2022).

[24] Worldwide emissions standards passenger cars and light duty vehicles. Delphi. Innovation for the real world. 2022/2023.

[25] Xiang H, Xin R, Prasongthum N, Natewong P, Sooknai T, Wang J et al. Catalytic conversion of bioethanol to value-added chemicals and fuels: a review. Resour Chem Mater. 2022;1(1):47-68. https://doi.org/10.1016/j.recm.2021.12.002

[26] Zacharewicz M, Kniaziewicz T. Model tests of a marine diesel engine powered by a fuel-alcohol mixture. Combustion Engines. 2022;189(2):83-88. https://doi.org/10.19206/CE-143486

Paulina Grzelak, DEng. – Institute of Environmental Protection – National Research Institute, Poland.
e-mail: *paulina.grzelak@kobize.pl*

Prof. Zdzisław Chłopek, DSc., DEng. – Institute of Environmental Protection – National Research Institute, Poland.
e-mail: *zdzislaw.chlopek@kobize.pl*

Krystian Szczepański, DSc., DEng. – Professor of IOS-PIB – Institute of Environmental Protection – National Research Institute, Poland.
e-mail: *krystian.szczepanski@ios.edu.pl*

Article citation info:
Marzec P, Kubica G. Dynamic parameters of a car with a SI engine fueled with LPG/DME blends. Combustion Engines. 2024;198(3): 48-53. https://doi.org/10.19206/CE-185955

Paweł MARZEC
Grzegorz KUBICA

Combustion Engines
Polish Scientific Society of Combustion Engines

Dynamic parameters of a car with a SI engine fueled with LPG/DME blends

ARTICLE INFO

Received: 6 September 2023
Revised: 11 March 2023
Accepted: 11 March 2023
Available online: 20 April 2024

The paper presents an analysis of the dynamic parameters of a compact class passenger car powered by LPG/DME blends. The presented results are part of the research cycle of this vehicle, the purpose of which was to check the possibility of using DME (dimethyl ether) as an additive in the fuel mixture with LPG. In the presented part of the experimental research, the acceleration times of the vehicle under specific conditions were measured. On the basis of the obtained results, the relations between the average acceleration in the tested speed ranges, the fuel composition, and the degree of engine load were developed. The results of the analysis indicate that in the examined range of changes in the DME share in the fuel, comparable or higher acceleration values were obtained for all engine load levels. This confirms the usefulness of DME as a fuel component used to power SI engines.

Key words: *LPG/DME, fuel blend, dynamic parameters, acceleration, SI engine*

1. Introduction

The analysis of scientific research on the use of DME clearly shows that it is used in many branches of the economy. Dimethylether is considered one of the best alternative fuels for internal combustion engines. It owes this to its physico-chemical properties, as an environmentally friendly, non-toxic, biodegradable product. DME can be produced from natural gas, coal or biomass. As a synthetic fuel, it is considered an excellent substitute for conventional diesel and LPG.

Many research units have started researching the use of DME in diesel engines [3, 15, 17, 21]. The properties of this fuel allow it to be used in a diesel engine due to its high cetane number and low auto-ignition temperature. Due to the very low PM emission during DME combustion, a high rate of exhaust gas recirculation (EGR) is possible in order to reduce the emission of nitrogen oxides [11, 22, 23]. Specific application solutions mainly concern CI engines [10, 12], but in the last few years, attempts have been made to power the SI engine. The high cetane number prevents the use of DME as a substitute fuel, but it is suitable for fueling the engine in the form of a mixture with gasoline [1, 8, 13, 18–20, 24] or with LPG [4, 5].

Research on the use of LPG/DME gaseous fuel mixtures has also been conducted for over 10 years at the Faculty of Transport and Aviation Engineering at the Silesian University of Technology. The results of these studies were published on an ongoing basis. The completed project included several research cycles, which included:

- preliminary tests on a chassis dynamometer at full engine load, in the range of mixtures with DME content up to 26% by weight [7]
- experimental tests on a chassis dynamometer at partial engine loads, in the range of mixtures with DME content up to 30% by weight [9]
- experimental tests on a chassis dynamometer at partial engine loads, in the range of mixtures with DME content up to 30% by weight, with correction of the ignition advance [14]
- simulation studies of thermodynamic processes occurring in the engine cylinder, based on the results of experimental studies (approved for publication)
- tests of vehicle dynamics parameters when fueled with LPG/DME mixtures.

This article elaborates on the research results obtained in the last of the above-mentioned stages. The assessment of the dynamic parameters of the vehicle is aimed at determining the impact of the composition change on the acceleration values achieved during acceleration. In fact, it is one of the factors of comfort of use. Users take this aspect into account and consider it one of the criteria for assessing the possibility of widespread use of fuel. These types of tests approximate actual operating conditions and may also be conducted to determine fuel consumption or exhaust emissions [2, 16].

2. Experimental studies

2.1. Measurement set-up

The popular passenger car powered by 1.6 liter engine, naturally aspirated with a compression ratio of 9.6, port fuel injection, two valves per cylinder, flat pistons and without external EGR was used in the experiments (Fig. 2). The engine has been adapted to run on LPG gas fuel and LPG and DME blends. The main features of the engine of the tested vehicle are presented in Table 1.

Table 1. Engine specification

Parameter	Value
Engine code	X16SZR
Cylinder number and layout	4 R
Maximum power	55 kW@5200 rpm
Maximum torque	128 N·m@2800 rpm
Displacement	1598 cm^3
Bore × stroke	79.0 × 81.5 mm
Compression ratio	9.6

The experiments were performed on a MAHA MSR500 chassis dynamometer. While examining the dynamic pa-

rameters of the vehicle, the acceleration time was measured using the built-in module 'Driving simulation'. The driving simulation reenacts a road drive and/or a certain load, which can be set with the drive cycles based on specific drive resistances. The measurement was performed by running the research procedure in the dynamometer software (Fig. 1).

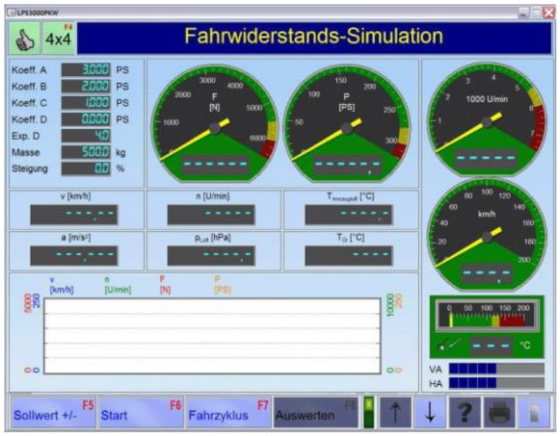

Fig. 1. View of the engine compartment of the tested vehicle on the dynamometer chassis

Then, the vehicle was accelerated to a speed that enabled it to drive at the given gear ratio (3 or 4). The test started when the lower speed range was reached. The dyno software measured the time to reach the upper driving speed range.

The vehicle-specific drive resistance characteristic including mass simulation is described by the following simulation model [17]:

$$F = \frac{C_A}{v_{ref}} + \frac{C_A \cdot v}{v_{ref}^2} + \frac{C_C \cdot v^2}{v_{ref}^3} + \frac{C_D \cdot v^{Exp\,D}}{v_{ref}^{Exp\,D+1}} + (M - m_{mech})\frac{dv}{dt} + (M \cdot g \cdot \sin\alpha)$$

where: F – tractive force target value, C_A – rolling resistance coefficient (constant), C_B – flexing resistance coefficient (linear), C_C – drag coefficient (square with n ≅ 2), C_D – drag coefficient (exp. with n being variable), Exp D – exponent D (1 ≤ n ≤ 3, one decimal place), M – vehicle mass, m_{mech} – mechanical mass, V – roller speed, V_{ref} – reference speed, α – gradient angle (±), dv/dt – roller acceleration, g – gravitational acceleration.

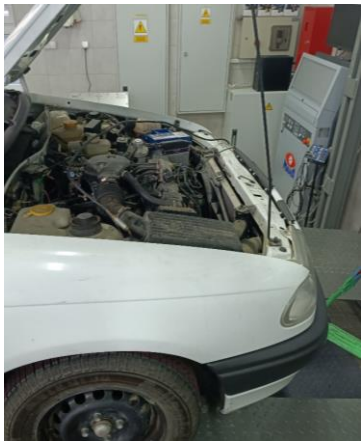

Fig. 2. View of the engine compartment of the tested vehicle on the dynamometer chassis

2.2. Methodology of research

Two series of tests were carried out:

– acceleration from 40 to 70 km/h in 3rd gear
– acceleration from 60 to 90 km/h in 4th gear.

Each series included 48 measurements; for eight fuels with different DME content and six engine load levels. The fuels used for the tests contained from 0% (LPG only) to 30% DME. The proportions of fuel components were determined by the gravimetric method. The gas fuel blend was produced immediately before a given measurement series. For this purpose, a fuel blend preparation station was used. (Fig. 3).

Fig. 3. Station for producing fuel blends

Physicochemical properties of the tested fuels are given in the Table 2. The selected engine load stages: 21%, 33%, 48%, 69%, 90% and 100% correspond to the position of the accelerator pedal and are determined by the TPS signal. An original device was used to apply partial loads to the engine, designed universally for the selected test object. The load was adjusted using replaceable washers that were mounted in the base of the device under the accelerator pedal.

Acceleration of the vehicle at a given degree of throttle opening was started below the starting speed to ensure stable engine load during the measurement. Time measurement was started at the moment of reaching the start speed and turned off simultaneously with reaching the final speed in the assumed range.

Table 2. Physicochemical properties of the tested fuels [6]

Properties	DME $(CH_3)_2O$	Propane C_3H_8	n-butane C_4H_{10}	Unit
Density of liquefied gas	667	582	579	kg/m^3
Molecular weight	46.07	44.1	58.12	g/mol
Evaporation pressure	530	830	210	kPa
Heat of vaporization	467	370	358	kJ/kg
Boiling point	–25	–42	–0.5	°C
Air to fuel ratio	9	15.7	15,46	kg/kg
Lower heating value (LHV)	28.8	46.4	48	MJ/kg
Cetane number	55–60	5	10	–
Octane number	–	112	88.9	–

3. Discussion of results

In order to test the dynamic properties of a car fueled with DME fuel blends, the acceleration times of the vehicle on a chassis dynamometer were measured. The dynamometer operating mode simulated an additional load, corresponding to the resistance to motion, which the vehicle must overcome in road conditions. The results of the measurement of the acceleration time in the adopted measurement ranges are presented in the tables (Table 3 and 4). In order to show the influence of the DME share on the vehicle dynamics, the obtained results were presented on graphs (Fig. 4 and 6). An alternative form was also introduced to the visualization of the results, which shows the changes in the acceleration time grouped for the tested engine load levels (Fig. 5 and 7).

Table 3. Acceleration time in 3rd gear in the speed range of 40–70 km/h

WOT	Acceleration time [s]							
	Mass percentage of DME in the blend							
	0%	7%	11%	14%	17%	21%	26%	30%
21%	13.22	14.17	12.76	12.63	12.30	12.02	12.67	12.74
33%	10.37	10.25	10.35	10.43	10.36	10.28	9.37	10.34
48%	6.06	5.96	6.17	6.63	6.40	6.19	6.57	6.75
69%	5.68	4.96	5.57	5.92	6.19	5.31	5.47	6.00
90%	5.05	5.08	5.68	5.7	5.67	6.03	6.11	5.96
100%	4.46	5.00	4.98	5.31	5.40	5.58	5.38	5.46

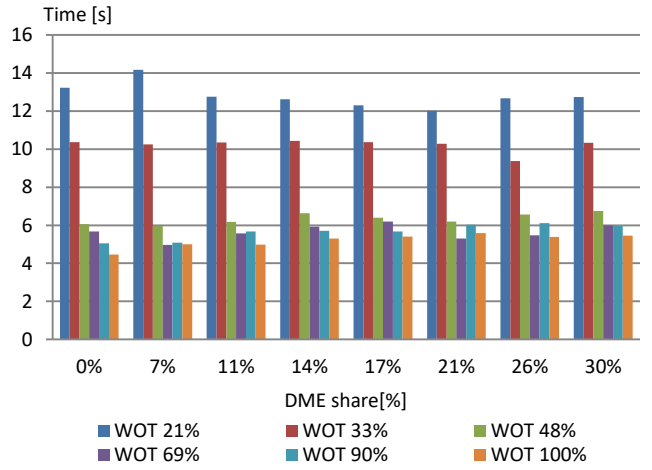

Fig. 4. Acceleration time depending on DME share, speed 40–70 km/h

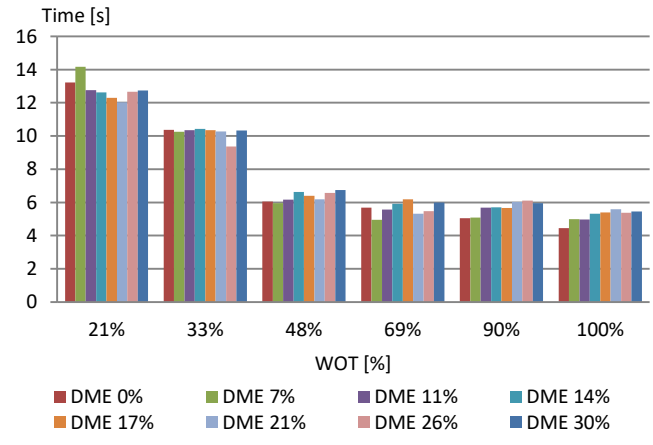

Fig. 5. Acceleration time depending on WOT, speed 40–70 km/h

Table 4. Acceleration time in 4th gear in the speed range of 60–90 km/h

WOT	Acceleration time [s]							
	Mass percentage of DME in the blend							
	0%	7%	11%	14%	17%	21%	26%	30%
21%	30.85	32.00	30.91	29.90	27.51	28.86	29.18	30.99
33%	22.14	20.55	19.44	19.35	19.62	20.36	20.04	20.33
48%	14.13	10.44	11.09	11.47	12.16	11.79	12.66	14.27
69%	10.81	9.97	9.78	9.93	10.84	9.84	11.18	12.91
90%	9.19	9.76	9.31	9.37	10.16	10.13	10.60	10.73
100%	8.99	9.41	9.54	9.21	9.38	10.93	10.19	10.91

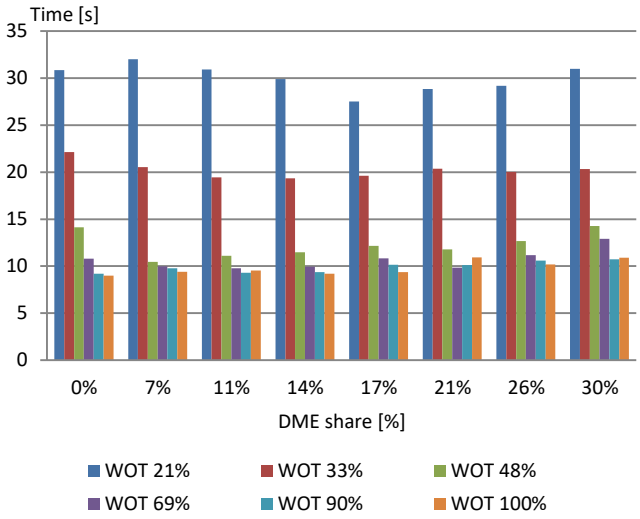

Fig. 6. Acceleration time depending on DME share, speed 60–90 km/h

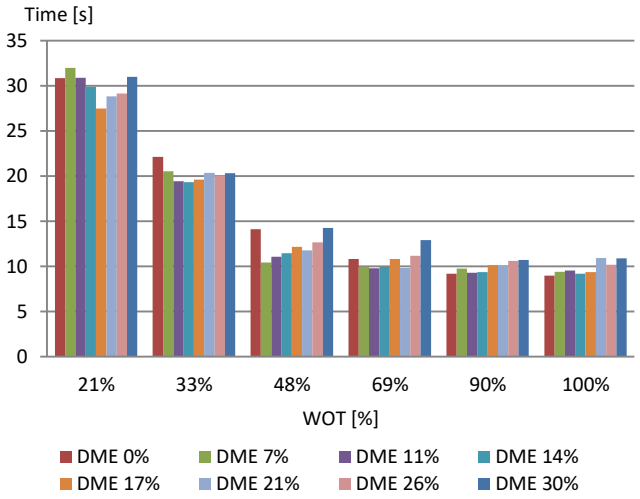

Fig. 7. Acceleration time depending on WOT, speed 60–90 km/h

Selected, exemplary ranges of speeds in gears 3rd and 4th correspond to the middle range of engine revolutions, which means that this is the area of the engine's performance characteristics, where a sufficiently high engine torque is available, which ensures smooth acceleration.

Next, specific acceleration values were calculated, based on the measured acceleration times in the assumed speed ranges. The accelerations are presented in three-dimensional graphs (Fig. 8 and 10), which allow to observe both the effect of the degree of engine load and the fuel

composition. Increasing the share of DME, which has a much lower heating value than LPG (Table 2), undoubtedly also reduces the calorific value of the fuel blend. However, the presence of oxygen in the chemical structure of DME also causes a decrease in the A/F ratio. Thanks to this, the energy value of the stoichiometric mixture remains quite constant. This is confirmed by the results obtained. Observation of the results allows, among other things, to conclude that, in general, increasing the share of DME blended with LPG, does not entail a significant reduction in dynamic parameters. The obtained results show a similar picture for both tested speed ranges.

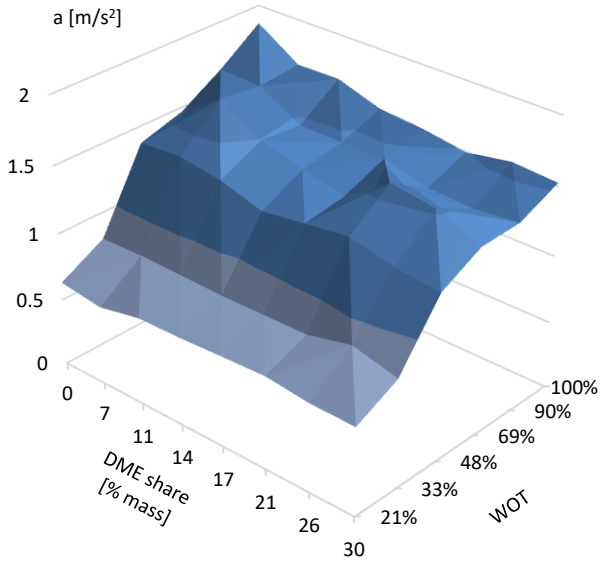

Fig. 8. Acceleration in 3rd gear in the speed range of 40–70 km/h

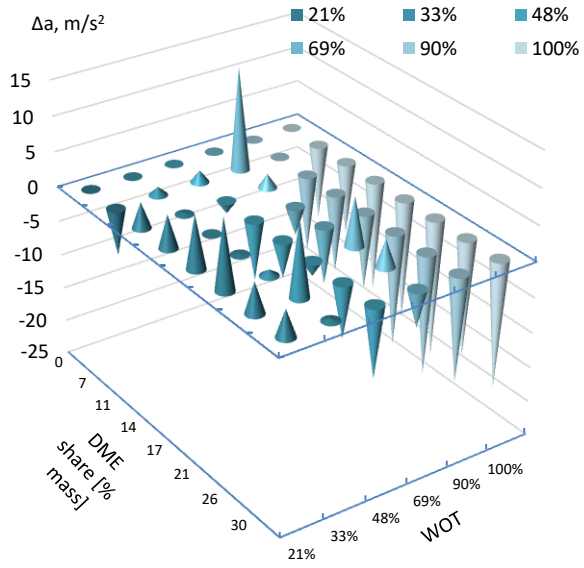

Fig. 9. Comparison of accelerations in 3rd gear in relation to LPG

Of course, the overarching goal of the conducted analyzes is to compare the results obtained when fueling with DME blends, with the dynamics of a vehicle powered only by LPG. This is the base fuel in this case. Therefore, in the further elaboration of the results, the differences in the achieved accelerations were presented in detail, in the form of changes Δa, expressed in [%]. They express the percentage increase/decrease in acceleration on a given fuel in relation to the value obtained for LPG without DME admixture. Changes in these values, in 3rd (Fig. 9) and 4th gear (Fig. 11), respectively, lead to interesting observations, as they allow to isolating areas where the vehicle dynamics improves or deteriorates. In addition, these areas are repeated in both measurement series. Namely, in the range of medium engine loads (33–69% WOT), the acceleration values increase. However, in the range of maximum loads, above 90%, the acceleration values are lower in relation to LPG-only operation. These trends are maintained for all tested mixtures with the participation of DME.

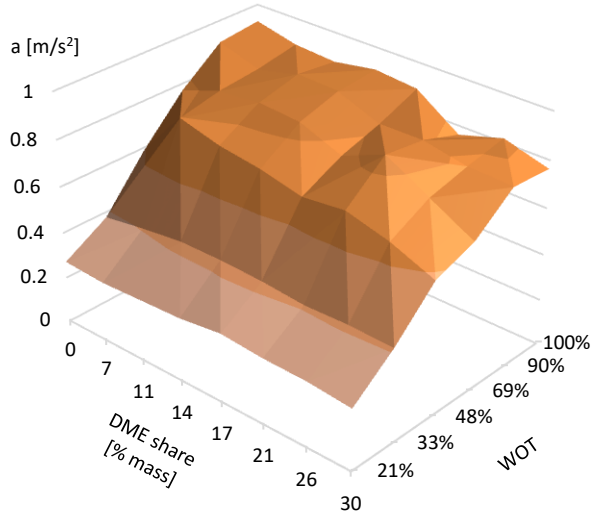

Fig. 10. Acceleration in 4th gear in the speed range of 60–90 km/h

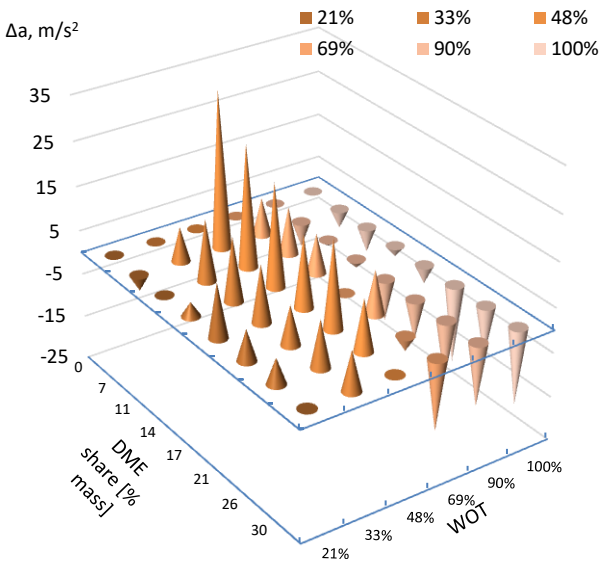

Fig. 11. Comparison of accelerations in 4th gear in relation to LPG

4. Conclusions

The conducted experimental studies complement the results obtained during the implementation of a wider cycle devoted to the use of LPG/DME mixtures in a spark-ignition engine. They make it possible to observe the influence of the DME share on the dynamic parameters of the tested engine.

Summing up the conducted research, the following conclusions can be drawn:

1. Similar physical and chemical properties enable the production of a mixture of LPG+DME fuels, its storage in standard tanks, and its use in LPG fueling systems. Such a solution is very important due to the utility aspect, which gives the opportunity to use existing and functioning installations.
2. Extending the research methodology with measurements at partial engine loads made it possible to compare the most useful areas of engine operation, most often used during vehicle operation.
3. As shown by vehicle acceleration measurements (on a chassis dynamometer), the dynamics of a vehicle powered by LPG+DME increases in the range of low and medium engine loads. The observed increase in vehicle dynamics occurs when fueled with mixtures containing DME from 7 to 26%. It amounted to an average of 4% in 3rd gear and approx. 8–12% in 4th gear.
4. At maximum loads, a decrease is observed, while maintaining the factory settings of the ignition timing. For a mixture containing 30% DME, the acceleration values decrease significantly. The recorded decrease was respectively: 17% in 3rd gear and 14.2% in 4th gear.
5. The results of the obtained research are complementary to a wide series of research, the results of which have been published in separate works. The use of the DME additive in a mixture with LPG is, from the point of view of observation of dynamic parameters and the combustion process, a fully valuable and useful fuel, which does not impair the performance of an engine fueled only with LPG.

Nomenclature

CA	crank angle
COV_{imep}	cyclic variation of indicating mean effective pressure
DME	dimethyl ether
EGR	exhaust gas recirculation
Exp.	exponential
HR	heat released
LPG	liquified petrolum gas
PM	particulate matter
SI	spark ignition
WOT	width opening of the throttle

Bibliography

[1] Baek S, Lee S, Shin M, Lee J, Lee K. Analysis of combustion and exhaust characteristics according to changes in the propane content of LPG. Energy. 2022;239:122297. https://doi.org/10.1016/j.energy.2021.122297

[2] Bieniek A, Graba M, Mamala J, Augustynowicz A, Szczepanek M. Analysis of passenger car powertrain system measurements in road conditions. Combustion Engines. 2023;195(4):144-151. https://doi.org/10.19206/CE-170207

[3] Cai P, Liu Z, Li M, Zhao Y, Li P, Li S et al. Experimental study of effect of equivalence ratio and initial turbulence on the explosion characteristics of LPG/DME clean blended fuel. Energy. 2022;250:123858. https://doi.org/10.1016/j.energy.2022.123858

[4] Donggon L, Chang Sik L. Effects of DME-isobutane blended fuels on combustion and emissions reduction in a passenger car diesel engine. J Energ Eng. 2017;143(41):04017003. https://doi.org/10.1061/(asce)ey.1943-7897.0000428

[5] Fabiś P. DME as a fuel for SI engines cars. Diagnostyka. 2021;22(1):93-99. https://doi.org/10.29354/diag/133476

[6] Flekiewicz M, Dykier M. Study on the use of a blend of DME and petroleum gases to power SI engines. Gas engines, selected issues (in Polish). Częstochowa University of Technology Publishing House. Częstochowa 2010.

[7] Flekiewicz M, Kubica G. The effects of blending dimethyl ether with LPG on the engine operation and its efficiency. Combustion Engines. 2013;154(3):86-95. https://doi.org/10.19206/CE-116991

[8] Flekiewicz M, Kubica G. The influence of selected gaseous fuels on the combustion process in the SI engine. Transport Problems. 2017;12:135-146. https://doi.org/10.20858/tp.2017.12.3.13

[9] Flekiewicz M, Kubica G, Marzec P. The possibilities of using DME (BioDME), as an additive to conventional gaseous fuels in SI engine. Combustion Engines. 2017;171(4): 150-155. https://doi.org/10.19206/CE-2017-425

[10] Kozak M. Exhaust emissions from a diesel passenger car fuelled with a diesel fuel-butanol blend. SAE Technical Paper 2011-28-0017. 2011. https://doi.org/10.4271/2011-28-0017

[11] Kozak M, Lijewski P, Fuć P. Exhaust emissions from a city bus fuelled by oxygenated diesel fuel. SAE Technical Paper 2020-01-2095. 2020. https://doi.org/10.4271/2020-01-2095

[12] Kozak M, Merkisz J. Oxygenated diesel fuels and their effect on PM emissions. Appl Sci. 2022;12(15):7709. https://doi.org/10.3390/app12157709

[13] Kubica G. An efficiency of energy conversion in a spark ignition engine fuelled with a low-carbon gaseous fuels. Monographic publishing series Library of Operational Problems – Studies and Dissertations, Publishing House of the Institute for Sustainable Technologies-National Research Institute in Radom. Radom 2013.

[14] Kubica G, Marzec P. An influence of correction of the ignition advance angle on the combustion process in SI engine fuelled by LPG with the addition of DME. Journal of KONES. 2019;26:285-292. https://doi.org/10.2478/kones-2019-0119

[15] Malte S, Ramy AE, Ouda S, Achim S, Sauer J, Hebling C. Power-to-DME: a cornerstone towards a sustainable energy system. Power to Fuel. 2021:123-151. https://doi.org/10.1016/B978-0-12-822813-5.00010-2

[16] Mamala J, Graba M, Bieniek A, Prażnowski K, Hennek K, Kołodziej S et al. Evaluation of energy consumption in the

acceleration process of a passenger car. Combustion Engines. 2022;190(3):35-44. http://doi.org/10.19206/CE-142553

[17] Original Operating Instructions LPS 3000 Dynamometer. MAHA Maschinenbau Haldenwang GmbH & Co. KG, Haldenwang D. 2011. BA052301-en.

[18] Pathak S, Sood V, Singh Y, Gupta S, Channiwala SA. Application of DME 20 fuel in a gasoline passenger car to comply with Euro IV emission legislation. SAE Technical Paper 2017-01-0872. 2017. https://doi.org/10.4271/2017-01-0872

[19] Sun C, Liu Y, Qiao X, Ju D, Tang Q, Fang X et al. Experimental study of effects of exhaust gas recirculation on combustion, performance, and emissions of DME-biodiesel fueled engine. Energy. 2020;197:117233. https://doi.org/10.1016/j.energy.2020.117233

[20] Mondal U, Yadav GD. Perspective of dimethyl ether as fuel: Part I. Catalysis. J CO_2 Util. 2019;32:299-320. https://doi.org/10.1016/j.jcou.2019.02.003

[21] Wang J, Yu H, Li M, Liang X, Liu H. Experimental and numerical study on effects of impingement parameters on fuel-air mixture formation in the near wall region for diesel-DME blended fuels. SAE Technical Paper 2018-01-0920. 2018. https://doi.org/10.4271/2018-01-0920

[22] Yanuandri P. Ocktaeck L. Dimethyl ether as the next generation fuel to control nitrogen oxides and particulate matter emissions from internal combustion engines: a review. ACS Omega. 2022;7(1):32-37. https://doi.org/10.1021/acsomega.1c03885

[23] Zhang Q, Chen Y, Fan T, Yuan M, Liu Z, Huang P et al. Flame dynamics and flammability limit of DME(30%)/LPG blended clean fuel in elongated closed pipeline under multi-factors. Fuel. 2019;254:115731. https://doi.org/10.1016/j.fuel.2019.115731

[24] Zubel M, Lehrheuer B, Pischinger S. Impact of increased injector nozzle hole diameters on engine performance, exhaust particle distribution and methane and formaldehyde emissions during dimethyl ether operation. Int J Engine Res. 2021;22:503. https://doi.org/10.1177/1468087419860954

Paweł Marzec, DEng. – Faculty of Transport and Aviation Engineering, Silesian University of Technology, Katowice, Poland.
e-mail: *pawel.marzec@polsl.pl*

Grzegorz Kubica, DSc. DEng. – Faculty of Transport and Aviation Engineering, Silesian University of Technology, Katowice, Poland.
e-mail: *grzegorz.kubica@polsl.pl*

Article citation info:
Hemlecki P, Fabiś P. Formula Student class electric vehicle energy storage – study and design assumptions. Combustion Engines. 2024;198(3):54-61. https://doi.org/10.19206/CE-186164

Piotr HEMLECKI
Paweł FABIŚ

Combustion Engines
Polish Scientific Society of Combustion Engines

Formula Student class electric vehicle energy storage – study and design assumptions

ARTICLE INFO

Received: 27 November 2023
Revised: 19 February 2024
Accepted: 16 March 2024
Available online: 20 April 2024

The goal of this article is to present the design assumptions of an energy storage for a Formula Student electric car equipped with one electric motor. The correct selection of the parameters of the energy storage is dictated by the regulations applicable to all cars competing in this class, especially the maximum battery power. The growing interest in electric cars visible on the passenger car market is also reflected in motorsport, where are created new competitions or classes specifically for BEV. In addition, the work contains a definition of BEVs, types of cells used in electric vehicle batteries, and a brief description of Formula Student. The study presents a description of the requirements contained in the competition regulations regarding the energy storage in the Formula Student vehicle, an overview of the cells that can be used in the battery, and the selection of the most optimal among several solutions. Based on specific requirements, the arrangement of cells inside the battery was designed, divided into smaller segments and their connection, and placed in a safe housing in the form of a container.

Key words: *energy storage, BEV, Formula Student*

1. Introduction

Formula student is a competition category intended for university students from around the world. Each team taking part in the competitions has to build its own vehicle in accordance with the competition regulations [8, 14, 15]. The number of teams starting to build vehicles powered by electric engines increases every year [4, 22]. This is due to the prevailing trend of promoting electromobility. Electric motors are also more efficient than combustion engines. The tank to wheel efficiency for electric cars is 65–82%, and for cars equipped with combustion engines – 19–25% [12]. Electric cars do not emit exhaust gases, so they are considered ecological vehicles [1, 9–11, 23]. Analysing data on vehicle sales, one can notice an annual increase in the number of registered new BEV cars [16, 17, 19, 20].

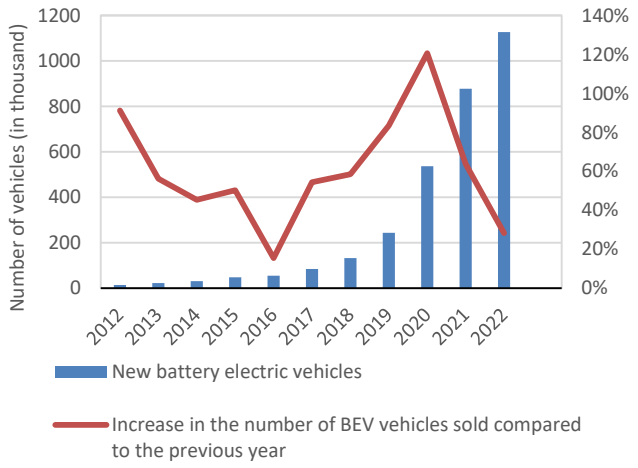

Fig. 1. New electric vehicles sold in Europe in 2012-2022 [21]

Figure 1 shows this situation in Europe. Many global car manufacturers are declaring a significant increase in the sales of BEV cars and phasing out combustion vehicles from their offer in the coming years [6,20]. According to forecasts, in 2035 more than half of new passenger cars sold worldwide will be BEVs, and in 2040 the share of these vehicles in total sales should be almost 2/3 [2]. Due to the growing interest in electric vehicles, special racing classes for these vehicles are also being created. The most famous are eTouring Car World Cup (ETCR) and Formula E. Considering the current and forecasted future of motor vehicles presented above, both on the market and in sport, it is highly probable that in the future, people with significant knowledge and experience in the field of building electric vehicles will be in high demand on the labour market. One of the goals of the Student Formula is also to develop knowledge in the field of motor vehicle construction. Being aware of this goal and the situation regarding the future of motor vehicles presented above, the increase in the number of teams building electric cars is fully understandable [8].

The main assumption when designing an electric car is to achieve the lowest possible weight of the vehicle while ensuring a range sufficient to complete the Endurance event, which involves driving twice on a closed track for approximately 11 km with one stop during which the driver is changed. The Endurance course must not have straights longer than 80 meters, continuous turns with a diameter of more than 50 meters, or sharp turns with an external diameter of less than 9 meters. In addition, the route may include slaloms with gaps between posts of 9 to 15 meters, chicanes or turns with variable radius, and the minimum track width cannot be less than 3 meters [3, 14]. This means that Formula Student vehicles perform many short accelerations, which place a significant load on the drive system and high energy demand. For this reason, it is common to equip vehicles with a braking energy recovery system. This increases the vehicle's range by charging during braking without increasing the size of the battery [7]. According to

the Formula Student regulations, each car must ensure maximum safety, so when designing electric vehicles, in addition to passive safety, which is to protect the driver during a collision, the risk of fire in electrical components and electric shock to the driver or people around the vehicle should be minimized. Each vehicle must undergo a mandatory technical inspection before being allowed to participate in dynamic events. The technical inspection includes a thorough inspection of the entire electrical installation of the vehicle. It involves a thorough comparison of the elements of the vehicle's electrical installation with the requirements of the regulations by visual inspection and, in case of doubt, conducting an interview with team members regarding the materials used and their certification. Another important part of the inspection is a rain test, which aims to check the insulation of the electrical installation from water. It involves simulating rain falling on the vehicle for 2 minutes and then assessing the operation of the installation [3, 4].

2. Methodology

2.1. Regulatory requirements for an electric vehicle

The Formula Student regulations require that the power of the tractive system does not exceed 80 kW and the maximum voltage in the system does not exceed 600 V (excluding control signals of engine controllers and inverter/power processing unit). It is permitted to install engines both inside the vehicle (with half-axles transmitting torque to the wheels) and in the wheels (transmitting torque to the wheels directly or via a single-stage gearbox).

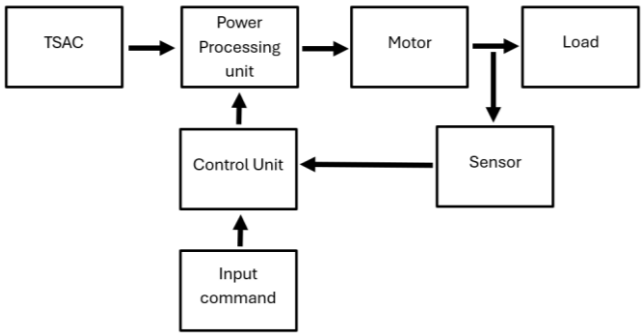

Fig. 2. Block diagram of a tractive system

In the case of traction system energy storage (TSES), the maximum voltage of a single segment must not exceed 120 V DC, 6 MJ of energy, and 12 kg of mass.

The bottom of the housing can be made of steel with a minimum thickness of 1.25 mm or aluminum with a minimum thickness of 3.2 mm, while the thickness of the external and internal walls is 0.9 mm for steel and 2.3 mm for aluminum, respectively. The height of internal walls cannot be less than 75% of the height of external walls. Walls cannot divide single energy storage segments, and all connections must be welded, glued or screwed [3, 4].

2.2. Selection and optimization of energy storage parameters

When designing an energy storage, the energy demand should be taken into account to ensure that there is no shortage of energy during competitions and at the same time to minimize the size and weight of the energy storage. It was assumed that the engine should not have a higher rated power than that permitted in the regulations, i.e. 80 kW. The EMRAX 228 engine in the Low Voltage specification was selected for the project, requiring a power supply of 160 V and 450 A [13]. Its technical parameter are presented in Table 1. Figure 3 shows the external characteristics of the motor, and its efficiency map is shown in Fig. 4.

Table 1. Selected parameters of the EMRAX 228 Low Voltage engine [13]

Parameter	Unit	Value
Weight	kg	12
Diameter/width	mm	228/86
Maximal battery voltage	Vdc	160
Peak motor power at max load rpm	kW	109
Continuous motor power	kW	50
Maximal rotation speed	rpm	5500
Peak motor current	A	900
Continuous motor current	A	450
Maximal motor torque	Nm	230
Continuous motor torque	Nm	96
Torque/motor current	Nm/1Aph rms	0.27
Motor efficiency	%	86–96

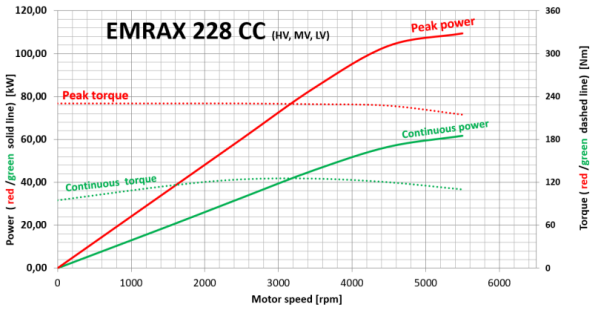

Fig. 3. External characteristics of the EMRAX 228 motor [13]

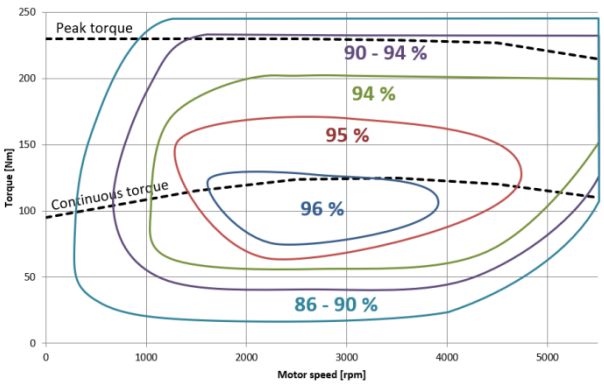

Fig. 4. Efficiency map of the EMRAX 228 motor [13]

After selecting the engine, a review of cells available on the market was carried out, from which 13 models were selected and compared. They has been shown in Table 2.

Table 2. Selected cells and their parameters [4]

Type	Cell	Nominal voltage	Capacity	Continuous discharge	Weight	Dimensions
		V	mAh	A	g	mm
Li-ion	ANR26650M1b	3.30	2500.00	50.00	76.00	ϕ26.00 × 68.00
	UR18650NSX	3.60	2600.00	20.00	45.80	ϕ18.30 × 64.85
	INR18650-25R	3.60	2500.00	20.00	45.00	ϕ18.40 × 65.00
	INR21700-30T	3.60	3000.00	35.00	69.00	ϕ21.22 × 70.30
	INR18650-33G	3.60	3150.00	6.50	48.00	ϕ18.40 × 65.20
	INR21700-50E	3.63	5000.00	9.80	69.50	ϕ21.10 × 70.15
	VTC5A	3.60	2600.00	35.00	44.00	ϕ18.35 × 65.20
	VTC6	3.60	3130.00	30.00	46.50	ϕ18.50 × 65.20
	MB18650	3.70	2600.00	3.90	45.00	ϕ18.50 × 65.50
LiPo	LP7843128	3.70	5000.00	5.00	98.50	43.00 × 7.80 × 127.50
	SLPB9395183	3.70	22000.00	110.00	358.00	94.00 × 9.00 × 182.50
$LiFePO_4$	LFP8167100	3.20	4100.00	82.00	100.00	67.00 × 7.70 × 100.00
	MB-IFR26650	3.20	3800.00	11.40	92.00	ϕ26.20 × 65.20

3. Results discussion

3.1. Selection of cells for the considered energy storage

The most important parameters of cells are their energy and power mass densities, which determine the amount of energy and power per unit of mass. Higher density values allow more energy and power to be stored in the battery at the lowest possible weight. As the weight increases, the performance and range deteriorate, which is crucial in the case of BEVs, which is why these parameters are so important. Equally important parameters include power and energy volume densities, i.e. the amount of power and energy per unit of volume. Formula Student vehicles have a very limited space to use, and any attempts to adapt the structure to accommodate a larger energy storage unit may significantly increase the weight. Also, a battery with the required capacity but too low volumetric density may increase the size of the vehicle beyond the permitted limits specified in the regulations.

To determine the power and energy density values, the power and energy values of each cell must be calculated. Power (P_d) is the product of the nominal voltage (U_N) and the maximum current (I_{dmax}) of the cell [18]:

$$P_d = U_N \cdot I_{dmax} \tag{1}$$

The cell energy (E) is the product of the nominal voltage (U_N) and the cell capacity (C_d) [18]:

$$E = U_N \cdot C_d \tag{2}$$

Table 3. Power and energy values of selected cells

Type	Cell	Cell power	Cell energy
		W	Wh
Li-ion	ANR26650M1b	165.00	8.25
	UR18650NSX	72.00	9.36
	INR18650-25R	72.00	9.00
	INR21700-30T	126.00	10.80
	INR18650-33G	23.40	11.34
	INR21700-50E	35.57	18.15
	VTC5A	126.00	9.36
	VTC6	108.00	11.27
	MB18650	14.43	9.62
LiPo	LP7843128	18.50	18.50
	SLPB9395183	407.00	81.40
$LiFePO_4$	LFP8167100	262.40	13.12
	MB-IFR26650	36.48	12.16

The determined power and energy values of each cell are presented in Table 3.

Referring to the PN-EN IEC 62660-1:2019. standard, and having the calculated power and energy values, it is possible to calculate the volume and mass densities of energy and power. the ratio of a cell's power (P_d) expressed in watts to its mass (m) in kilograms is called power mass density (ρ_{pd}) [18]:

$$\rho_{pd} = \frac{P_d}{m} \tag{3}$$

Energy mass density (ρ_{ed}) is the ratio of the cell's energy (E) expressed in watt-hours to its mass (m) in kilograms [18]:

$$\rho_{ed} = \frac{E}{m} \tag{4}$$

The ratio of a cell's power (P_d) to its volume (V) is called power volume density (ρ_{pvlm}) [18]:

$$\rho_{pvlm} = \frac{P_d}{V} \tag{5}$$

The value of bulk energy density (ρ_{evlmd}) is calculated by dividing the energy of the cell (E) by its volume (V) [18]:

$$\rho_{evlmd} = \frac{E}{V} \tag{6}$$

The values of mass and volume power and energy densities for each cell are presented in Fig. 5–8.

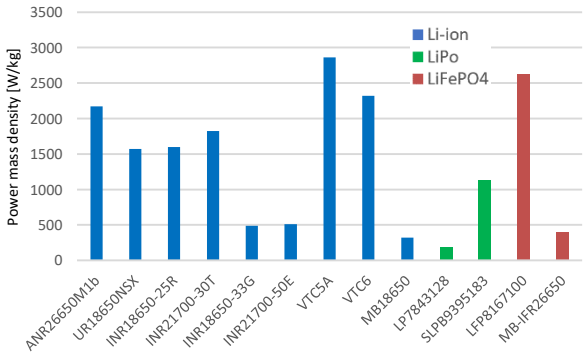

Fig. 5. Power mass density of selected cells

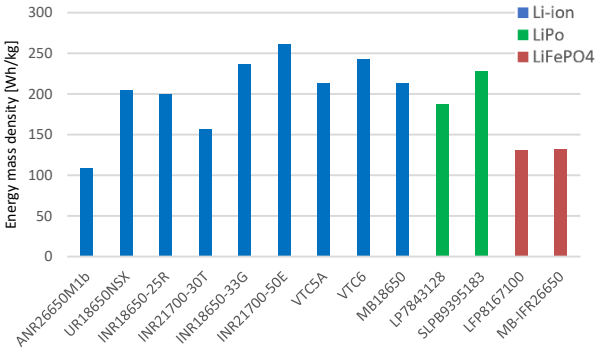

Fig. 6. Energy mass density of selected cells

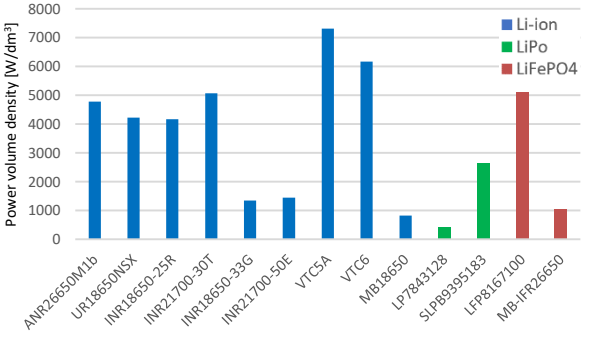

Fig. 7. Power volume density of selected cells

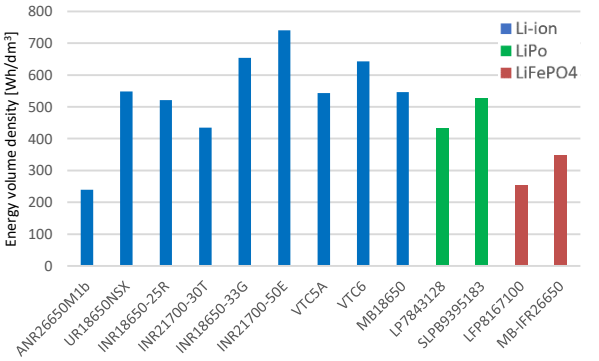

Fig. 8. Energy volume density of selected cells

There are huge differences in the considered densities. The biggest differences is in power volume density (Fig. 7): the best cell, VTC5A, has nearly 17 times more power volume density than LP7843128. Energy densities does not have such a big discrepancy, but even in energy volume density (Fig. 8) the difference between the best cell (INR21700-50E) and the worse one (ANR26650M1b) is 3 times. As it was said before, the best cells for power a vehicle should have the highest values of power and energy density, both volume and mass. To choose the best ones their power and energy densities were included in one graph for mass and one for volume. It shows the cells with the highest total density values, thanks to which it is possible to select the most efficient cells from among the tested (Fig. 9, 10).

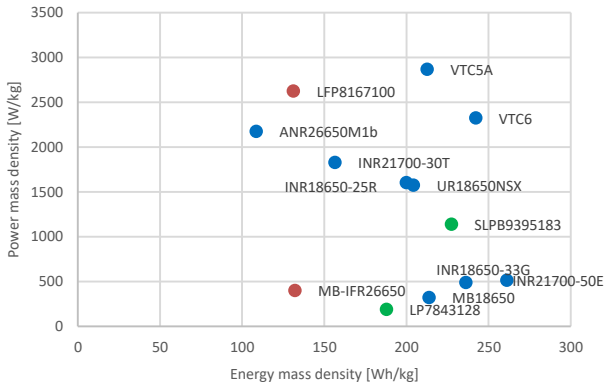

Fig. 9. Power mass densities of selected cells depend on energy mass density

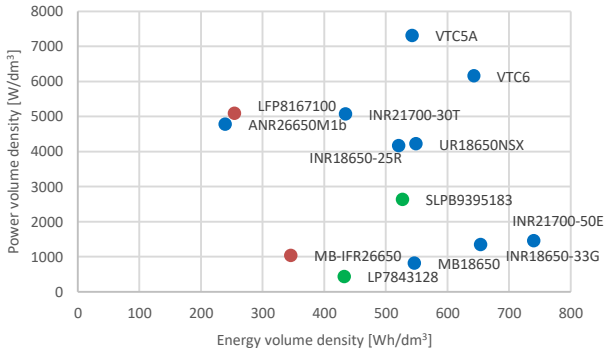

Fig. 10. Power volume densities of selected cells depend on energy volume density

After analyzing the obtained data, it can be seen that the overall best parameters among those considered are achieved by VTC5A and VTC6 cells. Moreover, some cells have very low energy density values. In order to illustrate the differences between cells in their use in the construction of energy storage to power the considered engine, the amount necessary to obtain voltage and current was calculated for each type and their masses were calculated (Table 4).

Table 4. Minimum quantities of selected cells, their total minimum capacities and masses to obtain appropriate parameters for operation with the EMRAX 228 engine in the Low Voltage version

Type	Cell	Minimum amount of cells	Minimum cells capacity	Minimum cell weight
			Ah	kg
Li-ion	ANR26650M1b	436	1090.91	33.16
	UR18650NSX	1000	2600.00	45.80
	INR18650-25R	1000	2500.00	45.00
	INR21700-30T	571	1714.29	39.43
	INR18650-33G	3077	9692.31	147.69
	INR21700-50E	2024	10119.75	140.66
	VTC5A	571	1485.71	25.14
	VTC6	667	2086.67	31.00
	MB18650	4990	12972.97	224.53
LiPo	LP7843128	3892	19459.46	383.35
	SLPB9395183	177	3891.89	63.33
$LiFePO_4$	LFP8167100	274	1125.00	27.44
	MB-IFR26650	1974	7500.00	181.58

Based on the study presented in Table 4, VTC6 cells were selected. Despite the 23% greater weight of the battery consisting of these cells for both variants of the engine in question compared to the lightest set consisting of VTC5A cells, the energy storage has a 40% larger capacity. In order to obtain the same capacity from VTC5A cells as we can obtain with the minimum demand for VTC6 cells, the weight of VTC5A cells would be 14% greater. An example of VTC6 cell is shown in Fig. 11.

Fig. 11. VTC6 cell used

To build the energy storage needed for the vehicle in question, 667 cells would be enough. Nevertheless, it was assumed that approximately 1000 cells would be used to increase the durability and capacity of the entire battery by limiting the maximum current drawn from a single cell, and therefore the cell load. As a result, the phenomenon of cells heating during operation will be reduced. For this reason, the cooling system will not have to achieve high efficiency, which will make it simpler. In addition, a larger number of cells increases the capacity of the energy storage, resulting in a greater range of the vehicle.

The energy storage must consist of smaller sections (so-called packages), with a weight not exceeding 12 kg, a voltage of 120 V and an energy of 6 MJ (point EV 5.3.2 of the regulations). The minimum number of sections used for 1000 VTC6 cells is 9. It was assumed that all packages, both in terms of construction (arrangement of cells inside) and connection, are to be the same. After careful analysis, it was decided to use 990 cells in the 45S22P (45 in series, 22 in parallel) configuration. Each package has an internal 5S22P (5 in series, 22 in parallel) configuration, and all sections are connected in series (Fig. 12). As a result, 162 V and less than 450 A were obtained while limiting the maximum current consumption from a single cell to 20 A. This connection system ensures the appropriate parameters to power the EMRAX 228 engine in the Low Voltage version, while ensuring the maximum battery power below the statutory 80 kW.

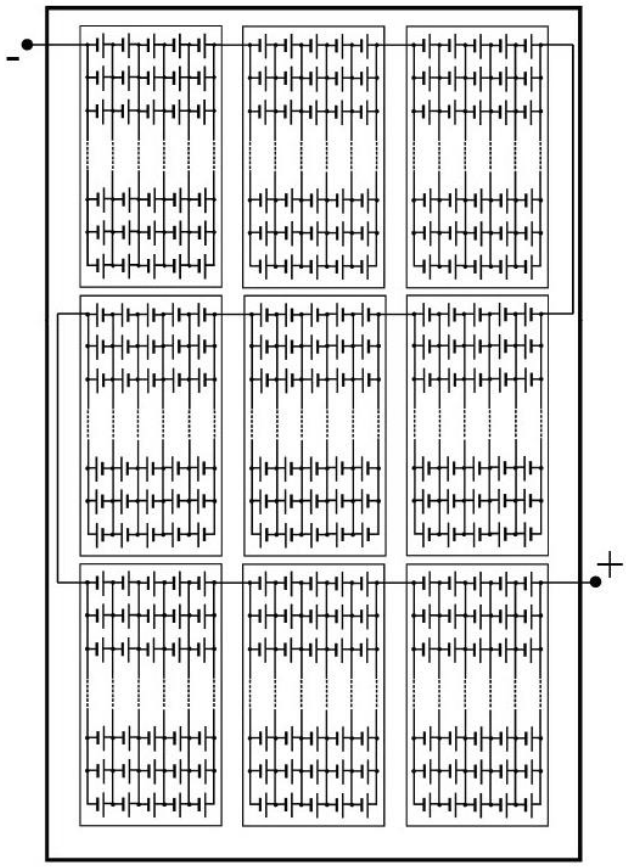

Fig. 12. Diagram of the cell system in an energy storage

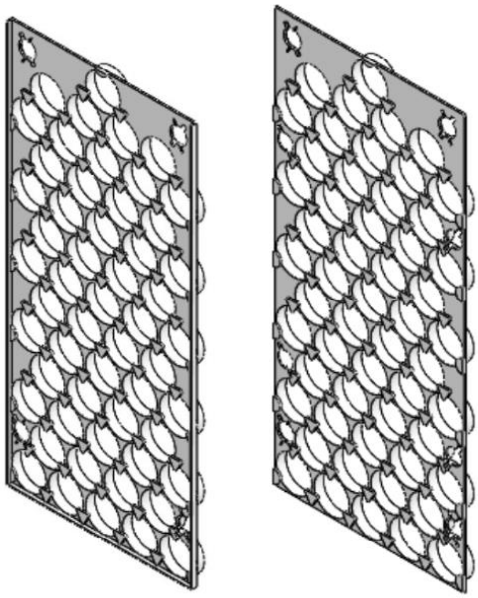

Fig. 13. Cell holder models

Knowing the configuration of individual sections and the entire energy storage, the exact arrangement of cells was determined in such a way as to make the best use of the space inside the vehicle frame and to reduce the vehicle's center of gravity as much as possible. For this purpose, the energy storage should occupy the largest possible area and

at the same time, the lowest possible height. It was calculated that it would be most convenient to arrange 3 packages in width and 3 in length. Each section consists of two identical parts, each of which has 55 links arranged longitudinally to the direction of travel, creating a pattern similar to a honeycomb. These elements are shown in Fig. 13. The cells were mounted in holders designed specifically for the energy storage in question and made using 3D printing technology. It was decided to make two types of handles: external and internal, intended to connect two parts of the package. The difference is the use of additional holes in the internal handles, enabling them to be connected both to each other and to external handles.

To ensure connections between the handles, special connectors were designed, which were also made using 3D printing (Fig. 14).

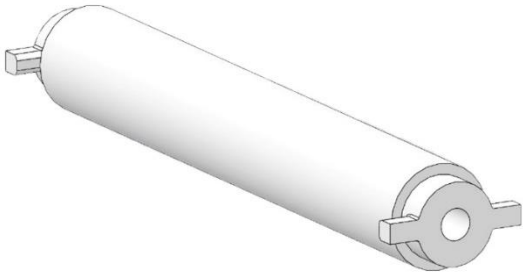

Fig. 14. Cell holder connectors models

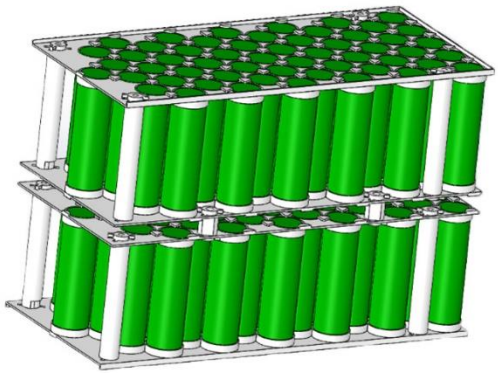

Fig. 15. One pack of energy storage model

3.2. Energy storage casing model

According to the regulations, the energy storage casing should provide protection against both mechanical damage and weather conditions. Materials that can be made include composite materials, steel or aluminum. When creating a metal casing, minimum sheet thicknesses should be considered, and adequate electrical insulation should be ensured. Additionally, walls should be made of the same material as the housing, and an insulating layer should be used between the packages.

Due to the prices of materials, their availability and the possibilities of their processing, it was decided to make the housing from steel. According to the regulations, the thickness of the steel sheet from which the floor is to be made cannot be thinner than 1.25 mm, and the side walls and interior partition walls – 0.9 mm. In order to achieve the lowest possible weight of the energy storage unit, it was decided to make the casing from the thinnest allowed sheet metal, as a box with a put-on cover. To ensure electrical insulation between the packs and the housing, it was decided to separate each of them from the housing with a 1 mm thick layer of fiberglass. The casing may contain only the necessary openings, which include holes for cable outlets, intended for mounting the energy storage device to the vehicle, and holes for ventilation. In the case of the latter, the regulations require that the driver should not be able to see them, even after dismantling the fire shield. Taking into account the small width of the energy store and its location directly behind the driver's back, the ventilation holes can only be located on the rear wall of the housing. A possible solution would be to design additional channels to supply air inside the energy storage, e.g. from the side sections. Due to the very small amount of space, this would result in significant complexity of the structure and the likelihood of shifting the energy storage towards the rear axle, increasing the already high load on this axle, which could worsen the traction properties of the vehicle. Figures 16 and 17 presents the storage casing.

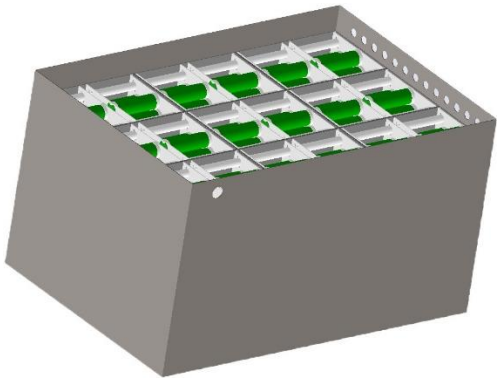

Fig. 16. Open storage casing

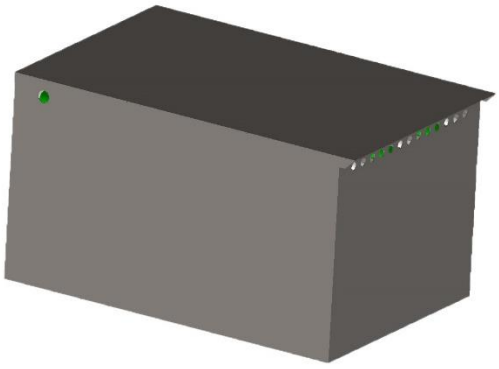

Fig. 17. Storage case with cover

3.3. Verification of TSAC

The battery test is scheduled after the vehicle is completed. The test involves uniformly loading the battery by accelerating the vehicle on a chassis dynamometer to a specified speed and maintaining a constant speed for a specified period of time. During the test, the cell voltage, resistance and temperature will be constantly monitored. At the end of the test, the results obtained will be compared with the results of calculations performed before the test. This will allow you to assess the actual condition and pa-

rameters of the battery in relation to theoretical values. Figure 18 shows the study flowchart.

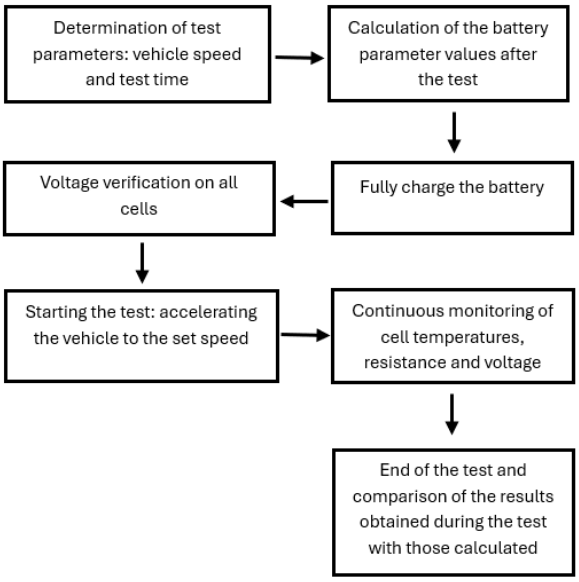

Fig. 18. Battery test flowchart

4.Conclusions

VTC6 cells were selected for the construction of the energy storage facility, which are characterized by high energy and power densities, which translates into high parameters with minimal weight and volume, and a very low cell mass necessary to ensure appropriate power parameters for the selected engine. In order to increase the capacity and reduce the load on the cells, 990 cells were used, which were divided into 9 sections (packs). The cells inside each pack were connected in a 5S22P (5 in series, 22 in parallel) configuration, and all packs were connected in series to each other. This resulted in a 45S22P (45 in series, 22 in parallel) energy storage configuration, a voltage of 162 V and a current close to 450 A while limiting the maximum current from a single cell to 20 A. The cells inside the packs are arranged in a honeycomb structure, thanks to which the volume of each package and the entire energy storage is as small as possible. The energy storage casing is made of steel with a floor thickness of 1.25 mm and walls and cover with a thickness of 0.9 mm. The ventilation holes are located on the back wall of the housing, just below the edge of the cover. Each package was insulated from the floor and walls of the energy warehouse with 1 mm thick glass fiber.

Nomenclature

BEV battery electric vehicle
C_d cell capacity
E cell energy
ETCR etouring car world cup
I_{dmax} maximal current
m cell weight
P_d cell power
TSES traction system energy storage
U_N nominal cell voltage
V cell volume
ρ_{ed} energy mass density
ρ_{pd} power mass density
ρ_{pvlm} power volume density
ρ_{evlmd} energy volume density

Bibliography

[1] Brdulak J, Pawlak P. Motor transport as an element of the Polish energy market (in Polish). Kwartalnik nauk o przedsiębiorstwie. 2021;1:31-42.
[2] Castelvecchi D. Electric cars: the battery challenge. Recycling batteries and reducing the use of scarce metals will be key to the world's transition to electric vehicles. Nature. 2021;596:336-339. https://www.nature.com/articles/d41586-021-02222-1
[3] Formula Student Rules 2023 v. 1.1. https://www.formulastudent.de/fileadmin/user_upload/all/2023/rules/FS-Rules_2023_v1.1.pdf
[4] Hemlecki P. Formula student class electric vehicle energy storage (in Polish). Master thesis. Silesian University of Technology. Gliwice 2022.
[5] Kęska A, Dziubek M, Michalik D. Market positioning of internal combustion engines and battery electric motors. Combustion Engines. 2023;195(4):136-143. https://doi.org/10.19206/CE-169803
[6] Kęska A, Dziubek M, Michalik D. The economic aspects of vehicle operation in the context of electromobility strategies. Combustion Engines. 2024;196(1):146-152. https://doi.org/10.19206/CE-172821
[7] Kropiwnicki J, Gawłas T. Evaluation of the energy efficiency of electric vehicle drivetrains under urban operating conditions. Combustion Engines. 2023;195(4):28-34. https://doi.org/10.19206/CE-169492
[8] Lai NYG, Wong KH, Halim D, Mareta S, Ran LY, Cheung H. Learning through formula student electric: Students and staff perspectives. 2021 IEEE International conference on engineering, Technology & education (TALE). 2021. https://ieeexplore.ieee.org/document/9678829
[9] Laskowski P, Zimakowska-Laskowska M, Zasina D, Wiatrak M. Comparative analysis of the emissions of carbon dioxide and toxic substances emitted by vehicles with ICE compared to the equivalent emissions of BEV. Combustion Engines. 2021;187(4);102-105. https://doi.org/10.19206/CE-141739
[10] Li L, Guo SL, Cai H, Wang JJ, Zhang J, Ni Y. Can China's BEV market sustain without government subsidies?: An explanation using cues utilization theory. J Clean Prod. 2020; 272:122589. https://doi.org/10.1016/j.jclepro.2020.122589
[11] Łosiewicz Z, Sendek-Matysiak E. The development of electromobility: in the aspect of the operation of cars with electric drive (in Polish). Autobusy. 2018;12:126-128. https://yadda.icm.edu.pl/baztech/element/bwmeta1.element.baztech-6acc55ae-70ff-4d72-9130-a2e1351235ac
[12] Mamala J, Graba M, Mitrovic J, Prażnowski K, Stasiak P. Analysis of speed limit and energy consumption in electric vehicles. Combustion Engines. 2023;195(4):83-89. https://doi.org/10.19206/CE-169370

[13] Manual for EMRAX Motors / Generators. 2020, Version 5.4. https://emrax.com/wp-content/uploads/2020/03/manual for_emrax_motors_version_5.4.pdf
[14] Martellucci L, Giannini M. Analysis of the performance and overall efficiency of a Formula Student electric car. Journal of Transportation Technologies. 2022;12:111-122. https://doi.org/10.4236/jtts.2022.121007
[15] Martínez CS, Ramos DGP, Santamaria EO, López VD. CFRP monocoque structure for formula student car. DYNA. 2020;95. https://www.revistadyna.com/search/carbon-fiber-reinforced-plastics-cfrp-monocoque-structure-for-formula-student-car
[16] Martins LS, Guimarães LF, Botelho Junior AB, Tenorio JAS, Espinosa DCR. Electric car battery: an overview on global demand, recycling and future approaches towards sustainability. J Environ Manage. 2021;295:113091. https://doi.org/10.1016/j.jenvman.2021.113091
[17] Passenger cars in the EU, Statistic Explained. Eurostat. 2022.
[18] PN-EN IEC 62660-1:2019. Lithium-ion cells for propulsion of electric road vehicles - Part 1: Properties test.
[19] Sobczak P, Kubat W. Analysis of changes in the structure of the vehicle in relation to the plans of a sustainable transport policy of the European Union as part of the transport management (in Polish). Autobusy. 2017;6:1762-1766. https://yadda.icm.edu.pl/baztech/element/bwmeta1.element.baztech-06fb9196-0970-4c3a-bf96-75c0ba8a0169
[20] Szumska EM, Jurecki R. Technological developments in vehicles with electric drive. Combustion Engines. 2023; 194(3):38-47. https://doi.org/10.19206/CE-168219
[21] Website: European Environment Agency. New registrations of electric vehicles in Europe. https://www.eea.europa.eu/en/analysis/indicators/new-registrations-of-electric-vehicles
[22] White G, Cunningham G, Doyle D. Design of an electric drive transmission for a formula student race car. SAE Technical Paper 2019-01-1295. 2019. https://doi.org/10.4271/2019-01-1295
[23] Wójtowicz S. Electric drive vehicles (in Polish). Prace Instytutu Elektrotechniki. 2012;258:237-248.

Piotr Hemlecki, MEng. – Faculty of Transport and Aviation Engineering, Silesian University of Technology, Katowice, Poland.
e-mail: *piotr.hemlecki@polsl.pl*

Paweł Fabiś, DSc., DEng. – Faculty of Transport and Aviation Engineering, Silesian University of Technology, Katowice, Poland.
e-mail: *pawel.fabis@polsl.pl*

Article citation info:
Kurzawska-Pietrowicz P, Maciejewska M, Jasiński R. Exhaust emissions from a jet engine powered by sustainable aviation fuel calculated at various cruising altitudes. Combustion Engines. 2024;198(3):62-67. https://doi.org/10.19206/CE-186211

Paula KURZAWSKA-PIETROWICZ
Marta MACIEJEWSKA
Remigiusz JASIŃSKI

Combustion Engines
Polish Scientific Society of Combustion Engines

Exhaust emissions from a jet engine powered by sustainable aviation fuel calculated at various cruising altitudes

ARTICLE INFO

Received: 21 December 2023
Revised: 13 March 2024
Accepted: 18 March 2024
Available online: 28 May 2024

The article focuses on emission analysis of non-CO_2 pollutions from aircraft engines on different flight levels: FL240, FL300 and FL350. The calculation was made based on the A320 flight from Berlin to Lisbon at flight level 350, which was the reference flight level in the analysis. Four sustainable aviation fuels have been taken into consideration: biofuel from jatropha and biofuel from camelina, which are used in different percentages of fuel: 20% of CSPK and JSPK and 40% of CSPK and JSPK. The results showed that the lowest emission of carbon monoxide is on the lowest tested flight level for flight on biofuel, and the lowest emission of nitrogen oxides is for Jet A-1 on the lowest tested flight level. Emission of every toxic gas compound has been compared to conventional jet fuel on flight level 350 to show the differences between flight levels.

Key words: *aviation, sustainable aviation fuel, emission, flight level, jatropha, camelina, biofuel*

1. Introduction

The aviation sector was responsible for 2% of global CO_2 emission from human activities and 12% of global transport-related CO_2 emission in 2019 and is forecast to be growing in the future years [14]. Aviation organizations have been trying to solve the problem of growing CO_2 emissions from the aviation sector for years. Greenhouse gases are not the only pollutants emitted by aircrafts, there are also pollutants such as nitrogen oxides, carbon monoxide, hydrocarbon, sulfur oxides, particulate matter and others [12, 18]. There are many solutions to reduce the impact of the aviation sector on the environment, for example, the development of electric propulsion, changes in the construction of the engines to reduce noise, more sustainable flight routes, and more ecological taxiing [7]. As one of the main aims for aviation is to reach net zero GHG emissions in the future, a lot of new technologies have to be developed as a more ecological solution. One of the most promising and mid-term solution is usage of Sustainable Aviation Fuels (SAF). According to European Aviation Environment Report 2019, Sustainable aviation fuel can reduce GHG emission by even 94% compared to conventional aviation fuel [9]. Sustainable aviation fuel can also reduce the emission of particulate matter by 50–70%, depending on the used fuel [17]. Regarding to Carbon Offsetting Reduction Scheme for International Aviation (CORSIA), sustainable aviation fuel (described as CORSIA eligible fuel) should be used in the aviation sector more often due to the offsetting requirements. CORSIA is a global offsetting scheme under which airlines and other aircraft operators offset any increase in CO_2 emission above 2019 levels. This means that net aviation CO_2 emissions will be stabilized while implementing other emissions reduction measures, such as technology, SAF, operational and infrastructure options [20].

This article focuses on the analysis of the emission of carbon monoxide, hydrocarbons, and nitrogen oxides depending on the flight level and also depending on the percentage usage of sustainable aviation fuels, which are, in this particular research, Camelina bio-synthetic paraffinic kerosene and Jatropha bio-synthetic paraffinic kerosene. The purpose of the article is to analyze the differences in harmful exhaust compounds depending on the flight level and to determine which flight level would have the least ecological impact. The primary focus of most analyses is on greenhouse gases, while toxic compounds are specifically examined only during the LTO test and in close proximity to the airport. Other exhaust compounds, like for example nitrogen oxides or sulfur oxides affect the radiative forcing and can indirectly contribute to the climate change [13].

The emission indexes for the Landing and Take-off cycle were obtained from the work of Biasco [3], and based on these indexes, emission indexes for the cruise phase were calculated using a trend line. That allowed to calculate emission of toxic exhaust compounds on different flight levels, based on formulas, that take into account changes in atmospheric parameters at different flight altitudes. The limitation of this approach is that the changes in aircraft weight were not taken into account in the calculations.

2. Sustainable aviation fuels

2.1. Requirements and production pathways

Alternative aviation fuel to be considered as ‘sustainable’ should meet a few requirements [11]:

– Reduce GHG emission through the life cycle by at least 10% compared to conventional aviation fuel
– Raw materials used in production of sustainable fuel should do not compete with food crops for land
– Raw materials used in the production of sustainable fuel should have limited demands on drinking water.

Sustainable aviation fuel should be a “drop in” fuel, which means that it can be used directly in aircraft engine, without any changes in engine construction, fuel infrastructure and fuel distribution systems.

The standard for alternative aviation fuel is ASTM D7566, which describes what physicochemical properties

the fuel should meet to be safely used in aircraft engines. The ASTM D7566 standard describes also certified pathways for production of SAF. Currently there are 8 certified pathways, which are [5, 16, 22, 25]:

1. Fischer-Tropsch Synthetic Paraffinic Kerosene (FT-SPK), approved in 2009. Raw material in this pathway is mostly biomass (wood waste, grass) but also Municipal Solid Wastes
2. Hydroprocessed Esters and Fatty Acids (HEFA-SPK), approved in 2011. Raw material in this pathway is oily biomass (jatropha, camelina)
3. Hydroprocessed Fermented Sugars to Synthetic Isoparaffins (HFS-SIP), approved in 2014. Raw material used in this pathway are sugars, which are converted into hydrocarbons in bacterial conversion
4. Fischer-Tropsch Synthetic Paraffinic Kerosene with aromatics (FT-SPK/A), approved in 2015. Raw material used in this pathway is renewable biomass (Municipal Solid Waste, agricultural and wood waste)
5. Alcohol-to-jet Synthetic Paraffinic Kerosene (ATJ-SPK), approved in 2016. The raw material used in this pathway is a feedstock that can be converted into alcohol, like agricultural wastes (corn shoots, grass, cellulosic biomass)
6. Catalytic Hydrothermolysis Synthesized Kerosene (CH-SK or CHJ), approved in 2020. Feedstock in this pathway is vegetable and animal fats, oils and greases
7. Hydroprocessed Hydrocarbons, Esters and Fatty Acids Synthetic Paraffinic Kerosene (HHC-SPK or HC-HEFA-SPK), approved in 2020
8. Alcohol to Jet Synthetic Kerosene with Aromatics (ATJ-SKA), approved in 2023. Feedstock in this pathway is similar to ATJ-SPK, which is for example cellulosic biomass. The blending limit is 50%.

There are also 3 co-processed pathways which are described in the ASTM D1655 standard with a blending limit of up to 5%. Co-processed pathways are: co-processed HEFA, which is co-hydroprocessing of esters and fatty acids in a conventional petroleum refinery; co-processed FT, which is co-hydroprocessing of Fischer-Tropsch hydrocarbons in a conventional petroleum refinery; co-processed biomass, which is co-hydroprocessing of biomass [15].

As the physicochemical parameters of fuel depend on the percentage volume of SAF in blend with Jet A-1, the selected physicochemical parameters required in ASTM D1655 standard are shown in Table 1. Every sustainable aviation fuel certified in ASTM D7566 standard has to meet the requirements described in ASTM D1655 [16].

Table 1. Selected physicochemical properties of ASTM D1655 standard [16]

Property	Unit	ASTM D1655
Density at 15°C	kg/m^3	775–840
Viscosity at –20°C	mm^2/s	max 8,0
Viscosity at –40°C	mm^2/s	–
Flash point	°C	min 38
Calorific value	MJ/kg	min 42.8
Aroma content	%	max 25
Naphthalene content	%	max 3.0
Crystallization temperature	°C	max –47

2.2. Second generation of biofuels

Sustainable aviation fuels are produced from different raw materials, as described in section 2.1. Aviation biofuels, which are produced from biomass, can be divided in three generations [4, 6]:

1. First generation, which contains food crops and edible plants, like sunflower and corn. First generation of biofuels can't be called as 'sustainable' as it doesn't meet the basic SAF requirements
2. Second generation, which contains inedible plants or wastes, like agricultural and forestry residues. Second generation doesn't compete with food crops for land use and doesn't have huge demands for water use so it can be described as sustainable
3. Third generation, which contain algae.

This article focuses on the emission indexes of alternative aviation fuel made from jatropha and camelina. Both of these plants are in the second generation of biofuels, and both are rich in oil. Jatropha and camelina are inedible and can be grown in difficult areas, so they do not compete with food crops for land, and they do not require a lot of water for cultivation. These features allow it to be classified as a sustainable raw material for the production of aviation fuel [2]. Jatropha oil is perceived as safe for use in aviation and as a raw material for sustainable aviation fuels, it may reduce CO_2 emissions [10].

Jatropha contains 27 to 40% of oil in seed mass. The seeds are inedible for human and animals. Jatropha has low requirements for water use and land use and can be grown in infertile soils and in difficult conditions. The plant is well adapted to tropical, semi-arid regions and marginal sites [1]. To be highly productive, jatropha needs from 4 to 5 years [1]. Oil made from jatropha seeds can be directly used in diesel engines due to parameters similar to those of fossil diesel fuel. Jatropha oil also has high stability in low temperatures, which makes it useful for jet engines [1]. Jatropha as a feedstock for sustainable aviation fuel and CORSIA eligible fuel has to reduce CO_2 emission during life cycle. A full-grown tree of jatropha absorbs around 8 kg of CO_2 per year. According to research, fuel made from jatropha can reduce 80% of CO_2 and 100% of SO_2 than fossil diesel [1].

Camelina is another plant in the second generation of biofuels, which can be a sustainable raw material for the production of SAF. Camelina is a short-season crop, from 85 to 100 days. As jatropha it can be cultivated in difficult areas, even in very cold regions, as it germinates at low temperatures and is frost tolerant [23]. It doesn't require a lot of water, can be cultivated in marginal lands and in drought stress conditions [23]. Camelina can be cultivated in temperate and tropical climates and has low demand in nutrition [8]. It doesn't compete with food crops for land and for water, so it can also be described as sustainable.

3. Calculation methods

The calculations were made for a flight of Airbus A320 from Berlin to Lisbon. Figure 1 shows the flight profile of the selected flight. The cruise phase was on an altitude from 36,000 to 37,000 ft; for calculation, the FL 350 has been chosen as the reference flight level. Calculations were made for three selected flight levels: FL260, FL300, and FL350.

The duration of flight remained consistent at each of the examined altitudes, enabling a comparison solely of emission variations based on flight altitude for different types of fuel. The ascent and descent times were not factored in, which would undoubtedly impact the overall flight duration at a specific altitude.

Fig. 1. Flight profile of the selected route

Based on the equations described in researches [11, 19, 24] emission for different altitudes has been calculated, based on the changes in emission indexes depends on flight level and used fuel. Changes in aircraft weight were not taken into account in the calculations.

The formulas used for the calculations [19]:

$$E_{CO} = EI_{CO} \cdot 10^{-3} \cdot K \cdot SFC \cdot t \cdot l \quad (1)$$

$$E_{NOx} = EI_{NOx} \cdot 10^{-3} \cdot K \cdot SFC \cdot t \cdot l \quad (2)$$

$$E_{HC} = EI_{HC} \cdot 10^{-3} \cdot K \cdot SFC \cdot t \cdot l \quad (3)$$

where: E_{CO}, E_{NOx}, E_{HC} – emission of particular exhaust gas compounds [kg], EI_{CO}, EI_{NOx}, EI_{HC} – emission indexes for particular substances, depended on the type of engine and the range of its run [g/kg], K – engine thrust [N], SFC – specific fuel consumption [kg/(N·h)], t – engine run time at a given thrust [h], l – number of engines.

$$EI_{CO} = EI_{COLTO} \cdot \frac{\theta^{3.3}}{\delta^{1.02}} \quad (4)$$

$$EI_{HC} = EI_{HCLTO} \cdot \frac{\theta^{3.3}}{\delta^{1.02}} \quad (5)$$

$$EI_{NOx} = EI_{NOxLTO} \cdot \sqrt{\frac{\theta^{3.3}}{\delta^{1.02}} \cdot e^{h}} \quad (6)$$

where: EI_{CO}, EI_{HC}, EI_{NOx} – CO, HC and NO_x emission indexes at a given altitude [g/kg], EI_{COLTO}, EI_{HCLTO}, EI_{NOxLTO} –emission indexes measured for LTO parameters [g/kg], θ – temperature change coefficient [–]:

$$\theta = \frac{T_c}{288.15\ K} \quad (7)$$

δ – pressure change coefficient [-]:

$$\delta = \frac{p_c}{101325\ Pa} \quad (8)$$

e – Euler number (e = 2.72), h – air humidity factor depended on the altitude [-]

$$h = -19 \cdot (\omega - 0.00634) \quad (9)$$

ω – specific humidity,

where

$$\omega = 10^{-3} \cdot e^{-0{,}0001426 \cdot (H - 12900)} \quad (10)$$

where H – cruising altitude [ft].

The fuel taken into analysis were Jet A-1 as reference fuel, and different mixtures of Camelina bio-synthetic paraffinic kerosene (CSPK) and Jatropha bio-synthetic paraffinic kerosene (JSPK) in the percentage use of: 20% of CSPK, 40% of CSPK, 20% of JSPK and 40% of JSPK. Every sustainable aviation fuel have been mixed with conventional aviation fuel. The maximum volume of SAF fuel in the fuel blend with Jet A-1 is described in the ASTM D7566 standard and is equal to 50%. All calculations have been done for engine CFM56-5A4 based on the results of the Landing and take-off (LTO) test in research of Biasco R. [3] for chosen fuels. Also, the fuel flow has been taken into calculation. Analyzes conducted by Biasco [3] allowed for the expansion of the ICAO database regarding emission indexes for individual engines with indexes for selected alternative fuels. The analyzes were carried out based on correction factors for given fuels and using the COPERT model, which enabled the calculation of emission factors from Jet A-1 for other fuels, taking into account their physicochemical properties. The emission indexes for LTO test obtained by Biasco R. [3] has been shown in Table 2.

Table 2. Emission indexes for CFM56-5A4 engine obtained by Biasco [3]

	Jet A-1	20% CSPK	40% CSPK	20% JSPK	40% JSPK
EI_{CO} [g/kg]					
Taxi	20.3	19.8128	19.3256	19,9752	19.6504
Approach	3.1	2.9946	2.8892	3.0132	2.9326
Climb out	1.1	1.0978	1.0956	1.0736	1.0472
Take off	1.1	1.1484	1.1968	1.0088	1.1018
EI_{HC} [g/kg]					
Taxi	1.75	1.75	1.75	1.75	1.75
Approach	0.5	0.5	0.5	0.5	0.5
Climb out	0.23	0.23	0.23	0.23	0.23
Take off	0.23	0.23	0.23	0.23	0.23
EI_{NOx} [g/kg]					
Taxi	4.04	4.3923	4.7446	4.2258	4.117
Approach	8.51	9.1057	9.7014	8.8334	9.1568
Climb out	19.11	20.2566	21.4032	19.7139	20.3178
Take off	22.64	23.5909	24.5418	23.0837	23.5275

Emission indexes for the cruise phase were calculated using a trend line based on the emission indexes obtained by Biasco [3] for the LTO cycle. This method is subject to errors, but due to the lack of appropriate field tests, it was decided to use it. R-squared for CO was equal to 0.99, R-squared for HC was equal to 0.994, and R-squared for NO_x was equal to 1. Emission indexes for the cruise phase were calculated based on the research [3] and are presented in Table 3.

Table 3. Emission indexes in cruise phase for selected fuels

	EI_{CO} [g/kg]	EI_{HC} [g/kg]	EI_{NOx} [g/kg]
Jet A-1	2.08	0.36	12.49
20% CSPK	2.09	0.36	13.21
40% CSPK	2.09	0.36	13.93
20% JSPK	1.99	0.36	12.86
40% JSPK	2.02	0.36	13.23

4. Results and discussion

Results show that the emission of hydrocarbon is the same for all used fuels because the emission index is the same for every tested fuel. Changes can be seen in the emission for different flight levels, which increases with flight altitude. For hydrocarbons, the lowest possible flight level will be the most ecological. The results are shown in Fig. 2.

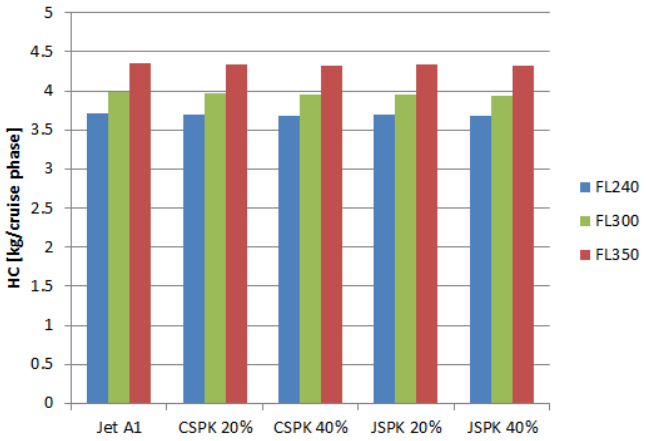

Fig. 2. Emission of hydrocarbons for selected fuels on different flight levels

The emission of carbon monoxide depends on the used fuel (Fig. 3). The lowest CO emission is for 20% JSPK, where reduction is 5% compared to Jet A-1 on every tested flight level. Emission reduction in CO is also for 40% JSPK and is equal to 4% compared to Jet A-1. Similar to hydrocarbons, the higher the flight level, the higher the emission of carbon oxides. For CSPK, the CO emission was almost the same as that of the Jet A-1 at every flight level.

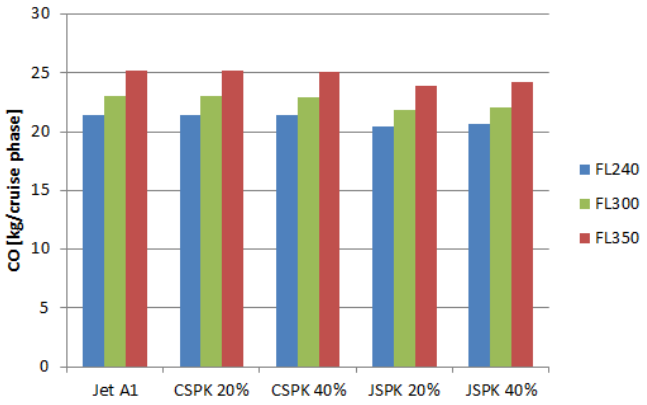

Fig. 3. Emission of carbon monoxide for selected fuels on different flight levels

The emission of nitrogen oxides grows with the increase of biofuel for CSPK and JSPK for every flight level (Fig. 4). The lowest emission of nitrogen oxides is for Jet A-1 on the highest calculated altitude. The changes in NO_x emission is different than in CO and HC and decrease with the increase of flight level.

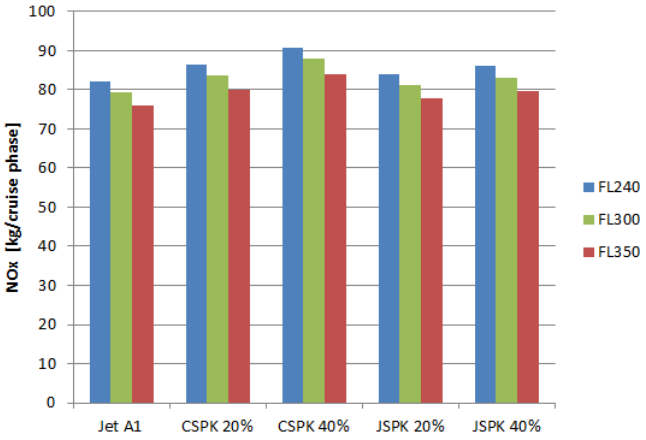

Fig. 4. Emission of carbon monoxide for selected fuels on different flight levels

Changes in the emission of particular toxic gas compounds of selected fuel are shown in Fig. 5. The changes are accurate for every calculated flight level. The biggest changes are for 40%CSPK for NO_x compared to Jet A-1, which is equal to 11%. The addition of JSPK has a positive impact on the emission of carbon monoxide and can reduce this emission by 4–5% compared to Jet A-1.

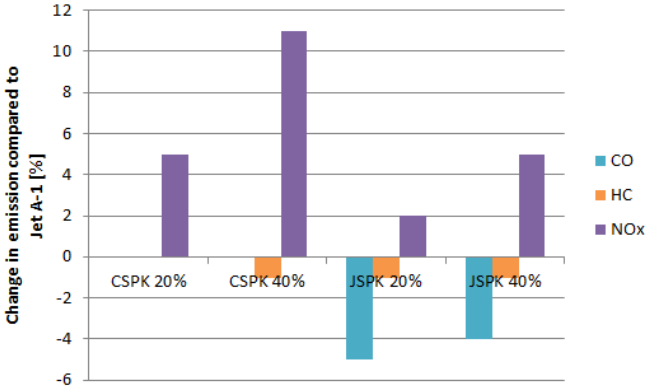

Fig. 5. Differences in emission of particular toxic gas compounds of selected fuels compared to Jet A-1

To analyze changes for different flight level and selected fuel, the Jet A-1 on the FL350 has been set us as reference values. Percentage changes has been shown in Table 4.

Table 4. Percentage differences in emission of particular pollutant depending on the flight level and used fuel, compared to flight on Jet A-1 on the FL350

	Jet A-1	20% CSPK	40% CSPK	20% JSPK	40% JSPK
CO					
FL240	–14.8%	–14.8%	–15%	–18.9%	–18.1%
FL300	–.6%	–8.6%	–8.9%	–13.1%	–12.2%
FL350	0%	0%	–0.3%	–4.9%	–3.9%
HC					
FL240	–14.8%	–15.2%	–15.4%	–15.3%	–16.6%
FL300	–8.6%	–9.1%	–9.3%	–9.2%	–9.6%
FL350	0%	–0.5%	–0.8%	–0.6%	–1%
NO_x					
FL240	8.1%	13.8%	19.6%	10.6%	13.3%
FL300	4.5%	10%	15.7%	7%	9.6%
FL350	0%	5.2%	10.7%	2.3%	4.8%

It can be seen that the flight on the lowest tested altitude can reduce CO emission by almost 15% on Jet A-1, and with 20% of JSPK and 40% of JSPK, it can reduce CO emission by approximately 18,9% and 18,1%. Flight on 20% and 40% of CSPK has almost the same reduction of about 15% compared to Jet A-1. Emission of HC can be reduced also on the lowest flight level by almost 15% on Jet A-1, and by 16.6% with 40% of JSPK fuel. Emission of nitrogen oxides is the lowest for Jet A-1 on the FL350 of all compared flight levels and biofuels.

5. Conclusions

As not only CO_2 affects climate change, it is important to also address other harmful compounds that are emitted by aircraft engines, such as NO_x, HC and CO. Some of the toxic compounds contained in exhaust gases affect radiative forcing, for example, NO_x emissions have warming and cooling effect: NO_x emissions contribute to the generation of ozone, which is a greenhouse gas; the cooling effect is related to methane removal from the atmosphere, while the breakdown of the NO_x gases results in increased OH content, which helps shorten the life of methane [3, 13].

This article focused on the calculation of CO, HC, and NO_x from Airbus A320 on selected flight routes to compare the usage of sustainable aviation fuel with conventional aviation fuel on different flight levels. The flight time at each of the analyzed levels was the same to compare only changes in emissions depending on flight altitude for different fuels. The time of climb and descent was not taken into account, which would obviously affect the flight time at a given flight level.

The calculation showed that for CO and HC, the lowest emission is on the lowest flight level, and the reduction in CO emission is almost 15% for Jet A-1 compared to flight level 350, which was the reference flight level. Flight on the lowest analyzed flight level on the 20% of Jatropha bio-synthetic paraffinic kerosene can reduce CO emission by almost 19% compared to Jet A-1 on the FL350 and by 5% compared to Jet A-1 at FL240. For the emission of nitrogen oxides, the reference flight on FL350 on Jet A-1 fuel has the lowest NO_x emission from all analyzed flight levels and fuels. The calculated results show that changes in flight level have a significant impact on emission due to changes in ambient conditions and atmospheric parameters at different altitudes at which the engine operates. CO and HC emissions increased with increasing altitude, and NO_x emissions decreased with increasing altitude. One of the main environmental factors influencing HC, CO and NO_x emissions may be atmospheric pressure. This is also confirmed by tests conducted on a diesel engine at high altitudes [21].

There are very few analyzes for emissions of harmful compounds at cruising altitude, such as CO, HC and NO_x. Most analyzes concern strictly GHG and toxic compounds are analyzed only in the LTO test and in the close vicinity of the airport. Upon comparing the calculated emissions with findings from other studies, it becomes apparent that the results obtained hold significance. However, due to the scarcity of similar articles, a more detailed examination of the results is not feasible at this time. Pawlak et al. [19] made related calculations for different flight altitudes, but the change in the aircraft's weight during the flight and changes in thrust force at individual altitudes were also taken into account, so the relationships between flight levels are different than in the presented analysis. However, alternative fuels were not taken into account in this paper, therefore it is not possible to compare the SAF blend emission results at different flight levels with other studies.

Due to the fact that the physicochemical properties of various SAF fuel blends depend on the volume share of SAF in the blend, it is difficult to assess at this stage of the analysis how individual properties affect the emission of toxic compounds at a given altitude. This topic should be developed and supplemented with an analysis of the physicochemical properties of various concentrations of SAF fuel with Jet A-1 and an attempt to assess the relationship between individual properties and emissions at a given altitude.

When comparing sustainable aviation fuels with conventional fuel, it is crucial to compare its life cycle emission, not only the combustion of the fuel in aircraft engines. That shows how many factors should be considered to fly more ecologically and that reduction in emission of one pollutant can grow emission of another pollutant.

Nomenclature

ATJ-SPK	alcohol-to-jet synthetic paraffinic kerosene
CHJ	catalytic hydrothermolysis jet fuel
CH-SK	catalytic hydrothermolysis synthesized kerosene
CO	carbon monoxide
CO_2	carbon dioxide
CSPK	camelina bio-synthetic paraffinic kerosene
FT-SPK	Fischer-Tropsch synthetic paraffinic kerosene
FT-SPK/A	Fischer-Tropsch synthetic paraffinic kerosene with aromatics
GHG	greenhouse gases
HC	hydrocarbons
HEFA	hydroprocessed esterts and fatty acids
HFS-SIP	hydroprocessed fermented sugars to synthetic isoparaffins
HHC-SPK	hydroprocessed hydrocarbons, esters and fatty acids synthetic paraffinic kerosene
JSPK	jatropha bio-synthetic paraffinic kerosene
NO_x	nitrogen oxides
SAF	sustainable aviation fuels

Bibliography

[1] Achten WMJ, Mathijs E, Verchot L, Singh VP, Aerts R, Muys B. Jatropha biodiesel fueling sustainability? Biofuel Bioprod Bior. 2007;1(4):283-291. https://doi.org/10.1002/bbb.39

[2] Achten WMJ, Verchot L, Franken YJ, Mathijs E, Singh VP, Aerts R et al. Jatropha bio-diesel production and use. Biomass Bioenerg. 2008;32(12):1063-1084. https://doi.org/10.1016/j.biombioe.2008.03.003

[3] Biasco R. Emissions analysis routine for subsonic aircrafts using biofuel. Politecnico di Torino. Torino 2021.

[4] Biofuels in the European Union a Vision for 2030 and Beyond, 2006. http://www.etipbioenergy.eu/images/2061rep.pdf

[5] Bosch J, Jong S, Hoefnagels R, Slad R. Aviation biofuels: strategically important, technically achievable, tough to deliver. 2017. https://www.imperial.ac.uk/media/imperial-college/grantham-institute/public/publications/briefing-papers/BP-23-Aviation-Biofuels.pdf

[6] Christian JA. Feasibility of second and third generation biofuel in general aviation: a research report and analysis. McNair Scholars Research Journal. 2014;1(4). https://commons.erau.edu/mcnair/vol1/iss1/4

[7] Czarnigowski J, Trendak M. Aircraft piston engine load distribution in steady state operating conditions. Combustion Engines. 2023;193(2):29-35. https://doi.org/10.19206/CE-160505

[8] Doliente SS, Narayan A, Tapia JFD, Samsatli NJ, Zhao Y, Samsatli S. Bio-aviation fuel: a comprehensive review and analysis of the supply chain components. Front Energy Res. 2020;8:110. https://doi.org/10.3389/fenrg.2020.00110

[9] EASA, European Aviation Environmental Report 2019.

[10] Ejilah RI, Ogbaneme AA, Agboneni OO, Adekunle SO. Analysis of jatropha oil-kerosene fuel mixtures on the performance of a variable-load direct injection CI engine. Combustion Engines. 2023;192(1):11-18. https://doi.org/10.19206/CE-153463

[11] Galant M, Kurzawska P, Maciejewska M, Kardach M. Analysis of the impact of wind on fuel consumption and emissions of harmful exhaust gas compounds on the selected flight route. Combustion Engines. 2019;179(4):93-101. https://doi.org/10.19206/CE-2019-415

[12] Galant-Gołębiewska M, Jasiński R, Nowak M, Kurzawska P, Maciejewska M, Ginter M. Methodical aspects of the LTO cycle use for environmental impact assessment of air operations based on the Warsaw Chopin Airport. https://doi.org/10.3846/aviation.2021.14972

[13] Grewe V, Dahlmann K, Matthes S, Steinbrecht W. Attributing ozone to NO_x emissions: implications for climate mitigation measures. Atmos Environ. 2012;59:102-107. https://doi.org/10.1016/j.atmosenv.2012.05.002

[14] Hasan MA, Mamun AA, Rahman SM, Malik K, Al Amran MIU et al. Climate change mitigation pathways for the aviation sector. Sustainability. 2021;13:3656. https://doi.org/10.3390/su13073656

[15] ICAO Environment, Global Framework for Aviation Alternative Fuels. https://www.icao.int/environmental-protection/GFAAF/Pages/default.aspx

[16] Kurzawska P, Jasiński R. Overview of sustainable aviation fuels with emission characteristic and particles emission of the turbine engine fueled ATJ blends with different percentages of ATJ fuel. Energies. 2021;14:1858. https://doi.org/10.3390/en14071858

[17] Kurzawska P. Overview of sustainable aviation fuels including emission of particulate matter and harmful gaseous exhaust gas compounds. Transp Res Proc. 2021;59:38-45. https://doi.org/10.1016/j.trpro.2021.11.095

[18] Majka A, Muszyńska-Pałys J. Analysis of the performance of an aircraft powered by hybrid propulsion. Combustion Engines. 2023;193(2):45-51. https://doi.org/10.19206/CE-161107

[19] Pawlak M, Majka A, Kuźniar M, Pawluczy J. Emission of selected exhaust compounds in jet engines of a jet aircraft in cruise phase. Combustion Engines. 2018;173(2):67-72. https://doi.org/10.19206/CE-2018-211

[20] Prussi M, Lee U, Wang M, Malina R, Valin H, Taheripour F et al. CORSIA: The first internationally adopted approach to calculate life-cycle GHG emissions for aviation fuels. Renew Sust Energ Rev. 2021;150:111398. https://doi.org/10.1016/j.rser.2021.111398

[21] Qi Z, Gu M, Cao J, Zhang Z, You C, Zhan Y et al. The effects of varying altitudes on the rates of emissions from diesel and gasoline vehicles using a portable emission measurement system. Atmosphere. 2023;14(12):1739. https://doi.org/10.3390/atmos14121739

[22] Radich T. The flight paths for biojet fuel. U.S. Energy Information Administration, Working Paper Series 2015.

[23] Shonnard D, Williams L, Kalnes TN. Camelina-derived jet fuel and diesel: sustainable advanced biofuels. Environ Prog Sustain. 20101;29(3):382-392. https://doi.org/10.1002/ep.10461

[24] Turgut ET, Usanmaz O. An assessment of cruise NO_x emissions of short-haul commercial flights. Atmos Environ. 2017;171:191-204. https://doi.org/10.1016/j.atmosenv.2017.10.013

[25] Yang J, Xin Z, He Q, Corscadden K, Niu H. An overview on performance characteristics of bio-jet fuels. Fuel. 2019; 237:916-936. https://doi.org/10.1016/j.fuel.2018.10.079

Paula Kurzawska-Pietrowicz, MEng. – Faculty of Civil and Transport Engineering, Poznan University of Technology.
e-mail: *paula.kurzawska@put.poznan.pl*

Remigiusz Jasiński, DSc., DEng. – Faculty of Civil and Transport Engineering, Poznan University of Technology.
e-mail: *remigiusz.jasinski@put.poznan.pl*

Marta Maciejewska, DEng. – Faculty of Civil and Transport Engineering, Poznan University of Technology.
e-mail: *marta.maciejewska@put.poznan.pl*

Article citation info:
Rutkowska-Gorczyca M, Dziubek M, Wiśniewski M. Response of hydrogen charging diffusion of the austenitic stainless steel AISI 310s. Combustion Engines. 2024;198(3):68-73. https://doi.org/10.19206/CE-186591

Małgorzata RUTKOWSKA-GORCZYCA
Mateusz DZIUBEK
Marcin WIŚNIEWSKI

Combustion Engines
Polish Scientific Society of Combustion Engines

Response of hydrogen charging diffusion of the austenitic stainless steel AISI 310s

ARTICLE INFO

Received: 11 July 2023
Revised: 28 March 2024
Accepted: 28 March 2024
Available online: 4 June 2024

The subject of hydrogen embrittlement seems to be more and more up-to-date and needed to be explored. World research teams working on this issue have not developed a clear method of preventing this process. The conclusion is that this issue should be approached individually, depending on the type of material, its structure and operating conditions. The problem will escalate in the near future as a result of the planned replacement of the traditional energy sources used so far with hydrogen energy. The paper presents the method of electrochemical hydrogenation, which reflects the conditions of galvanic coating of metallic materials used in the automotive industry. The aim of the research was to determine the influence of the time of hydrogenation on the properties and microstructure of austenitic steel.

Key words: *hydrogen embrittlement, metallic materials, potentiostatic tests*

1. Introduction

The presence of hydrogen in metallic materials may result in a decrease in plasticity and the formation of locally brittle damage, in a phenomenon called hydrogen embrittlement (HE) [4, 5, 9, 13, 16, 17, 20]. This phenomenon, despite the huge amount of research devoted to it, has still not been fully explained. The mechanism of the negative impact of hydrogen on mechanical properties still requires precise explanations. Research and tests to determine the impact of the chemical composition and microstructure of steel on degradation caused by the presence of a corrosive environment will enable the correct selection of materials for specific hydrogen applications. Hydrogen embrittlement (HE) represents the deterioration of the mechanical properties of metals and alloys due to the presence of dissolved hydrogen in the lattice. The hydrogen embrittlement results in the loss of ductility, the decrease of fracture toughness, the increase in fatigue fracture growth rate, and brittle fracture failure in steel at low or subcritical stress levels. The fatigue behavior of hydrogen embrittled steel, including the fracture toughness, fatigue crack growth rate, fatigue life, and fracture surface or crack morphology, has been studied extensively in many research centers. The source of hydrogen supply to the metal is mainly hydrogen, which can enter the steel as a result of exposure to a hydrogen-rich gaseous environment at high pressure or by cathodic charging.

Nowadays, advanced research is being carried out on alternative, innovative ways to reduce the negative impact of transport on exhaust emissions into the environment [15]. One of the researched solutions that is gaining more and more attention is the use of hydrogen-powered internal combustion engines. Hydrogen engines open new perspectives for the automotive sector, but also pose new construction problems to be solved. A direct threat resulting in damage to engine components operating in a hydrogen environment is the phenomenon of hydrogen embrittlement of the material. This important issue results in a weakening of the material structure and an increase in susceptibility to cracking [12]. Especially this problem applies to metal materials. Hydrogen, which is the smallest known atom, has the ability to penetrate the metal structure. This is due to the diffusion of hydrogen into the material, which results in changes in the crystal structure of the material. As a result, the internally rebuilt material has a greater tendency to crack under load and brittleness.

Various materials are used for the construction of motors, depending on the requirements of the characteristics of the elements and the working conditions of the motor [7, 20–22, 25]. One of the groups of materials used due to their high strength and corrosion resistance are austenitic steels. The study of different grades of this stainless-steel aims to understand the influence of the hydrogen element on the structure and properties of the steel [1–3, 6, 8, 10–12, 14, 18, 19, 22, 23, 28]. Hydrogen embrittlement in austenite steels causes a change in strength parameters, therefore an important aspect in designing is the appropriate study of materials that will be selected as materials cooperating in the H_2 environment. AISI 310s heat resistant steel is an austenitic chromium-nickel grade with increased nickel content, showing high strength, ductility, resistance in air and oxidizing atmosphere to high temperatures up to 1050°C. Steel is used for mechanically loaded parts that work at high temperatures. Incorrect technological processes and working conditions at elevated temperatures can cause the formation of hard phases in austenitic steels. Depending on the chemical composition of the steel, $M_{23}C_6$ carbides may form [4, 10, 24–26].

Numerous literature items contain studies on the effect of heat treatment on the properties of materials made of austenitic steels. Long-term exposure to these steels at elevated temperatures (500–900°C) leads to the release of structural components by diffusion, which leads to a significant reduction in physical, chemical, and mechanical properties. Austenitic steels tend to form carbides along grain boundaries at elevated temperatures, this is called sensitization of the steel. In such a material, the grain boundary zone is depleted in chromium and more susceptible to intergranular corrosion and deformation-induced martensite formation.

This paper presents an analysis of the effect of the time of hydrogenation during electrolytic current processes on the microstructure, strength and hardness of metallic membranes made of heat sensitized AISI 310s steel. The steel was sensitized to the possibility of the presence of an alloyed austenite structure with $M_{23}C_6$ carbide precipitates, intended to simulate the conditions of incorrectly conducted welding processes or unfavorable operating conditions.

2. Materials and methodology

2.1. Steel AISI 310s

The material in the form of commercially available AISI 310s steel was selected for the tests. The tested steel showed a microstructure, equiaxed alloy austenite grains with precipitations of carbides forming a shell at the grain boundaries (Fig. 1). In the delivery state, according to the supplier, the material was characterized by the chemical composition given in Table 1. and showed the properties presented in Table 2. Membranes for the tests were prepared in the form of plates with a thickness of 0.7 mm, dimensions shown in Fig. 2. The area of interaction with the electrolyte during electrochemical processes was about 550 mm^2 and was the same for each sample. The surface of the materials before the electrochemical process was cleaned in an ultrasonic scrubber in an acetone solution for 10 min.

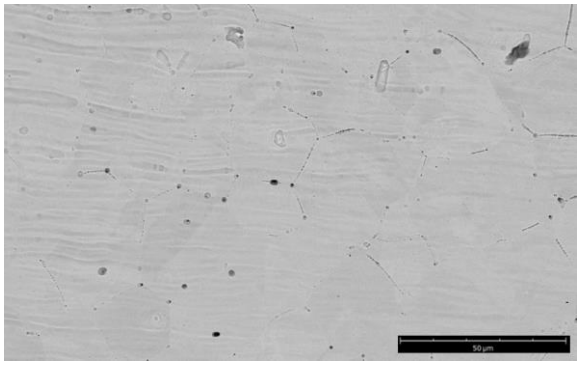

Fig. 1. Microstructure of alloyed austenite with evolved carbons at grain boundaries in AISI 310s steel in the supply state; SEM

Table 1. Chemical composition of steel AISI 310s

AISI 310s	C < 0.2	Mn < 1.5	Si < 1.0
P < 0.045	S < 0.030	Cr 22.0–25.0	Ni 17.0–20.0
Mo < 0.5	V < 0.2	W < 0.5	Fe rest

Table 2. Mechanical properties of steel AISI 310s

tensile strength Rm	Elongation A	Hardness
500–700 MPa	33%	192HB

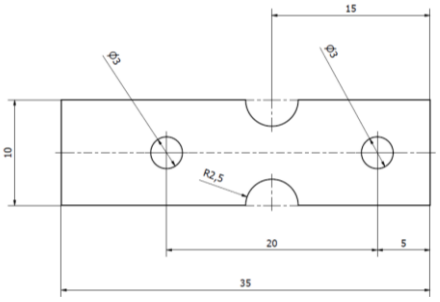

Fig. 2. Austenitic steel membrane dimensions

2.2. Methodology

Electrochemical measurements were performed using a BioLogis SP50ze potentiostat/galvanostat. The current waveforms were carried out in an electrolyte with a concentration of 0.5M H_2SO_4 acid and a pH of 1. Voltamperometry (CV measurement) was carried out in a three-electrode system, where the metallic membrane was the working electrode, the Ag/AgCl electrode was the reference electrode, and the platinum electrode was the counting electrode. The measurement procedure began with a 10-minute open circuit (OCV) measurement in the applied electrode system, on the basis of which the open circuit potential Ewe was determined, which was used to determine the range of the voltammetry process. The open circuit voltage consists of the period during which no potential or current is applied to the working electrode. The cell is disconnected from the power amplifier. Potential measurements are available on the cell. Thus, the evolution of the resting potential can be recorded. This period is commonly used as a preconditioning time or to equilibrate an electrochemical cell.

Measurements of CV voltammetry were carried out in the range below the Ewe open circuit value to eliminate the oxidation process and force the hydrogen evolution process. Cyclic voltammetry (CV) is the most pitchfork used technique for acquiring qualitative information about electrochemical reaction. CV provides information on redox processes, heterogeneous electron-transfer reactions and adsorption processes. It offers a rapid location of re-dox potential of the electroactive species. A CV consists of scanning linearly the potential of a stationary working electrode using a triangular potential waveform. During the potential sweep, the potential measures the current resulting from electrochemical reactions. The cyclic voltammogram is a current response as a function of the applied potential. The paper presents the results for two ranges of hydrogenation cycles in the voltammetry process, 25 (1 h) cycles and 50 cycles (2 h), and their influence on the microstructure and properties of steel was determined. The system was cyclically charged between the potential of –0.200 V and –1.4 V, with a scan rate of 20 mV/s.

After the hydrogenation processes, the samples were immediately tensile tested in a Deben Micro test strain gauge (Thermo Fisher Scientific), compatible with the Phenom XL scanning electron microscope. The holder enables strength tests up to 1000 N and *in-situ* observations in scanning microscope mode and all operating modes. Examination of the surface of the material after hydrogenation was also carried out with the use of scanning electron microscopy methods from the Phenom XL company. Then, microhardness measurements were carried out in accordance with PN-EN ISO 6507-1:2018-05, using the Vickers method and the Leco LM-248AT microhardness tester. The measurements were carried out with a load of 2.94 N.

3. Results and discussion

3.1. Voltammetry

Voltammetry measurements CV showed in all cycles similar shape of the curves, during observations the hydrogenation process showed an increasingly intense and violet process of hydrogen evolution in the lower parts of the

graph. The most intensive hydrogenation process took place in the range below 0.5 Ewe, numerous hydrogen bubbles were visible, concentrating on the surface of the metallic membrane constituting the working electrode. In subsequent hydrogenation cycles, the current values decreased in the range of –2.5 mA/cm to –3.5 mA/cm for 25 cycles (Fig. 3). For hydrogenation in 50 cycles, the current values were lower and oscillated from –3.0 mA/cm to –6 mA/cm (Fig. 4). Differences in the initial values result from differences in the closed-circuit measurement values in a given electrode system. There is a clear tendency to decrease the current values in successive hydrogenation cycles. This proves the changes taking place in the metallic membranes and the change of their electrochemical potentials in relation to the material in the delivery state.

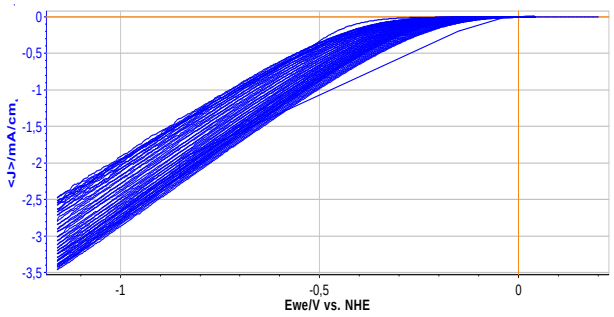

Fig. 3. Cyclic Voltammetry (CV) curve after 25 hydrogen cycles in $0.5MH_2SO_4$

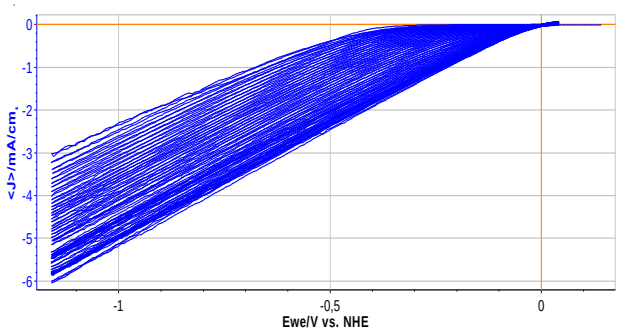

Fig. 4. Cyclic Voltammetry (CV) curve after 50 hydrogen cycles in $0.5MH_2SO_4$

3.2. Surface of membranes after hydrogenation

Observation of the surface of the metallic membranes after the hydrogenation process did not show any changes in the form of local bubbles or dissolution of alloy austenite grain boundaries. Observations indicate the lack of processes of surface degradation of metallic materials at the assumed potentiation parameters in the process of hydrogenation. The surface of the membrane, as supplied shows a texture after the treatments of the grinding process, visible in the form of parallel lines (Fig. 5). Analysis of the surface of the membranes after the hydrogenation process also showed an analogous texture and the presence of parallel lines after the grinding process (Fig. 6 and Fig. 7).

3.3. Stretch curves

The samples, after the hydrogenation process, were subjected to axial tensile testing at a constant speed of 0.5 mm/s inside a scanning electron microscope chamber equipped with a tensile holder with a maximum measurement force of 1 kN. All the tensile tests were conducted in a single setup, creating geometric notches in the central part of the samples. As a result of the tensile testing, the maximum force and elongation were determined, which were considered as comparative values due to the identical geometry of the samples (Fig. 8).

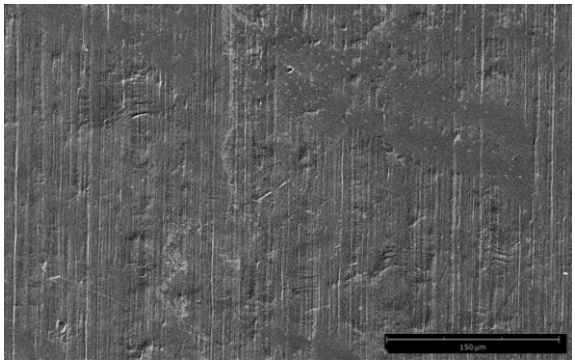

Fig. 5. Surface of AISI 310s metallic steel membrane in delivery state; SEM

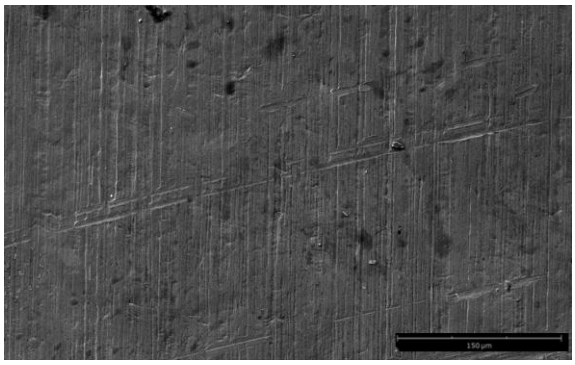

Fig. 6. Surface of AISI 310s metallic membrane after 25 cycles of hydrogenation; SEM

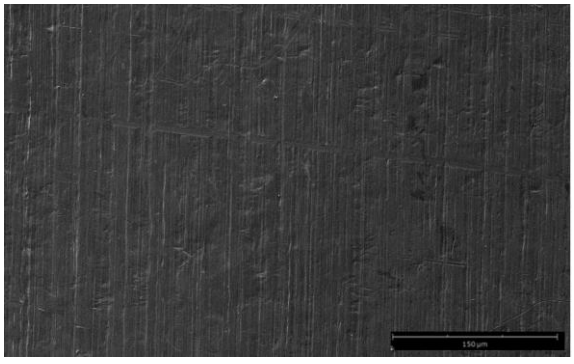

Fig. 7. Surface of AISI 310s metallic membrane after 50 cycles of hydrogenation; SEM

The hydrogenation process after 25 and 50 cycles resulted in a slight strengthening of the material, increasing the maximum force value by 3%, which represents a minor change. On the other hand, the elongation value underwent a significant reduction, decreasing by 9% after 25 cycles of hydrogenation and 13% after 50 cycles of hydrogenation compared to the reference state. This indicates a negative impact of the hydrogen environment on AISI 310S steel.

The steel becomes brittle and more prone to cracking, which can result in sudden and uncontrolled material fracture. This effect is most intense in the first hours of hydrogenation [26, 27].

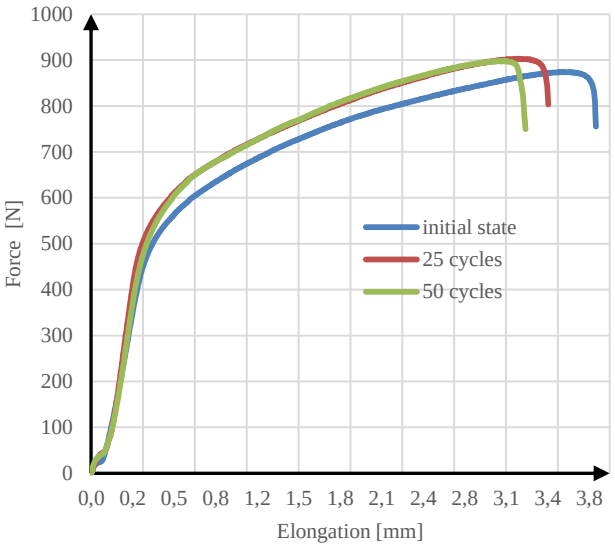

Fig. 8. Tensile curves for delivery state AISI 310s, hydrogenation after 25 cycles and 50 cycles

3.4. Fractographic observations

Fractographic examination of the surface of the material, both in the initial state and after the hydrogenation process, showed the characteristics of plastic fracture. No areas of hydrogen embrittlement are visible in any area. Due to the high degree of elongation of the sample, the observed fracture belongs to ductile fractures. The surface of the membrane in the area at the fracture focus shows the presence of numerous irregular plastic striations parallel to the crack front (Fig. 9, 11 and 13). The location of the stripes coincides with the texture after surface treatment and is a mirror image of the scratches from the abrasive papers, which are the places of their formation initiation. It has been observed that striations appear during the stretching of the membranes from the initial stages of strain. Fractographic examinations of fractures show clear changes, which indicate the formation of a plastic fracture. Dimples of various sizes are visible, and typical sliding cracks with fine scales are also visible (Fig. 10, 12 and 14).

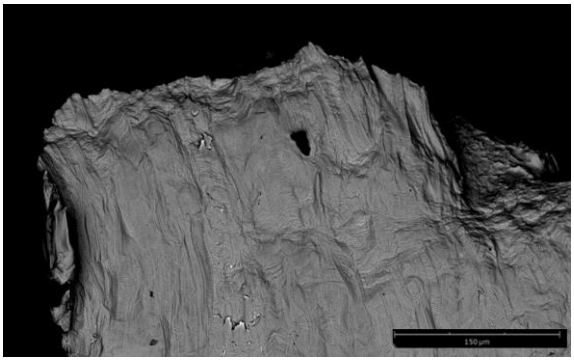

Fig. 9. Plastic breakthrough of the membrane in the state of delivery AISI 310s; SEM

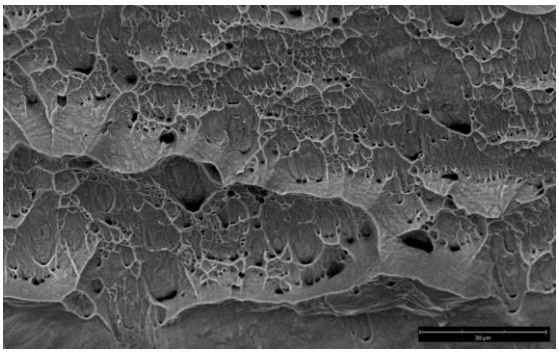

Fig. 10. Fractography breakthrough material in the state of delivery AISI 310s; SEM

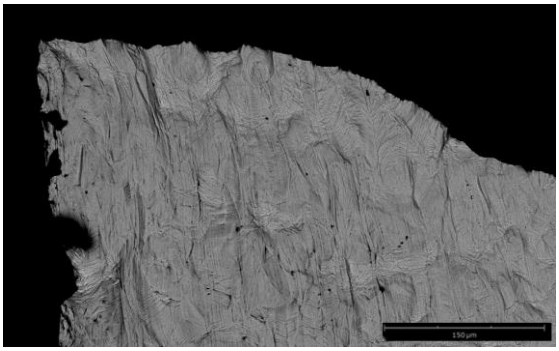

Fig. 11. Plastic membrane breakthrough after hydrogenation after 25 cycles; SEM

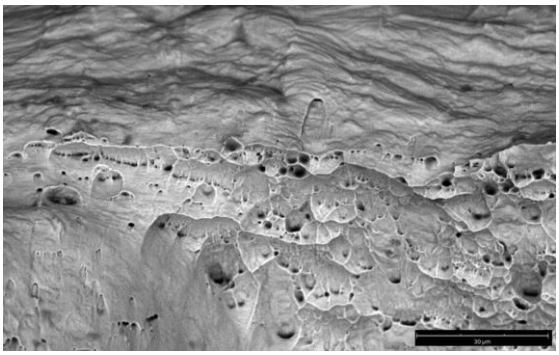

Fig. 12. Fractography of material breakthrough after hydrogenation after 25 cycles; SEM

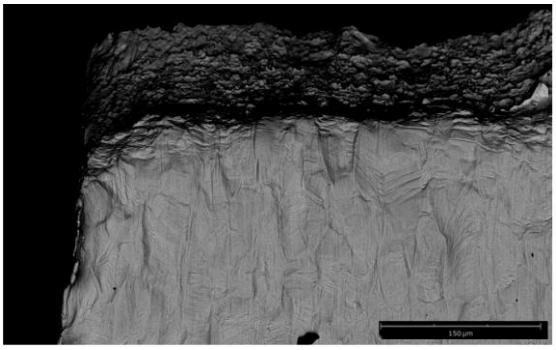

Fig. 13. Plastic membrane breakthrough after hydrogenation after 50 cycles; SEM

Grain boundaries and numerous micropores formed in places of stress concentration are clearly outlined. Crystal lattice defects, usually dislocations, which form clusters on

obstacles blocking their movement, play a large role in the formation of micropores. As the plastic deformation progressed, the micropores grew larger and closer together. Bridges were formed in these areas, which formed fibrils as a result of thinning, the resulting fractures have the characteristics of fibrous fractures.

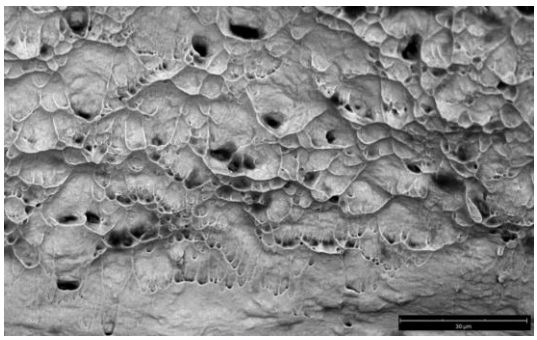

Fig. 14. Fractography of material breakthrough after hydrogenation after 25 cycles; SEM

3.5. Hardness measurements

Microhardness tests are one of the simplest methods to determine changes in the form of strengthening in the material after the hydrogenation process. Hardness measurements were carried out on the surface of the membranes, on the undeformed elements of the sample after the hydrogenation process. Analysis of the microhardness results showed that the H_2 environment affects the surface hardening of AISI 310s steel (Fig. 15). The increase in the microhardness value is directly proportional to the cycles of electrolytic hydrogenation. Before the hydrogenation process, the average hardness of the material as supplied was 154 HV0.2. The results of the hydrogenation showed an increase in hardness for the membranes after 25 cycles to an average value of 163 HV0.2. The highest value increase was obtained with the longest exposure of the material to hydrogen, after 50 cycles the hardness increased to 170HV0.2.

4. Conclusion

The presented paper presents the process of hydrogen loading membranes of AISI 310s austenitic steel in order to assess the influence of hydrogen on the properties of this steel. Based on the test results, it was found that the material was strengthened by the process of electrochemical hydrogenation in 0.5M H_2SO_4 solution. The increase in strengthening is directly proportional to the amount of hydrogen supplied to the material (number of cycles), confirmed by strength tests and hardness measurements. This indicates a negative impact of the hydrogen environment on AISI 310S steel. The steel becomes brittle and more prone to cracking, which can result in sudden and uncontrolled material fracture. This is likely due to the diffusion of hydrogen into the material, which causes changes in the material's crystal structure and mechanical properties. As a result, the internally remodeled material has a greater tendency to strengthen and crack under load. The occurrence of the features of the form of hydrogen embrittlement known from the literature in the form of local brittle fracture zones was not observed in any of the materials.

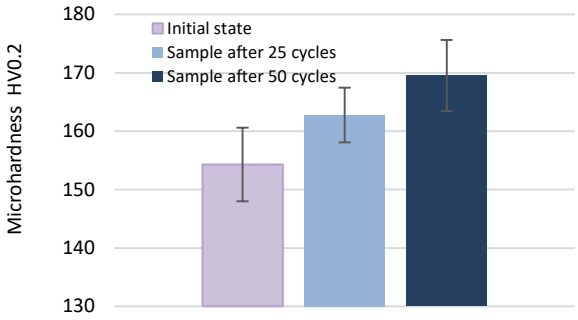

Fig. 15. Averaged results of material hardness in the delivery state, after 25 cycles and 50 hydrogenation cycles

Based on the research, it was found that the process of cathodic hydrogen charging in the electrolytic process in a solution of 0.5MH_2SO_4 significantly affects the strengthening of AISI 310s steel, while maintaining the plastic character of the breakthrough. No areas of brittle fractures characteristic of hydrogen embrittlement were found in fractographic studies. Additively, the presence of carbides at grain boundaries can act as areas of stress concentration, which can increase susceptibility to hydrogen embrittlement in these areas. Where carbides are present, hydrogen can accumulate more easily and lead to localized weakening of the material's structure. However, this mechanism was not confirmed in the study.

Acknowledgements

The work was carried out as part of a funding project from the National Science Centre Miniatura 6 with the number 02NA/0005/22. We would also like to thank PIK Instruments and Termo Fisher Scientific for providing the research equipment.

Bibliography

[1] Au M. Mechanical behavior and fractography of 304 stainless steel with high hydrogen concentration. No WSRC-TR-2002-00558 Savannah River Site (US). 2003;865. https://www.osti.gov/servlets/purl/807672

[2] Bertsch KM, Nagao A, Rankouhi B, Kuehl B, Thoma DJ. Hydrogen embrittlement of additively manufactured austenitic stainless steel 316 L. Corros Sci. 2021;192:109790. https://doi.org/10.1016/j.corsci.2021.109790

[3] Caskey GR. Fractography of hydrogen-embrittled stainless steel. Scripta Metallurgica. 1977;11(12):1077-1083. https://doi.org/10.1016/0036-9748(77)90311-8

[4] Das T, Legrand E, Brahimi SV, Song J, Yue S. Evaluation of material susceptibility to hydrogen embrittlement (HE): an approach based on experimental and finite element (FE) analyses. Eng Fract Mech. 2020;224:106714. https://doi.org/10.1016/j.engfracmech.2019.106714

[5] Gavriljuk VG, Hänninen H, Tarasenko AV, Tereshchenko AS, Ullakko K. Phase transformations and relaxation phenomena caused by hydrogen in stable austenitic stainless steels. Acta Metallurgica et Materialia. 1995;43(2):559-568. https://doi.org/10.1002/9781118803363.ch78

[6] Hamaad ASAA, Tawfik M, Khattab S, Newir A. Device for using hydrogen gas as environmental friendly fuel for automotive engine (GREEN & ECO H2). Procedia Environ Sci. 2017;37:564-571. https://doi.org/10.1016/j.proenv.2017.03.043

[7] Hatano M, Fujinami M, Arai K, Fujii H, Nagumo M. Hydrogen embrittlement of austenitic stainless steels revealed by deformation microstructures and strain-induced creation of vacancies. Acta Mater. 2014;67:342-353. https://doi.org/10.1016/j.actamat.2013.12.039

[8] Khanchandani H, Gault B. Atomic scale understanding of the role of hydrogen and oxygen segregation in the embrittlement of grain boundaries in a twinning induced plasticity steel. Scr Mater. 2023;234:115593. https://doi.org/10.1016/j.scriptamat.2023.115593

[9] Kim HP, Park YM, Jang HM, Lim SY, Choi MJ, Kim SW et al. Early-stage M23C6 morphology at the phase boundary in type 304L austenitic stainless steel containing δ ferrite. Metals. 2022;12(11):1794. https://doi.org/10.3390/met12111794

[10] Komatsu A, Fujinami M, Hatano M, Matsumoto K, Sugeoi M, Chiari L. Straining-temperature dependence of vacancy behavior in hydrogen-charged austenitic stainless steel 316L. Int J Hydrogen Energy. 2021;46(9):6960-6969. https://doi.org/10.1016/j.ijhydene.2020.11.148

[11] Lai CL, Tsay LW, Chen C. Effect of microstructure on hydrogen embrittlement of various stainless steels. Materials Science and Engineering: A. 2013;584:14-20. https://doi.org/10.1016/j.msea.2013.07.004

[12] Lang F, Huang F, Yue J, Li L, Xu J, Liu J. Hydrogen trapping and hydrogen embrittlement (HE) susceptibility of X70 grade high-strength, acid-resistant, submarine pipeline steel with Mg treatment. Journal of Materials Research and Technology. 2023;24:623-638. https://doi.org/10.1016/J.JMRT.2023.03.011

[13] Li X, Ma X, Zhang J, Akiyama E, Wang Y, Song X. Review of hydrogen embrittlement in metals: hydrogen diffusion, hydrogen characterization, hydrogen embrittlement mechanism and prevention. Acta Metallurgica Sinica (English Letters). 2020;33:759-773. https://doi.org/10.1007/s40195-020-01039-7

[14] Longwic R, Tatarynow D, Kuszneruk M, Wozniak-Borawska G. Preliminary tests of a Diesel engine powered by diesel and hydrogen. Combustion Engines. 2023;195(4):35-39. https://doi.org/10.19206/CE-169485

[15] Mamala J, Graba M, Mitrovic J, Prażnowski K, Stasiak P. Analysis of speed limit and energy consumption in electric vehicles. Combustion Engines. 2023;195(4):83-89. https://doi.org/10.19206/CE-169370

[16] Matsuo T, Yamabe J, Matsuoka S. Effects of hydrogen on tensile properties and fracture surface morphologies of type 316L stainless steel. Int J Hydrogen Energy. 2014;39(7):3542-3551. https://doi.org/10.1016/j.ijhydene.2013.12.099

[17] Nicho K, Yokoyama K. Marked degradation of tensile properties induced by plastic deformation after interactions between strain-induced martensite transformation and hydrogen for type 316L stainless steel. Metals. 2020;10(7):928. https://doi.org/10.3390/met10070928

[18] Rieck RM, Atrens A, Smith IO. Stress corrosion cracking and hydrogen embrittlement of cold worked AISI type 304 austenitic stainless steel in mode I and mode III. Materials Science and Technology. 1986;2(10):1066-1073. https://doi.org/10.1179/mst.1986.2.10.1066

[19] Saborío-González M, Rojas-Hernández I. Review: hydrogen embrittlement of metals and alloys in combustion engines. Revista Tecnología en Marcha. 2018;31(2). https://doi.org/10.18845/tm.v31i2.3620

[20] Safyari M, Khossossi N, Meisel T, Dey P, Prohaska T, Moshtaghi M. New insights into hydrogen trapping and embrittlement in high strength aluminum alloys. Corros Sci. 2023;223:111453. https://doi.org/10.1016/J.CORSCI.2023.111453

[21] Tomaszewski S, Grygier D, Dziubek M. Assessment of engine valve materials. Combustion Engines. 2023;194(3):48-51. https://doi.org/10.19206/CE-166569

[22] Toribio J, Lorenzo M, Aguado L. Innovative design of residual stress and strain distributions for analyzing the hydrogen embrittlement phenomenon in metallic materials. Materials. 2022;15(24):9063. https://doi.org/10.3390/ma15249063

[23] Verhelst S, Wallner T. Hydrogen-fueled internal combustion engines. Progress in Energy and Combustion Science. 2009;35(6):490-527. https://doi.org/10.1016/j.pecs.2009.08.001

[24] Wang L, Fang X, Wang J, Zhang Z. The precipitation control of grain boundary M23C6 phases and the ductility improvement in aged 22Cr-25Ni-WCuNbN austenitic stainless steel by Co addition. Mater Lett. 2020;264:127348. https://doi.org/10.1016/j.matlet.2020.127348

[25] Wang Y, Wang X, Gong J, Shen L, Dong W. Hydrogen embrittlement of catholically hydrogen-precharged 304L austenitic stainless steel: effect of plastic pre-strain. Int J Hydrogen Energy. 2014;39(25):13909-13918. https://doi.org/10.1016/j.ijhydene.2014.04.122

[26] Wu X, Zhang H, Yang M, Jia W, Qiu Y, Lan L. From the perspective of new technology of blending hydrogen into natural gas pipelines transmission: mechanism, experimental study, and suggestions for further work of hydrogen embrittlement in high-strength pipeline steels. Int J Hydrogen Energ. 2022;47(12):8071-8090. https://doi.org/10.1016/j.ijhydene.2021.12.108

[27] Xue J, Wu H, Zhou C, Zhang Y, He M, Yan X et al. Effect of heat input on hydrogen embrittlement of TIG welded 304 austenitic stainless steel. Metals. 2022;12(11):1943. https://doi.org/10.3390/met12111943

[28] Ye F, Zhu T, Mori K, Xu Q, Song Y, Wang Q et al. Effects of dislocations and hydrogen concentration on hydrogen embrittlement of austenitic 316 stainless steels. J Alloys Compd. 2021;876:160134. https://doi.org/10.1016/j.jallcom.2021.160134

Malgorzata Rutkowska-Gorczyca, DEng. – Faculty of Mechanical Engineering, Wroclaw University of Science and Technology. Poland.
e-mail: *malgorzata.rutkowska-gorczyca@pwr.edu.pl*

Mateusz Dziubek, MEng. – Faculty of Mechanical Engineering, Wroclaw University of Science and Technology. Poland.
e-mail: *mateusz.dziubek@pwr.edu.pl*

Marcin Wiśniewski, Eng. – student research group of Materials Science, Mechanical Engineering, Wroclaw University of Science and Technology, Poland.
e-mail: *255206@student.pwr.edu.pl*

Article citation info:
Rybak A, Hunicz J, Szpica D, Mikulski M, Gęca M, Woś P. Comparative analysis of waste-derived pyrolytic fuels applied in a contemporary compression ignition engine. Combustion Engines. 2024;198(3):74-81. https://doi.org/10.19206/CE-186697

Arkadiusz RYBAK
Jacek HUNICZ
Dariusz SZPICA
Maciej MIKULSKI
Michał GĘCA
Paweł WOŚ

Combustion Engines
Polish Scientific Society of Combustion Engines

Comparative analysis of waste-derived pyrolytic fuels applied in a contemporary compression ignition engine

ARTICLE INFO

Received: 10 November 2023
Revised: 8 January 2024
Accepted: 2 April 2024
Available online: 27 June 2024

The outcomes of research regarding pyrolysis oils obtained from waste sources (WPO) used to power a compression-ignition engine have been presented in this paper. Oils obtained in an industrial process based on polypropylene (PPO), polystyrene (PSO) and used car tires (TPO) were used. Prior to conducting engine tests, a in-depth examination of the tested fuels parameters was undertaken. An advanced single-cylinder research engine utilizing split fuel injection technique was used for the tests. Emission analysis was performed using multi-compound FTIR analytical system. The WPO were blended with diesel fuel in proportions of 20%, on the mass basis and tested at middle engine load and variable EGR rates. Tests have shown that modern combustion systems compliant with the Tier 4/Stage IV standard with multi-pulse injection can handle fuels with a WPO content of 20% without the need for recalibration. The addition of PPO did not significantly affect the emission, while mixing with PSO resulted in elevated levels of hydrocarbon and carbon monoxide emissions. Regarding to the mixture with TPO, increased levels of particulate matter, sulfur oxides, aromatic compounds and formic acid were observed.

Key words: *waste, pyrolysis oil, fuel blending, diesel engine combustion, exhaust*

1. Introduction

Worldwide economic growth led to a significant rise in the demand for energy resources. Among these resources, petroleum products continue to play a pivotal role, serving as the primary source of propulsion in the ever-expanding transportation sector [7]. As a result of ongoing electrification, a slight decrease in gasoline consumption is estimated, while the consumption of diesel fuel (DF) increases [3]. The continuing interest in compression-ignition engines results primarily from the fact that they are used in the long-distance heavy transport sector, maritime transport, and off-road applications. The specificity of these sectors significantly limits their electrification, while the development of diesel engine technology has allowed them to consolidate their position. All forecasts indicate that in the foreseeable future, combustion engines will remain the main driving force in the transport sector [6].

The aspirations to meet the global warming targets outlined in the 2015 Paris Agreement are driving the expansion of the renewable energy sector. Renewable fuels are estimated to contribute about 15% of primary energy production by 2040 [7]. Nevertheless, the same projections suggest that this will only suffice to meet half of the rising energy demand. It is therefore reasonable to intensify research in the area of fuels from renewable sources. Currently, two varieties of renewable diesel, fatty acid methyl esters (FAME) and hydrotreated vegetable oil (HVO), present a high level of technological feasibility, allowing production on an industrial scale. However, some specific properties make it difficult to use mentioned fuels independently to power an internal combustion engine [22]. While their use in a mixture with conventional DF is possible to a limited extent. A significant disadvantage for both FAME and HVO, in the case of first generation fuels, is the necessity to compete for raw material with the food industry [26].

The solution to the above issues is the introduction of feedstock diversification in the production of alternative fuels. To ensure continuity and profitability of production, the raw material should be easily available in large quantities and affordable. An example of such raw material are the end-of-life tires (ELT) [20]. Approximately seventeen million tons of them is produced worldwide annually [21]. ELTs are characterized by huge availability [24], but from the waste management side it is a cumbersome raw material, difficult to store and process [26]. Among the available ELT recycling technologies, pyrolysis process deserves special attention.

Pyrolysis is a technology that perfectly fits into the strategy of sustainable development. The process encompasses the thermal decomposition of solids within an environment devoid of oxygen [2]. It allows simultaneous synthesis of both synthetic and biological materials [9]. It provides a waste management possibility that is unavailable to other recycling methods. Referring to recent studies [10], the tire pyrolysis process is divided into four stages depending on the temperature.

The process parameters and reactor type are selected to maximize the yield of the desired fraction. Regardless of them we get rid of problematic waste and obtain (33–39%) weight char, (34–55%) weight oil, and pyrolytic gases [8, 25]. The high calorific value of pyrolysis gases, reaching approximately 30–40 MJ/kg, enable the execution of the pyrolysis process, making it self-sufficient [5, 8].

Obtained oil, called tire pyrolysis oil (TPO) is dark brown fluid exhibiting properties akin to diesel oil and gasoline [4, 18].

Nevertheless, this prospective fuel possesses several characteristics that hinder its direct utilization in an internal combustion engine. The sulphur content is considerably higher compared to DF [17]. Raw TPO contains it from 0.55 to 3.95% [11]. The presence of heteroatomic molecules and the elevated concentration of aromatic compounds are deemed unacceptable considering environmental protection and necessitate the refinement of the fuel.

Another example of waste materials, suitable for the pyrolysis, which do not contain sulphur are plastics. It is worth emphasizing that the stream of waste generated in Poland and in the world has remained at a constant level for many years. In Europe, collect of the post-consumer plastic waste amounted to 27.3 million tonnes in the year 2016 [14]. This allows to treated plastic waste as a continuous source of energy that can be used in fuels' production. Analysis of the morphology of mixed plastic waste indicates the following percentage distribution of different types of plastics in the overall waste composition: polyethylene terephthalate (PET): 25%, polymer films: 19%, polypropylene (PP): 11%, high-density polyethylene (HDPE): 8%, polystyrene (PS): 4%, other types of plastics: 3% [19].

The advantage of plastic waste is its high amount of energy, confirmed by the elevated value of the heat of combustion. The main thermochemical methods used during waste conversion include gasification, pyrolysis, and combustion. The latest research of Szwaja et al. [23] confirmed high combustion process similarity between conventional DF and pyrolytic oils. However, pyrolysis allows the production of a liquid fraction with properties similar to conventional fuel used today [1]. The pyrolytic oils from plastic feedstock have already been thoroughly researched in terms of processing technologies and fuel properties; however, feasibility tests in compression ignition engines are scarce, especially if modern engine platforms are considered.

Even partial substitution of fossils with waste pyrolytic oils (WPO) may turn out beneficial considering factors such as depletion of fossil fuel reserves, and overall emissions in the well-to-wheel approach (even considering elevated tailpipe emissions). Reasonable waste disposal may give additional value to the entire process.

Given that researchers employed diverse engines and various pyrolysis oils, comparing the results becomes challenging. Nevertheless, some overall picture of the WPOs as diesel engine fuels appear based on the available studies. When compared to diesel, most of the WPOs exhibit lower cetane numbers and higher amounts of unsaturated hydrocarbons. It can have a detrimental impact on exhaust emissions and decrease engine thermal efficiency [16]. Hence, in the majority of studies, a combination of pyrolytic oil and diesel fuel blends was utilized [16].

The above introduction clearly outlines the significant potential of WPO fuels. Nevertheless, an extensive literature review by Mikulski et al. [15] clearly revealed knowledge gaps regarding the use of them. This study aims to presenting a thorough comparative analysis of the most popular WPO varieties. The WPO used in this study was obtained through a process optimized specifically for engine fuel applications. To enhance our understanding of the combustion process, the study determined the key physicochemical parameters of the obtained fuels. Engine tests were conducted using a cutting-edge testing platform, with consistent testing procedures applied to each fuel. The outcomes of this research offer valuable and unprecedented comparative data, guiding future investigations into the potential of WPO fuels.

2. Materials and methods

2.1. Pyrolysis oils used in the experiment

The research involved pyrolysis oils derived from two distinct input materials: used tires and plastic.

The TPO was obtained through an industrial process in which the reactor was fed with used tires without any preprocessing. In contrast, the plastic pyrolysis oil was produced from a homogeneous material on a laboratory scale. Specifically, commercial granulated polypropylene (PP) and polystyrene (PS) with granulation of 2 × 4 mm were used as the input materials. The acquired oils underwent a two-step filtration process, involving a Buchner funnel with a 13 mm mesh on the fine-filter side. Process of obtaining the tested oils has been extensively discussed in another work by Januszewicz et al. [12].

The derived oils underwent both physical and chemical analysis. The gas chromatography and mass spectrometry (GC-MS) technique was employed to ascertain the detailed molecular structure of them. In the authors' previous research can be found a detailed description of fuel testing methods, for TPO [16] and for plastic pyrolysis oils [12]. The key properties of the examined fuels were collected in Table 1.

Table 1. Physical and chemical parameters of the fuels

Parameter	DF	TPO	PPO	PSO
Density @ 15°C [kg/m^3]	826	948	776	942
Viscosity @ 40 °C [mm^2/s]	2.3	3.7	1.69	1.22
Flashpoint [°C]	61	90	< 24	34
Sulphur content [mg/kg]	6.1	5000	–	–
Water content [mg/kg]	11	410	–	–
Higher heating value [MJ/kg]	44.8	44.7	44.7	40.5
Cetane number	55.3	22.3	27.5	–

Many of the mentioned properties indicate the necessity of blending WPO and DF. It is undertaken to guarantee the secure and efficient working of the engine when using pyrolysis oils. Consequently, a decision was made to create mixtures consisting of pyrolysis oil in 20% proportions, combined with the suitable quantities of EN 590:2004/ASTM D975-compliant automotive diesel without any bio components. The formulation of these blends was determined by the mass ratios of the individual components. The crude TPO underwent distillation due to its elevated viscosity and low flashpoint. Further research was conducted on the fraction obtained within the temperature range of 330–375°C, designated as TPO F4.

The mixtures of TPO F4 and DF were labelled as TPO. A similar naming convention was applied to label the mixtures of polypropylene oil (PPO) and polystyrene oil (PSO) with DF.

2.2. Research engine test stand

The experimental work encompassed a comprehensive analysis of an engine operation at Lublin University of Technology. The research focused on an advanced single-cylinder AVL 5402 research engine, as detailed in Table 2.

Table 2. Research engine specifications

Type	AVL 5402
Configuration	four-stroke, single-cylinder
Bore/stroke	85/90 mm
Displacement	510.5 cm^3
Compression ratio	17:1
Swirl ratio	1.7:1
Combustion chamber	Mexican hat, toroidal type
Injection system	CR, Bosch CP4.1; 180 MPa; multi-pulse capability
Intake path	Electrically driven Eaton M45 compressor; with thermal management
EGR system	high-pressure, with thermal management
Engine management	AVL-RPEMS, ETK7-Bosch
IVO/IVC	712/226 CAD
EVO/EVC	488/018 CAD

In order to replicate real operating conditions, the AVL asynchronous motor dynamometer with speed control was connected to the engine. Figure 1 illustrates the test stand setup.

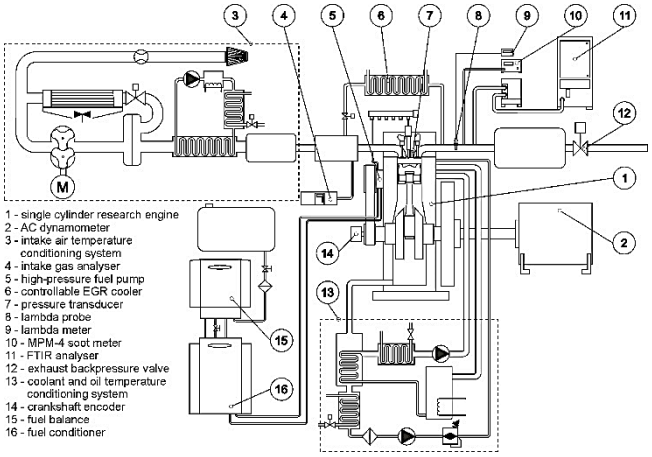

Fig. 1. Diagram of the engine test bench

The combustion system featured a four-valve head and a toroidal in-piston combustion chamber. To condition the fuel, the AVL 753C temperature conditioner and AVL 733 S dynamic fuel meter were employed. Fuel was introduced into the combustion chamber through a Bosch CP 4.1 high-pressure pump, employing a seven-hole electromagnetic injector featuring a 145° spray angle. The injection parameters were managed through ETAS INCA software and a fully open Bosch controller.

Electrically powered Roots compressor Eaton M45 supplied the high pressure. A proprietary thermal conditioning system was implemented to sustain consistent temperatures for coolant, lubricant, and charge air, with an accuracy level within ±0.5°C.

In order to evaluate the excess air ratio and account for compensation of the pressure, as discussed in reference [16], the experiment employed a Bosch LSU 4.2 lambda probe and an ETAS LA4 lambda meter.

The concentrations of 23 exhaust gas components, both regulated and non-regulated, were monitored using an AVL FTIR multi-component analytical system. Additionally, particulate concentration was measured by a Maha MPM-4 analyzer.

For combustion analysis, an AVL GU22C piezoelectric pressure transducer was installed directly in the engine head. The initiation of the pressure signal recording was carried out by an optical encoder, ensuring a consistent angular resolution 0.1 CAD.

2.3. Research engine matrix

The research was performed at a single operating point, at IMEP set at 0.5 MPa, and at a constant engine speed of 1500 rpm. This aligns with a specific point in the previous tests, which significantly contributes to the overall emissions. Injection timings (SOI), and the EGR ratio were varied to examine the engine's response to variable control parameters when fueled with WPO in comparison to DF. Four distinct levels of EGR were investigated for each tested SOI.

Experiments were conducted under controlled thermal conditions, with the engine coolant, lubricating oil, and recirculated exhaust gas at the manifold inlet maintained at a temperature of 85°C. The intake air temperature was held constant at 35°C. The final aspirated charge temperature was determined by the enthalpy balance between fresh air and EGR, and was left uncontrolled, typical conditions encountered during standard engine operation. The temperature of the fuel supplied to the high-pressure pump was consistently held at 30°C. The engine calibration was meticulously tailored for the standard diesel fuel, with the primary goal of minimizing overall emissions while preserving a high indicated thermal efficiency. Details regarding the engine calibration for all operating points can be found in Table 3.

Table 3. Engine operating conditions and control parameters.

IMEP [MPa]	0.5				
MAP [MPa]	0.125				
SOI1 [CAD]	336	338	340	342	344
SOI2 [CAD]	350	352	354	356	358
Fuel pressure [MPa]	80				
Pilot fuel quantity [mg]	1.6				

The testing procedure initiated with the reference DF, followed by the blended fuels, each following an identical protocol. To ensure the intended ratios of the tested fuels, the entire fuel system underwent thorough draining and multiple flushing cycles with the chosen fuel during each fuel transition. Each blend underwent three repetitions of the test sequence.

At each engine operating point, once all parameters had stabilized, in-cylinder pressure was meticulously recorded for 100 cycles, and slowly changing data were continuously monitored during the 30-second measurement interval. The presented data represents the mean values derived from three separate engine runs for each testing point. For the reference DF, supplementary measurements were conducted to ascertain the precision of emission measurements.

2.4. Data analysis procedures

The combustion analysis, utilizing the AVL Boost software, relied on in-cylinder pressure data. This analysis incorporated gas-flow models, internal EGR estimation, and the computation of heat transfer through the cylinder walls. The latter was determined utilizing the Hohenberg correlation [13]. The heat release rate (HRR) was determined by analyzing the cylinder pressure using a first-law analysis. The HRR values reported in the paper are gross values, which consider the calculated heat transfer rate (Q_{ht}). The cumulative HRR values were then used as the foundation for computing the mass fraction burned (MFB), which, in turn, facilitated the calculation of combustion timing indicators.

To determine the maximum measurement error for directly measured values, we considered either the standard deviation from three samples or the accuracy of the measuring device, depending on which value was greater. For indirectly calculated values, the measurement error was determined using the partial derivatives method, as outlined by Kline and McClintock [13].

For a more in-depth exploration of uncertainty analysis readers are directed to Mikulski et al. [16].

3. Results

3.1. Analysis of combustion

The impact on the combustion of the examined fuels evaluate with reference to the diesel combustion. Figure 2 show in-cylinder pressures and HRR curves at reference conditions. Figure 3 illustrates HRR curves for WPO blends, with DF as a reference. The figure also demonstrates the combustion response to external EGR.

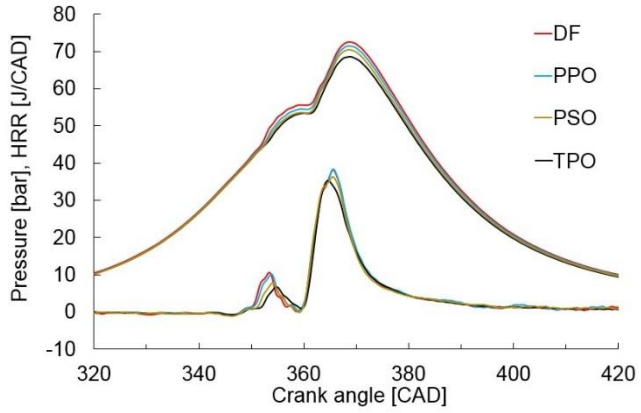

Fig. 2. In-cylinder pressure for all investigated fuels at reference conditions

Figure 2 clearly shows that the addition of WPO at a level of up to 20% does not negatively affect the combustion process. The pressure curves have the shape of a typical diesel combustion characteristic. The intense rate of pressure increase begins at the top dead center (TDC) regardless of the added WPO. After the initial injection of pilot fuel, a minor reduction in HRR occurs due to fuel vaporization. Following this, low-temperature reactions occur, yielding reactive species that do not contribute significantly to heat generation but cause earlier ignition of the pilot fuel spray. The initial prominent peaks observed in the HRR curves stem from the high temperature heat release associated with the predominantly premixed pilot fuel. At 354 CAD, the injection of the main fuel commences. The auto-ignition of the main fuel spray occurs shortly after it enters the heated region of the pilot combustion. When examining the principal HRR peak, one can identify the shift from kinetic to mixing-controlled combustion. This transition occurs at roughly 363 CAD for all cases illustrated in Fig. 2. The final phase, denoted as the afterburning period, commences at 375 CAD, marked by declining (HRR) values, and maintains consistent across for all fuel blends.

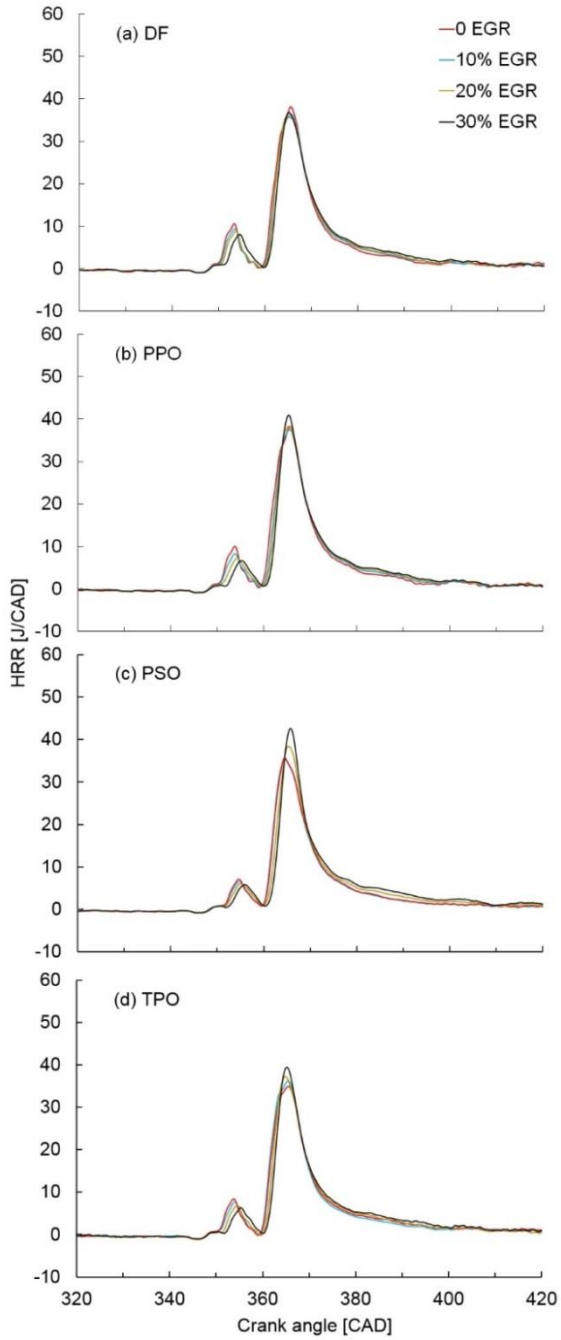

Fig. 3. EGR effects on HRR for tested fuels; 0.5 MPa IMEP, reference SOI

Regardless of the used fuel combustion reaches completion at around 410–420 CAD.

The observed delay in pilot fuel ignition doesn't influence the initiation of main fuel combustion but does result in a somewhat larger amount of unburnt fuel as combustion transitions to the mixing-controlled phase.

The impact of PPO on combustion is negligible compared to the same admixture of TPO or PSO. In the case of TPO, the delay of approximately 3 CAD is due to the much lower cetane number and lower volatility. The most significant influence of the pilot fuel dosage was noted in the case of the PSO combustion process. This is because PPO consists primarily of aromatic hydrocarbons characterized by comparatively low auto-ignition properties.

From Fig. 3, it is clear that the EGR introduction inhibits the premixed combustion of the pilot fuel. The volumetric, kinetic combustion is highly sensitive to the EGR rate, with a proportional delay of approximately 1 crank angle degree for every 10% increase in EGR. This delay results in less fuel being burned before the main fuel injection ignites, which reduces the heat release rate in this stage of combustion. This energy is subsequently discharged during the combustion of the main charge, leading to higher HRR peaks and longer combustion times. This is especially noticeable in the case of TPO combustion.

3.2. Analysis of emissions

As already mentioned, the authors of this work have shown in previous studies that the impact on emissions of DF blends with the addition of WPO up to 20% can be considered negligible in the case of heavy and medium loads. Therefore, in this study, the case of low load is considered. In Fig. 4 were compared, indicated specific emissions of both, regulated and non-regulated exhaust compounds under reference conditions for all tested fuels.

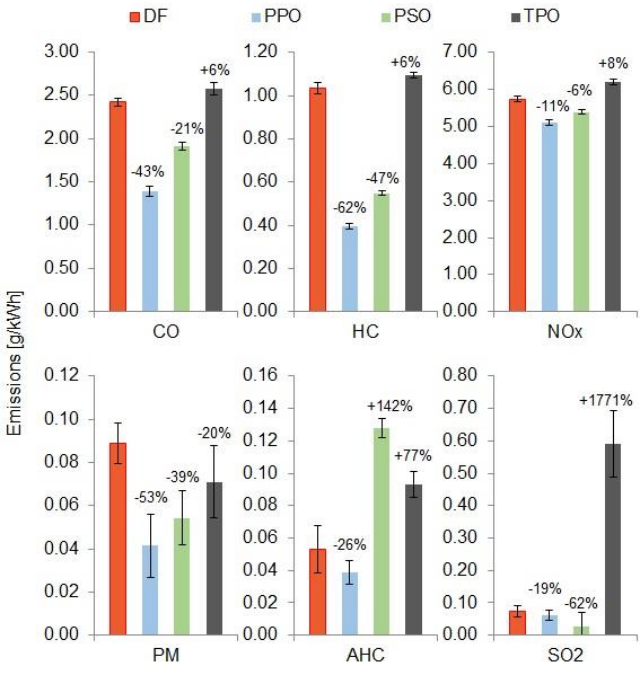

Fig. 4. Indicated specific emissions of regulated and non-regulated exhaust compounds at reference conditions

In this load regime, PPO and PSO samples cause improvement the regulated emissions. The elevated CO levels arise due to the delayed combustion of TPO, extending into the expansion phase and consequently experiencing flame extinction as the piston approaches the opening of the exhaust valve. The rise in NO_x levels for TPO blends is attributed to the CI reduction, causing a shift in combustion to the main high-temperature stage. Increased temperature values during TPO combustion straight result in increased NO_x formation. Considering the measurement uncertainty, the incorporation of a 20% TPO blend does not exhibit any significant impact on particulate matter (PM) emissions.

The exceptionally high emission of aromatic hydrocarbons when using PSO correlates perfectly with the chemical composition of this fuel. PSO contains up to 98% of aromatic compounds.

A similar trend can be observed when using TPO. The high sulfur content in this fuel results in a sharp increase in sulfur dioxide emissions. It should be noted that PPO and PSO fuels do not contain sulfur. The SO_2 emissions recorded during the combustion of these mixtures are solely due to the sulfur contained in the DF. However, the impact of the addition of PPO and PSO is very positive in reducing SO_2 emissions, by 19 and 62%, respectively.

In the ensuing section of the investigation, a PPCI (Partially Premixed Compression Ignition) strategy was employed, using EGR and SOI as parameters to manage emissions, with the goal of achieving a favorable trade-off between NO_x and PM emissions for the various WPO blends tested. The outcomes for PM and NO_x emissions are depicted in Fig. 5 and Fig. 7, showing absolute values for the reference DF fuel. Moreover, for the WPO blends, the differences in PM and NO_x emission values between each specific fuel and DF are illustrated in Fig. 6 and Fig. 8, respectively.

The EGR trade-off between PM and NO_x is evident when comparing the results for the reference fuel DF in Fig. 5 and 7. The minimal PM emissions are attained at lower EGR rates, while the lowest NO_x values occur on the opposite side of the calibration map (note the inverted EGR axis values on Fig. 7).

Significantly, with the utilization of the highest tested EGR rates and advanced SOI, emissions of both NO_x and PM are lower in comparison to DF baseline value for all fuels tested. This combustion regime corresponds to a greater amount of pre-mixing. For the SOI advanced by 4 CAD and 30% EGR, PSO has the capability to achieve a 0.21 g/kWh reduction of PM emission compared to DF. This effect decreases significantly both by decreasing the amount of EGR and by decreasing the injection timing of the pilot dose. We observe similar trends for each blends, but for the PPO and PSO the gain from ignition advance is much more visible than in the case of TPO. The deterioration of the emission rate on the PM side occurs much earlier in the case of TPO, and further delaying the ignition causes an increase in emissions by 0.27 g/kWh compared to DF.

At the same time, the calibration with the lowest particulate content when operating without EGR is accompanied by the highest NO_x emissions, for PPO and TPO. Interest-

ingly, all tested blends showed an improvement in NO_x emission reduction at the highest EGR.

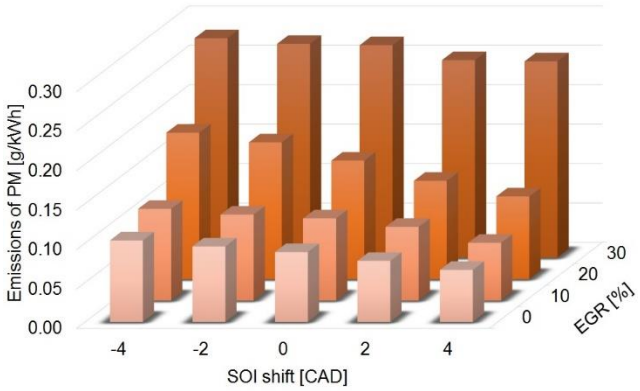

Fig. 5. Indicated specific emissions of PM for DF at variable SOI and EGR rates

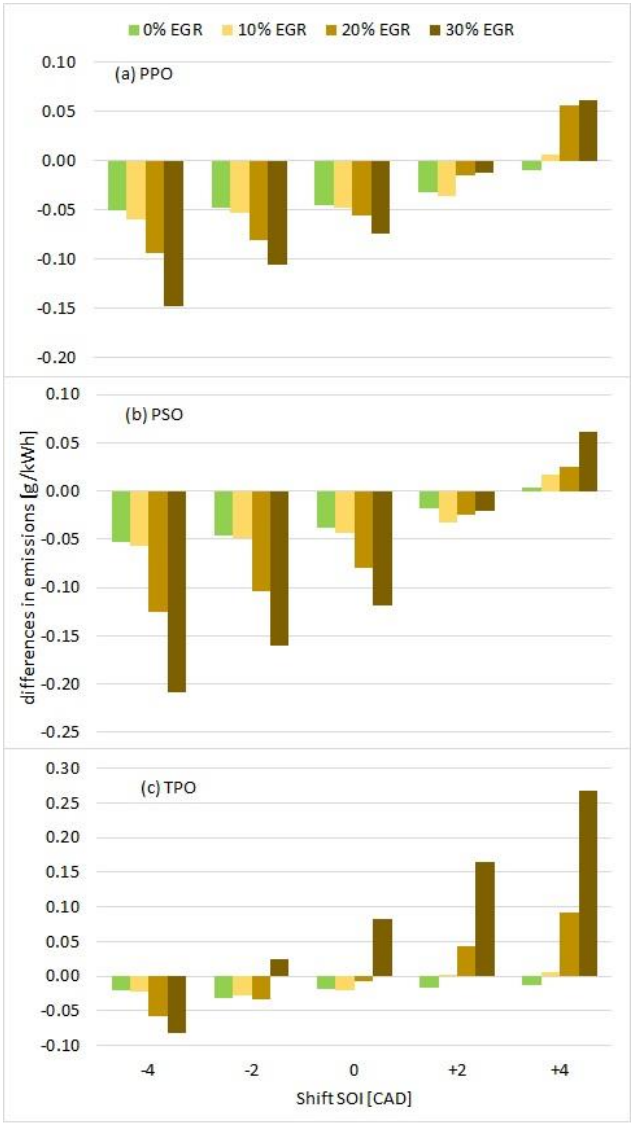

Fig. 6. Differences in PM emissions between DF and tested WPO at variable SOI and EGR rates

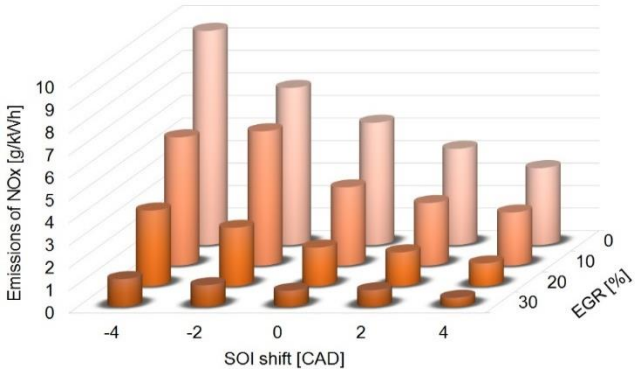

Fig. 7. Indicated specific emissions of NO_x for DF at variable SOI and EGR rates

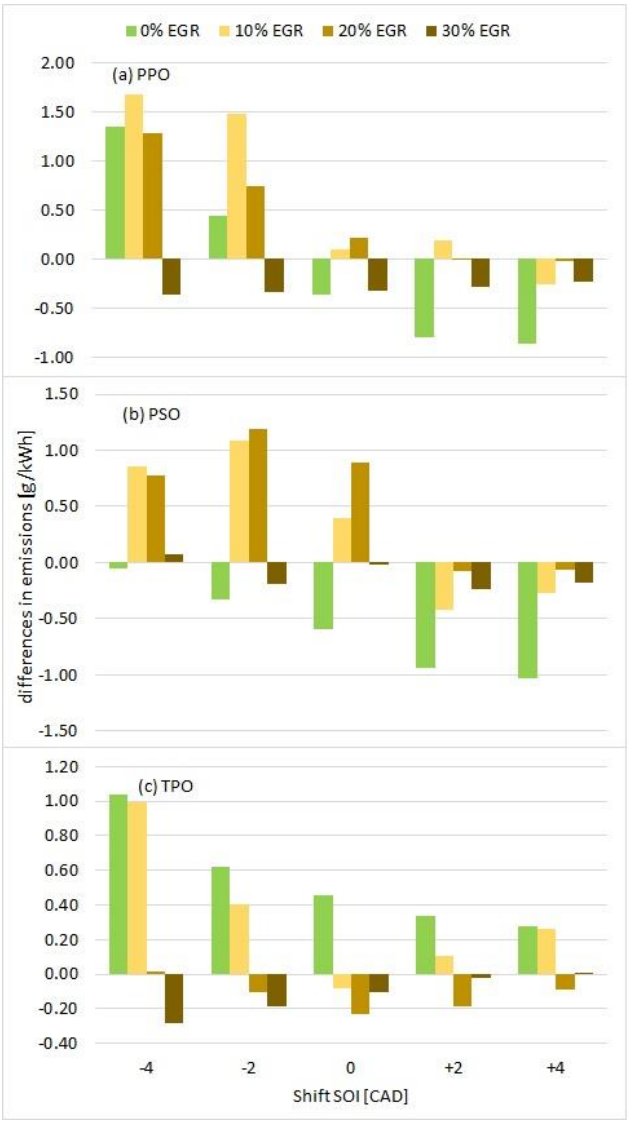

Fig. 8. Differences in NO_x emissions between DF and tested WPO at variable SOI and EGR rates

4. Conclusions

Presented outcomes of thorough comparison of the Common Rail diesel engine operating parameters, were focusing on the use of WPO fuels. The following requests were received:

1. Creating blends of WPO with DF produces fuels that meet stringent fuel standards in all parameters except sulfur content.
2. With split fuel injection, diminished pyrolysis fuels CI is mainly manifested by delayed ignition of the pilot fuel. Introduction of WPO causes a delay in the commencement of combustion by up to 3 CAD.
3. NO_x emissions do not depend on the used fuel blends.
4. The high content of aromatics in PSO causes increased formation of AHC.
5. The high sulfur content in TPO excludes this fuel from direct use in mixtures with DF. Additional desulfurization is necessary after the pyrolysis process.
6. TPO can realize low-temperature combustion, partially pre-mixed, across a broader range of the engine working area. The favorable NO_x/PM level extends to elevated values of EGR and early injection modes due to the prolonged delay of TPO ignition . Its promote the formation of a pre-mixed charge before auto-ignition.
7. PSO can achieve a PM emission reduction of 0.21 g/kWh compared to DF with maintain indicated efficiency target of 42%.
8. The low viscosity of PPO combined with low reactivity causes excessive mixing of the charge in the cylinder before combustion begins. This is manifested by increased CO and HC emissions.

In summary, the obtained results clearly indicate that there are no restrictions on the use of PPO oils in blends with DF. Observed combustion delay can be eliminated by engine calibration. At the same time, limitations were observed in the use of PSO oils due to high aromatic content resulting in high AHC emissions. In the case of TPO oil, its high sulfur content precludes its use as a fuel for road vehicles. However, the path to non-road applications remains open, but requires further research on reducing sulphur compounds.

Acknowledgements

The authors wish to thank AVL List GmbH for making the simulation software available within the AVL University Partnership Program framework.

The research leading to these results has received funding from the commissioned task entitled “VIA CARPATIA Universities of Technology Network named after the President of the Republic of Poland Lech Kaczyński” contract no. MEiN/2022/DPI/2575 action entitled “In the neighborhood – inter-university research internships and study visits.”

Nomenclature

AHC	aromatic hydrocarbon
CI	compression ignition
CO	carbon monoxide
DF	diesel fuel
EGR	exhaust gas recirculation
ELT	end-of-life tires
FAME	fatty acid methyl esters
FTIR	Fourier-transform infrared
HC	hydrocarbon emissions
HRR	heat release rate
HVO	hydrotreated vegetable oil
IMEP	indicated mean effective pressure
MFB	mass fraction burned
NO_x	nitrogen oxides
PM	particulate matter
PP	polypropylene
PPO	polypropylene oil
PS	polystyrene
PSO	polystyrene oil
SO_2	sulfur dioxide
SOI	start of injection
TDC	top dead center
TPO	tire pyrolysis oil
WPO	waste pyrolytic olis

Bibliography

[1] Alawa B, Chakma S. Investigation in compression ignition engine performance using alternative fuels produced from waste packaging materials. Resour Conserv Recy Adv. 2022;14:200075. https://doi.org/10.1016/j.rcradv.2022.200075

[2] Aydin H, Ilkiliç C. Optimization of fuel production from waste vehicle tires by pyrolysis and resembling to diesel fuel by various desulfurization methods. Fuel. 2012;102:605-612. https://doi.org/10.1016/j.fuel.2012.06.067

[3] Bae C, Kim J. Alternative fuels for internal combustion engines. P Combust Inst. 2017;36(3):3389-3413. https://doi.org/10.1016/j.proci.2016.09.009

[4] Cunliffe AM, Williams PT. Composition of oils derived from the batch pyrolysis of tyres. J Anal Appl Pyrol. 1998; 44(2):131-152. https://doi.org/10.1016/S0165-2370(97)00085-5

[5] Czajczyńska D, Krzyżańska R, Jouhara H, Spencer N. Use of pyrolytic gas from waste tire as a fuel: a review. Energy. 2017;134:1121-1131. https://doi.org/10.1016/j.energy.2017.05.042

[6] Energy demand: three drivers | ExxonMobil. https://corporate.exxonmobil.com (accessed on Jan. 06, 2022).

[7] Energy Outlook 2020 edition. https://www.bp.com (accessed on Jan. 06, 2022).

[8] González JF, Encinar JM, Canito JL, Rodríguez JJ. Pyrolysis of automobile tyre waste. Influence of operating variables and kinetics study. J Anal Appl Pyrol. 2001;58-59(59): 667-683. https://doi.org/10.1016/S0165-2370(00)00201-1

[9] Grigiante M, Ischia M, Baratieri M, Dal Maschio R, Ragazzi M. Pyrolysis analysis and solid residue stabilization of polymers, waste tyres, spruce sawdust and sewage sludge. Waste Biomass Valor. 2010;1:381-393. https://doi.org/10.1007/s12649-010-9038-2

[10] Han J, Li W, Liu D, Qin L, Chen W, Xing F. Pyrolysis characteristic and mechanism of waste tyre: a thermogravimetry-mass spectrometry analysis. J Anal Appl Pyrol. 2018;129:1-5. https://doi.org/10.1016/j.jaap.2017.12.016

[11] Ilkiliç C, Aydin H. Fuel production from waste vehicle tires by catalytic pyrolysis and its application in a diesel engine. Fuel Process Technol. 2011;92(5):1129-1135. https://doi.org/10.1016/j.fuproc.2011.01.009
[12] Januszewicz K, Hunicz J, Kazimierski P, Rybak A, Suchocki T, Duda K et al. experimental assessment on a diesel engine powered by blends of waste-plastic-derived pyrolysis oil with diesel. Energy. 2023;281:128330. https://doi.org/10.1016/j.energy.2023.128330
[13] Kline S, McClintock F. Describing uncertainty in single sample experiments. Mech Engineering. 1953;75:3-8.
[14] Mangesh VL, Padmanabhan S, Tamizhdurai P, Ramesh A. Experimental investigation to identify the type of waste plastic pyrolysis oil suitable for conversion to diesel engine fuel. J Clean Prod. 2020;246:119066. https://doi.org/10.1016/j.jclepro.2019.119066
[15] Mikulski M, Ambrosewicz-Walacik M, Hunicz J, Nitkiewicz S. Combustion engine applications of waste tyre pyrolytic oil. Prog Energ Combust. 2021;85:100915. https://doi.org/10.1016/j.pecs.2021.100915
[16] Mikulski M, Hunicz J, Duda K, Kazimierski P, Suchocki T, Rybak A. Tyre pyrolytic oil fuel blends in a modern compression ignition engine: a comprehensive combustion and emissions analysis. Fuel. 2022;320:123869. https://doi.org/10.1016/j.fuel.2022.123869
[17] Murugan S, Ramaswamy MC, Nagarajan G. A comparative study on the performance, emission and combustion studies of a DI diesel engine using distilled tyre pyrolysis oil-diesel blends. Fuel. 2008;87(10-11):2111-2121. https://doi.org/10.1016/j.fuel.2008.01.008
[18] Pakdel H, Pantea DM, Roy C. Production of dl-limonene by vacuum pyrolysis of used tires. J Anal Appl Pyrol. 2001; 57(1):91-107. https://doi.org/10.1016/S0165-2370(00)00136-4
[19] Roosen M, Mys N, Kusenberg M, Billen P, Dumoulin A, Dewulf J et al. Detailed analysis of the composition of selected plastic packaging waste products and its implications for mechanical and thermochemical recycling. Environ Sci Technol. 2020;54(20):13282-13293. https://doi.org/10.1021/acs.est.0c03371
[20] Sienkiewicz M, Janik H, Borzędowska-Labuda K, Kucińska-Lipka J. Environmentally friendly polymer-rubber composites obtained from waste tyres: a review. J Clean Prod. 2017;147:560-571. https://doi.org/10.1016/j.jclepro.2017.01.121
[21] Sienkiewicz M, Kucinska-Lipka J, Janik H, Balas A. Progress in used tyres management in the European Union: a review. Waste Manage. 2012;32(10):1742-1751. https://doi.org/10.1016/j.wasman.2012.05.010
[22] Sikora M, Orliński P. Hydrotreated vegetable oil fuel within the Fit for 55 package. Combustion Engines. 2023. https://doi.org/10.19206/CE-174554
[23] Szwaja M, Szymanek A. Combustion comparative analysis of pyrolysis oil and diesel fuel under constant-volume conditions. Combustion Engines. 2023;195(4):90-96. https://doi.org/10.19206/CE-169805
[24] Torretta V, Rada EC, Ragazzi M, Trulli E, Istrate IA, Cioca LI. Treatment and disposal of tyres: two EU approaches. A review. Waste Manage. 2015;45:152-160. https://doi.org/10.1016/j.wasman.2015.04.018
[25] Yaqoob H, Teoh YH, Jamil MA, Gulzar M. Potential of tire pyrolysis oil as an alternate fuel for diesel engines: a review. J Energy Inst. 2021;96:205-221. https://doi.org/10.1016/j.joei.2021.03.002
[26] Zhang Z, Lohr L, Escalante C, Wetzstein M. Food versus fuel: what do prices tell us? Energ Policy. 2010;38(1):445-451. https://doi.org/10.1016/j.enpol.2009.09.034

Arkadiusz Rybak, MEng. – Faculty of Mechanical Engineering, Lublin University of Technology, Poland.
e-mail: *a.rybak@pollub.pl*

Prof. Jacek Hunicz, DSc., DEng. – Faculty of Mechanical Engineering, Lublin University of Technology, Poland.
e-mail: *j.hunicz@pollub.pl*

Dariusz Szpica, DSc., DEng. – Faculty of Mechanical Engineering, Bialystok University of Technology, Poland.
e-mail: *d.szpica@.pb.edu.pl*

Prof. Maciej Mikulski, DEng. – School of Technology and Innovations, University of Vaasa, Finland.
e-mail: *maciej.mikulski@uwasa .fi*

Michał S. Gęca, DSc., DEng. – Faculty of Mechanical Engineering, Lublin University of Technology, Poland.
e-mail: *michal.geca@pollub.pl*

Paweł Woś, DSc., DEng. – Faculty of Mechanical Engineering and Aeronautics, Rzeszów University of Technology, Poland.
e-mail: *pawel.wos@prz.edu.pl*

Article citation info:
Szymański GM, Waligórski M, Misztal W. Assessment of the effectiveness of mounting the aircraft piston combustion engine on a test stand. Combustion Engines. 2024;198(3):82-92. https://doi.org/10.19206/CE-186702

Grzegorz M. SZYMAŃSKI
Marek WALIGÓRSKI
Wojciech MISZTAL

Combustion Engines
Polish Scientific Society of Combustion Engines

Assessment of the effectiveness of mounting the aircraft piston combustion engine on a test stand

ARTICLE INFO

Received: 11 December 2023
Revised: 2 April 2024
Accepted: 2 April 2024
Available online: 18 June 2024

The subject of the considerations described in the paper is the problem of the efficiency of mounting an aircraft engine on a dyno test bench. The paper presents the empirical research results of vibroacoustic signal application to the evaluation of the correctness of positioning of the Rotax 912 piston aircraft engine. The variability of selected parameters and vibroacoustic characteristics for real engine operating conditions was assessed, and functional relations and their discrete representations were developed, reflecting the efficiency of mounting the object on the frame. Thanks to this process, quantitative measures of the diagnostic assessment of the object were obtained, which can be used in periodic or continuous operational control of the object.

Key words: *aircraft engine, vibration isolation, mounting efficiency, empirical research, vibration accelerations-velocities-displacements*

1. Introduction

Empirical research on systems in which thermodynamic processes are carried out, characterized by high dynamics of changes in parameters and indicators of their operation, is conducted based on the assumptions of obtaining the most reliable measures and characteristics defining them [1, 4, 8]. Their purpose is not only the ongoing assessment of the quality of main processes, which is based on the analysis of the overall efficiency of the facility for specific operating conditions but also the process of generating and forecasting changes in operational characteristics with the time and intensity of use of the object in stationary and non-stationary conditions [22, 27, 28]. Thanks to this, it is possible to fill the multidimensional working space of the object with the representation of processes of a specific nature and properties observed there. The result is a more complete description of the mathematical behavior of the machine in real conditions of its operation, including conditions of conscious modification within the parameters of the system state vector, a control vector or an operational vector.

Regardless of the research objectives and evaluation criteria as well as limiting conditions (internal and external), the primary action of the scientific approach to research on modern systems is to ensure the most faithful representation of the course of dynamic processes in operating and accompanying parameters, such as in the case of mapping: rotational speed or valve clearance of the engine in its vibration equivalent [2, 7], identification of specific vibration parameters during the process of transporting ingredients of the feeding process [14] or bearing lubrication conditions [15], assessment of thermodynamic processes occurring in turbojet or piston engines [29, 33], the impact of a specific fuel on the efficiency of the combustion process and emissions of harmful exhaust gas components [18–20, 36]. This is particularly important in the case of diagnosis using vibroacoustic processes, which may have different partial goals and application areas, such as: searching for the most effective method of reducing the number of parameters used to evaluate [23], using vibrations to assess the operation of multi-stage wind turbine gearboxes [24, 35], methodology for research process depending on the type of process and its nature [26], taking into account safety criteria in the diagnostic assessment [30], using the process of optimizing structures and systems with high dynamics of changes in thermodynamic processes [37]. The active value of the measurement signal and its effectiveness in describing the observed partial process is also dependent on the quality of mounting the engine on the test stand, the issue of which is very important and its importance is greater the more complex the structure of the object and the correlation between its various parameters are.

In order to reduce vibration amplitudes in technical facilities where dynamic processes are carried out, it is necessary to use appropriate methods to reduce their movement between the source of vibrations and the object absorbing vibroacoustic energy [9]. For this purpose, an intermediate element or system is used, thanks to which the value of the above energy is reduced or even the value of the vibration amplitude is completely dampened (a vibration isolator). The phenomenon of decreasing the amplitude of vibrations when passing from their source to the receiver is called vibroisolation. In the case of modeling mechanical systems in which a vibration isolator is used, their linearity (the superposition of effects) and stationarity are assumed, and the interactions between them are treated as determined or stationary random processes. Thanks to this, the analysis of excitations and their mathematical description can be carried out using frequency analyzes and in the field of system properties (transmittances as system characteristics regarding a susceptibility). In reality, the connections between the source, the vibroisolator and the receiver of vibroacoustic energy are multi-point or surface (modeling of extended finite systems or discrete matrix models). Minimization of vibration amplitudes can be achieved by separating dynamic forces from the isolated area (force vibration isolation), or by

reducing dynamic displacements of the vibration-sensitive system (displacement vibration isolation) [5, 16, 17].

An object generating mechanical vibrations is a source of dynamic force from the process occurring within it. This machine is placed on a supporting structure. If its vibrations exceed the permissible values, the source of these exceedances is too high a resultant dynamic force is transferred from the machine to the supporting frame and inappropriate selection of the properties of the subsystems (a source, a vibration isolator, a vibration receiver). In order to reduce the force transmitted to the frame of the supporting structure, the dynamic system should be compared without and with a vibroisolator, using the appropriate susceptibility matrices α^0 i α (after applying the insulation, Fig. 1).

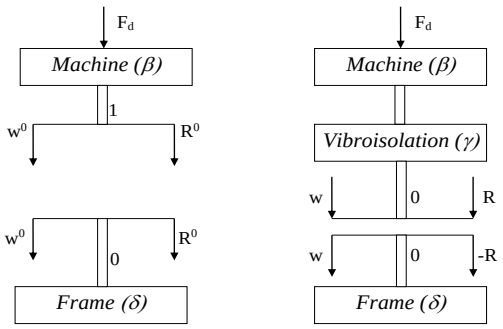

Fig. 1. General diagram of the definition of force vibration isolation [5]

The effectiveness of vibration isolation can be defined by the following equation [5, 16]:

$$E_{WI} = \left|\frac{R^0}{R}\right| = \left|\frac{w^0}{w}\right| > 1 \tag{1}$$

where: R^0 – force transmitted to the supporting structure for the system without a vibration isolator, R – force transferred to the supporting structure for the system with a vibroisolator (value after passing through the isolator), w^0 – displacement for a system without a vibration isolator, w – displacement for a system with a vibroisolator (after passing through the vibroisolator).

If the displacements from eq. (1) are expressed by the susceptibility as the amplitude of the response to the unit harmonic excitation at point i, measured at point j as [5]:

$$w^0 = -\delta_{00}R^0 \tag{2}$$

$$w = -\delta_{00}R \tag{3}$$

where: δ_{00} – susceptibility of the frame structure at the point of contact with the insulator
then the following relationship is obtained after taking into account the properties of the systems, in accordance with the susceptibility method:

$$w^0 = \alpha_{k0}^0 F_d = \frac{\delta_{00}\beta_{k1}}{\beta_{11}+\delta_{00}} F_d \tag{4}$$

$$w = \alpha_{k0} F_d = \frac{\gamma_{10}\delta_{00}\beta_{k1}}{(\delta_{00}+\gamma_{00})(\beta_{11}+\gamma_{11})-\gamma_{10}^2} F_d \tag{5}$$

where: α^0 – susceptibility matrix for a system without vibration isolation, α – susceptibility matrix for a system with vibration isolation, F_d – value of the force from the source of excitation, γ_{00}, γ_{11}, γ_{10} – susceptibility of the machine and the foundation (a primary connection), and on the direct and cross-impact susceptibility of the isolator, β – machine susceptibility for a specified side.

By transforming equations (4) and (5), the final dependency on the effectiveness of vibration isolation is obtained in the form [5]:

$$E_{WI} = \left|\frac{\alpha_{k0}^0}{\alpha_{k0}}\right| = \left|\frac{(\delta_{00}+\gamma_{00})(\beta_{11}+\gamma_{11})-\gamma_{10}^2}{(\beta_{11}+\delta_{00})\gamma_{10}}\right|, \tag{6}$$

The assessment of the effectiveness of vibration isolation depends on the susceptibility of the machine and the foundation (a primary connection) and on the direct and cross-impact susceptibility of the isolator γ_{00}, γ_{11}, γ_{10}.

In the case of displacement vibration isolation (Fig. 2), the goal is to provide vibration protection to a system with a susceptibility matrix β located on a foundation with properties δ. The source of forcing F_d determines the vibrations of the foundation, and the effectiveness of their isolation is equal to [5]:

$$E_z = \left|\frac{z}{w}\right| = \left|\frac{\alpha_{k0}^0}{\alpha_{k0}}\right| > 1 \tag{7}$$

where: z – displacement for a system without a vibration isolator, w – displacement for a system with a vibration isolator (before the isolator).

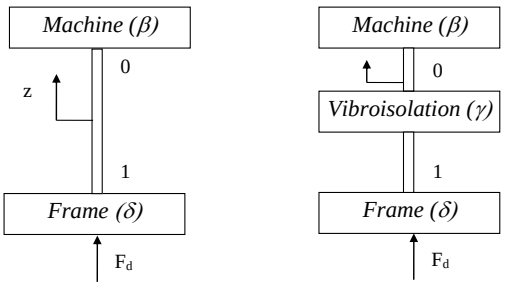

Fig. 2. Diagram of displacement vibration isolation definition [5]

Analysis using the susceptibility method allows obtaining the appropriate value for the primary system and the system with a vibroisolator:

$$\alpha_{k0}^0 = \frac{\beta_{11}\delta_{k0}}{\delta_{00}+\beta_{11}} \tag{8}$$

$$\alpha_{k0} = \frac{\beta_{11}\delta_{k0}\gamma_{10}}{(\beta_{11}+\gamma_{11})(\delta_{00}+\gamma_{00})-\gamma_{10}^2} \tag{9}$$

Substituting the above equations into the formula (7), the equation for the effectiveness of a displacement vibration isolation is given as [5]:

$$E_z = \left|\frac{z}{w}\right| = \left|\frac{\alpha_{k0}^0}{\alpha_{k0}}\right| = \left|\frac{(\beta_{11}+\gamma_{11})(\delta_{00}+\gamma_{00})-\gamma_{10}^2}{(\delta_{00}+\beta_{11})\gamma_{10}}\right| \tag{10}$$

The mathematical relationships obtained for the force and displacement vibration isolations are equal. Depending on needs, one can use force or displacement vibration isolation systems. In the case of the force isolation on a rigid foundation, it is equivalent to the displacement isolation for a kinematic forcing. In assessing the effectiveness of a system isolation from mechanical vibrations, the dynamic

properties of the component systems are undoubtedly important. If no external energy is supplied, then these systems have passive elements, which makes the vibration isolator is a symmetrical mechanical system (the susceptibility at the beginning is equal to its value at the end). In the low frequency range, the properties of the vibration isolator are elastic, so the isolation will take place if the susceptibility of the insulator (1/k, where k – isolator stiffness) will be greater than the absolute value of the sum of the susceptibilities of a machine β_{11} and a frame structure δ_{00}. Thanks to this, it is possible to conclude what dynamic characteristics of the machine and foundation should be used in the above assessment. The above parameters can also be obtained based on empirical research.

If the direct susceptibility of the isolator is much greater than that of the machine or a foundation, then [5]:

$$\left|\frac{\delta_{00}}{\gamma_{11}}\right| \ll 1, \left|\frac{\beta_{11}}{\gamma_{11}}\right| \ll 1 \tag{11}$$

and therefore:

$$E = \left|\frac{\gamma_{11}^2-\gamma_{10}^2}{(\beta_{11}+\delta_{00})\gamma_{10}}\right| \gg 1 \tag{12}$$

hence:

$$\left|\frac{\gamma_{11}^2-\gamma_{10}^2}{\gamma_{10}}\right| \gg |(\beta_{11}+\delta_{00})| \tag{13}$$

The conditions defined by the inequalities in (13) are not met if the absolute value of γ_{11} is close to 0. These conditions are met for an elastic isolator, hence the mutual susceptibility γ_{10} is important. In this case, the best vibration isolation is provided by a symmetrical isolator in which $|\gamma_{11}| >> 1$ and $|\gamma_{10}| \approx 0$. The susceptibility of the isolator also depends on the frequency. The above inequality will be fulfilled if the resonance value in the direct susceptibility is significantly greater than the mutual susceptibility. The issues of vibration isolation of systems require further detailed studies and empirical research, especially in the context of the development of materials engineering, regarding e.g.: nanoparticles and composite structures [3, 6], coating on fiber insolation of thermal and vibration processes [10, 21], external composite systems [25], acoustic metamaterials for low-frequency broadband vibration and sound insulation [31, 32], composites structures studied for specified boundary conditions [34].

Taking into account the problems related to the incorrectly selected type and design of a vibroisolator for a given machine (damage to the structure, occurrence of resonant vibrations), the following research goal was formulated: to assess the effectiveness of the designed vibroisolator for an aircraft piston engine placed on a dynamometer test stand.

2. Research methodology

The research was carried out based on the author's development methodology for empirical tests of engines in bench conditions. The research methodology was based on the passive experiment. The engine speed and torque were chosen as the input parameters. Vibration accelerations of the engine block and engine frame were taken into consideration as the output parameters.

The accelerometers were put on the engine block and the engine frame. Such a position was selected to obtain a high vibration signal sensitivity regarding the observed process and a low sensitivity to the other vibrations. Placements and orientations of the accelerometer on the engine block and frame were considered. The optimal positions for the transducers were selected based on the analysis of the dynamic process related signal to noise ratio. The research dimensions of digital signals were chosen as: X dimension – parallel to the cylinder axis (and perpendicular to the frame surface), Y dimension – parallel to the frame surface and perpendicular to the crankshaft axis, Z dimension – parallel to the crankshaft axis and perpendicular to the cylinder axis.

Values of the engine speed and load were selected within the engine operative area. Digital data was sampled during experiments once coolant and temperatures were stabilized. Software algorithms were developed by the authors and were used to manage the data post-processing analysis. The sampling frequency during the research process was 65,536 Hz for each channel of the measurement system.

Measurement of selected parameters of the vibroacoustic process for specific engine performance was carried out following the principle of finding a reliable diagnostic parameter for accurate evaluation of the effectiveness of mounting the aircraft piston combustion engine on a test stand.

3. Engine test stand and research equipment

All researches were performed for the engine test stand conditions, and the working points of the engine were chosen from the engine speed and torque operating ranges (Fig. 3, 4).

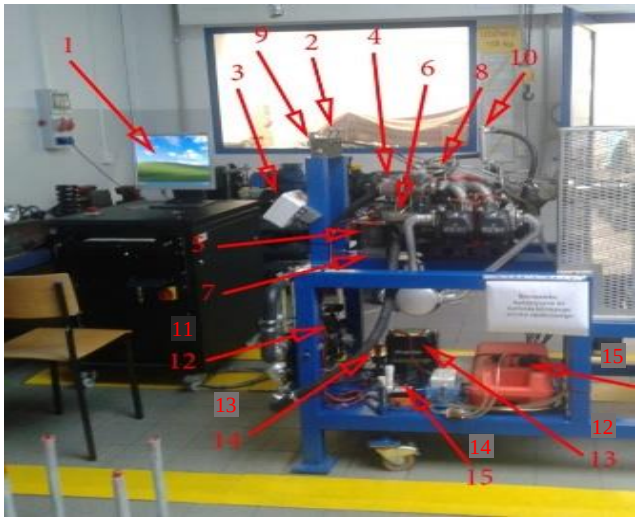

Fig. 3. The view and components of the test stand: 1 – computer, 2 – throttle and choke levers, 3 – desktop, 4 – air filter, 5 – oil tank, 6 – starter, 7 – regulator, 8 – magnetos, 9 – oil pressure gauge, 10 – oil cooler, 11 – coolant radiator, 12 – battery, 13 – main power switch, 14 – electromagnet, 15 – fuel tank

The research was carried out using a six-channel measurement system with a B&K LAN-XI type 3050-A-060 card (possibility of parallel recording with a band frequency of up to 51.2 kHz) – Table 1, Fig. 4.

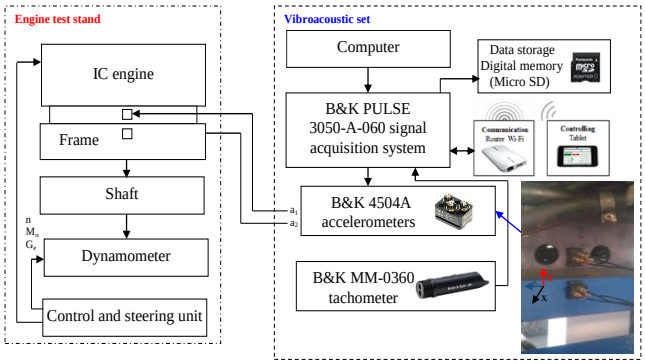

Fig. 4. The scheme of the measurement circuit connections and installation of vibration transducers to the engine and frame

Table 1. The technical specification of a LAN-XI 3050-A-060 [12]

B&K LAN-XI 3050-A-060	
Number of channels	6
Frequency passband [Hz]	1–51200
DC input [V DC]	10–32
Temperature range [°C]	–25–70
Absolute amplitude precision, 1 kHz, 1 V_{input}	±0.05 dB, typ. ±0.01 dB
Amplitude linearity	±0.01–0.02 dB (from 0–140 dB)
Weight [g]	750
Output	CCLD/microphone preamplifier (0 or 200 V polarization voltage), charge
Data handling	16 GB SD card (4 h of recording with 6 channels at 25.6 kHz bandwidth

The recorded signals and the obtained results were observed on a computer screen using the PULSE Reflex Core software. Vibration acceleration measurements were carried out using two three-axis piezoelectric transducers of the B&K 4504A type (Table 2). The above accelerometers were calibrated separately for each measurement axis. Aluminum housing and lead piezoelectric element, DC power supply and high resonance frequency are some of the advantages of the transducer, thanks to which the transducer's low weight, high sensitivity and low sensitivity to external factors (including environmental factors) are achieved.

Table 2. The technical specification of a Bruel&Kjær 4504A accelerometer [12]

Bruel&Kjær 4504A	
Frequency [Hz]	1–10,000
Senitivity [mV/g]	10
Temperature range [°C]	–50–125
Residual noise level in spec. freq. range (RMS) [mg]	±0.4
Maximum operational/shock level (peak) [g]	±750/±3000
Weight [g]	15
Output	CCLD
Resonance frequency [kHz]	50
Triaxial/TEDS/Electrical connector	Yes/No/10-32 UNF

The placements of the vibration acceleration transducers (Bruel&Kjær 4504A) were located on the engine block and the engine frame, nearby generated dynamic processes. Measurements were done for 3 perpendicular dimensions, and the recorded cyclic processes were defined using an angle encoder B&K MM0360 (Table 3).

Table 3. The technical specification of the B&K MM0360 angle encoder [12]

Feature \ Sensor	
Transducer type	MM0360
Velocity range [rpm]	0–300,000
Operating range	1.5 (0.6) to > 70 cm (27") and > 30° from centre line
Laser spot	< ∅5 mm at 70 cm distance
Maximum continuous input voltage [V]	–5 to +30
Laser class	3R. Visible 660–690 nm, CW, P [optical] < 2 mW. Complies with EN/IEC 60825-1:2007
Temperature range [°C]	–10 to +50
Input type	CCLD (DeltaTron or ICP® inputs from 3 to 20 mA), U ≥ 20V

4. Research engine

A spark-ignition internal combustion engine of the Rotax 912 type was used as the research object. The above-mentioned four-cylinder naturally aspirated engine is a design with a counter-rotating arrangement of cylinders (boxer type), in which there are two carburetors (BING) with a central fuel chamber (supplied by a mechanical fuel pump), and the pressure lubrication system (with the so-called dry sump) has 2 oil pumps and an oil cooler. This engine has a mixed cooling system, where the cylinders are cooled by air and the heads by liquid (the liquid pump is driven by a gear transmission from the engine's crankshaft). Each head is equipped with two valves (intake, exhaust) hydraulically controlled, with the possibility of adjusting valve clearances (Fig. 5).

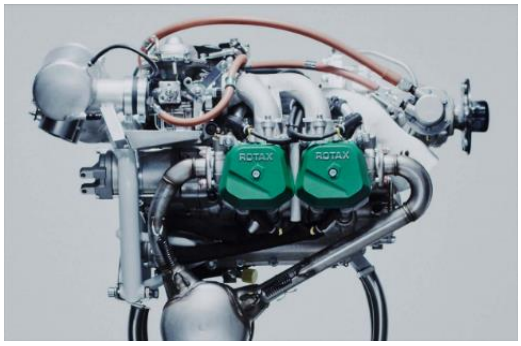

Fig. 5. The view of the Rotax 912 engine [13]

Table 4. Operating and geometric parameters of the Rotax 912 engine [11]

Parameter type	Value
Rated effective power [kW]	59.6 (at 5800 rpm)
Engine displacement [cm^3]	1211
Cylinder diameter/piston stroke [m/m]	0.0795/0.0610
Compression ratio [–]	9.1
Fuel consumption [dm^3/h]	15.0 (by 5000 rpm in 75% of rated effective power)
Mass power coefficient [kW/kg]	0.98
Engine length/width [m/m]	0.561/0.576
Engine mass [kg]	60

5. Research conditions

Empirical research was done under the following research conditions:

- ambient conditions at the engine test stand area: t_o = = 20°C and p_o = 1012 hPa
- operating conditions: stationary, for each constant engine speed value and constant torque (7 engine speed values from the range 700–1400 rpm) and the torque values were 0 Nm (Table 5)
- vibroacoustic conditions: vibration acceleration passband range: 1–24,000 Hz, sampling rate: 65.536 kHz
- placement of a vibration transducer: first on the engine block (recording in the 3 perpendicular directions) and second at the engine frame (3 perpendicular directions).

Table 5. The reproduction of stand operating conditions and recorded vibroacoustic parameters carried out in the research program

Operating conditions		Recorded parameters	
n [rpm]	M_o [N·m]	Engine block	Engine frame
700	0	$a_{x,block}$ $a_{y,block}$ $a_{z,block}$	$a_{x,frame}$ $a_{y,frame}$ $a_{z,frame}$
900			
1000			
1100			
1200			
1300			
1400			

Obtained vibration accelerations were directed to the analog inputs of the acquisition card. Signals were filtered in the card (by analog and digital filters) and were converted from analog to digital form, which were stored in a computer memory then. The recorded all-time history courses of the signals were subjected to the time selection process, in which all recorded signals were divided into signal sequences including single IC engine working cycles.

The rotational speed values were measured using an angle encoder placed after the reducer, therefore, to obtain the rotational speed on the engine crankshaft, the following equation had to be used:

$$n_e = 2.27 \cdot n \tag{14}$$

where: 2.27 – geometric transmission ratio of the reducer, n_e – the engine crankshaft speed [rpm], n – the rotation speed measured after the reducer [rpm].

6. Measurement results

6.1. Assessment of the effectiveness of vibration isolation of the engine mounting

The correctness of the selection of vibration isolating elements is assessed based on the measurement of vibration signals before and after the vibration isolator. Figure 6 shows the time history of vibration acceleration signals recorded on the engine and on the frame of the test stand (in two perpendicular directions).

Based on the analysis of Fig. 6, it can be concluded that the maximum vibration acceleration amplitudes have decreased for both directions of vibration measurement. The vibration acceleration signals were analyzed by calculating the damping coefficient based on the eq. (10). The analysis results regarding the maximum vibration acceleration values are presented in Table 6.

Table 7 presents the results of analyzes regarding vibration damping in the energetic sense, based on the values of the RMS vibration accelerations.

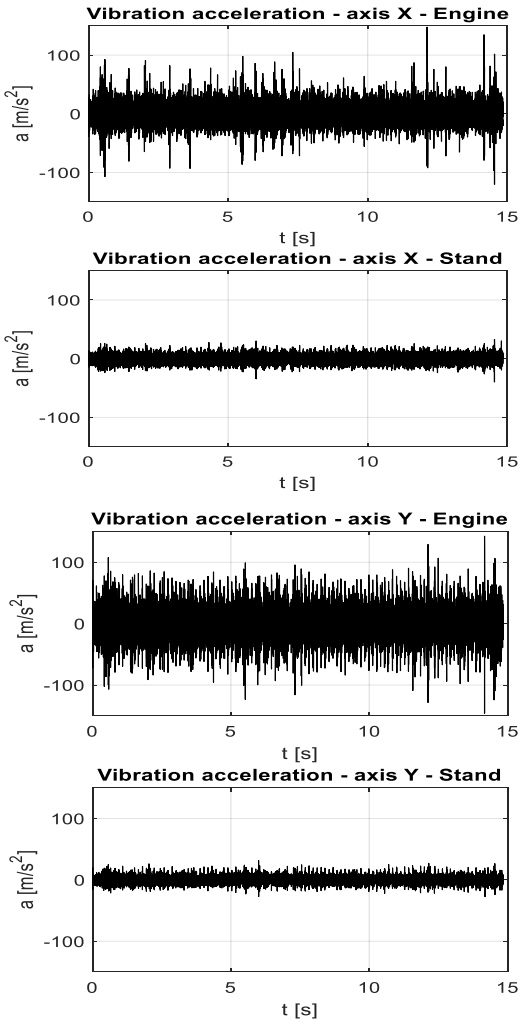

Fig. 6. The time history of vibration acceleration for two measurement points and two orthogonal directions

Table 6. The list of damping coefficients of vibration acceleration signal parameters regarding maximum values

n [rpm]	Vibration acceleration damping [–]	
	X axis	Y axis
700	3.70	4.63
900	3.46	4.65
1000	4.33	6.18
1100	2.73	4.90
1200	2.79	2.95
1300	3.47	6.03
1400	3.01	3.27

Table 7. The list of damping coefficients of vibration acceleration signal parameters in terms of energy (for the RMS estimator)

n [rpm]	Vibration acceleration damping [–]	
	X axis	Y axis
700	1.82	3.58
900	1.83	3.58
1000	2.36	4.81
1100	2.27	3.47
1200	2.21	3.88
1300	2.08	4.06
1400	2.27	2.69

Based on the analysis of the damping coefficients listed in Table 6 and Table 7, it was found that for all engine operation settings during the tests, the vibration acceleration signals were damped.

Figure 7 shows the time history of vibration velocity signals recorded on the engine and on the frame of the test stand (in two perpendicular directions).

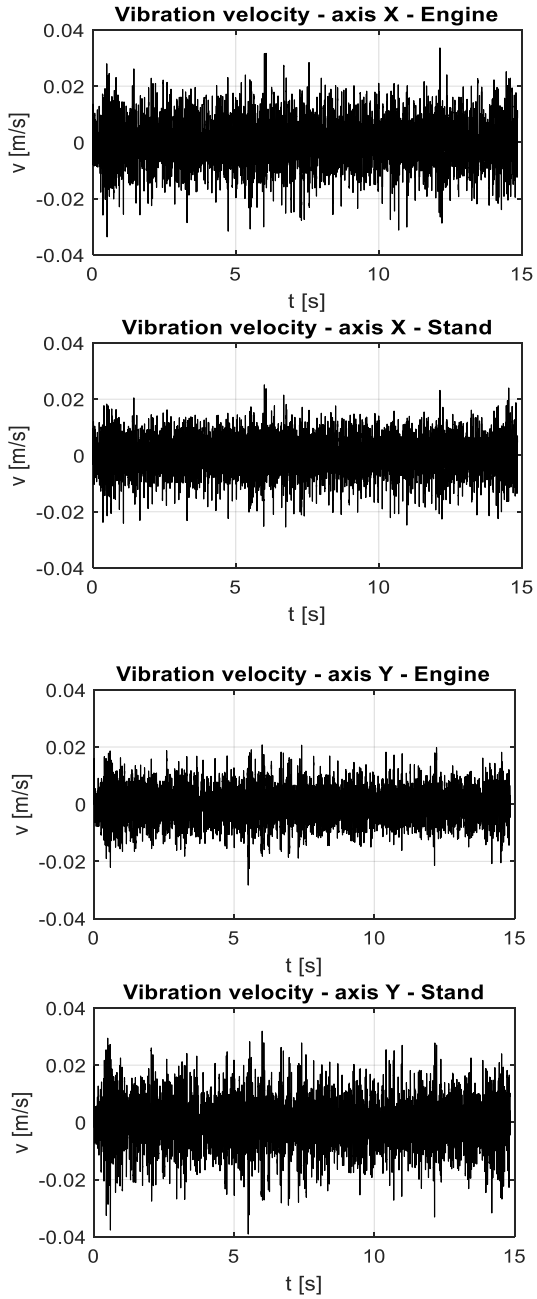

Fig. 7. The time history of vibration velocity for two measurement points and two orthogonal directions

Based on the analysis of Fig. 7, it can be concluded that the maximum vibration velocity amplitudes were reduced in the X direction, while they were strengthened in the Y direction. The vibration velocity signals were analyzed by calculating the damping coefficient. The analysis results regarding the maximum vibration acceleration values are presented in Table 8.

Table 8. The list of damping coefficients of vibration speed signal parameters regarding maximum values

n [rpm]	Vibration velocity damping [–]	
	X axis	Y axis
700	1.32	0.72
900	1.22	0.64
1000	1.26	0.74
1100	1.37	0.58
1200	1.01	0.72
1300	1.36	0.65
1400	1.31	0.66

Table 9. The list of damping coefficients of vibration speed signal parameters in terms of energy (for the RMS estimator)

n [rpm]	Vibration velocity damping [–]	
	X axis	Y axis
700	1.29	0.60
900	1.33	0.53
1000	1.20	0.62
1100	1.35	0.54
1200	1.19	0.69
1300	1.37	0.66
1400	1.29	0.62

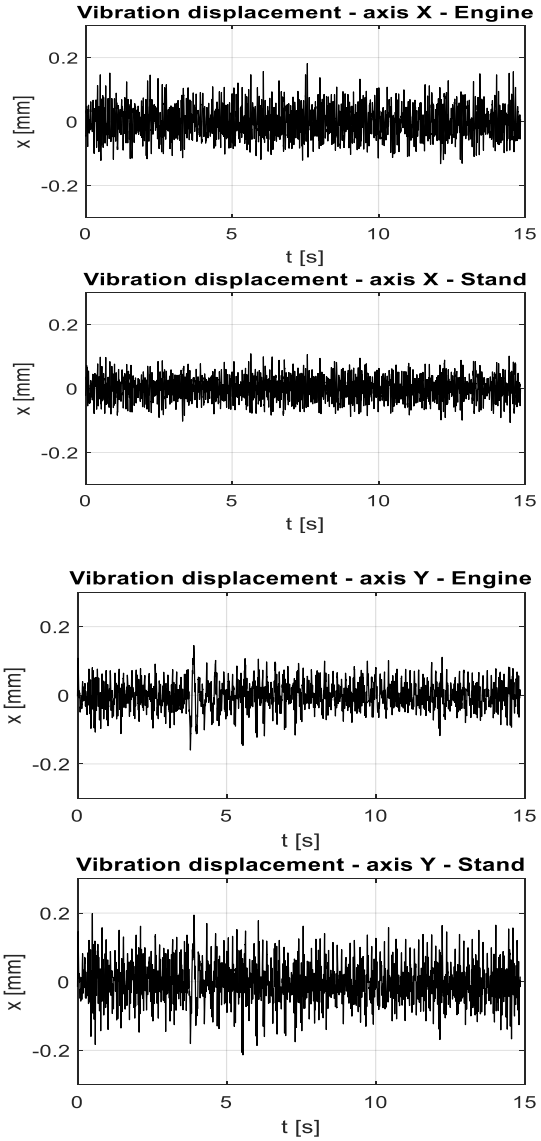

Fig. 8. The time history of a vibration displacement for two measurement points and two orthogonal directions

Table 9 presents the results of analyzes regarding vibration damping in the energetic sense, based on the values of RMS vibration velocities.

Based on the analysis of the damping coefficients listed in Table 8 and Table 9, it was found that for all engine operation settings during the tests, the vibration speed signals were damped in the X direction and strengthened in the Y direction.

In a similar way, the effectiveness of damping vibration displacements was analyzed, the time history of which is presented in Fig. 8. It was found that the maximum amplitudes of vibration displacements were reduced in the X direction, and strengthened in the Y direction.

The vibration displacement signals were analyzed by calculating the damping coefficient. The results of the analyzes regarding the maximum values of vibration acceleration are presented in Table 10, and the results of calculations regarding vibration damping in the energy sense, based on the values of effective vibration velocities, are presented in Table 11.

Table 10. The list of damping coefficients of vibration displacement signal parameters regarding maximum values

n [rpm]	Vibration displacement damping [–]	
	X axis	Y axis
700	1.67	0.75
900	1.49	0.63
1000	1.40	0.81
1100	1.71	0.71
1200	1.62	0.66
1300	1.90	0.55
1400	1.58	0.56

Table 11. The summary of the results of attenuation of vibration displacement signal parameters in terms of energy (for the RMS estimator)

n [rpm]	Vibration displacement damping [–]	
	X axis	Y axis
700	1.34	0.69
900	1.25	0.61
1000	1.13	0.69
1100	1.31	0.57
1200	1.30	0.66
1300	1.65	0.59
1400	1.83	0.53

Based on the analysis of the damping coefficients listed in Table 10 and Table 11, it was found that for all engine operation settings during the tests, the vibration displacement signals were damped in the X direction and strengthened in the Y direction.

6.2. Frequency analysis

Since the broadband analysis was not clear, a frequency analysis was performed to explain the discrepancies between the results of the calculated damping coefficients for accelerations, velocities and vibration displacements, especially in the Y direction.

Figure 9 shows the amplitude spectra of the vibration acceleration signals recorded at different rotational speed settings of the propeller shaft. It was found that for the presented engine operation settings, the spectra are of a similar nature, i.e. they differ in amplitudes for similar frequencies. With this in mind, the rest of the article presents the analysis results for measurements at a propeller shaft rotation speed of 700 rpm.

Figure 10a,c,e compares the spectra of accelerations, velocities and vibration displacements in the entire recorded frequency band (for the engine and the stand frame in the X direction), while Fig. 10b,d,f shows a comparison of spectra for the same conditions only in the 4–200 Hz band, which corresponds to the first five rotational harmonics of the engine crankshaft.

The analysis of the results presented in Fig. 10 allows for the following conclusions to be drawn regarding the effectiveness of vibration isolation in the X direction in the case of:

- vibration acceleration, and damping occur in most of the frequency range except for the following bands: 65–75 Hz, 145–200 Hz, 270–720 Hz, 1200–2000 Hz. The greatest attenuation occurs at higher frequencies above 2 kHz
- vibration speeds, the amplification occurs only in the band: 65–75 Hz
- vibration displacements, and damping occur for the entire range of analyzed frequencies.

A comparison of the spectra of accelerations, velocities and vibration displacements in the entire recorded frequency band (for the engine and the stand frame in the Y direction) is shown in Fig. 11a,c,e, while Fig. 11b,d,f shows a comparison of spectra for the same conditions only in the 4–200 Hz band, which corresponds to the first five rotational harmonics of the engine crankshaft.

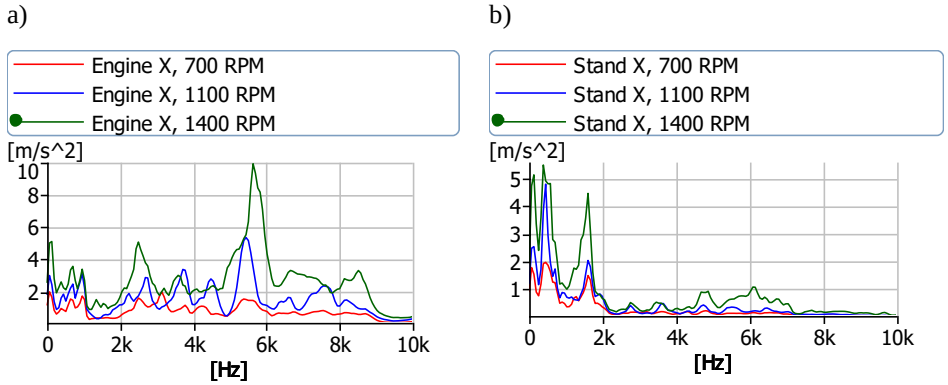

Fig. 9. The amplitude spectra of vibration accelerations at different shaft rotational speed settings recorded on: a) the engine, b) the frame of a test stand

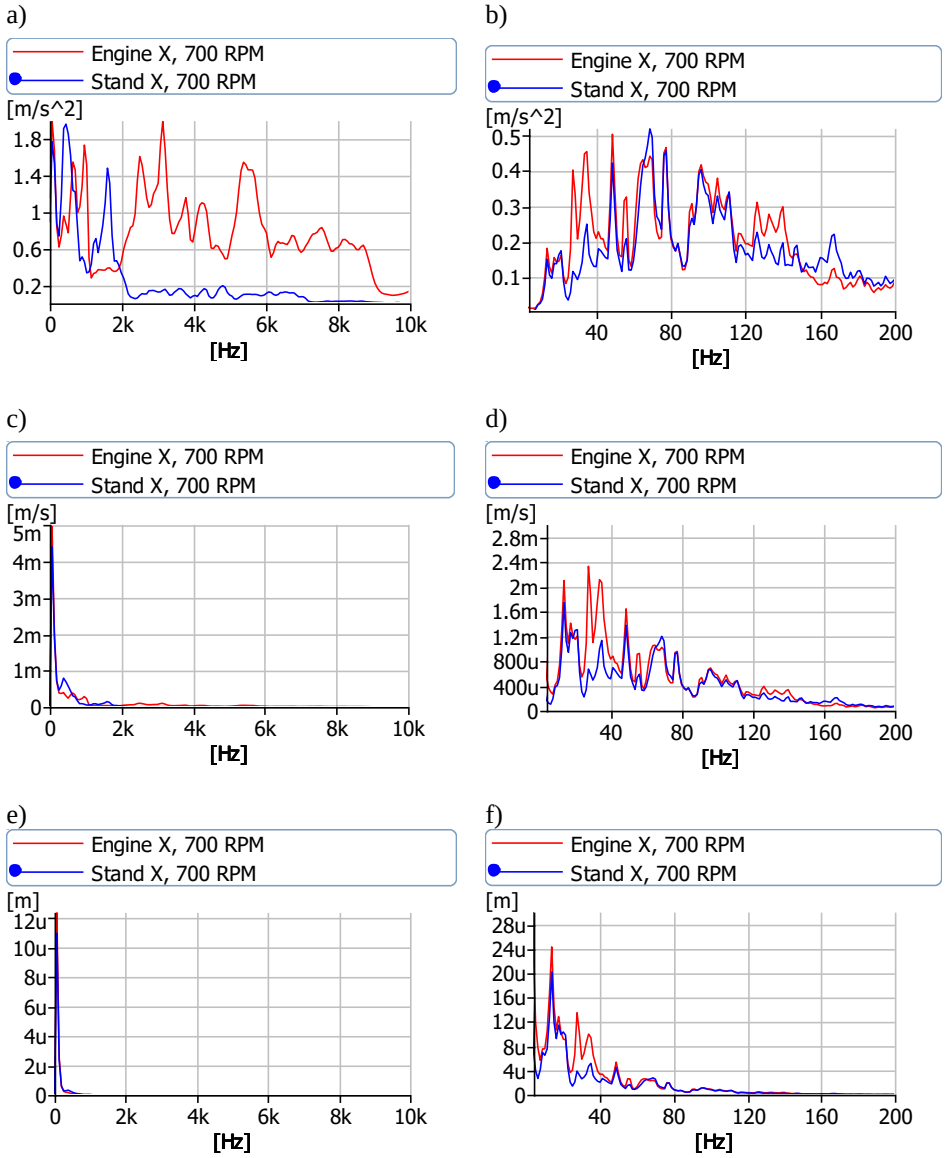

Fig. 10. The spectra of signals in the X direction: a, c, e) accelerations, velocities and vibration displacements in the entire recorded frequency band and b, d, f) accelerations, velocities and vibration displacements in the 4–200 Hz band (m – mil, u – micro)

Based on the analysis results presented in Fig. 11, the following conclusions were made regarding the effectiveness of vibration isolation in the Y direction in the case of:

- vibration accelerations, the damping occurs at frequencies above 500 Hz, while the vibration amplification is observed at frequencies lower than 500 Hz
- vibration velocities, the damping and amplification occur in the same frequency ranges as in the case of vibration accelerations
- vibration displacements, the amplification occurs for the entire range of analyzed frequencies.

Conclusions

The presented work is based on empirical research carried out by its authors within the study of the effectiveness of mounting the aircraft piston combustion engine on a test stand.

The analysis of damping effectiveness carried out in the amplitude domain using dimensional point measures such as peak value and RMS, based on the determination of the damping coefficient for the X and Y directions and various engine rotation speeds, confirmed the damping effectiveness in the case of vibration accelerations for both recorded directions of the measurement signal. In the case of vibration speed only in the X direction, reductions in the peak vibration amplitude and their RMS values were observed. A similar situation occurred for vibration displacements. Hence, the analysis was supplemented with those carried out in the frequency domain.

In the case of the frequency domain assessments, the effectiveness of vibration isolation for vibration acceleration in the X direction was proved in most of the frequency range (except 65–75 Hz, 145–200 Hz, 270–720 Hz, 1200–2000 Hz). The greatest vibration decrease occurred at frequencies above 2 kHz. In the case of vibration speeds, the amplification occurs only in the band 65–75 Hz, and for vibration displacements damping occurs for the entire range of analyzed frequencies.

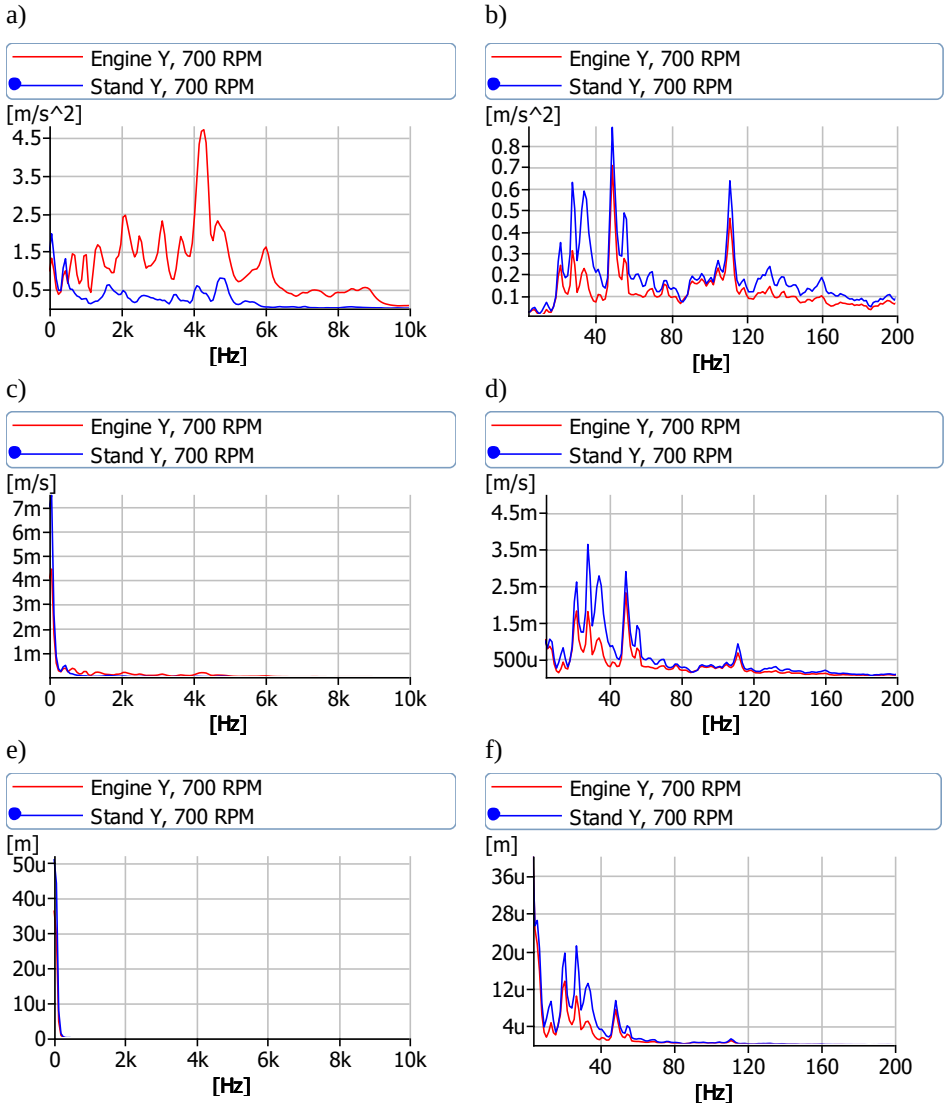

Fig. 11. The spectra of signals in the Y direction: a, c, e) accelerations, velocities and vibration displacements in the entire recorded frequency band and b, d, f) accelerations, velocities and vibration displacements in the 4–200 Hz band (m – mil, u – micro)

In the case of vibration accelerations in the Y direction, the damping occurs at frequencies above 500 Hz, while the vibration amplification is observed at frequencies lower than 500 Hz. The same situation occurred in the case of vibration velocities. The amplification occurs for the entire range of analyzed frequencies for vibration displacements.

Acknowledgements

This work was partly supported by Polish Ministry of Education and Science fund for Statutory Activities of: the Institute of Combustion Engines and Powertrains, PUT (PL) 0415/SBAD/0342, and the Institute of Transport, PUT (PL) 0416/SBAD/0005.

Nomenclature

a_1	vibration accelerations obtained from the transducer placed at the engine block
a_2	vibration accelerations obtained from the transducer placed at the engine frame
$a_{x,block}$	vibration accelerations in X direction at the engine block
$a_{y,block}$	vibration accelerations in Y direction at the engine block
$a_{z,block}$	vibration accelerations in Z direction at the engine block
$a_{x,frame}$	vibration accelerations in X direction at the engine frame
$a_{y,frame}$	vibration accelerations in Y direction at the engine frame
$a_{z,frame}$	vibration accelerations in Z direction at the engine frame
CCLD	constant current line drive
E_{WI}	efficiency of force vibration isolation
E_z	efficiency of displacement vibration isolation
F_d	value of the force from the source of excitation
G_e	stream mass of fuel consumption

IC	internal combustion
m	mil
M_o	torque
n	rotation speed measured after the reducer
n_e	engine crankshaft speed
P	power
p_o	ambient pressure
R	force transferred to the frame structure for the system with a vibroisolator (value after passing through the isolator)
R^0	force transmitted to the supporting structure for the system without a vibration isolator
RMS	root mean square
SD	secure digital
TEDS	transducer electronic datasheet
t_o	ambient temperature
u	micro
U	voltage
w	displacement for a system with a vibration isolator (after passing through the vibration isolator)
w^0	displacement for a system without a vibration isolator
z	displacement for a system without a vibration isolator
α	susceptibility matrix for a system with vibration isolation
α^0	susceptibility matrix for a system without vibration isolation
β	machine susceptibility
δ	susceptibility of the frame structure
γ	vibration isolator susceptibility

Bibliography

[1] Arroyo J, Muñoz M, Moreno F, Bernal N, Monné C. Diagnostic method based on the analysis of the vibration and acoustic emission energy for emergency diesel generators in nuclear plants. Appl Acoust. 2013;74(4):502-508. https://doi.org/10.1016/j. apacoust.2012.09.010

[2] Avramchuk VS, Kazmin VP. Estimation of combustion engine rotation speed based on vibration signal analysis. KEM. 2016;685:436-440. https://doi.org/10.4028/www.scientific.net/kem.685.436

[3] Berberova-Buhova N, Nedelchev L, Mateev G, Stoykova E, Strijkova V, Nazarova D. Influence of the size of Au nanoparticles on the photoinduced birefringence and diffraction efficiency of polarization holographic gratings in thin films of azopolymer nanocomposites. Opt Mater. 2021;121: 111560. https://doi.org/10.1016/j.optmat.2021.111560

[4] Brzeziński K. Active-passive: on preconceptions of testing. Journal of Telecommunications and Information Technology. 2011;3:63-73. https://yadda.icm.edu.pl/baztech/element/bwmeta1.element.baztech-article-BAT8-0021-0008

[5] Cempel C. Vibroacoustic machines diagnostics. Polish Scientific Publishing Houses. Warsaw 1989.

[6] Chen Y, Li F. Analysis of vibration and sound insulation characteristics of functionally graded sandwich plates. Compos Struct. 2020;249:112515. https://doi.org/10.1016/j.compstruct.2020.112515

[7] Czechyra B, Szymański GM, Tomaszewski F. Assessment of cam valves clearance in internal combustion engine based on parameters of vibration – methodological assumption. Combustion Engines. 2004;118(1):51-59. https://doi.org/10.19206/CE-117424

[8] Delvecchio S, Bonfiglio P, Pompoli F. Vibro-acoustic condition monitoring of internal combustion engines: a critical review of existing techniques. Mech Syst Signal Pr. 2018; 99:661-683. https://doi.org/10.1016/j.ymssp.2017.06.033

[9] Fiebig W, Wróbel J. Two stage vibration isolation of vibratory shake-out conveyor. Arch Civ Mech Eng. 2017; 17(2):199-204. https://doi.org/10.1016/j.acme.2016.10.001

[10] He D, Ou D, Gao H, Jiao F. Thermal insulation and anti-vibration properties of $MoSi_2$-based coating on mullite fiber insulation tiles. Ceram Int. 2022;48(2):1844-1850. https://doi.org/10.1016/j.ceramint.2021.09.267

[11] https://www.altair.com.pl/news/view?news_id=3780 (accessed on 17.12.2009).

[12] https://www.bksv.com (accessed on 04.02.2024).

[13] https://www.flyrotax.com/pl/products/912-ul-a-f (accessed on 05.03.2024).

[14] Idaszewska N, Szymański GM. Identification of characteristic vibration signal parameters during transport of fruit and vegetable. Vibrations in Physical Systems. 2020;31(1): 2020111-1-2020111-10. https://vibsys.put.poznan.pl/?s=Idaszewska

[15] Jałowiecki A, Fidali M, Krol A. Investigation of rolling bearing lubrication condition. Diagnostyka. 2021;22(4):51-58. https://doi.org/10.29354/diag/144123

[16] Korbicz J, Kościelny J. Modeling, diagnostics, and mastering processes. DiaSter implementation. Scientific and Technical Publishing House. Warsaw 2010.

[17] Korbicz J, Kościelny JM, Kowalczuk Z, Cholewa W. Process diagnostics. Science and Technology Publishing House. Warsaw 2002.

[18] Kozak M, Lijewski P, Fuć P. Exhaust emissions from a city bus fuelled by oxygenated diesel fuel. SAE Technical Paper 2020-01-2095. 2020. https://doi.org/10.4271/2020-01-2095

[19] Kozak M, Lijewski P, Waligórski M. Exhaust emissions from a hybrid city bus fuelled by conventional and oxygenated fuel. Energies. 2022;15(3):1123. https://doi.org/10.3390/en15031123

[20] Lijewski P, Kozak M, Fuć P, Rymaniak Ł, Ziółkowski A. Exhaust emissions generated under actual operating conditions from a hybrid vehicle and an electric one fitted with a range extender. Transport Res D-Tr E. 2020;78:102183. https://doi.org/10.1016/j.trd.2019.11.012

[21] Ma N, Han Q, Han S, Li Ch. Hierarchical re-entrant honeycomb metamaterial for energy absorption and vibration insulation. Int J Mech Sci. 2023;250:108307. https://doi.org/10.1016/j.ijmecsci.2023.108307

[22] Nowakowski T, Komorski P. Diagnostics of the drive shaft bearing based on vibrations in the high-frequency range as a part of the vehicle's self-diagnostic system. Eksploat Niezawodn. 2021;24(1):70-79. https://doi.org/10.17531/ein.2022.1.9

[23] Orczyk M, Tomaszewski F. Method of reduction of diagnostic parameters during observation on the example of a combustion engine. MATEC Web of Conferences. 2017;118: 00034-1-00034-7. https://doi.org/10.1051/matecconf/201711800034

[24] Peeters C, Leclerc Q, Antoni J, Guillaume P, Helsen J. Vibration-based angular speed estimation for multi-stage wind turbine gearboxes. J Phys Conf Ser. 2017;842:012053. https://doi.org/10.1088/1742-6596/842/1/012053

[25] Roozen NB, Urbán D, Piana EA, Glorieux C. On the use of dynamic vibration absorbers to counteract the loss of sound insulation due to mass-spring-mass resonance effects in external thermal insulation composite systems. Appl Acoust. 2021;178:107999. https://doi.org/10.1016/j.apacoust.2021.107999
[26] Sujatha C. Vibration, acoustics and strain measurement, theory and experiments. Springer 2023. https://doi.org/10.1007/978-3-031-03968-3
[27] Szymański GM, Tabaszewski M. Engine valve clearance diagnostics based on vibration signals and machine learning methods. Eksploat Niezawodn. 2020;22(2):331-339. https://doi.org/10.17531/ein.2020.2.16
[28] Szymański GM, Tomaszewski F. Diagnostics of automatic compensators of valve clearance in combustion engine with the use of vibration signal. Mech Syst Signal Pr. 2016;68-69:479-490. https://doi.org/10.1016/j.ymssp.2015.07.015
[29] Waligórski M, Batura K, Kucal K, Merkisz J. Empirical assessment of thermodynamic processes of a turbojet engine in the process values field using vibration parameters. Measurement. 2020;158:107702. https://doi.org/10.1016/j.measurement.2020.107702
[30] Waligórski M, Batura K, Kucal K, Merkisz J. Research on airplanes engines dynamic processes with modern acoustic methods for fast and accurate diagnostics and safety improvement. Measurement. 2020;154:107460. https://doi.org/10.1016/j.measurement.2019.107460
[31] Yang X-H, Kang Y, Xie X, Zhang Q, Shangguan W-B. Multilayer coupled plate-type acoustic metamaterials for low-frequency broadband sound insulation. Appl Acoust. 2023209;109399. https://doi.org/10.1016/j.apacoust.2023.109399
[32] Zhang L, Bai Z, Chen Y. Dual-functional hierarchical mechanical metamaterial for vibration insulation and energy absorption. Eng Struct. 2022;271;114916. https://doi.org/10.1016/j.engstruct.2022.114916
[33] Zhang P, Gao W, Li Y, Wei Z. Combustion parameter evaluation of diesel engine via vibration acceleration signal. Int J Engine Res. 2021;23(10):1760-1781. https://doi.org/10.1177/14680874211030878
[34] Zhu Z, Wang G, Sheng Z, Zhang Y, Xu R. Sound insulation properties of embedded co-cured composite damping sandwich panel under arbitrary boundary conditions. Mech Syst Signal Pr. 2023;204:110810. https://doi.org/10.1016/j.ymssp.2023.110810
[35] Zimroz R, Urbanek J, Barszcz T, Bartelmus W, Millioz F, Martin N. Measurement of instantaneous shaft speed by advanced vibration signal processing – application to wind turbine gearbox. Metrol Meas Syst. 2011;4:701-712. https://doi.org/10.2478/v10178-011-0066-4
[36] Zacharewicz M, Socik P, Wirkowski P, Zadrąg R, Bogdanowicz A. Evaluation of the impact of supplying a marine diesel engine with a mixture of diesel oil and n-butanol on its efficiency and emission of toxic compounds. Combustion Engines. 2023;195(4):40-47. https://doi.org/10.19206/CE-169484
[37] Żurawski PK. Optimization of the combustion chamber strength of aluminum pistons in diesel engines using the DuralBowl technology. Combustion Engines. 2023;192(1):91-96. https://doi.org/10.19206/CE-153000

Prof. Grzegorz M. Szymański, DSc., DEng. – Institute of Transport, Poznan University of Technology, Poland.
e-mail: *grzegorz.m.szymanski@put.poznan.pl*

Wojciech Misztal, DEng. – Institute of Combustion Engines and Powertrains, Poznan University of Technology, Poland.
e-mail: *wojciech.misztal@put.poznan.pl*

Prof. Marek Waligórski, DSc., DEng. – Institute of Combustion Engines and Powertrains, Poznan University of Technology, Poland.
e-mail: *marek.waligorski@put.poznan.pl*

Article citation info:
Rymaniak Ł, Ratajczyk F, Szymlet N, Woźniak F. Issues in the conservation and restoration of powertrains as engineering art monuments. Combustion Engines. 2024;198(3):93-97. https://doi.org/10.19206/CE-187379

Łukasz RYMANIAK
Franciszek RATAJCZYK
Natalia SZYMLET
Filip WOŹNIAK

Combustion Engines
Polish Scientific Society of Combustion Engines

Issues in the conservation and restoration of powertrains as engineering art monuments

ARTICLE INFO

Received: 30 November 2023
Revised: 4 March 2024
Accepted: 17 April 2024
Available online: 16 June 2024

The article discusses issues related to the behavior of powertrains understood as monuments of engineering art. The theoretical part analyzed the most important issues related to the maintenance and renovation of vehicles, their share in Poland in the age category, as well as the regulations regarding the classification of historic vehicles. The next part of the article presents the renovation process of two powertrains – the K-750 motorcycle and the Volkswagen Type 117 passenger car, along with a short production history. Then, recommended procedures for unique objects were discussed in the context of their state of preservation and occurrence based on the authors' experience.

Key words: *combustion engine, conservation, monuments of engineering art, powertrains, renovation*

1. Introduction

The renovation of monuments of engineering art, which includes all types of vehicles, is a constantly developing field of science. Within its area, coherent activities must be carried out in the field of history, conservation, construction, technology, chemistry, and other fields related to a given object. However, maintenance work often requires a compromise between the above-mentioned areas. Moreover, in many areas of technology, it is difficult to determine whether a given solution is already a monument of engineering art and has some value. Therefore, scientists are developing tools that are intended to unify activities in the undertaken area and support the decision-making process. This is achieved through classification and evaluation related to multi-criteria assessment of objects [1, 2, 6, 9]. In the renovation of transport facilities, the most important decision is whether a given facility is to be kept in operation while maintaining partial or full functionality.

The heritage of engineering art allows us to learn about the level of technical culture, construction, and technology of their creation, as well as the reasons for their production in terms of social and individual needs [6, 9, 17]. Learning about old solutions combined with modern technologies can be an impulse for technical development work [13, 16]. When maintaining and renovating historic vehicles, many issues should be considered, including: originality of parts and their condition, safety during operation, and the original operation of individual units. Aesthetic values are also important, but they raise a lot of controversy because facility owners often decide to completely renovate paint coatings, often using technologies other than the original ones. However, this is debatable because the historical value is also determined by the preserved elements of the painting and varnish from the production times. In addition, for historic vehicles, the issue of preserving modifications made to the facility should also be considered. They are often a component of the historical identity of the object and resulted, for example, from a direct utilitarian need [15].

In Poland, in 2022, according to the central vehicle register, 29 727 303 passenger cars, motorcycles, and mopeds were registered [13]. Of this, a significant 20.71% were historical objects aged at least 31 years (Table 1). It should be noted that most of these vehicles no longer exist and have not been removed from the register. Some of them are still used without recognizing their historical context. However, historic objects constitute a small share of this population. At the end of 2022, there were 56,290 historic vehicles registered in the country (this group also includes heavy and agricultural vehicles). The largest share in this group are post-war objects. During World War II, the automotive industry in Poland was almost completely destroyed [8].

Table 1. Share of vehicles over 31 years of age and older [14]

	Passenger cars	Motorcycles	Mopeds	Whole
Total [pcs]	26 457 659	9 490 427	1 830 963	29 727 303
≥ 31 years [pcs]	4 999 558	2 958 423	816 922	6 155 839

2. Regulations regarding the classification of historic vehicles

In the European Union, there are no clear provisions regarding the protection of monuments of engineering art, apart from general provisions relating to monuments in general. Detailed data are defined by member states, mainly by ministries related to culture and transport.

Historic vehicles are becoming more and more popular, not only in Poland but also throughout the European Union. Very often, such objects are not formally registered as monuments despite their condition and age. This is due to users' prejudices and very often their ignorance. However, due to the policy of sustainable development and care for the natural environment, additional fees and restrictions are imposed on older vehicles. Therefore, owners are increasingly seeking entry into the register of monuments with the Provincial Conservators of Monuments. The most important normative acts in Poland in this regard are:

- Act of 20 June 1997, road traffic law (Journal of Laws of 2023, item 1047, as amended) [13]
- Act of 14 June 1960 – Code of Administrative Procedure (Journal of Laws of 2023, item 775)
- Regulation of the Minister of Infrastructure on detailed activities of authorities in matters related to the admission of vehicles to traffic and templates of documents in these matters of August 31, 2022 (Journal of Laws of 2022, item 1849, as amended)
- Regulation of the Minister of Transport, Construction and Maritime Economy on tests for compliance with the technical conditions of historic vehicles of February 27, 2013 (Journal of Laws of 2013, item 337)
- Act of April 14, 2023 on approval systems for vehicles and their equipment (Journal of Laws of 2023).

The above legislative provisions show that a historic vehicle is a vehicle that has been entered into the register of monuments or is in the provincial register of monuments on the basis of separate regulations, as well as a vehicle entered in the inventory of museum objects, in accordance with separate regulations [13]. To obtain entry in the register of monuments (depending on the region), the facility includes, among others: it must be at least 30 years old, its type has been out of production for 15 years, it has not undergone any significant design changes, and the degree of originality of the parts must be at least 75%. Moreover, such a vehicle should no longer serve its original purpose on a daily basis. To confirm these requirements, it is necessary to provide an expert's opinion. Vehicles that are at least 25 years old are unique, and have significant historical significance in the context of technology, related events, or people may also be considered a historic vehicles.

The legislative guidelines are defined differently in Germany. In addition to the minimum age requirement, modifications using non-original parts are not allowed, and the vehicle itself must meet the criteria to obtain a positive assessment following §23 of the German Road Traffic Act [12]. As part of this assessment, the expert classifies the condition of the vehicle, giving it a rating from 1 "Perfect condition" (German: makelloser Zustand) to 5 "Condition requiring renovation" (restaurierungs-bedürftiger Zustand). Additionally, the vehicle is classified as "Original" (the entire vehicle maintained in its original condition), "Authentisch" (a vehicle or its elements restored following the original) or "Nicht Authentisch" (a vehicle significantly modified, not corresponding to its original condition).

3. Renovation of powertrains of historic vehicles

3.1. General thoughts

Renovation and workshop work must be carried out with particular caution and, at the same time, analyze wear and causes of damage. This allows you to diagnose weak structure nodes and features characteristic of a given solution. Within the scope of work carried out, basic conditions should be met, taking into account, e.g., theoretical preparation. This is about theoretical knowledge of the structure in question – its purpose/function and the method of assembly and disassembly of individual and subassemblies. Such information should be included in repair manuals, but it sometimes happens that there is no documentation for a given object. Therefore, it is necessary to collect literature regarding the solutions of this manufacturer or twin units from a given era. Military literature is particularly useful, as it is always richly illustrated and has detailed operating guidelines, e.g. [5]. It is also very important to prepare the workshop, including the development and use of tools and workshop aids (often dedicated to a given facility). Using a torque wrench to disassemble drive system components can provide a lot of information that is useful for assembly or defining the causes of a given fault. When undertaking conservation work, the object should be thoroughly cleaned, but the original coatings and seals should be retained as much as possible in order to collect information regarding their restoration or replacement.

3.2. K-750 motorcycle engine and gearbox

The subject of the renovation was a two-cylinder boxer combustion engine, Soviet production, with a displacement of 750 cm^3 (Table 2). It was used to power motorcycles M-72, MW-750, K-750, and all their varieties from factories in Moscow, Irbit, and the Urals (Fig. 1). The engine design was taken from the German BMW R-71 military motorcycle in 1939. Due to its use, the engine had to be characterized by high durability and power because it powered a machine equipped with a sidecar, where the total weight of the vehicle, including equipment and weapons, exceeded 450 kg (Fig. 2). After the war, the production of motorcycle harnesses was not discontinued; their design was slightly changed to make them more suitable for urban driving, for example, the gear ratios in the gearbox were changed.

Table 2. Technical data of the combustion engine mounted in the K-750 motorcycle [4]

Type	4-stroke, bottom-valve, spark ignition
Number of cylinders	2
Cylinder diameter [mm]	78
Piston stroke [mm]	78
Displacement [cm^3]	746
Compression ratio	6:1
Maximum power [kW] at [rpm]	19.1 at 4600
Maximum torque [Nm]	39.2
Power system	carburetor K-37A

In accordance with conservation and engineering guidelines, the drive system was dismantled, and parts were verified. Previous users have not modified the engine and gearbox and have never thoroughly overhauled them, as evidenced by the condition of individual parts. It was also interesting to discover traces of foundry sand inside the engine block (in the upper parts) in hard-to-reach places, which remained after the production process. This made it possible to conduct a thorough analysis of component wear and obtain information about the weakest nodes in the engine. Examples include cracked pistons and uneven wear marks caused by the rings in the liners. This data contributed to improving the axial positioning of the elements in the cylinders and ensuring proper lubrication. However, severe wear of the camshaft slide bearing prompted a deeper analysis of this system and the implementation of material

changes in the node. Scratches on the pistons indicated that the filter in the power supply system and the mechanical oil filter should be checked frequently.

Fig. 1. Object undergoing renovation: K-750 motorcycle produced in Kiev in 1962

No significant design changes were introduced throughout the production period. Only retail changes were introduced, most often driven by economic reasons. During the main overhaul, several solutions were proposed to improve the operation and increase the failure-free operation of the engine. They are concerned with the power supply system, changing the type of crankshaft bearing, modernizing the engine cover seal, and using a different material (phosphobronze CuSn10P) in the camshaft slide bearing. Moreover, these changes bring the repaired structure closer to its prototype, i.e., the BMW engine. When Soviet designers were transforming the engine structure, simplifications were introduced that had a negative impact on the quality and durability of the historic vehicle.

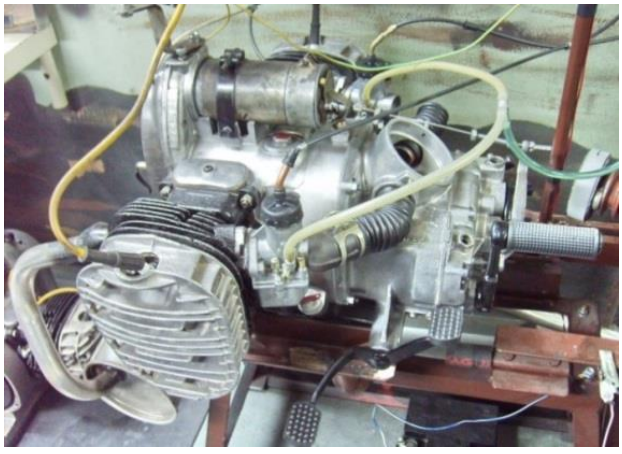

Fig. 2. The engine and gearbox of the K-750 motorcycle on the engine stand

After repairing the parts (regeneration of the crankshaft, camshaft, and camshafts), the engine and gearbox were assembled. All original and serviceable parts were used in the process. The assembly process was carried out in several stages – given nodes were assembled and disassembled several times to obtain the best fits and tolerances. After initial lapping activities, the heads were installed, and the electrical system was checked. Break-in was carried out using an electric motor connected to the gearbox output shaft. During the start-up phase, engine brake-in was an important issue. Achieving proper tightness in this process ensures that the intended power is obtained and the period until the next major repair is extended [10].

3.3. Volkswagen Type 117 vehicle: engine and gearbox

Another object undergoing renovation was a four-cylinder boxer combustion engine, made in Germany, with a displacement of 1,192 cm^3 (Table 3, Fig. 3). Its history began in 1934, when Ferdinand Porsche began design work on a vehicle intended to motorize post-war Germany. Unfortunately, the ambitious plans were interrupted by the outbreak of World War II, during which most of the units produced were used for military vehicles, such as the 4-seater Kübelwagen light off-road vehicle or the Schimmwagen floating all-wheel drive vehicle, as well as for power generators. After World War II, the engine was used in vehicles such as the Volkswagen Type 1 "Beetle", Type 2 "Transporter" and Type 14 "Karmann-Ghia" [7]. The latter, based on the "Beetle" chassis, had a special, sports body manufactured at the plant in Osnabrück. In the following years, this unit underwent several modifications aimed at improving efficiency. The most important changes included: the addition of a Bosch L-Jetronic injection system with electronic control in 1974 and the introduction of a liquid cooling system in 1982, used in the third-generation Transporter model [3].

Table 3. Technical data of the combustion engine mounted Volkswagen Type 117 [7]

Type	4-stroke, OHV, spark ignition
Number of cylinders	4
Cylinder diameter [mm]	77
Piston stroke [mm]	64
Displacement [cm^3]	1192
Compression ratio	6:1
Maximum power [kW] at [rpm]	22 at 3400
Power system	carburetor Solex 28 PCI

The renovation process of the presented engine began with disassembly, carried out in accordance with conservation and engineering guidelines, based on the service manual from the vehicle's production period. The visual assessment revealed advanced corrosion of metal covers designed to increase engine cooling efficiency. Apart from typical signs of use of the piston-cylinder assembly, such as moderate abrasion, no signs of excessive wear were found, so after cleaning, these components were reassembled. The upper cylinder covers required the use of an appropriate reconstruction technique. Knowledge from the literature and information from brand enthusiasts revealed that from January to July 1954, these covers were assembled from three separate pieces, formed by cold forming and then joined by a spot welding process. Due to the advanced corrosion of the original covers, three copies were purchased from the secondary market, based on which a set was prepared for use. All covers were covered with thermosetting black polymer-based paint with a gloss similar to the varnish originally used (based on metal oxides).

Fig. 3. Object undergoing renovation: Volkswagen Type 117 car produced in Wolfsburg in 1954

In parallel to the engine renovation, renovation works on the gearbox were carried out. The vehicle's transmission was equipped with synchronizers and helical gears for 2nd, 3rd, and 4th gear for easier operation and lower noise emission. During conservation work, it was found that the synchronizers had visible damage on the surface, which may indicate that the material was too plastic or that the impact load was too high. The element that could not be replaced due to lack of availability was the shaft transmitting torque from the engine to the transmission. Pitting occurred around the sealant, so it was decided to apply several layers of technical chrome to the damaged surface and then reduce the diameter to the nominal diameter in the process of abrasive machining. The last stage was the final assembly with the addition of lubricating liquid (Fig. 4).

Fig. 4. The engine of a Volkswagen Type 117 car at the assembly station

4. Conservation and renovation of unique powertrains

The examples of powertrains presented in the previous chapter concern historical objects. However, they are not unique because, due to the volume of production, there are still hundreds of such copies. The changes introduced in the publication do not affect their functionality. They are primarily used to improve the durability of drives and extend their service life. This offers the prospect of maintaining greater originality in the long term. Moreover, the implemented changes are inconsistent with the technologies originally used, but they constitute a small contribution to the originality of the objects.

Based on the authors' experience and in consultation with conservators, certain guidelines for the protection of unique objects have been formulated (Fig. 5). During conservation work carried out by both enthusiasts and conservators, it is very important to create documentation of the progress of the work. This not only has a positive impact on expanding operational knowledge but also allows for the preservation of the history of a specific object. Any documentation assigned to a vehicle should accompany it when transferred/sold to subsequent owners.

When referring to monuments of engineering art, unique in their existence or related to historical figures, the conservation process and possible renovation should be considered individually. For objects in a poor state of preservation, renovation means replacing most of the parts with new ones. In such a case, a better solution is to preserve the remnant and create a vehicle modeled on what remains of its original structure. Operation (even for demonstration purposes) is also not recommended for unique objects because each start-up of, e.g., a heat engine, involves its destruction. Examples of such objects that require special conservation care include a two-stroke stationary engine manufactured by "Motor Polski" from Żnin (1930, Fig. 5a), the prototype Ursus C-342 (1965, Fig. 5b), or the concept Polish car FSM Beskid. All objects have been preserved in fewer than 10 pieces, which makes them unique in the world. They are all in museums.

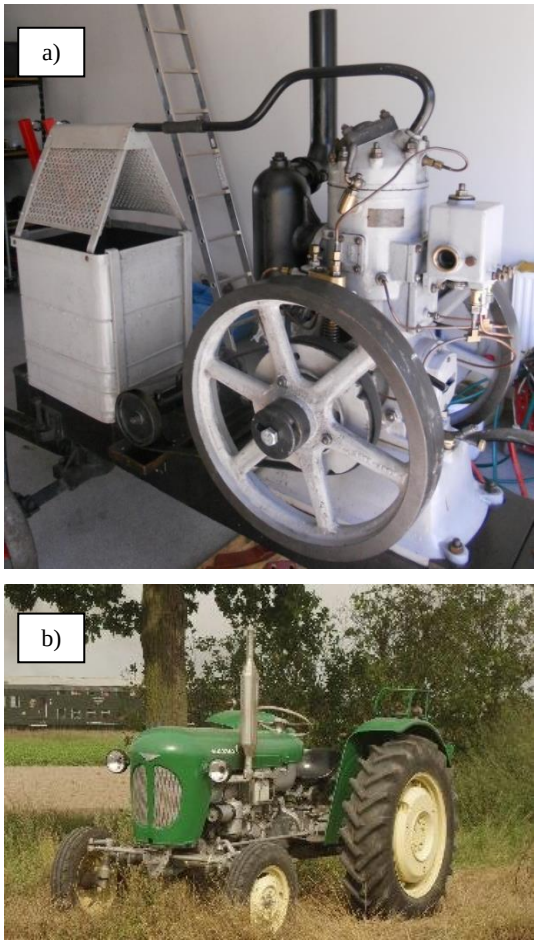

Fig. 5. Unique monuments of engineering art in the collections of the National Museum of Agriculture and Food Industry in Szreniawa: a) Motor Polski produced in Żnin in 1930, b) Ursus C-342 produced in Warsaw in 1965

Currently, it is very important to build awareness among people, especially those related to technical activities in the field of saving monuments of engineering art. Referring to

the topic of the article, each historic object related to powertrains and their operation or service should be protected against weather conditions. Consultations with historians or conservators should then be carried out, and on this basis, a decision should be made on further activities related to it. At the same time, conservators without technical education or experience should consult with engineers related to the field. Creating international organizations and societies will allow us to identify these types of facilities with greater precision and select the best security measures.

5. Summary

The article discusses the current issue of the protection and renovation of historic vehicles. Current national regulations apply to the entire facility, with no specific attention given to powertrains. German regulations are more restrictive. However, there are no guidelines for the entire European Union, which could unify activities and facilitate the exchange of information between member states, especially in the field of unique objects. It is necessary to disseminate knowledge about monuments of engineering art, unique objects. However, history enthusiasts and conservators have the greatest opportunities to save historic vehicles. It is also important to define guidelines and, later, regulations for the maintenance and renovation of powertrains. In the presented work, the authors of the article proposed certain procedures that are fundamental in the field of the problem being discussed.

An example of activities related to protecting unique objects on a larger scale was establishing the Tarpan Museum at the National Museum of Agriculture and Food Industry in Szreniawa. Many objects and documentation were collected there, and the memories of living employees and users were recorded. The collection is constantly being expanded, but significant promotional and research activities are required.

Bibliography

[1] Affelt A. All that's not fit to print. Emerald Publishing Limited. Leeds 2019. https://doi.org/10.1108/9781789733617

[2] Affelt W. Dziedzictwo techniki, jego różnorodność i wartości. Kurier konserwatorski (in Polish). 2009;5:5-20. https://bazhum.muzhp.pl/czasopismo/384/?idno=11528

[3] Bauer H, Dietsche K, Crepin J, Dinkler F. Bosch, Kraftfahrtechnisches Taschenbuch. 2003.

[4] Dmowski R, Winiarski J. Ciężkie motocykle radzieckie (in Polish). 2nd ed. Motopublica. 2008.

[5] Instrukcja o budowie, eksploatacji i obsłudze technicznej motocykla K-750 W (in Polish). Ministerstwo Obrony Narodowej. Warszawa 1966.

[6] Kontochristou M, Tzanavara A. Museums as a vehicle of cultural diplomacy. An international perspective. 2019. 110.

[7] Kuch J. VW Personenwagen mit Luftkühlung 1938-2003. Bucheli Verlag. 2014.

[8] Merkisz J. Engine manufacturing industry in Poland. Combustion Engines. 2005;122(3):12-21. https://doi.org/10.19206/CE-117396

[9] Pietrzak K. Revitalization of historical lifting devices: a challenge for the engineering art heritage protection in the context of incoherence between technical supervision regulations and heritage protection law. Wiadomości Konserwatorskie – Journal of Heritage Conservation. 2021;68:156-167.

[10] Rymaniak L. Restoration of K-750 motorcycle (in Polish). In: 4th International Conservation Conference – materials: Problems Connected with Keeping and Conservation of Collections in Museum. Szreniawa. 2010:123-131.

[11] Sawczuk W, Merkisz-Guranowska A, Rilo Cañás AM. Assessment of disc brake vibration in rail vehicle operation on the basis of brake stand. Eksploat Niezawodn. 2021; 23(2):221-230. https://doi.org/10.17531/ein.2021.2.2

[12] Straßenverkehrs-Zulassungs-Ordnung (StVZO). Bundesministerium fur Justiz. 2023. https://www.gesetze-im-internet.de/stvzo_2012/BJNR067910012.html

[13] The Act of 20 June 1997. The Law on Road Traffic. Chancellery of the Sejm, 1997. https://www.global-regulation.com/translation/poland/8881079/the-act-of-20-june-1997%252c-the-law-on-road-traffic.html

[14] Transport – wyniki działalności w 2022 r. Główny Urząd Statystyczny (in Polish). 2022.

[15] Walentynowicz J. Historia rozwoju silników cieplnych (in Polish). Wydawnictwa Naukowe Instytutu Lotnictwa. Warsaw 2011.

[16] Wisłocki K. Selected aspects of education of conservators for relics of engineering art. Museion Poloniae Maioris: Rocznik Naukowy Fundacji Muzeów Wielkopolskich. 2016; 3:52-53.

[17] Zhang C, Yang J. A history of mechanical engineering. Springer. Singapore 2020. https://doi.org/10.1007/978-981-15-0833-2

Prof. Łukasz Rymaniak, DSc., DEng. – Faculty of Civil and Transport Engineering, Poznan University of Technology, Poland.
e-mail: *lukasz.rymaniak@put.poznan.pl*

Natalia Szymlet, DEng. – Faculty of Civil and Transport Engineering, Poznan University of Technology, Poland.
e-mail: *natalia.szymlet@put.poznan.pl*

Franciszek Ratajczyk – Faculty of Mechanical Engineering, Poznan University of Technology, Poland.
e-mail: *franciszek.ratajczyk@student.put.poznan.pl*

Filip Woźniak – Faculty of Mechanical Engineering, Poznan University of Technology, Poland.
e-mail: *filip.wozniak@student.put.poznan.pl*

Article citation info:
Khrulev A, Saraiev O, Saraieva I, Vorobiov O. Modeling of thermodynamic processes in internal combustion engine cylinder during cranking in compression measurement tests. Combustion Engines. 2024;198(3):98-109. https://doi.org/10.19206/CE-187380

Alexander KHRULEV
Oleksii SARAIEV
Iryna SARAIEVA
Oleksandr VOROBIOV

Combustion Engines
Polish Scientific Society of Combustion Engines

Modeling of thermodynamic processes in internal combustion engine cylinder during cranking in compression measurement tests

ARTICLE INFO

Received: 22 January 2024
Revised:19March2024
Accepted: 17April2024
Available online: 1 July 2024

The thermodynamics of in-cylinder processes of the internal combustion engine in cranking mode when measuring compression were examined. Analysis of various theoretical models and comparison of known data showed that the problems of constructing mathematical models of the engine operating cycle remain unresolved. The vast majority of practical data and recommendations for measuring cylinder compression are based on empirical knowledge, numerous experiments, and tests. In accordance with this, there is a need for computational models of the compression measurement process and their theoretical justification. To solve the identified problems, a mathematical model of the thermodynamic processes in the cylinder was developed. Unlike existing ones, the model describes the processes in the cylinder step by step, taking into account the real nature of the intake-exhaust processes, air leakage through the interfaces of parts, and heat exchange with the walls. Using modeling, the main patterns of changes in compression depending on the modes, the nature of damage to the associated parts of the valve mechanism and cylinder-piston group, the amount of leakage, and engine temperature were found. Based on the results of the study, the properties of the model which make its use effective in diagnosing and monitoring the technical condition of engines in operation were concluded.

Key words: *cold cranking, compression, diagnostics, hydrolock, modeling*

1. Introduction

It is known that measuring the maximum pressure – compression in the cylinders of an internal combustion engine is one of the most common methods for diagnosing technical conditions and determining the causes of various faults in operation [9]. This check is usually provided at the preliminary stage of research since it does not require dismantling numerous engine parts and units. Thus, compression measurement is a non-destructive method for monitoring the technical condition in which the object under study fully retains its functions. This property of the method is essential for some types of research, for example, during automotive technical expertise.

Another undoubted advantage of measuring compression is the simplicity and low cost of the measuring device itself, a compression meter, as well as the simplicity of the algorithm for its use (Fig. 1). As a result, the method has become extremely widespread in practice as one of the most universal diagnostic methods, and the maximum pressure in the cylinder has been included in almost all service and repair manuals for most automotive engine brands and models [6].

At the same time, the vast majority of practical data and recommendations for the use of the method under consideration are based on empirical knowledge, numerous experiments, and tests [21]. The consumer is encouraged to trust the recommendations of specialists, who usually associate the amount of compression drop from a certain "normal" level with a specific type of damage and/or fault. However, the consumer does not have any models or methods for calculation or checking any parameters that he measures for its adaptation to his engine. Therefore, the consumer cannot check this or that figure, recommendation, or assumption about the connection of a measurement result with a fault and also adjust the received data in accordance with his own conditions.

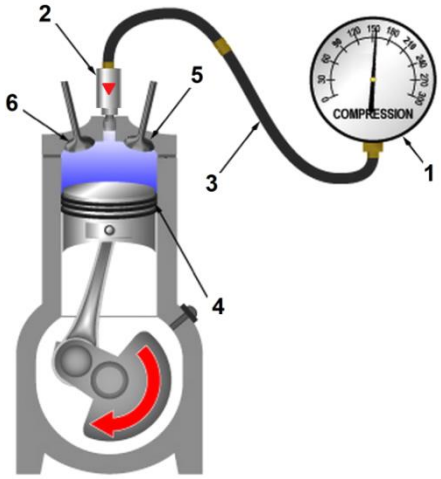

Fig. 1. Scheme for measuring compression in the engine cylinder and the main points of air leakage from the cylinder: 1 – pressure gauge, 2 – check valve, 3 – connecting tube, 4 – piston rings, 5 – intake valve, 6 – exhaust valve

At the same time, such a check may be important for practice due to the design features of the engine under study, which may influence changes in the compression value under various operational damages. However, quantitative assessments and, especially, verification of certain data related to the magnitude of compression are extremely expensive since they require experimental studies of large volume and complexity. Hence, the need arises for computational models of the compression measurement process and their theoretical justification.

2. Sources review and problem statement

The method of measuring compression itself is extremely simple and is accessible not only to a qualified or initial mechanic but also to an ordinary driver. Therefore, a significant number of sources provide numerous practical recommendations on the algorithm and interpretation of the results obtained. Thus, in [11], data are presented that make it possible to determine many malfunctions of the valve mechanism and cylinder-piston group by changes in compression, including burnout of valves, wear and sticking of piston rings, etc.

However, available data indicate that compression measurements should be treated with caution due to the inaccuracy of the method itself and the large variation of measuring results. As a result, erroneous conclusions may be obtained not only about the cause but generally about the presence of a fault as such. This is due to the strong influence of rotation speed on compression noted in many sources [26], which may be caused by differences in test conditions. Such differences are due to changes in ambient temperature, engine temperature, battery and starter condition, oil viscosity, etc.

Moreover, only one compression value measured by a compression meter (and other similar devices) generally does not provide a complete picture of the current engine's technical condition. As a result, other methods have become widespread in diagnostic practice.

One such method is pressure oscillography in cylinders. Indeed, with the help of a pressure transducer [23], an oscilloscope makes it possible to identify deviations of the instantaneous pressure diagram in a cylinder from the normal profile and thereby localize and find the cause [27]. However, the oscillography method has the same disadvantages and features as conventional compression measurements. To apply the method, it is necessary to have detailed information on how the shape of the diagram is affected by various damage and faults. And this knowledge is currently based only on experimental data [11, 21].

An alternative to measuring compression can also be methods such as measuring the power balance of cylinders on the one hand and building an indicator diagram (including its modeling) on the other. These methods require the presence of expensive measuring equipment (for example, motor testers to determine the power balance) or even special preparation of the engine (for example, for installation of a pressure sensor). However, the power balance is not informative enough for fault determination, even compared to compression measurements [32]. The study of the indicator diagram is further complicated by the need to test the engine under load, which for an automobile engine is only possible on extremely expensive special test benches [19]. In addition, large amplitudes of pressure and temperature, as well as the relatively high frequency of the process, characteristic of measurements during the operation of automobile engines, create problems for both measurement and analysis of the resulting diagrams, including the determination of the influence of various faults on them [36]. Similar problems arise when modeling these processes. Moreover, some serious engine damage and faults prevent the ignition of the fuel and operation of the cylinder altogether, which makes it difficult to analyze the indicator diagram of such a cylinder.

These problems impose restrictions on the widespread practical use of power balance and indicator diagram analysis for diagnosing automobile engines in operation. In this regard, the experimental study, modeling, and analysis of a compression diagram in cold cranking mode seem to be a much simpler, technically, and financially accessible diagnostic method. Therefore, there is reason to believe that this method is more promising for further research and practical use of the results obtained.

Another problem that requires a detailed analysis of the diagram of pressure changes in the cylinder during cold cranking of the engine (without fuel combustion) is associated with determining the characteristics of a cold start [20]. Startup simulation allows you to evaluate the starting properties of the engine, especially at low temperatures. This task is close to the problem of measuring compression. However, it is not aimed at diagnosing the technical condition of a particular engine in operation but most often at design work to improve the starting characteristics of the engine [4], determining the starting fuel supply [25], assessing harmful emissions [30], etc.

It was in the study of engine starting characteristics and not in diagnostics and monitoring that various theoretical models of cold cranking became widespread [29]. The next step in this direction can be considered probabilistic-statistical methods [24, 35], in which data arrays are considered, and the probabilistic values of parameters are analyzed. Such methods can be effective for diagnostics, including when used in software diagnostic systems [33]. However, the models that usually form the basis of such methods are quite far from the process model of the engine under study. They can be conditionally called integral since they do not detail the instantaneous processes occurring in the engine but operate only with external signs and parameters [34].

At the same time, it should be noted that the need for detailed calculation of starting processes and characteristics required the development of theoretical methods and models that allow step-by-step modeling of processes based on the angle of rotation of the crankshaft. The simplest solutions are provided by analytical methods built on the basis of dependencies for polytropic compression-expansion processes [28]. However, it is difficult to obtain quantitative data to identify various damages and faults using such methods.

Mathematical modeling methods have received the greatest development in the programs for calculating the operating cycle of engines. A number of programs have acquired well-known status and become standard – these are AVL-Boost [1], Ricardo-Wave [5], GT-Power [3] and Lotus Engine Simulation [18]. These programs are built on the basis of a 0-dimensional thermodynamic representation of a cylinder as a control volume with instantaneous parameters of the working fluid uniformly distributed throughout the volume [7].

This approach makes it possible to calculate instantaneous cycle parameters based on the angle of rotation of the crankshaft at any operating mode [22], that is, exactly what

is required when studying compression in the cylinder and/or cold start. However, when trying to simulate, a problem is revealed: due to limitations, not all standard programs have the function of simulating the cold cranking mode without fuel combustion in the cylinder, taking into account various damages and other necessary functions [28]. As a result, the development of a user model of the engine cold cranking mode, designed to study the patterns of measuring compression in the cylinder, has virtually no alternative.

In accordance with this, the purpose of the work is to study the working process in the cylinder of an internal combustion engine during cold cranking and obtain quantitative characteristics of compression under various operational damages.

To achieve the goal, it is necessary to solve the following tasks:

1) develop a mathematical model of the process in the cylinder during engine cold cranking
2) carry out modeling in different modes and under different conditions of the cylinder-piston group and valve mechanism, compare the results obtained with experimental data
3) validation and setting-up the model
4) analyze the results obtained, determine general patterns connecting the amount of compression with various types of damage to engine parts.

3. Mathematical model of the process in the cylinder during engine cold cranking

To derive the design equations, consider the diagram of the cylinder (Fig. 2).

From the 1st law of thermodynamics [7], written for the cylinder, it follows:

$$dU = dQ - dL + idM \tag{1}$$

where dU is the change in the internal energy of the air in the cylinder; dQ is amount of heat supplied (+) or removed (–); L is work of air; i is enthalpy of air; dM is change in air mass in the cylinder due to inflow into the cylinder (+) or outflow (leakage) from the cylinder (–).

Let's transform equation (1):

$$d(MC_VT) = dQ - pdV + idM \tag{2}$$

The value $idM = \sum i_i dM_i$ takes into account the mixing of air flows with different temperatures. In the cold cranking mode at a low rotation speed, when air flows out of the cylinder, it has a temperature T, close to the ambient temperature T_0. At the same time, air flows into the cylinder when there is a vacuum in it during the intake stroke, when the temperature of the air in the cylinder is also close to the temperature of the environment and the incoming air. In accordance with this, we can neglect the difference in flow temperatures and accept $idM = i\sum dM_i$. From where, taking into account the ideal gas equation of state

$$p = \frac{M}{V}RT \tag{3}$$

from equation (2) we get:

$$MC_V dT + C_V T dM = dQ - \frac{MRT}{V}dV + C_p T dM \tag{4}$$

where p is pressure in the cylinder; V is the volume of gas in the cylinder; R is gas constant; C_V, C_p are heat capacities at constant pressure and volume.

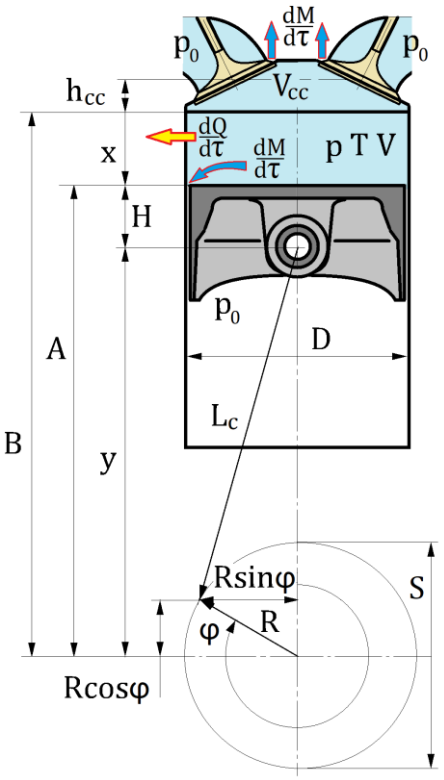

Fig. 2. Calculation diagram of the process in the cylinder during cold cranking

Further transformations of equation (4) give:

$$C_V\frac{dT}{T} = -R\frac{dV}{V} + (C_p - C_V)\frac{dM}{M} + \frac{dQ}{MT} \tag{5}$$

The heat capacities are related by the relation $C_p = \gamma C_V = \gamma R/(\gamma - 1)$, where γ is the air heat capacity ratio (adiabatic index). In addition, the current volume of air in the cylinder is equal to

$$V = V_x + V_{cc} = V_x + \frac{V_h}{\varepsilon - 1} = F_p x + \frac{F_p S}{\varepsilon - 1} = \\ = F_p(x + h_{cc}) \tag{6}$$

where V_x is current cylinder volume; V_{cc} is volume of combustion chamber; V_h is the working volume of the cylinder; ε is geometric compression ratio; F_p is piston area; x is piston coordinate from top dead center [2]; $h_{cc} = V_{cc}/F_p = S/(\varepsilon - 1)$ is reduced height of the combustion chamber, S is piston stroke.

Obviously, the change in the volume of the cylinder $dV = F_p dx$, according to which equation (5) can be rewritten as:

$$\frac{dT}{T} = \frac{(\gamma - 1)}{R}\left[-R\frac{dV}{V} + \left(\frac{\gamma}{\gamma - 1} - \frac{1}{\gamma - 1}\right)R\frac{dM}{M} + \frac{dQ}{MT}\right] \tag{7}$$

This implies a differential equation for the air temperature in the cylinder:

$$\frac{dT}{T} = \frac{(\gamma - 1)}{x + h_{cc}}\left[-dx + \frac{RT}{pF_p}\left(dM + \frac{dQ}{RT}\right)\right] \quad (8)$$

On the other hand, differentiating the equation of gas state (3), we obtain:

$$dp = \frac{dM}{V}RT + \frac{dT}{V}MR - \frac{MRT}{V^2}dV \quad (9)$$

or

$$\frac{dp}{p} = \frac{dM}{M} + \frac{dT}{T} - \frac{dV}{V} \quad (10)$$

Now, substituting equation (7) into equation (10), we obtain a differential equation for the air pressure in the cylinder in the form:

$$\frac{dp}{p} = \frac{\gamma}{x + h_{cc}}\left[-dx + \frac{RT}{pF_p}\left(dM + \frac{\gamma - 1}{\gamma}\frac{dQ}{RT}\right)\right] \quad (11)$$

As it is known from engine theory [10], the position of the piston in the cylinder x is determined by the angular position of the crankshaft φ, measured from top dead center when the valves overlap. In accordance with Fig. 2, the x coordinate can be expressed by the formula:

$$x = A - B = (R + L_c + H) - (y + H) = R + L_c - \\ -R\cos\phi - \sqrt{L_c^2 - R^2\sin^2\phi} \quad (12)$$

where R, L_c are the radius of the crank and the length of the connecting rod; H is the compression height of the piston.

Taking into account the fact that the piston stroke S is equal to two radii of the crank, the position of the piston from top dead center will be

$$x = \frac{S}{2}\left(1 + r - \cos\phi - \sqrt{r^2 - \sin\phi}\right) \quad (13)$$

where $r = 2L_c/S$ is relative length of the connecting rod.

It is known [27] that the value of the desired compression in the cylinder is largely determined by leakage from the cylinder and heat losses, which depend mainly on the process time. In accordance with this, it is convenient to seek a solution to the problem from the time of the process associated with the angular position of the crankshaft by the formula:

$$d\phi = \omega d\tau = \frac{\pi n}{30}d\tau \quad (14)$$

where n is the crankshaft rotation speed, rpm (to the 1st approximation, the rotation speed during cranking is assumed to be constant and independent of the process time and the angular position of the crankshaft).

Then, if all equations (8) and (11) are divided by the time increment dτ, we can obtain a mathematical model of the process under study [8, 13] as the system of 1st order differential equations resolved with respect to the derivative, in the form:

$$\begin{cases} \frac{dT}{d\tau} = \frac{(\gamma - 1)}{x + h_{cc}}T\left[-\frac{dx}{d\tau} + \frac{RT}{pF_p}\left(\frac{dM}{d\tau} + \frac{1}{RT}\frac{dQ}{d\tau}\right)\right] \\ \frac{dp}{d\tau} = \frac{\gamma}{x + h_{cc}}p\left[-\frac{dx}{d\tau} + \frac{RT}{pF_p}\left(\frac{dM}{d\tau} + \frac{\gamma - 1}{\gamma RT}\frac{dQ}{d\tau}\right)\right] \end{cases} \quad (15)$$

To solve system (15), in addition to the initial conditions, it is necessary to determine some quantities and variables included in the equations.

Thus, the piston speed can be obtained analytically by differentiating equation (13), which determines the current position of the piston

$$\frac{dx}{d\tau} = \frac{\pi Sn}{60}\sin\phi\left(1 + \frac{\cos\phi}{\sqrt{r^2 - \sin\phi}}\right) = \\ = v_m\frac{\pi}{2}\sin\phi\left(1 + \frac{\cos\phi}{\sqrt{r^2 - \sin\phi}}\right) \quad (16)$$

where $C_m = Sn/30$ is average piston speed.

The change in air mass in the cylinder is determined by the airflow through the valves and leak points. When the pressure in the cylinder is higher than atmospheric, the airflow from the cylinder through a certain hole (gap, slot) is determined by the well-known formula [12]:

$$\frac{dM_i}{d\tau} = -\mu\frac{\rho f_i}{\sqrt{RT}}\left(\frac{p_0}{p}\right)^{\frac{1}{\gamma}}\sqrt{\frac{2\gamma}{\gamma - 1}\left[1 - \left(\frac{p_0}{p}\right)^{\frac{\gamma - 1}{\gamma}}\right]} \quad (17)$$

where μ is flow coefficient; f_i is the cross-sectional area through which flow or leakage occurs; p_0 is ambient pressure (it is assumed that at a low speed corresponding to the compression measurement, the pressure in all channels adjacent to the cylinder and in the crankcase is equal to the ambient pressure).

When the pressure drop changes to reverse (vacuum in the cylinder) and air flows into the cylinder, formula (17) takes the form:

$$\frac{dM_i}{d\tau} = \mu\frac{\rho_0 f_i}{\sqrt{RT_0}}\left(\frac{p}{p_0}\right)^{\frac{1}{\gamma}}\sqrt{\frac{2\gamma}{\gamma - 1}\left[1 - \left(\frac{p}{p_0}\right)^{\frac{\gamma - 1}{\gamma}}\right]} \quad (18)$$

In general, air can flow into (and out of the cylinder) several flows: through the intake valve dM_{in}/d, exhaust valve $dM_{ex}/d\tau$, leaks (gaps, damage) in the interface of intake valves $dM_{lin}/d\tau$ and exhaust valves with seats $dM_{lex}/d\tau$ as well as piston rings with cylinder and ton $dM_{lc}/d\tau$. Rare cases of head gasket failure, cracks in the cylinder head and block can be taken into account by analogy. In accordance with this, the total air flow into or out of the cylinder (change in air mass) is defined as

$$\frac{dM}{d\tau} = \frac{dM_{in}}{d\tau} + \frac{dM_{ex}}{d\tau} + \frac{dM_{lin}}{d\tau} + \frac{dM_{lex}}{d\tau} + \frac{dM_{lc}}{d\tau} \quad (19)$$

To determine the airflow through the valve, consider the connection between the valve and the seat (Fig. 3a).

Let us assume, to the 1st approximation and for simplifying the calculating formulas, that the valve, when lifted by an amount h, opens a section f_v, equal to the area of the lateral surface of the truncated cone, which is perpendicular

to the working chamfer of the valve, of the seat and to the direction of airflow. Then, from the obvious geometric relationships:

$$f_v = \frac{\pi}{2}(d + d_1)h\cos\alpha \qquad (20)$$

where α is valve chamfer angle; d is valve head diameter; $d_1 = d - 2h\sin\alpha\cos\alpha$ is the diameter of the small base of the cone in Fig. 3a.

After the transformations, we obtain the area opened by the valve (inlet or outlet) depending on the height of its lift:

$$f_v = \pi dh\left(1 - \frac{h}{d}\sin\alpha\cos\alpha\right)\cos\alpha \qquad (21)$$

Instead of the approximate formula (21), you can also use more accurate relationships for the flow area that is opened by the valve [14]. However, the expression (21) for the problem under consideration is simpler. The reason is that at low rotation speeds during cold cranking, the pressure drops across the valves are small (this can be seen in the diagrams of compression measuring [26, 34]). Therefore, the airflow should be influenced mainly by the valve timing, i.e., the moments of opening and closing of valves, but not by the valve lift profiles and/or the flow area they open.

a)

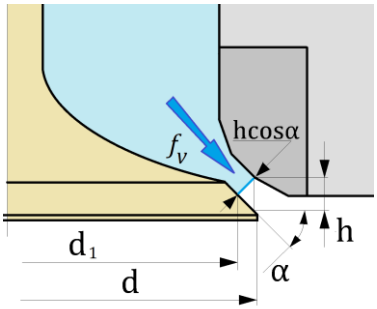

b)

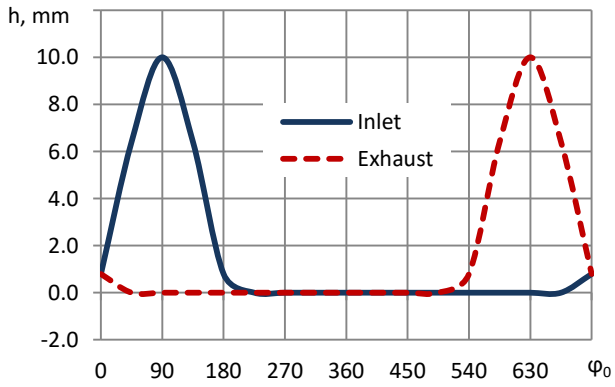

Fig. 3. Calculation diagram for the cross-sectional area opened by the valve (a) and the program for controlling the valve timing (b), adopted when simulating cold cranking

According to [14], at a low rotation speed of 200–300 rpm, usually corresponding to compression measurements, the flow coefficient μ included in formulas (17) and (18) can be taken equal to 1.0 with sufficient accuracy. Then, to determine the air flow using these formulas, it remains to find the valve lift height. To do this, let us set the valve lift profile within the crankshaft rotation angles that correspond to the valve timing. To a first approximation, it is possible to assume for both valves a lift profile corresponding to the sinusoidal law [22]. The simplest form of this is the relationship (Fig. 2b):

$$h = \begin{cases} 0.5h_0(1 + \sin\beta) - \delta, & h > 0, \varphi_{VO} < \varphi < \varphi_{VC} \\ 0, & \varphi < \varphi_{VO}, \varphi > \varphi_{VC} \end{cases} \qquad (22)$$

where h_0 is the maximal lift; δ is a clearance in the valve drive; φ_{VO}, φ_{VC} are valve opening and closing angles, $\Delta\varphi_V = \varphi_{VC} - \varphi_{VO}$ is valve opening duration (Fig. 3b); β is auxiliary angle determined by the crankshaft rotation angle φ:

$$\beta = 2\pi\frac{\varphi - \varphi_{VO}}{\varphi_{VC} - \varphi_{VO}} - \frac{\pi}{2} = 2\pi\frac{\varphi - \varphi_{VO}}{\Delta\varphi_V} - \frac{\pi}{2} \qquad (23)$$

To calculate the airflow caused by leaks from the cylinder, the area fi of the elements through which the leak occurs must be determined. Such elements can be a gap between the valve and the seat of size λ_v and cross-sectional area f_c, a gap between the piston ring and the cylinder of size λ_p and area f_p, a sector on the valve head from a chip or burnout of size c, as well as a burnout hole on the piston with a diameter of Δ:

$$f_v = \pi D\lambda_v,\ f_p = \pi D\lambda_p,\ f_c = \frac{\pi}{8}c^2,\ f_\Delta = \frac{\pi}{4}\Delta^2 \qquad (24)$$

The last parameter that needs to be determined in the system of equations (15) is the heat flow from the air into the walls of the cylinder and combustion chamber. The assumption that the temperature of the engine walls T_w is constant over time and uniform across sections approximately corresponds to the condition for measuring the compression of a "warm" engine. Then, the heat flow from the air into the wall (and from the wall to the air) can be determined by the formula:

$$\frac{dQ}{d\tau} = (F_p + F_x + F_{cc_1} + F_{cc_2})\alpha_w(T - T_w) \qquad (25)$$

where α_w is heat transfer coefficient between air and walls; F_x is area of the cylinder side surface opened by the piston; F_{cc_1} is area of the side surface of the combustion chamber; F_{cc_2} is area of the end surface of the combustion chamber.

If we approximately assume that the area of the end surface of the combustion chamber is equal to the area of the piston F_p, and the area of the side surface of the combustion chamber is proportional to its reduced height h_{cc}, then the formula (25) can be written as:

$$\frac{dQ}{d\tau} = -\pi D\alpha_w\left(\frac{D}{2} + x + h_{cc}\right)(T - T_w) \qquad (26)$$

The main difficulty in taking into account heat losses in the process under study is the correct determination of the heat transfer coefficient. Well-known formulas for calculating the heat transfer coefficient for engines are usually obtained for other conditions. In the general case, they are not suitable for the cold scrolling mode, which is characterized by tens of times lower rotation speeds, the absence of combustion, radiant heat transfer, etc. However, in [28] for the cold scrolling mode, the choice of the Woschni formula

was justified, which gives the dependence on the heat transfer coefficient in the form:

$$\alpha_w = 130\frac{(p\cdot 10^{-5})^{0.8}\omega_m^{0.8}}{T^{0.53}D^{0.2}} \quad (27)$$

where $\omega_m = 2.28C_m$ for gas exchange and compression.

To simplify the debugging of the calculation algorithm, heat transfer in the cylinder was not taken into account. According to the equations of system (15), the heat flow from the air to the walls (and vice versa) affects the temperature and pressure of the air in the cylinder, similar to the effect of airflow during leaks. For example, when pressure increases, leaks from the cylinder are accompanied by heat loss from heated air into the walls. And vice versa, when air flows into the cylinder, heat is supplied to it from the heated walls. This feature made it possible, to a first approximation, not to determine heat losses but to take into account their influence on the process by increasing the area of air leakage from the cylinder. In this case, system (15) will take the following simplest form [15]:

$$\begin{cases}\dfrac{dT}{d\tau} = (\gamma-1)\,\psi\,T\\ \dfrac{dp}{d\tau} = \gamma\,\psi\,p\\ \psi = \dfrac{1}{x+h_{cc}}\left(-\dfrac{dx}{d\tau}+\dfrac{RT}{pF_p}\dfrac{dM}{d\tau}\right)\end{cases} \quad (28)$$

System (28) is solved numerically with initial conditions: at $\tau = 0$, $\varphi = 0$, $x = 0$, $T = T_0$, $p = p_0$. For the solution, the 2nd order Runge-Kutta method (modified Euler method) was used [17]. However, when carrying out test calculations, it turned out that the solution had signs of instability (self-oscillations of pressure) at small pressure drops during the intake-exhaust process, especially near valve overlap. Self-oscillations manifested themselves most strongly with significant leaks from the cylinder in the case of modeling serious damage (for example, burnt valves).

It was not possible to suppress the oscillations by reducing the step and increasing the order of the method above the 2nd, and with large leaks from the cylinder, the simple Euler method of the 1st order gave even less instability than the Runge-Kutta method of the 2nd and higher orders. Ultimately, to improve the stability of the solution in the intake-exhaust region, artificial smoothing was applied for pressure using an additional term with a smoothing coefficient ϑ:

$$p_i = p_{i-1} + \frac{\Delta\tau}{2}\left(\frac{dp_i}{d\tau}+\frac{dp_{i-1}}{d\tau}\right) + \vartheta(p_i + p_{i-2} - 2p_{i-1}) \quad (29)$$

As follows from (29), smoothing does not affect the calculated pressure value if the pressure is constant or changes smoothly (straightforward), but in the case of a sharp change in pressure, smoothing affects it in the opposite direction.

Artificial smoothing was introduced only when the intake and/or exhaust valves were open. At a low value of the coefficient ϑ, smoothing did not have any effect on the calculation results (the difference in the maximum compression value did not exceed 0.1%). As a result of test calculations, the smoothing coefficient was accepted to 0.2 from the condition of maximum suppression of self-oscillations of pressure in the cylinder during intake and exhaust. Self-oscillations were also noted for temperature, but its smoothing was not carried out due to small amplitude.

Debugging of the model and algorithm was carried out in Excel environment. The angle step was set from the condition of 1000 points per 1 cycle (2 revolutions of the crankshaft), which at a rotation speed of 200 min^{-1} corresponded to a time step of 0.0006 s. The choice of step was due to the fact that its decrease did not lead to a change in the accuracy of the calculation and improvement of stability, while its increase caused an increase in instability.

4. Validation and setting up the model

To validate the model, we used experimental data obtained by measuring compression on different engines of the same type, having different technical conditions [31]. The main patterns of cold cranking in the process of measuring compression were studied using the example of an engine with dimensions D × S = 76 × 71 mm, compression ratio $\varepsilon = 9.9$, with a 2-valve cylinder head, with valves with a diameter of 37 and 32 mm, a working chamfer angle $\alpha = 45^o$, valve lift of $h_0 = 10$ mm and valve timing: the intake valve opening $\varphi_{OV} = 696^o$ (24^o to the top dead center) with a duration of 264^o and the exhaust valve opening $\varphi_{OV} = 486^o$ (54^o to the bottom dead center) with a duration of 258^o.

During the experiments, instantaneous pressure in the cylinder was measured over time using a strain gauge of the MD-10B model, which was screwed into the hole for the spark plug (Fig. 4).

a)

b)

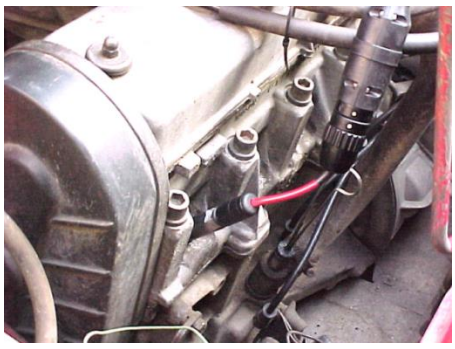

Fig. 4. MD-10B pressure sensor (a) and its connection to the spark plug hole on the engine (b)

The sensor signal, after amplification and conversion in an analog-to-digital converter, was recorded in the comput-

er memory. To process the recording, a user program was used [31], which presented the measurement results in the form of tables (Fig. 5) and a time sweep (oscillogram) of pressure.

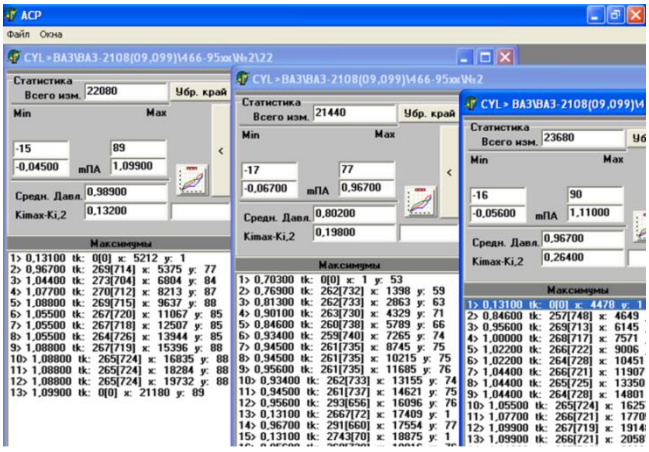

Fig. 5. Program interface for recording and processing compression measurement results

Under the assumption of a constant rotation speed when measuring compression, the pressure diagrams were saved both over time (Fig. 6a) and over the crankshaft rotation angle (Fig. 6b) [31].

a)

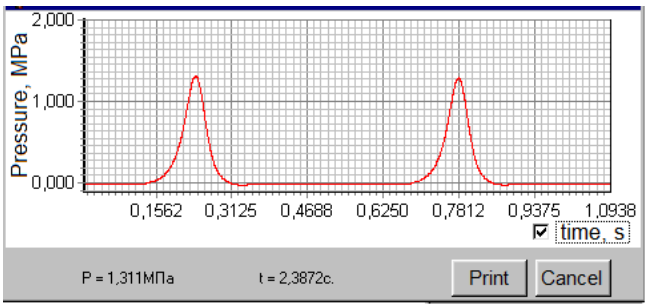

b)

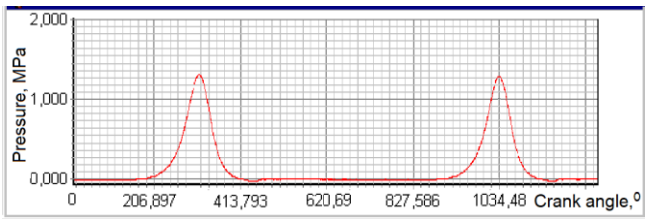

Fig. 6. Diagrams of cylinder pressure over time (a) and by crankshaft rotation angle (b), obtained using a data processing program

This data was used to set-up the model. For this purpose, parametric modeling was performed, in which the amount of leakage through the piston rings was changed by changing the conditional gap in the interface between the ring and the cylinder. From the condition that the maximum compression value corresponds to the experimental data shown in Fig. 6, the value of the conventional gap between the piston ring and the cylinder was determined to be λ_v = 0.028 mm.

In Figure 7a,the results of calculating the cold cranking cycle of an engine with a leak specified using the model settings are presented. After this, the experimental and calculated diagrams were superimposed (Fig. 7b).

a)

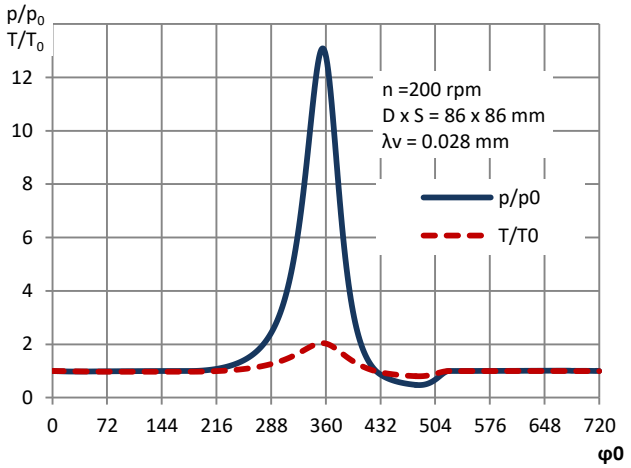

b)

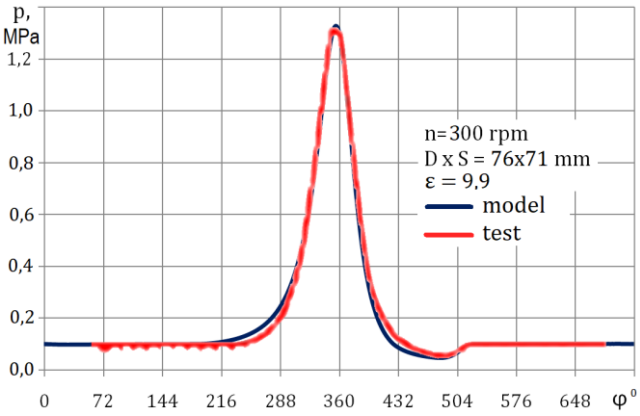

Fig. 7. Results of validation and setting-up the model: modeling pressure and temperature in the cylinder for a given leakage through the piston rings (a) and comparison of calculated and experimental diagrams by superimposing them on each other with the same coordinate axes (b)

The resulting curves show, on the whole, a satisfactory agreement between the calculations and the experiment. It is noteworthy that the obtained curve corresponds to the experimental diagram both in form and quantitatively. However, the clearest results were obtained when various types of damage were introduced into the model. For this purpose, several of the most characteristic ones were selected from the existing database of compression tests [31] (Fig. 8).

A comparison of modeling results and experimental data was carried out for several types of damage, including leakage of the valve-seat interface (Fig. 9).

The obtained data not only shows the consistency of the simulation data with the tests but also allows for adjustment of the model in case the characteristic size of the damage is not accurately determined. This makes it possible to model a variety of damage to specific engines, including those for which there is currently insufficient data.

a)

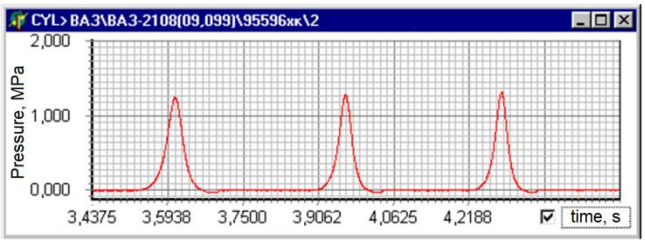

b)

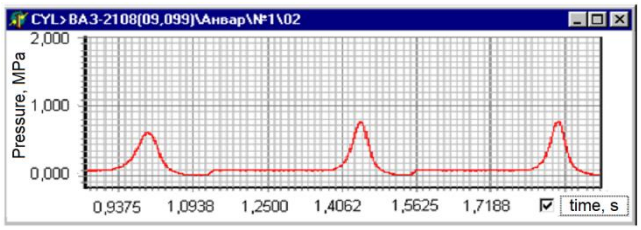

c)

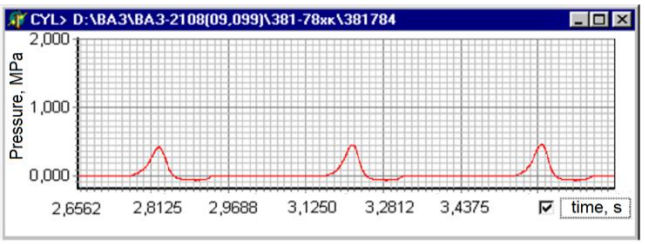

d)

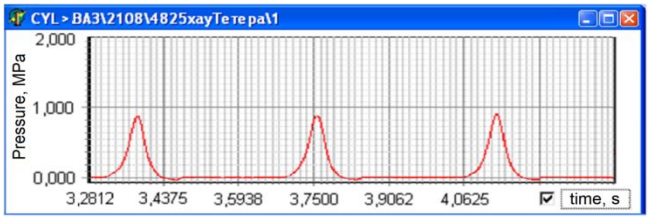

Fig. 8. Diagrams of pressure in the cylinder obtained during testing of one type of engine [33]: a) cylinder-piston group and valve mechanism in normal condition, b) severe wear of the piston rings, c) leakage of the valve-seat interface; d) presumably a drop in pressure due to hydrolock and deformation of the connecting rod

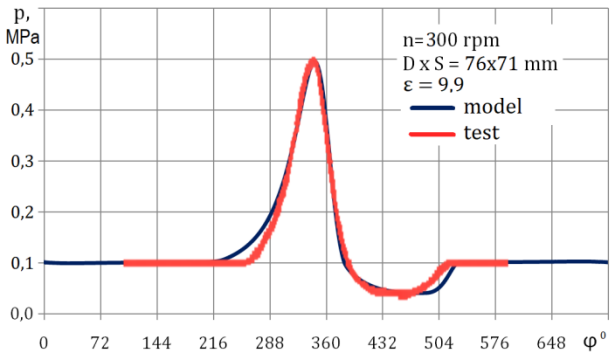

Fig. 9. Comparison of damage modeling results with experimental data for leaking valve-seat interface (diagram c in Fig. 8)

5. Simulation results for different conditions of the cylinder-piston group and valve mechanism, comparison with experimental data

The general picture of the influence of various types of damage on compression, calculated using the model, is presented in Fig. 10.

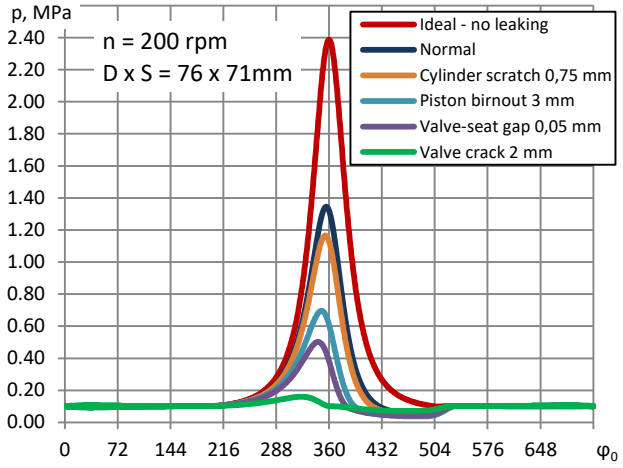

Fig. 10. The influence of various types of damage on compression obtained by modeling

Pressure change curves during cold cranking are shown sequentially for the following damage:

1) deep vertical scratch on the cylinder 0.75 mm wide
2) burnout of the piston with an equivalent flow area corresponding to a hole with a diameter of 3 mm
3) non-adhesion of the valve to the seat by 0.05 mm
4) burnout or chip on the valve head 2 mm wide.

For comparison, the diagram (Fig. 10) also shows pressure curves in a normal state (with a given leakage through the rings) and in an ideal engine with no leaks at all.

The capabilities of the developed model are demonstrated in Fig. 11, in which you can see the calculated effect of a scratch (scuff) on the cylinder surface on compression (Fig. 11a). At the same time, the most important for operational practice and diagnostics is the dependence of compression on rotation speed during cold cranking (Fig. 11b).

a)

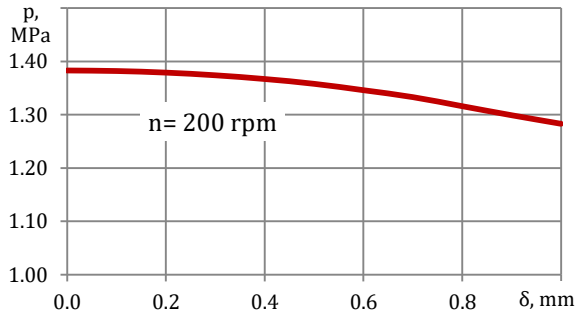

b)

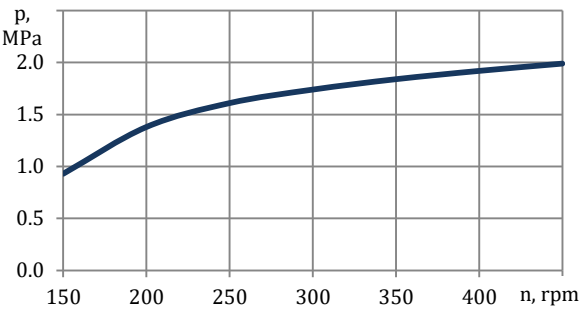

Fig. 11. Results of modeling the influence of the size of a vertical scratch on the cylinder (a) and rotational speed (b) on compression

The introduction of an additional module for calculating heat losses into the calculation model and the use of the system of equations (15) instead of (27) made it possible to further identify the effect of heat losses on compression (Fig. 12).

In the case under consideration, with a given geometry and cold cranking mode at an engine temperature of 50°C, heat losses calculated using the Woschni formula caused a decrease in compression from 1.21 to 1.11 MPa, i.e. by approximately 8%.

The model also makes it possible to simulate and predict the magnitude of compression in the event of faults for which there is currently no reliable statistical data. For example, during a hydraulic lock from liquid entering the cylinder [16], longitudinal deformation (shortening due to buckling) of the connecting rod is possible. In this case, the engine geometric compression ratio will be reduced, which will cause an obvious decrease in the maximum pressure in the cylinder. The model makes it possible to fairly accurately describe this process on a pressure diagram when measuring compression (Fig. 13).

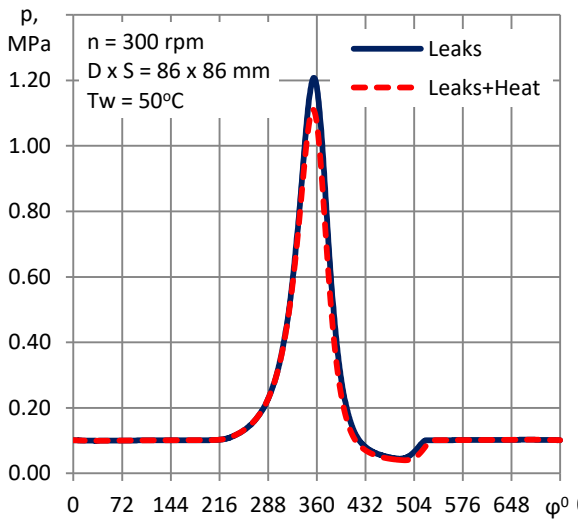

Fig. 12. Calculated effect of heat exchange on compression (engine temperature 50°C)

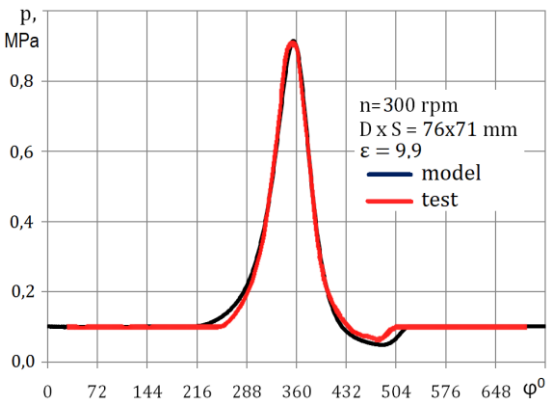

Fig. 13. Comparison of the calculated and experimental diagram of the pressure in the cylinder after hydrolock (diagram d in Fig. 3d). This diagram corresponds to longitudinal deformation (shortening) of a connecting rod of 2.6 mm

A comparison of diagrams for different damage, but with approximately close maximum compression values (Fig. 14), shows the following. During a hydrolock, if the parts of the cylinder-piston group do not receive significant damage (the engine remains operational), the difference in the diagrams of normal and damaged engines is observed only in the upper part of the pressure curve. But if the drop in compression is caused by damage associated with air leaks from the cylinder, the differences in the diagrams will also be significant in the lower part, namely, in the shape and size of the compensation pocket. The reason for such differences requires analysis and explanation.

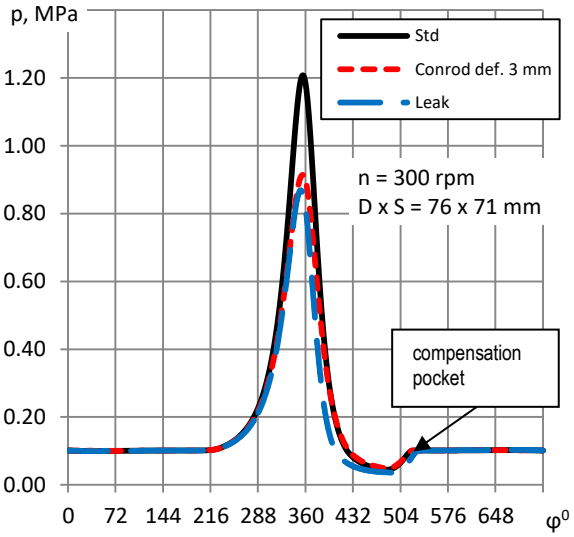

Fig. 14. Influence of the type of damage on the pressure diagram: deformation (shortening) of the connecting rod during hydrolock affects only the upper part of the curve, while additional air leaks from the cylinder also affect the size and shape of the compensation pocket.

Encouraging simulation results also allow us to study the effect of repair defects on compression. Figure 15 shows the results of modeling the variation of the compression diagram due to an error in setting-up the valve timing.

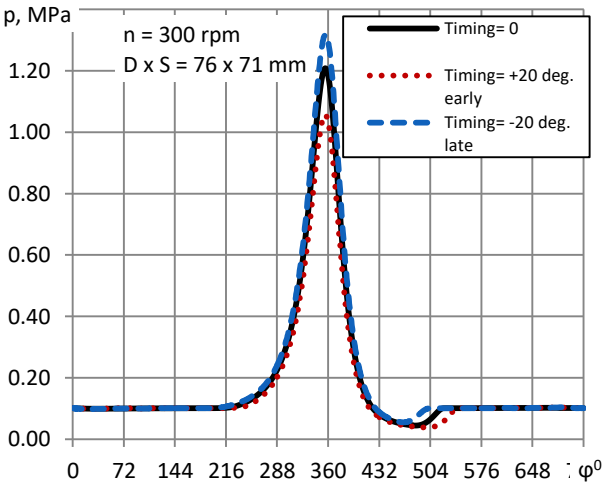

Fig. 15. The influence of the valve timing shift on the compression diagram

The effect of the maximum pressure in the cylinder of a shift in the setting angle of the valve timing from the nominal value is shown in Fig. 16.

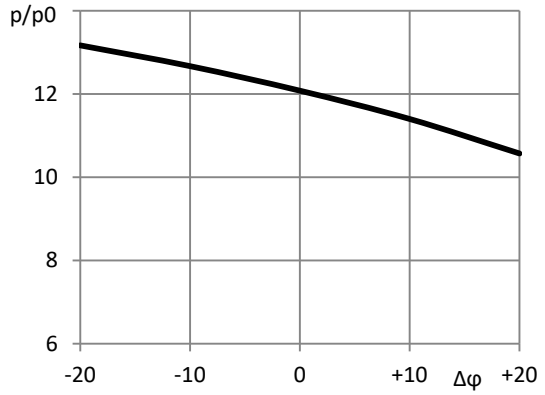

Fig. 16. Maximum pressure in the cylinder as a function of changing the valve timing angle from the nominal zero value

The model as a whole well confirms the nature of compression changes known from practice. So, a clockwise shift of the camshaft relative to the crankshaft (early valve timing, for example, due to a repair error) causes a decrease in compression. A shift in the opposite direction (later valve timing, for example, due to driving belt or chain jumping), on the contrary, leads to an increase in compression. This is important for some engines of previous years of production that did not have a camshaft position sensor when an error in setting up the valve timing is not shown by the control system. However, the most important is quantitative data, including changes in the width of the compensation pocket (Fig. 15), which may be important for the correct diagnosis of faults.

6. Analysis of the results obtained, determination of general patterns connecting the amount of compression with various types of damage to engine parts and measurement conditions

When analyzing the reliability of the developed model, two features that confirm the results obtained should be especially noted. Thus, the convergence of the model is determined by the coincidence or at least very close values of the input and output cyclic values of pressure and temperature in the cylinder. In the case under consideration, such a coincidence occurs in both pressure and air temperature (Fig. 7, 9, 10), and the convergence in temperature is more important, and the discrepancy here does not exceed 1%.

In addition, an important confirmation of the correctness of the obtained results is the shape and size of the characteristic compensation (expansion) pocket on the curves after the expansion section (downward stroke of the piston after compression). This pocket occurs as a result of air leaking from the cylinder during compression, causing the cylinder pressure at the bottom dead center to be lower than ambient pressure.

As follows from the experiments [31], the real engines have a compensation pocket that is close to the calculated one not only in shape, but also in the value of the parameters (Fig. 7, 9). It is also obvious that the larger the pocket, the higher the air loss due to leakage from the cylinder [27]. Conversely, as leakage decreases, the size of the pocket will decrease. In the limit, in the absence of leaks and heat losses, a pocket does not form (Fig. 10). All these features can be easily simulated using the model.

The influence of various factors in the form of operational damage on the compression value generally corresponds to real practice [26, 27]. Indeed, damage to the valve mechanism has the greatest impact on compression, while damage to the cylinder-piston group is less critical. The simulation results shown in Fig. 7 and 10 generally confirm the known experimental data [31, 34].

Separately, the effect of heat losses from the cylinder on compression (Fig. 12) should be noted. As follows from the data obtained, any type of leakage from the cylinder reduces compression noticeably more than the heat loss calculated using the Woschni formula (Fig. 10). On the one hand, this result confirms the initial assumption that it is possible to simplify the model by taking into account heat losses using additional leakage, which constitutes only a small fraction of the total. On the other hand, there is currently no reliable data on the effect of heat loss under cold cranking conditions. Therefore, perhaps in the future the model should be refined based on heat losses from the cylinder.

From the point of view of the model's practical use, the dependence of compression on rotation speed is of the greatest importance (Fig. 11b). As it is possible to see, an increase in rotation speed from 150 to 450 rpm causes a 2-fold increase in compression. The simulation data actually confirms the fact known from practice and research [26] that compression always increases noticeably with increasing rotation speed. This dependence is quite obvious, since any leaks from the cylinder occur in a time process which decreases in inverse proportion to the frequency. It turned out to be difficult to introduce such a correction using empirical and statistical methods [24, 33]. Thus, the model allows what is difficult to do with the help of experiments, namely, to predict with sufficiently high accuracy how the compression in a particular engine will change when the rotation speed changes.

That means, the model makes it possible to introduce a correction for any compression meter readings, if the rotation speed at which the test was performed is known. Moreover, this amendment is extremely important for correct engine diagnostics. This allows you to determine the effect on the readings of the device of changes in speed for any reason, including changes in the characteristics of the battery, starter, engine oil, engine temperature, pressure and ambient temperature, etc. That is, the model allows you to almost completely exclude (or, conversely, take into account) the influence of any operational factors on compression as an important diagnostic parameter. And this is something that usually cannot be done in other ways.

As shown in Fig. 13 and 14, modeling processes during cold cranking can significantly expand the diagnostic capabilities of certain types of faults, including hydraulic lock in the cylinder [16]. If the sealing properties of the piston rings do not deteriorate during hydrolock (and this is so what usually happens in practice), then leaks from the cylinder do not increase with increasing pressure. In accord-

ance with this, despite a noticeable drop in the maximum pressure due to deformation (buckling) of the connecting rod, the lower part of the pressure diagram in general and the compensation pocket in particular will not change during hydrolock. This fundamentally distinguishes this type of damage from any others, which are usually associated with an increase in air leaks from the cylinder and, accordingly, with a significant expansion of the compensation pocket (Fig. 14).

The shape of the compensation pocket is also characteristic if the valve timing is shifted (Fig. 15a), when the pocket width actually changes only by the movement of the exhaust valve opening point. Then, if there is a certain reference compression diagram for a given engine, the indicated defect can be detected by a disproportionate change in the width of the pocket.

It follows that with a correct comparative analysis of the compression diagram and comparing it with the simulation results, it becomes possible not only to localize the damaged area (cylinder), but also to obtain reliable data on the nature and cause of serious damage in the operation. All this is possible even without engine disassembly and can prevent the destruction of a damaged engine [16], including significantly, many times, to reduce the cost of restoration repairs.

At the same time, it should be noted that the results obtained represent only the first experience of using the developed model. They show that it is necessary, among other things, to further improve the model, and, firstly, to improve the stability of the calculation algorithm when describing intake-exhaust processes at low rotation speeds. In addition, it is necessary to remove some simplifications that may affect the results. For example, it seems necessary to introduce and take into account a variable crankshaft rotation speed, since uneven rotation at low speed can be significant. In addition, it is necessary to continue research of the model itself for various types of leaks. For full compliance with the real process, you can also include the volume of the connecting tube in the model and take into account the hydraulic resistance of the check valve of the compression meter. That is, in this case, the greatest importance is to compare the calculation results with experimental data in order to identify quantitative characteristics and patterns that could make the model suitable for use in diagnostic and monitoring practice.

7.Conclusions

A thermodynamic model has been developed to calculate the in-cylinder processes of an internal combustion engine in cranking mode when measuring compression. The model describes the processes in the cylinder step by step, taking into account the real patterns of the intake-exhaust processes, air leakage through the interfaces of parts and heat exchange with the walls.

To test the developed model, control mathematical modeling was performed. The results obtained were compared with known experimental data on oscillography of pressure in the cylinder during cold cranking. When analyzing the accuracy and reliability of the model, it was found that the model has convergence in pressure and temperature up to 1%. After setting up the model, this made it possible to obtain the shape of the pressure diagram in the cylinder, including a characteristic compensation pocket in the curve, consistent with the experimental data.

Using modeling, the main patterns of changes in compression depending on the modes, the nature of damage to the parts of the valve mechanism and cylinder-piston group, the amount of leakage and engine temperature were found. It has been established that heat losses reduce compression by approximately 8%, and when the cold cranking frequency increases from 150 to 450 rpm, the compression value can double. As a result, the model allows you to introduce a correction to any compression meter readings if the rotation speed at which the test was performed is known, and thereby eliminate the influence of operational factors on the measurement results. These properties of the model make its use effective in diagnosing and monitoring the technical condition of engines in operation.

As a prospect for further research, it is expected to improve the model to improve the stability of the calculation algorithm for simulating intake-exhaust processes at low rotation speeds, taking into account variable crankshaft rotation speed, as well as continuing the study of the model itself for various types of damage and associated leaks.

Bibliography

[1] Bellér G, Árpád I, Kiss JT, Kocsis D. AVL Boost: a powerful tool for research and education. J Phys Conf Ser. 2021; 1935(1):012015. https://doi.org/10.1088/1742-6596/1935/1/012015

[2] Blair GP. Design and simulation of four-stroke engines. Warrendale: Society of Automotive Engineers, 1999.

[3] Borowski G, Ghazal O. Use of water injection technique to improve the combustion efficiency of the spark-ignition engine: a model study. Journal of Ecological Engineering. 2019;20(2):226-233. https://doi.org/10.12911/22998993/99689

[4] Burrows JA. An investigation into the cold start performance of automotive diesel engines. Doctoral Thesis. University of Nottingham 1998.

[5] Cordon D, Dean C, Steciak J, Beyerlein S. One-dimensional engine modeling and validation using Ricardo WAVE. Final Report KLK434-B, N07-09. National Institute for Advanced Transportation Technology. University of Idaho; 2007. https://www.academia.edu/18805887/one_dimensional_engine_modeling_and_validation_using_ricardo_wave

[6] Denton T. Advanced automotive fault diagnosis. 2nd edition. Oxford: Elsevier Butterworth-Heinemann 2006.

[7] Ferguson CR, Kirkpatrick AT. Internal combustion engines: applied thermosciences. 3rd ed. Chichester: John Wiley & Sons 2016.

[8] Fygueroa S, Villamar C, Fygueroa O. Thermodynamic study of the working cycle of a direct injection compression ignition engine. Internal combustion engines. IntechOpen. 2016: 75-112. https://doi.org/10.5772/50028

[9] Gilles T. Automotive engines: diagnosis, repair and rebuilding. 6th ed. Cengage Learning, Delmar 2011.

[10] Gupta HN. Fundamentals of internal combustion engines. PHI Learning Pvt. Ltd. Delhi 2012.

[11] Halderman JD. Automotive technology. principles, diagnosis, and service. 4th ed. New Jersey: Pearson Education 2012.

[12] Heywood JB. Internal combustion engine fundamentals. 2nd ed. McGraw-Hill Education, New York 2018.
[13] Kalikatzarakis M, Coraddu A, Theotokatos G, Oneto L. Development of a zero-dimensional model and application on a medium-speed marine four-stoke diesel engine. Proceedings of MOSES2021 Conference. 3rd International Conference on Modelling and Optimisation of Ship Energy Systems. 2021. https://www.researchgate.net/publication/352119154
[14] Kastner LJ, Williams TJ, White JB. Poppet inlet valve characteristics and their influence on the induction process. Proc Inst Mech Eng S. 1963;178(l):955-975. https://doi.org/10.1177/0020348363178001137
[15] Khrulev A. Analysis of pneumatic catapult launch system parameters, taking into account engine and UAV characteristics. Advanced UAV. 2023;3(1):10-24. https://publish.mersin.edu.tr/index.php/uav/article/view/1045
[16] Khrulev A, Dmitriev S. Study of the conrod deformation during piston interaction with liquid in the internal combustion engine cylinder. J Mech Eng Sci. 2019;14(2):6557-6569. https://doi.org/10.15282/jmes.14.2.2020. 03.0515
[17] Lanlege DI, Kehinde R, Sobanke DA, Garba UM. Comparison of Euler and Range-Kutta methods in solving ordinary differential equations of order two and four. Leonardo Journal of Sciences. 2018;32:10-37. https://www.researchgate.net/publication/331993886_Comparison_of_Euler_and_Range-Kutta_methods_in_ solving_ordinary_differential_equations_of_order_two_and_four
[18] Magdas VB, Mastan DC, Burnete N. Simulation possibilities of the internal combustion engine management elements using Lotus Engine Simulation software. IOP Conf Ser: Mater Sci Eng. 2020;997(1),012121. https://doi.org/10.1088/1757-899x/997/1/012121
[19] Martyr AJ, Plint MA. Engine testing. Theory and practice. 3rd ed. Elsevier Ltd. Oxford 2007.
[20] Martyr AJ, Rogers DR. Engine testing. Electrical, hybrid, IC engine and power storage testing and test facilities. 5th ed. Oxford: Elsevier Ltd. 2021.
[21] Maurya RK. Reciprocating engine combustion diagnostics. In-cylinder pressure measurement and analysis. Cham: Springer 2019. https://doi.org/10.1007/978-3-030-11954-6
[22] Medina A, Curto-Risso PL, Hernández AC, Guzmán-Vargas L, Angulo-Brown F, Sen AK. Quasi-dimensional simulation of spark ignition engines. From thermodynamic optimization to cyclic variability. Springer-Verlag, London 2014.
[23] Neumann S. Integrated cylinder pressure measurement for gas engine control. Combustion Engines. 2011;146(3):16-23. https://doi.org/10.19206/CE-117087
[24] Orczyk M, Tomaszewski F. Diagnostic and reliability model of an internal combustion engine. Combustion Engines. 2020;180(1):41-46. https://doi.org/10.19206/CE-2020-107
[25] Pacaud P, Perrin H, Laget O. Cold start on diesel engine: is low compression ratio compatible with cold start requirements? SAE Int J Engines. 2009;1(1):831-849. https://doi.org/10.4271/2008-01-1310.
[26] Pressure School. Part 2: A running diagnosis by Pico Technology. Garage Lube. https://www.garagelube.com/ online-training/pressure-school-part-2-running-diagnosis/
[27] Pressure School. Part 1: Introduction to the pressure transducer by Pico Technology. Garage Lube. https://www.garagelube.com/online-training/pressure-school-part-1-introduction-pressure-transducer/
[28] Pszczółkowski J. The model for cylinder charge parameters during engine starting. Combustion Engines. 2022;188(1): 60-66. https://doi.org/10.19206/CE-142029
[29] Reißig M. Modeling the cold start process of spark ignition engines. Dissertation zur Erlangung des akademischen Grades Doktor-Ingenieur der Fakultat fur Maschinenbau und Schiffstechnik der Universitat Rostock. Lehrstuhl fur Technische Thermodynamik. Universitat Rostock 2012.
[30] Roberts A, Brooks R, Shipway P. Internal combustion engine cold-start efficiency: a review of the problem, causes and potential solutions. Energ Convers Manage. 2014;82: 327-350. https://doi.org/10.1016/j.enconman.2014. 03.002
[31] Saraieva IY. Improving the process of diagnosing cylinder-piston group and tightness of valves in a gasoline car engine: Dissertation. National Aerospace University n.a. N.E. Zhukovsky "Kharkov Aviation Institute" 2006.
[32] Saraieva I, Beketov D. Analysis of diagnostic method of engine piston-cylinder-unit using «Bosch» equipment. Automobile Transport. 2010;27:56-60. https://api.dspace.khadi.kharkov.ua/server/api/core/bitstreams/38c86152-e537-4abc-aaef-aa9dfa8ebe16/content
[33] Saraieva I, Khrulev A, Vorobiov O. Development of mathematical criteria for assessing the quality of diagnosing the cylinder-piston group of a car engine. Vehicle and Electronics. Innovative Technologies. 2022;22:92-103. https://doi.org/10.30977/VEIT.2022.22.0.10
[34] Saraieva I, Khrulev A, Vorobiov O, Sebko D. Digital diagnostics for determining the tightness of the combustion camera of the car engine. Vehicle and Electronics. Innovative Technologies. 2020;18:52-64. https://doi.org/10.30977/VEIT.2020.18.0.52
[35] Stotsky AA. Automotive engines. Control, estimation, statistical detection. Heidelberg: Springer-Verlag, Berlin 2009. https://doi.org/10.1007/978-3-642-00164-2
[36] Witkowski K. The issue of the indicator diagram analysis for the purpose of diagnosis of marine diesel engines. Journal of KONES Powertrain and Transport. 2015;22(2):293-298. https://doi.org/10.5604/12314005.1165456

Alexander E. Khrulev, PhD – Senior Researcher, forensic auto expert, International Motor Bureau, Ukraine.
e-mail: *info@engine-expert.com*

Iryna Y. Saraieva, PhD, Ass. Prof. – Automobile Faculty, Department of Automobile Kharkiv National Automobile and Highway University, Ukraine.
e-mail: *sarayeva9@gmail.com*

Prof. Oleksii V. Saraiev, DSc., DEng.– Automobile Faculty, Department of Automobile Kharkiv National Automobile and Highway University, Ukraine.
e-mail: *sarayev9@gmail.com*

Oleksandr M. Vorobiov – graduate student, Automobile Faculty, Department of Automobile Kharkiv National Automobile and Highway University, Ukraine.
e-mail: *sanechek007@icloud.com*

Article citation info:
Szwajca F, Gawrysiak C, Pielecha I. Effects of passive pre-chamber jet ignition on knock combustion at hydrogen engine. Combustion Engines. 2024;198(3):110-122. https://doi.org/10.19206/CE-189738

Filip SZWAJCA
Cezary GAWRYSIAK
Ireneusz PIELECHA

Combustion Engines
Polish Scientific Society of Combustion Engines

Effects of passive pre-chamber jet ignition on knock combustion at hydrogen engine

ARTICLE INFO

Received: 5 May 2024
Revised: 3 June 2024
Accepted: 6 June 2024
Available online: 3 July 2024

The use of gaseous fuels, including hydrogen, to fuel an engine enables an increase in efficiency and a significant reduction in toxic exhaust emissions. The research reported in this paper concerns a two-stage passive hydrogen combustion system for analyzing knock combustion under varying process conditions. The research was conducted using a single-cylinder AVL 5804 engine to determine the effect of the center of combustion (CoC) and excess air ratio (λ) on engine knock conditions and other engine parameters. The tests were carried out at a constant speed of n = 1500 rpm, variable CoC adjustments (2–18°CA aTDC), and a variable value of λ = 1.25–2.0. It was determined that at λ = 1.25–1.5, knocking combustion is quite intense, and further increases in λ this knocking are needed. The excess air ratio λ was found to have a much greater effect on the knock appearance in the engine than the center of combustion position.

Key words: *hydrogen combustion, turbulent jet ignition, knock combustion, knock indexes, thermodynamic indexes*

1. Introduction

1.1. Combustion of hydrogen in the internal combustion engines

The necessity to reduce fuel consumption is driving the exploration of new fuels or changes in the design of internal combustion engines. One substitute for fossil fuels is the use of hydrogen (a zero-emission fuel) and the use of a two-stage combustion system to increase the attractiveness of the internal combustion engine.

Hydrogen as a fuel allows the operation of an internal combustion engine in a wide range of excess air ratio (λ), from a highly enriched mixture to a very lean mixture, from 0.14 to 10 under conditions of 1 atm and 298 K [2]. This range of boundary values is due to the flammability limit of hydrogen in air of 4–76% [36]. The stoichiometric mixture during hydrogen combustion assumes a value of 34.5:1 (air to fuel) [36]. Under conditions of increased temperature in the combustion chamber and the following conditions: stoichiometric mixture, high load, speed characteristic of high power, and higher compression ratio, the probability of knock increases decisively – the difficult issue is its elimination [29].

Das [10] and White [35] analyzed the controllability of hydrogen combustion in an internal combustion engine and found that at $\lambda \geq 2$, NO_x concentrations can be reduced to less than 100 ppm without additional exhaust gas after treatment using, for example, a three-way catalytic reactor. Nagalingam [24] studied the exhaust emissions of a supercharged engine with a mechanical compressor at an intake system pressure of 2.6 bar and $\lambda > 2.5$ and evaluated NO_x concentrations below 100 ppm. Natkin [25] also evaluated the concentration of NO_x in the exhaust gas at $\lambda = 4$, which was 90 ppm. The same author, in a Ford engine powered by a mechanical compressor, conducted a hydrogen combustion process at $\lambda = 4.34$ and determined NO_x concentrations of 3–4 ppm [25].

In summary, it can be concluded that at $\lambda \geq 1.8$, the concentration of NO_x in the exhaust gas is significantly reduced, and this is done without additional systems such as a three-way catalytic reactor [33]. However, an unfavorable feature of lean mixtures is that the flame propagation rate is dramatically reduced as λ increases. In addition, with very lean mixtures, two spark plugs may be required.

Hydrogen as a fuel for the internal combustion engine is a promising step toward low-emission propulsion [14]. Harmful compounds formed in the combustion process are NO_x, the concentration of which can be controlled and even reduced to 3–4 ppm at specific engine operation points. Table 1 shows the properties of hydrogen, which are compared with other commonly used fuels such as CNG, gasoline, and diesel.

The heating value of hydrogen is 3 times that of gasoline and diesel fuel (at very low density). The minimum ignition energy indicates high flammability relative to the other fuels, and the laminar flame speed in the air is also 4 times greater than theirs. Gasoline and diesel fuels have narrow flammability limits (the window of the volumetric limit is about 6%). For CNG, this range is slightly wider (about 10%). However, for hydrogen, the flammability limit is 72%. On the other hand, the lower flammability limit for hydrogen in air is higher: it is 4%, which is higher than for gasoline (1%) and diesel (0.6%).

1.2. Combustion in the TJI system

The two-stage combustion technology, called TJI, was developed for Formula 1 by the German company Mahle [23]. Units equipped with this system have two chambers: a pre-combustion chamber and a main chamber. Control of the mixture concentration in both chambers requires an individual fuel supply for each chamber. The pre-chamber is called active when equipped with a fuel supply system or passive – in the absence of direct fuel injection into the pre-chamber. In the active configuration, a fuel dose of about 2–5% of the main dose is delivered to the pre-chamber. An indirect injection system delivers the rest of the fuel to the main chamber [5].

Table 1. Physical and chemical properties of hydrogen versus conventional fuels [36]

Property	Hydrogen	CNG	Gasoline	Diesel
Carbon content [% mass]	0	75 [e]	84	86
Lower heating value [MJ/kg]	119.7	45.8	44.8	42.5
Density [a,b] [kg/m^3]	0.089	0.72	730–780	830
Volumetric energy content [MJ/m^3]	10.7	33	33×10^3	35×10^3
Molecular weight	2.016	16.043 [e]	~110	~170
Boiling point [a] [K]	20	111 [e]	298–488	453-633
Auto-ignition temperature [K]	858	813 [e]	~623	~523
Minimum ignition energy in air [a,d] [mJ]	0.02	0.29	0.24	0.24
Stoichiometric air/fuel mass ratio	34.5	17.2 [e]	14.7	14.5
Stoichiometric volume fraction in air [%]	29.53	9.48	~2 [f]	–
Quenching distance [a,c,d] [mm]	0.64	2.1 [e]	~2	–
Laminar flame speed in air [a,c,d] [m/s]	1.85	0.38	0.37–0.43	0.37–0.43 [g]
Diffusion coefficient in air [a,b] [m^2/s]	8.5×10^{-6}	1.9×10^{-6}	–	–
Flammability limits in air [% vol.]	4–76	5.3–15	1–7.6	0.6–5.5
Adiabatic flame temperature [a,c,d] [K]	2480	2214	2580	2300

[a] at 1 bar, [b] at 273 K, [c] at 298 K, [d] at stoichiometry, [e] methane, [f] vapor and [g] n-heptane.

Combustion is initialized in the pre-chamber, which contains the injector and spark plug or the spark plug itself (passive system). Ignition of the mixture in the pre-chamber causes burning jets to pass through narrow channels into the main chamber, initializing the combustion of the lean fuel-air mixture. Such initialization is multi-point, so the mixture in the main chamber is ignited in several volumes simultaneously, resulting in rapid combustion of the main charge [5].

1.3. Purpose of the investigation

The main research problem of the present work is to expand knowledge in the following areas:

- evaluation of the hydrogen combustion thermodynamic characteristics as a function of the excess air ratio of the hydrogen-air mixture
- the effect of varying the center of combustion as a control parameter in hydrogen combustion
- occurrence of knock combustion in a hydrogen engine
- determination of mixture leanness and the center of combustion angle favoring the occurrence of knock combustion phenomenon.

The above research problems were solved using experimental tests on a single-cylinder research engine. Fast-varying processes and techniques were used to analyze the processes occurring in the combustion chambers of a hydrogen-powered engine.

2. Knock combustion

2.1. Essence of knock combustion

Knock combustion, also known as detonation combustion, is an undesirable phenomenon in an engine, resulting in decreased power and efficiency. Knock combustion can also cause the engine to run unevenly or lead to engine failure (caused by excessive stresses and temperatures exceeding these components' strength).

Knock combustion is a key topic due to very strict emission standards. This forces corporations to design powertrains that achieve maximum efficiency while maintaining optimal power and torque.

There are many reasons for the abnormal combustion process; however, spark knock and surface ignition are considered the most characteristic. It is worth noting that knock itself is understood as the sound associated with the self-ignition of the fuel-air mixture or part of it before the progressive form of the flame initiated by the ignition spark. A spark knock is a repetitive knock controlled by the ignition advance angle, which directly affects the intensity of this phenomenon. Heywood proposed this division and definition [15]. The division described above is very important from the point of view of engine control. In both cases, knock is identified; however, only in one of them is the engine control unit able – simply and quickly – to respond effectively. This is done by delaying the ignition advance angle, and thus, it is possible to reduce the intensity of the phenomenon or eliminate it altogether.

2.2. Conditions for the occurrence of knock combustion

The characteristic of knock combustion is the accompanying extremely sudden release of energy, which causes intense pressure changes in the cylinder. The sudden pressure changes introduce vibrations of significant amplitude into the combustion chamber and propagate to the entire engine structure [21]. It is assumed that this pressure amplitude during knock combustion in spark-ignition engines is 5–7 kHz [16]. There are scientific papers in which the authors extend this range to 20 kHz [7].

Knock combustion is very likely in the stoichiometric mixture area (Fig. 1). The research conducted by Szwaja et al. [31] was intended to force intense knock combustion. It was emphasized that in order to force this phenomenon, the compression ratio and stoichiometric mixture were selected accordingly.

The authors [31] present several factors that affect the occurrence of knock combustion. These factors are compression ratio, ignition timing, and air excess ratio λ. Any action to increase the pressure inside the combustion chamber increases the probability of knock combustion. In Figure 2, the dependence of the combustion chamber pressure intensification on the ignition timing is shown. Increasing the ignition advance increases the probability of knock

combustion. It is also worth noting that hydrogen is much more sensitive to changes in ignition advance than gasoline.

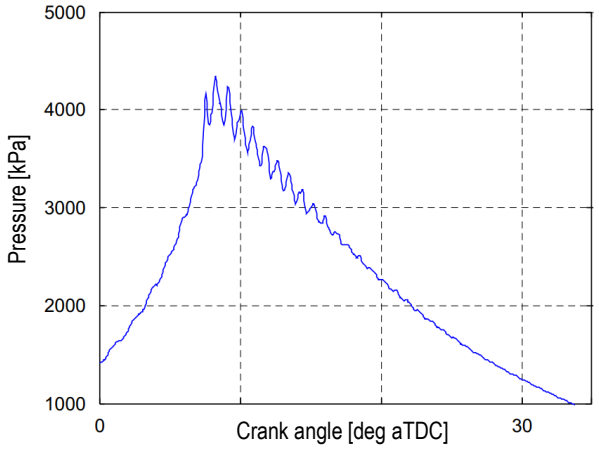

Fig. 1. Cylinder pressure with knocking combustion (ε = 12:1; n = 900 rpm; λ = 1) [31]

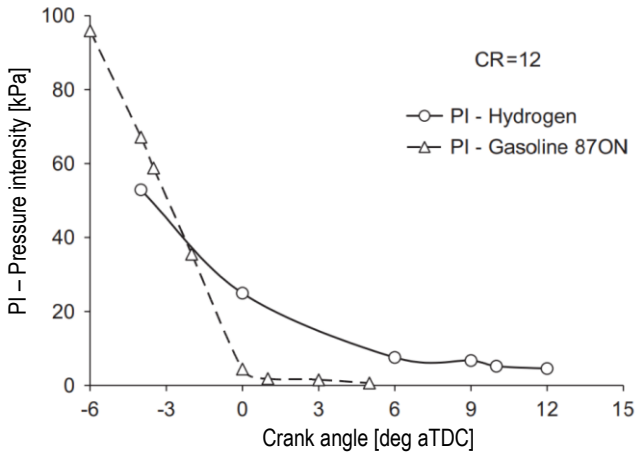

Fig. 2. Dependence of pressure intensification on ignition timing during hydrogen and gasoline combustion [31]

In summary, the first factor causing the knock combustion is use the stoichiometric mixture at which the phenomenon occurs. The next factor is the compression ratio. A compression ratio of 12 can be categorized as quite large for a range of spark-ignition engines. Units based on spark-ignition direct injection and equipped with supercharging are based on compression ratios of ε = 9.3 (e.g. VW 2.0 TFSI) and ε = 10.5:1 (e.g. VW 1.5 TSI EVO2). The last condition for the occurrence of knock combustion is the ignition advance. Karim [17] concludes that with hydrogen combustion in an internal combustion engine, optimizing the ignition advance is far more effective than with other fuels and allows for the control of knock combustion.

2.3. Detection methods for knock combustion

An index using the pressure pulsation maximum amplitude (MAPO) and another using the average value of the absolute pressure pulsation (IMPO) are the most commonly used knock indexes. Both indices rely on measuring the frequency of pressure in a cylinder with a high-pass filter [28]. Typical knock indices are shown below:

– MAPO – Maximum amplitude of pressure oscillations [6, 9, 13, 22]:

$$\mathrm{MAPO} = \max|p_{osc}| \tag{1}$$

where: p_{osc} – oscillatory component of combustion pressure;

– IMPO – integral modulus of pressure oscillations [3]:

$$\mathrm{IMPO} = \frac{1}{\theta_c}\int_0^{\theta_p}|p_{osc}|d\theta \tag{2}$$

where: θ_c – engine cycle time, θ_p – duration of the variable component p_{osc}, θ – crank angle;

– IMPOG – integral modulus of pressure oscillations gradient [11, 12]:

$$\mathrm{IMPOG} = \int_{\theta_{stp}}^{\theta_{stk}}\left|\frac{dp_{osc}}{d\theta}\right| d\theta \tag{3}$$

where: θ_{stp} – crank angle for knock start, θ_{stk} – crank angle for knock end;

– D3PDθ – maximum value from the third-order derivative of the pressure pulsation [8]:

$$\mathrm{D3PD\theta} = \max\left(\frac{d^3 p_{osc}}{d\theta}\right) \tag{4}$$

– KI20 – Knock Index – indicator of knocking intensity in the window of 20°CA [19]:

$$\mathrm{KI20} = \sum_{i=1}^{n}\frac{(p_{osc}(i)-p_{av})^2}{\theta_{20}} \tag{5}$$

where: n – numbers of combustion cycles, $p_{osc}(i)$ – sample of the oscillatory component of the combustion pressure, p_{av} – average value of pressure oscillations, θ_{20} – number of samples in a window of width 20°CA.

Figure 3 shows a graphical representation of the indicators presented previously.

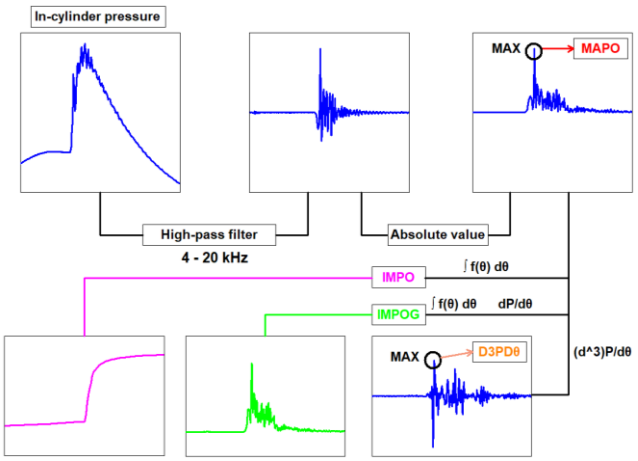

Fig. 3. Graphical representation of index calculation for MAPO, IMPO, IMPOG, and D3PDθ

2.4. Knock categorization

The limit for the occurrence of knock combustion at the MAPO index takes different values in the literature. Aramburu [1] conducted a study that used a 6-cylinder engine with a displacement of 5.883 dm^3 and adopted a MAPO limit value = 4 bar. Szwaja and Naber [32] adopted a limit value of MAPO = 0.1 MPa to distinguish be-

tween the correct mixture combustion process initiated by the spark plug and the combustion process initiated by the self-ignition of the mixture. They found that at the self-ignition of the mixture, the maximum pressure pulsations take values much higher than 0.1 MPa. The limit MAPO = = 1 bar [26, 30, 34] is the most widely accepted value to distinguish a correct combustion process from one in which knocking combustion has occurred.

The MAPO limit is a very individual indicator that takes on different values due to the displacement volume or compression ratio. Taking into account the displacement volume of the AVL 5804 engine of swept volume 0.5107 dm^3 and the fact that the most commonly accepted limit value in publications is MAPO = 1 bar, this work also adopts this value to identify the phenomenon of knock combustion.

3. Research methodology

3.1. Engine test bench

The tests were carried out using an AVL 5804 test unit (Fig. 4), which is a single-cylinder engine adapted for hydrogen combustion. The engine is equipped with a two-stage combustion system and a passive pre-chamber. The technical parameters of the engine are shown in Table 2.

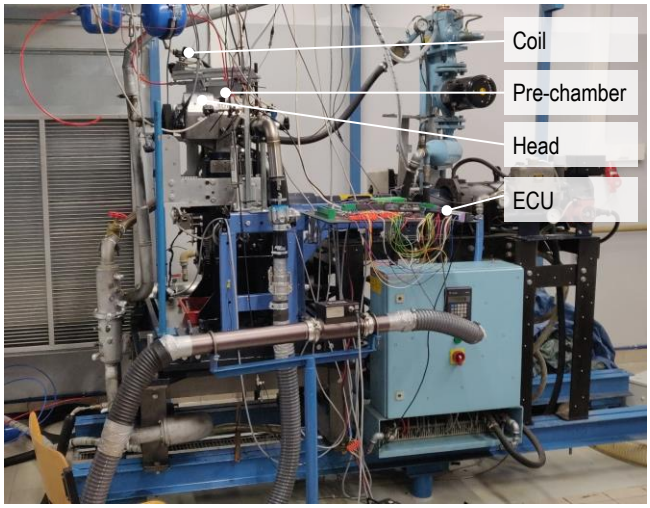

Fig. 4. AVL 5804 single-cylinder engine with TJI system

Table 2. Technical parameters of the AVL 5804 engine

Parameter	Unit	Value
Engine	–	1-cyl., 4-valve, SI, TJI
Cylinder volume	dm^3	0.5107
Bore	mm	85
Stroke	mm	90
Compression ratio	–	14.5:1
Air intake	–	supercharged

The pre-chamber was equipped with 6 radially distributed nozzles with a diameter of 1.7 mm leading to the main chamber. A spark plug is fitted in the pre-chamber. The volume of the pre-chamber is 6.6% of the main combustion chamber above the piston in the TDC. Fuel was supplied to the main chamber via an electromagnetic injector, located in the intake manifold.

3.2. Research apparatus

A schematic of the test stand and measuring apparatus is shown in Fig. 5. Hydrogen was supplied from a 40 dm^3 cylinder, in which the initial pressure of 150 bar was reduced to 6.5 bar (into the main chamber). In addition, two 2.5 dm^3 tanks (to reduce pressure pulsation) were mounted in front of the injector, connected in series. Fuel dose was calculated based on mass flow rate using a Bronkhorst 111B flow meter.

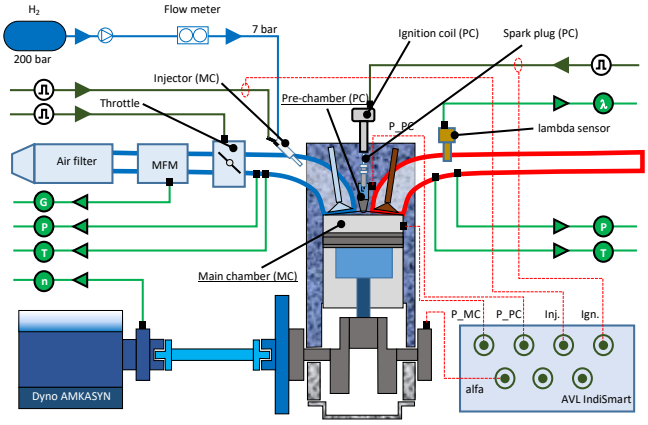

Fig. 5. Layout of engine and test apparatus

The start of hydrogen injection was fixed at 260°CA before TDC. Ignition and throttle position were controlled by Ecumaster's EMU Black controller. Adjustment of the throttle position by the mentioned controller made it possible to adjust the excess air ratio (a constant air overpressure of 1 bar was provided by an external mechanical compressor).

To analyze the combustion process, combustion pressures in the main chamber (AVL GH14D pressure sensor: 0–25 MPa) and pre-chamber (Kistler 6081 AQ22: 0–25 MPa) were recorded using AVL IndiSmart together with a crankshaft position sensor (AVL 364C01; 0.1 deg).

The excess air ratio was determined using IMFSoft's LCP80 controller and a Bosch LSU 4.9 wideband oxygen sensor (measurement range 0.7–12.5) mounted in the engine's exhaust system.

3.3. Scope of research

The tests were carried out at a constant engine speed of n = 1500 rpm, with different values of excess air ratio and a variable center of combustion CoC (CoC angle for 50% of the heat released). The IMEP value was the value resulting from the fuel dose at the specified adjustment λ. Table 3 shows the test plan.

Table 3. Variable and constant values during engine tests

No.	λ value	Throttle	CoC [α]		Fuel dose
	–	%	Start	End	mg/cycle
1	1.25	30	2	14	4.32
2	1.35	32	2	18	4.16
3	1.50	38			4.13
4	1.60	43			4.20
5	2.00	64			4.25

Research conducted by Qiang et al. [27] indicates similar values of the air excess ratio when using a passive combustion chamber (tests were conducted at λ = 1.8).

3.4. Research procedure

The recorded high-speed variable quantities are shown in Fig. 6. The measured quantities were analyzed using AVL Concerto software with an implemented library of calculation procedures.

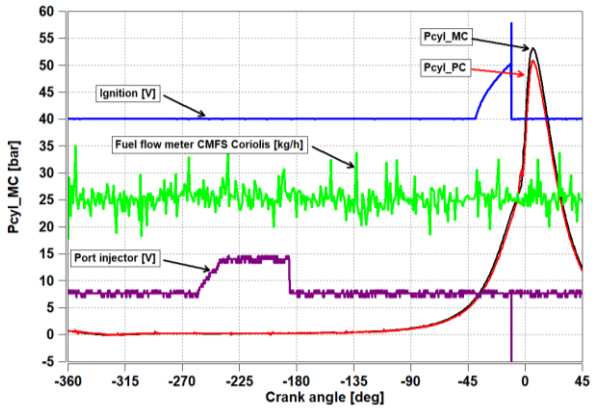

Fig. 6. Examples of parameters recorded during engine operation

The following parameters were analyzed:

– Averaged cylinder pressure from 100 post-measurement cycles:

$$P_{cyl}(\alpha) = \frac{\sum_{i=1}^{100} P_{cyl\_i}(\alpha)}{100} \quad (6)$$

where: P_{cyl} – in-cylinder pressure, α – crank angle;

– Incremental cylinder pressure dP_{cyl}

$$dP_{cyl}(\alpha) = \frac{dP_{cyl}(\alpha)}{d\alpha} \quad (7)$$

– Indicated mean effective pressure (IMEP):

$$IMEP = \frac{1}{V_s} \cdot \sum P_{cyl}(\alpha) \cdot dV \quad (8)$$

where: V_s – swept volume, V – actual cylinder volume;

– Heat rate released (dQ):

$$dQ/d\alpha = \frac{\kappa}{\kappa-1} \cdot P_{cyl}(\alpha) \cdot \frac{dV}{d\alpha} + \frac{1}{\kappa-1} \cdot V \frac{dP_{cyl}(\alpha)}{d\alpha} \quad (9)$$

where: κ – specific heat ratio $\left(\frac{c_p}{c_v}\right)$;

– Heat released (Q):

$$Q = \int_{SOC}^{EOC} \frac{dQ}{d\alpha} dv \quad (10)$$

where: SOC – start of combustion, EOC – end of combustion;

– Ni – indicated power

$$N_i = \frac{V_s \cdot IMEP \cdot n}{\tau} \quad (11)$$

where: n – engine speed, τ – engine cyclicality.

4. Experimental row results

The basic parameter and also the most important carrier of information about the conditions in the combustion chamber is the pressure in the cylinder. Examples of pressure waveforms in the main chamber (MC) and pre-chamber (PC) are shown in Fig. 7.

The variation of CoC position was achieved by changing the ignition timing advance (Fig. 8). Changes in CoC were made in increments of ΔCoC = 2°CA (ignition angle was adjusted to obtain the correct CoC value). At λ = 1.25 the CoC was changed in the range of 2–14°CA aTDC, at the other test points 2–18°CA aTDC.

a)

b)

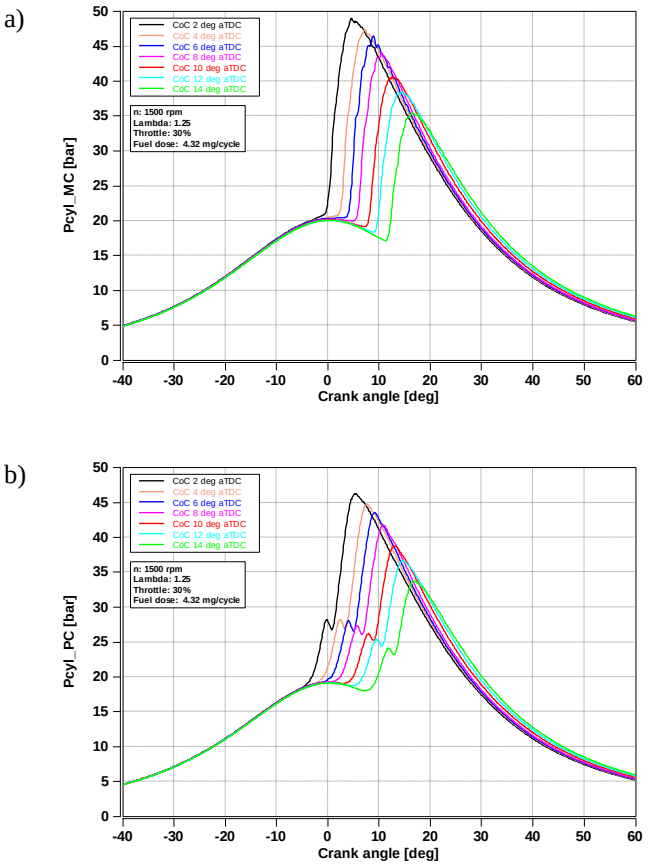

Fig. 7. Example of cylinder pressure waveform with λ = 1.25 and different CoC = 2–14°CA aTDC: a) in main chamber; b) in pre-chamber

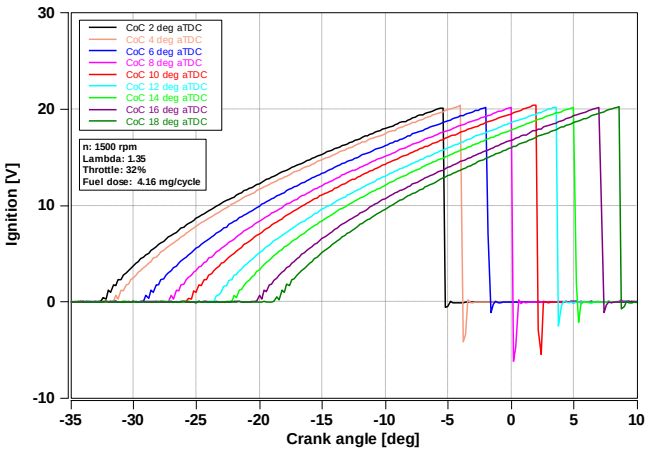

Fig. 8. Current in the primary circuit of the ignition coil for different values of CoC at the λ = 1.35

A complete center of combustion analysis as a function of ignition timing is shown in Fig. 9. It shows that as the

excess air ratio increases, obtaining the same combustion centers requires more ignition advance. At λ = 1.25, achieving CoC = 10°CA aTDC requires ignition at SOI = 2–3°CA aTDC. However, at λ = 1.5, the same CoC angle already requires an ignition advance of 2–3°CA (to SOI = 0°CA). Further increasing the excess air ratio to λ = 2 results in CoC = 10°CA aTDC, requiring a further ignition advance of 3°CA to a value of SOI = 3°CA bTDC.

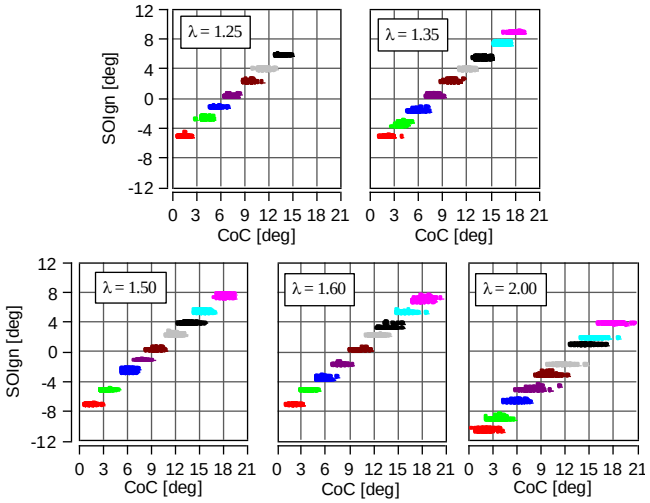

Fig. 9. Values of the ignition timing relative to the center of combustion CoC for all lambda λ values analyzed

In simulation studies conducted by Aljabri et al. [2], similar pressure curves were obtained in the cylinder and in the pre-chamber. The tests were carried out using a similar geometry of the combustion system (ε = 14.5), but with higher values of the excess air coefficient (λ > 2.8).

5. Combustion process thermodynamic indicators evaluation

5.1. Cylinder pressure

By delaying the CoC, the maximum pressure value in the combustion chambers is reduced. At each excess air ratio, the maximum value of combustion pressure in both chambers is reached at CoC = 2°CA aTDC, while the lowest pressure value occurs at the highest value of CoC: at λ = = 1.25 – CoC = 14°CA aTDC, and for other values of excess air ratio at CoC = 18°CA aTDC.

Further, an interesting relationship at different excess air ratios and different values of CoC angles was observed in the peak angular window of the main combustion phase. The part of the combustion process in point is presented in Fig. 10, which shows a narrow angular window for successively the richest and the leanest mixture. The different rates of pressure rise after ignition can be seen. Tap burning occurs at virtually any value of CoC (at λ = 1.25), which is not observed at λ = 2.0.

Similar changes (decrease in P_{mx} – from 23 to 16 bar at CoC = 1–15 deg aTDC). depending on CoC was reported in the study by Qiang et al. [27] (research was carried out at n = 1600 rpm and λ = 1.8).

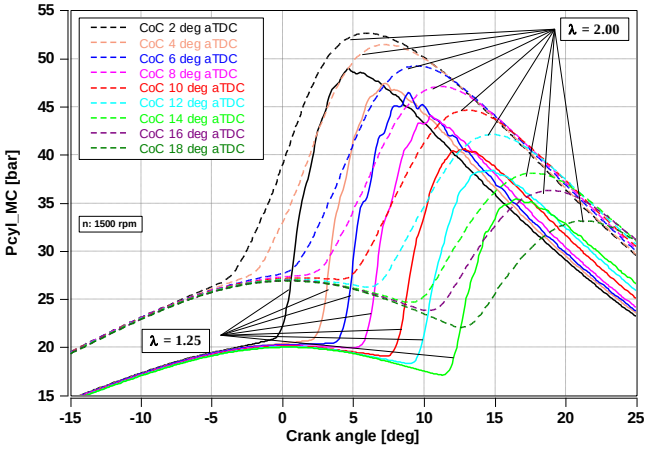

Fig. 10. Cylinder combustion pressure for λ = 1.25 and λ = 2.00 at the full range of CoC values analyzed

The relationship of pressure rise in both chambers at λ = = 1.25 is shown in Fig. 11a. A rapid increase in pressure is observed, suggesting that the combustion process was assisted by knocking combustion. At CoC = 2–8°CA aTDC, very significant pressure increments are observed. With further increases in CoC, dP_{cyl} values decrease. Despite the smaller maximum values, knock combustion was still observed.

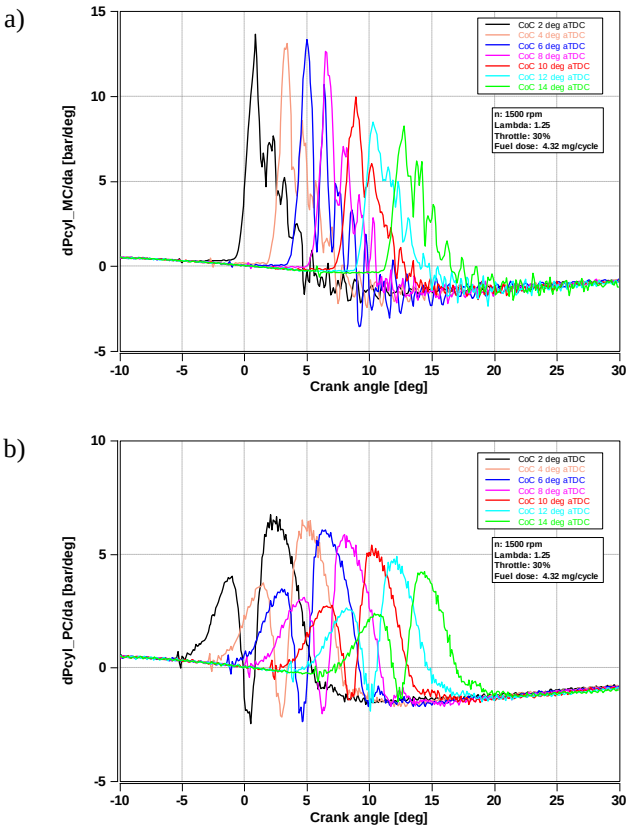

Fig. 11. Pressure rise rate for λ = 1.25 at the full range of analyzed CoC values in a) cylinder, b) pre-chamber

Figure 11b shows the same pressure rise changes in the pre-chamber. Such rapid changes as in the cylinder are not

observed, but there is also knocking combustion. It can be seen that the pressure rise peaks characteristic of two-stage combustion with a pre-chamber is reached twice.

Figure 12 shows the combustion pressure P_{cyl} in both chambers (Fig. 12a) and the pressure rise $dP_{cyl}/d\alpha$ at λ = = 1.35 (Fig. 12b).

The pressure difference between the chambers is a feature of the two-stage combustion system and inter-chamber throttling. Regardless of the CoC value, an increased pressure value in the pre-chamber is observed when the mixture is ignited around the spark plug (Fig. 12a). Subsequently, the burning charge in the pre-chamber is transferred to the main chamber, causing combustion to begin in the cylinder. In the MC chamber, higher pressure values are obtained regardless of the CoC change.

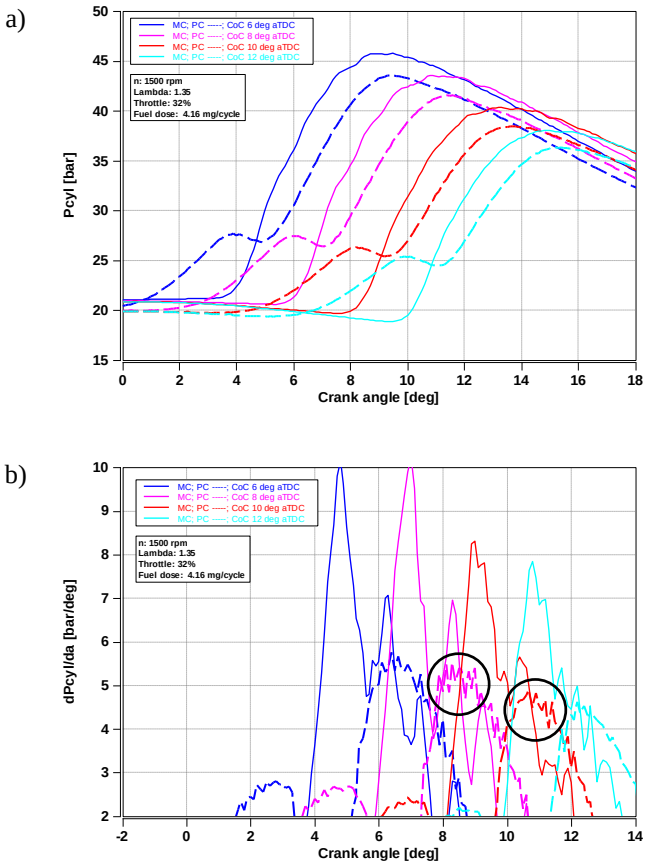

Fig. 12. Cylinder pressure P_{cyl} (a) and pressure rise $dP_{cyl}/d\alpha$ (b) at λ = 1.35 and CoC = {6, 8, 10, 12°CA} in a narrow window of crankshaft angle

Analyzing the pressure rise rate in both chambers $dP_{cyl}/d\alpha$ (Fig. 12b), some oscillations (also present in Fig. 11b) can be observed, which do not indicate knock combustion. This is due to the values of these oscillations. They may be due to the lack of filtering of the measurement signal. As mentioned earlier, it was assumed that knock combustion is characterized by oscillations of 1 bar, and here a maximum of Δp = 0.2 bar was obtained.

5.2. Indicated mean effective pressure

Indicated mean effective pressure (IMEP) is a basic thermodynamic indicator that is a measure of operating efficiency for engine displacement. Figure 13 shows the IMEP values for both combustion chambers depending on CoC. The IMEP in the pre-chamber is lower than that in the main chamber. This is due to the previously described pressure and charge flow dependency.

It was observed that at two values of excess air ratio λ = = 1.25 and λ = 1.35, the trend of IMEP change increased with each successive CoC position. There is no decreasing trend due to the absence of successively higher CoC values (due to lack of combustion or very high ignition dropout). At the aforementioned excess air ratio values, IMEP takes on a maximum value of 3.79 and 3.96 at CoC = = 14°CA aTDC and CoC = 18°CA aTDC angles in the main chamber. The situation is slightly different in more dilute mixtures. At λ = 1.50 and λ = 2.00, the peak IMEP occurs at CoC = 12°CA aTDC in the MC. In contrast, at λ = = 1.60, the maximum value of 4.27 occurs at CoC = {8, 10, 12°CA} in MC.

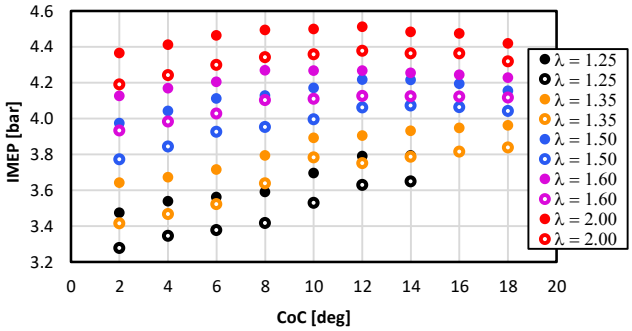

Fig. 13. The value of the indicative mean effective pressure as a function of the center of combustion for the main and pre-chamber (● – MC, ○ – PC)

Research conducted by Attard et al. [4] indicate that maximum brake torque (MBT) falls within the combustion center angle of 6–9 deg aTDC. They also define knocking combustion limits: for fuels with a high octane number (FON) the CoC limit is 2 deg aTDC (at FON = 96). The knocking combustion limit shifts towards higher CoC values with a limited fuel octane number (at FON = 75, the CoC limit is 20 deg aTDC).

The maximum IMEP value occurs at λ = 2.00 in each of the analyzed CoCs, which correlates with the benefits of lean combustion. The IMEP increases each time the mixture dilution increases, starting at λ = 1.25, for which it assumes the lowest values. This situation is due to the fact that the increase in charge dilution was realized by increasing the amount of air and not by reducing fuel dosing. Such adoption of the test methodology was due to the requirement to ensure a constant flow of hydrogen (limiting the possibility of reducing the hydrogen injection time).

Moreover, it is worth looking at the difference between the IMEP in the main chamber and the pre-chamber, as presented in Fig. 14. The difference between the IMEP values in the two chambers successively decreases with increasing CoC regardless of the value of λ. Such a condition can be explained by long-duration combustion leading to a decrease in differences in both chambers. Mild anomalies were noted at λ = 1.35 and CoC = {8, 10°CA}, where

the function strongly deviates from the other excess air ratios.

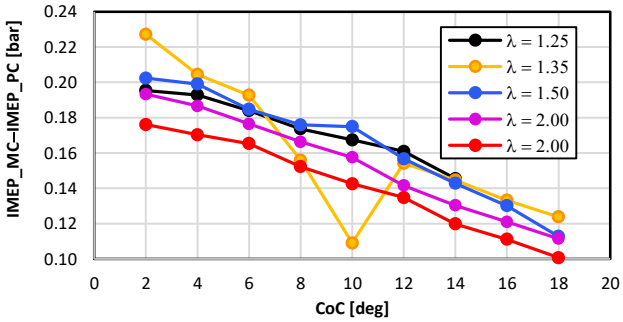

Fig. 14. IMEP difference between MC and PC chambers as a function of CoC

5.3. Heat release characteristics

Heat release analysis was carried out according to the thermodynamic index equations presented in subsection 4.4.

Figure 15 shows the heat release curves in the main chamber for all CoCs and selected curves in the pre-chamber for successively the smallest, middle and largest CoC angle for the excess air ratio λ = 1.25. A decrease in the heat release results in a certain maximum. Such a pattern may suggest a rapid loss of heat to the walls whose temperature, due to the hydrogen supply, was significantly reduced.

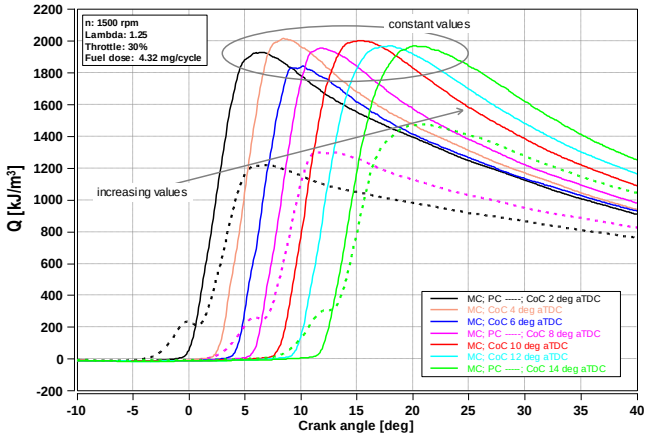

Fig. 15. Heat released in the main chamber and pre-chamber at different values of CoC and λ = 1.25

It is observed that at CoC = {8, 12, 14°} the course of heat release in the main chamber is similar, this also applies to the maximum values. The analysis of Q in the main chamber shows an increasing value of the maximum heat release with the delay of CoC. It means that delaying the CoC positively affects the quality of combustion in the pre-chamber. Such a delay in CoC (and thus ignition) is conducive to improving the quality of the charge accumulated in the pre-chamber.

In addition, as the CoC increases, the difference between the maximum values in the main chamber and the pre-chamber decreases, due to the increasing maximum values of the amount of heat released in the pre-chamber.

An analysis of the maximum amount of heat released for a number of λ and CoC variants is shown in Fig. 16. It shows that an increase in λ results in a decrease in the maximum amount of heat in the main chamber. In the pre-chamber, regardless of λ and CoC, the heat value is significantly lower.

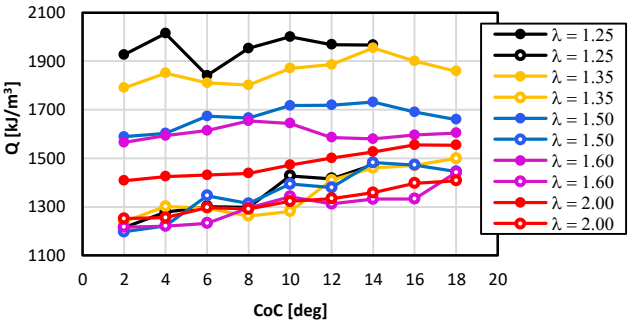

Fig. 16. Maximum values of heat released at different excess air coefficients as a function of CoC (● – MC, ○ – PC)

Analysis of the heat release rate shows that there are dependencies related to λ and CoC (Fig. 17). At a constant λ, increasing CoC by 6°CA causes the maximum of the heat release rate to shift by about 5°CA. Increasing λ causes much smaller values of dQ/dα to be observed at the same CoC with a simultaneous acceleration of about 2°CA. Changing λ from 1.25 to 2.0 causes the heat release rate to be reduced by 3 times regardless of CoC.

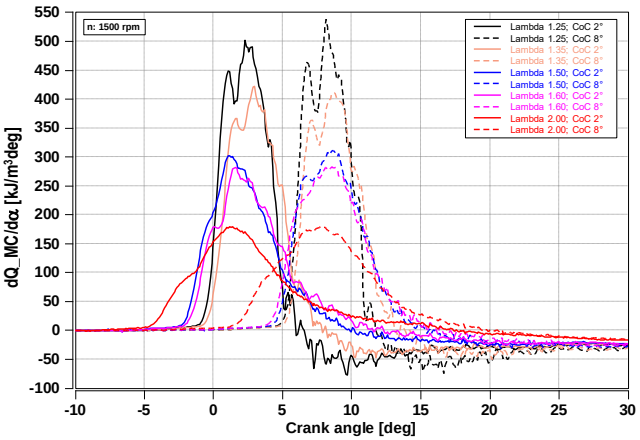

Fig. 17. Heat release rate for CoC 2° and 8°CA and all analyzed values λ

The last thermodynamic indicators analyzed in this section are HR10 – the start of combustion (defined as the angle at which 10% of the heat is released) and HR90 – the end of combustion (defined as the angle at which 90% of the heat is released), which are presented in Fig. 18. The difference between these two thermodynamic indicators is the combustion duration HR90–HR10. At λ = 1.25, the start of the combustion follows CoC. At the maximum value of CoC, maximum IMEP is observed. Similar parameters were observed at λ = 1.35. The start of combustion ranges from 6 to 8°CA. Further increasing the value of λ results in a characteristic maximum IMEP. $IMEP_{mx}$ values occur in the range of CoC = 8–12°CA aTDC at high values of λ. At

λ = 2.00, the combustion time increases and is about 10°CA.

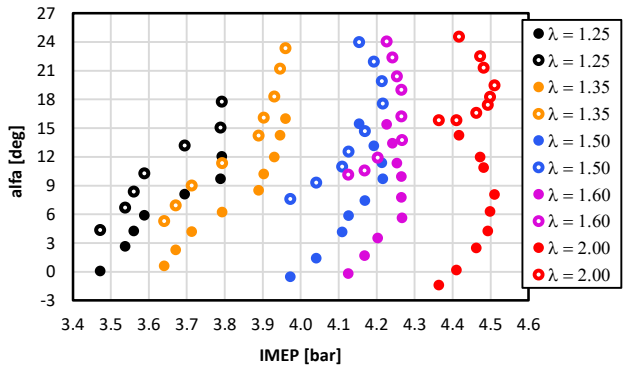

Fig. 18. The angle of 10% HR10 and HR90 90% of the heat released relative to IMEP (● – HR10, ○ – HR90)

Concluding the analysis in this section, the combustion durations were tabulated (Fig. 19). It was observed that for excess air ratios λ = 1.25 and 1.35, increasing the CoC angle increases the combustion time. It has to do with delaying the beginning of combustion and, at the same time, ending it later. The maximum combustion time with higher CoC values is increased at both λ values. At λ = 1.5 and 1.6, almost constant combustion duration values are observed, averaging 9°CA. Combustion conditions at λ = 2.0 cause the combustion time to decrease with increasing CoC. At CoC = 2°CA, the combustion time was 17°CA, and at CoC = 18°CA aTDC decreased to 10°CA. The combustion time values are consistent with the results of Wang et al. [34], who, at λ = 2.0 (for a supercharged DISI engine without a two-stage combustion system), obtained a combustion time of 15°CA (keeping CoC in the range of 8–9.7°CA aTDC).

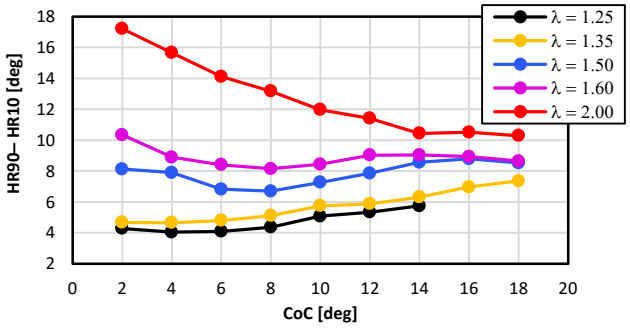

Fig. 19. Combustion duration HR90-HR10 relative to CoC

Research conducted by Qiang et al. [27] (λ = 1.8) indicates a similar trend (slow increase) of combustion time in the range of λ = 1.25–1.6. The author's own research found that at λ = 2.0, the trend is reversed.

5.4. Engine performance indicator

Indicated power is shown in Fig. 20 as a function of variable CoC and variable excess air ratio. It is observed that the indexed power increases with the dilution of the mixture. The analysis in terms of the changing CoC is no longer clear. At λ = 1.25 and λ = 1.35 each time, the indicated power increases with increasing CoC. For successive values of excess air coefficients, the indicated power value reaches a maximum in the range CoC = 8–12°CA aTDC. At λ = = 2.0, the indicated power is highest at CoC = 12°CA aTDC.

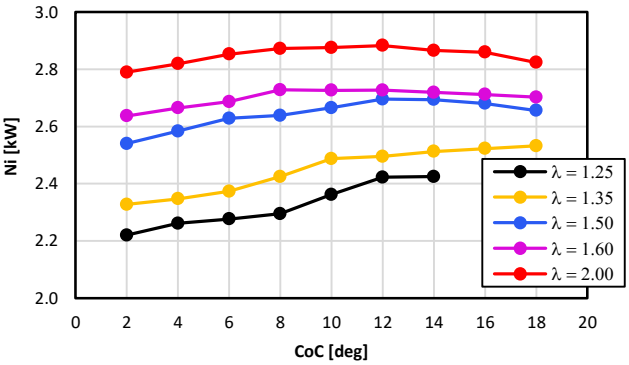

Fig. 20. Indicated power Ni relative to CoC

6. Knock combustion indicators

Equation (1) presents the maximum amplitude of pressure pulsation (MAPO). The MAPO values were determined by measuring the indicated pressure in both chambers. Then, the measured pressure is subjected to filtering using a high-pass filter. The frequency analysis range is 4–20 kHz in the window of 0–70°CA with a measurement resolution of 0.1° increments. Figure 21 below shows the measured pressure in the main and pre-chamber and the resulting function after filtering in a narrowed window of 0° to 30°CA.

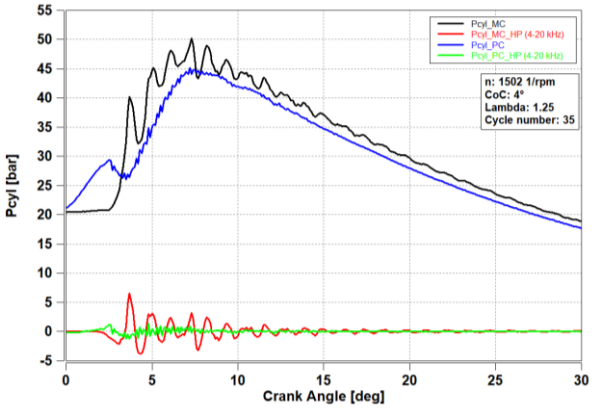

Fig. 21. The effect of using a high-pass filter. Pressure waveform in the cylinder (black line) and pre-chamber (blue line) along with the filtered part – red line (cylinder), green line (pre-chamber)

The next step was to calculate the value of the maximum pulsation in both chambers (red and green lines in Fig. 21). This maximum value is the MAPO knock index, which was presented for the main chamber (Fig. 22) and for the pre-chamber (Fig. 23). It was observed that at λ = 1.25 the knock is most intense with a maximum value of MAPO = 7.996 bar for cycle number 95 and CoC = 8°CA aTDC. In total, only five cycles exceeded the 7 bar pressure oscillation value. At λ = 1.25, it was noted that CoC in the range of 2–6°CA aTDC resulted in similar knock combustion

patterns (similar MAPO distributions in Fig. 22a). Further retardation of the CoC causes the maximum knock intensity to decrease (but far exceeds the 1 bar limit). At $\lambda = 1.35$, similar characteristics were observed – but the maximum knock mostly does not exceed 5 bar (Fig. 22b). The most intense knock occurred at CoC = 6°CA aTDC. Then, there was a slight reduction in the intensity of the phenomenon. However, further on, the appearance of knock combustion is undeniable. The next level of mixture dilution – $\lambda = 1.50$ – reduced the intensity of knocking to MAPO = = 3 bar (Fig. 22c). A further increase in $\lambda > 1.60$ (Fig. 22d, e) again reduced the intensity of knock combustion. The great majority of measurement cycles exceeded the limit MAPO = 1 bar. However, only a few cycles took values ≥ 2 bar. In the case of the last excess air ratio, $\lambda = 2.00$, the knock combustion phenomenon did not occur, as MAPO takes values < 1 bar (Fig. 22e).

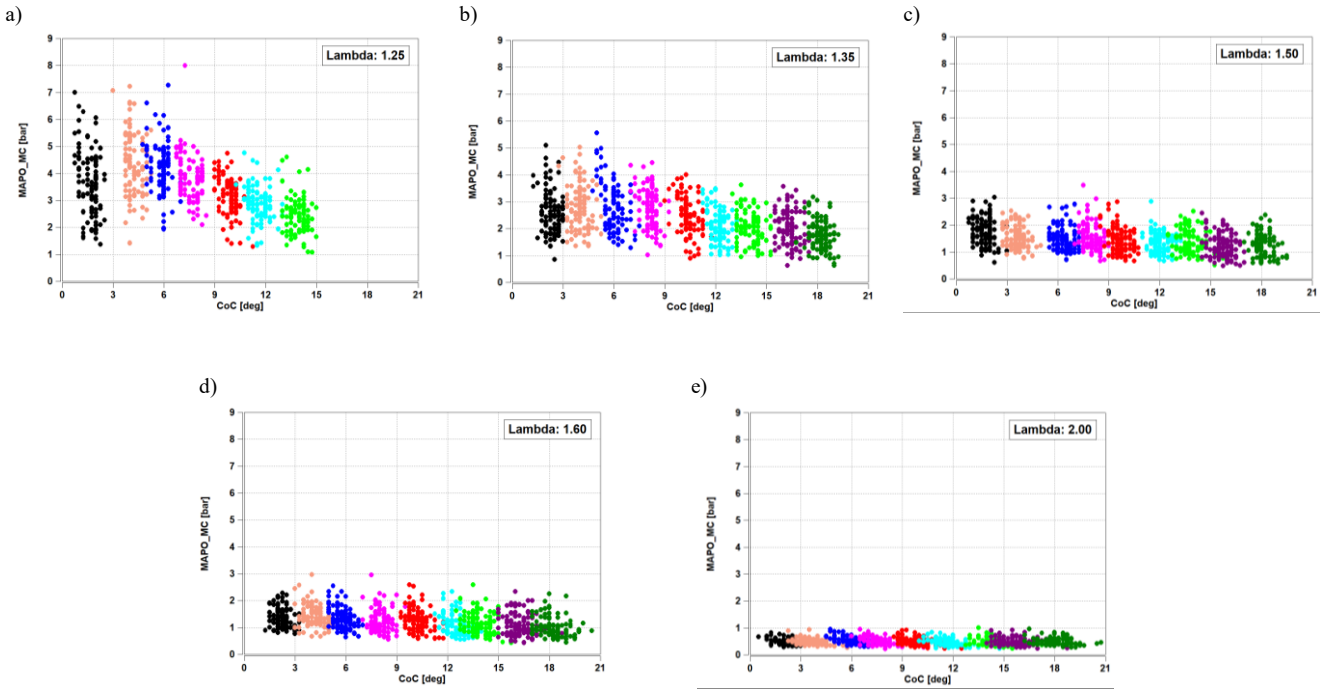

Fig. 22. Dependence of MAPO knock at different excess air ratios in the main chamber as a function of CoC

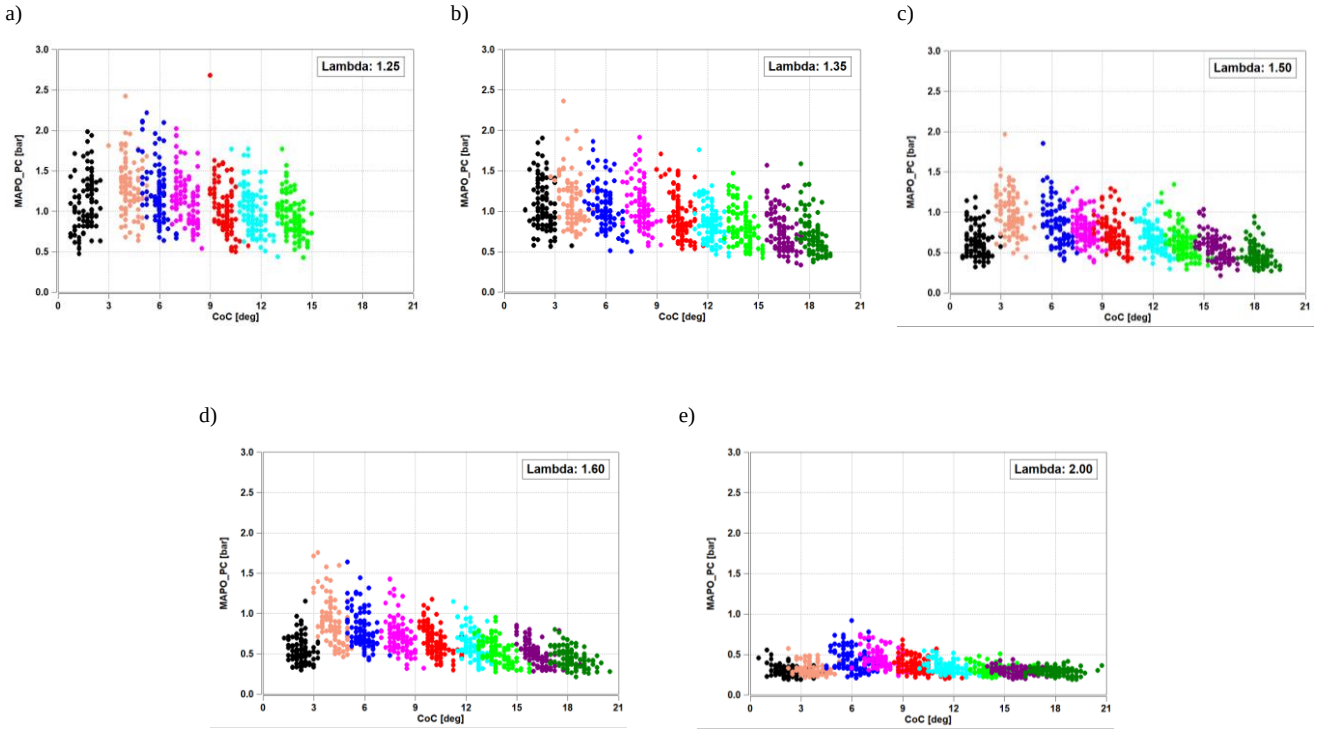

Fig. 23. Dependence of MAPO knock at different excess air ratios in the pre-chamber as a function of CoC

The MAPOs characterizing the pre-chamber are much smaller relative to those corresponding to the main chamber. At λ = 1.25, the maximum value of MAPO = 2.68 bar was obtained for CoC = 10°CA aTDC (Fig 23a). At λ = = 1.35, and with a change in CoC, continuous knocking conditions (MAPO > 1 bar) are observed – Fig. 23b. At λ = = 1.50 and λ = 1.6, the MAPO value did not exceed 2 bar, with most cycles reaching values below the MAPO = 1 bar limit (Fig. 23c) – corresponding to correct combustion (no knocking). As in the case of the main chamber, the entire measurement series at λ = 2.00 did not exceed the value of 1 bar, so combustion in the pre-chamber proceeded without the occurrence of knocking combustion. In addition, in the case of the leanest mixture, a slight increase in the maximum amplitude of pressure pulsations was noted at CoC = = 6°CA and CoC = 8°CA, but their value did not exceed 1 bar.

The reason for the reduction in maximum MAPO in the pre-chamber relative to the main chamber is twofold.

First, most of the charge is burned in the main chamber, where there is better purging from residual exhaust gas. Second, the pre-chamber volume is many times smaller than the main chamber. Knocking combustion occurs when there is a much more sudden heat release than in the case of a correct combustion process. Due to the intensification of pressure and the non-uniform nature of its distribution, pressure waves or shock waves are created, which then propagate through the chamber [15]. The lower intensity of this phenomenon in the pre-chamber is due to the smaller volume of the chamber, in which these shock waves do not develop to the same extent as in the main chamber.

Sun et al. [30] conducted tests using an SI engine without a pre-chamber and indicated that much higher ignition advance angle values were required to achieve knocking combustion (above 30 deg bTDC). In the current tests, an ignition angle of 5 deg bTDC caused very significant knocking combustion (at λ values < 2.0).

7. Conclusions

Investigations of the hydrogen combustion process using a two-stage combustion architecture under knock combustion conditions were carried out with lean mixtures in the range of λ = 1.25 to 2.0. It was found that under two-stage combustion conditions up to λ = 1.6, we are dealing with knock combustion. Under the analyzed conditions, a significant reduction is possible only by increasing the excess air ratio. Despite the fact that the research was conducted under conditions of limited IMEP loading, knock ranges were obtained that are in line with other studies [18, 20]. The main conclusions of the study are presented below.

1. Maintaining a constant CoC with increasing excess air requires increasing the ignition advance due to the extension of the combustion process.
2. The CoC delay results in a decrease of the maximum combustion pressure in the preliminary and main combustion chambers. In the analyzed range of CoC, the highest combustion pressure occurred at CoC 2°CA aTDC while the lowest occurred at the center of combustion fixed furthest from TDC, that is, at λ = 1.25 – CoC = 14°CA aTDC and for the remaining values of the excess air ratio at CoC = 18°CA aTDC.
3. At high values of excess air ratio, the maximum IMEP value was obtained at CoC = 12°CA aTDC. Analysis of the IMEP difference in both chambers indicates that increasing CoC reduces the IMEP difference in both chambers. The IMEP difference values for both combustion chambers decrease twice at extreme CoC setpoints.
4. The dependence of the combustion duration on the applied mixture composition and the position of CoC is shown. For mixtures in the range of λ = 1.25–1.35, the combustion time increases with the delay of CoC; increasing the dilution of the mixture to the value of 1.5 and 1.6 is characterized by the absence of significant differences in combustion time with changing CoC. For λ = 2.00, delaying CoC results in shorter combustion times.
5. The quantification of the knock combustion phenomenon is presented based on the MAPO index. The excess air ratio is a factor that affects knock much more significantly than changing the CoC. At small values of λ = = 1.25–1.6, knocking occurs regardless of the CoC setting with a maximum value of MAPO ~ 7. Increasing the CoC over this range λ slightly reduces the intensity of knocking. At λ = 2.0, no knocking combustion (MAPO up to 1 bar) is observed over the entire CoC range.
6. Pre-chamber combustion analysis indicates the occurrence of knock in the range λ = 1.25–1.6. In this range, knock in the pre-chamber is characterized by three times lower MAPO values. At λ = 2, MAPO averages about 0.5 bar.

The presented research and analysis results do not exhaust the subject matter. Further research work will focus on:

- analyzes hydrogen knock combustion in terms of the active combustion chamber with a variable excess air ratio
- assessment of the ammonia combustion process in the TJI system as a zero-emission fuel
- co-combustion of hydrogen (injected into the pre-chamber) and ammonia (injected into the main chamber) in terms of knock combustion, excess air coefficient, and engine efficiency.

Acknowledgements

This work was supported by the Poznan University of Technology [interdisciplinary grant 0415/SIGR/7286].

Nomenclature

aTDC	after top dead center
bTDC	before top dead center
CNG	compressed natural gas
CoC	center of combustion
dPcyl	pressure rise rate
dQ	heat rate released

D3PDθ maximum value from the third-order derivative of the pressure pulsation
EOC end of combustion
FON fuel octane number
HR10 the start of combustion (angle at which 10% of the heat is released)
HR90 – the end of combustion (angle at which 90% of the heat is released)
IMEP indicated mean effective pressure
IMPO integral of modulus of pressure oscillations
IMPOG integral modulus of pressure oscillations gradient
KI20 Knock Index – indicator of knocking intensity
MAPO maximum amplitude of pressure oscillations
MBT maximum brake torque
MC main chamber
n engine speed
Ni indicated power
NO_x nitrogen oxides
Pcyl cylinder pressure
PC pre-chamber
PI pressure intensity
Q heat released
SOC start of combustion
SOIgn start of ignition
TDC top dead center
TJI Turbulent Jet Ignition
λ air excess ratio

Bibliography

[1] Aramburu A, Guido C, Bares P, Pla B, Napolitano P, Beatrice C. Knock detection in spark ignited heavy duty engines: an application of machine learning techniques with various knock sensor locations. Measurement. 2023;224:113860. https://doi.org/10.1016/j.measurement.2023.113860

[2] Aljabri H, Silva M, Houidi MB, Liu X, Allehaibi M, Almatrafi F et al. Comparative study of spark-ignited and pre-chamber hydrogen-fueled engine: a computational approach. Energies. 2022;15(23):8951. https://doi.org/10.3390/en15238951

[3] Arrigoni V, Cornettti G, Gaetani B, Ghezzi P. Quantitative systems for measuring knock. P I Mech Eng. 1972;186(1): 575-583. https://doi.org/10.1177/002034837218600137

[4] Attard WP, Blaxill H, Anderson EK, Litke P. Knock limit extension with a gasoline fueled pre-chamber jet igniter in a modern vehicle powertrain. SAE Int J Engines. 2012;5(3): 1201-1215. https://doi.org/10.4271/2012-01-1143

[5] Attard WP, Parsons PA. Normally aspirated spark initiated combustion system capable of high load, high efficiency and near zero NO_x emissions in a modern vehicle powertrain. SAE Int J Engines. 2010;3(2):269-287. https://doi.org/10.4271/2010-01-2196

[6] Benson G, Fletcher EA, Murphy TE, Scherrer HC. Knock (detonation) control by engine combustion chamber shape. SAE Technical Paper 830509. 1983. https://doi.org/10.4271/830509

[7] Brecq G, Le Corre O. Modeling of in-cylinder pressure oscillations under knocking conditions: Introduction to pressure envelope curve. SAE Technical Paper 2005-01-1126. 2005. https://doi.org/10.4271/2005-01-1126

[8] Checkel MD, Dale JD. Pressure trace knock measurement in a current S.I. production engine. SAE Technical Paper 890243. 1989. https://doi.org/10.4271/890243

[9] Chun KM, Heywood JB. Characterization of knock in a spark-ignition engine. SAE Technical Paper 890156. 1989. https://doi.org/10.4271/890156

[10] Das L. Hydrogen engines: a view of the past and a look into the future. Int J Hydrogen Energ. 1990;15(6):425-443. https://doi.org/10.1016/0360-3199(90)90200-I

[11] Ferraro CV, Marzano M, Millo F, Bochicchio N. Comparison between heat transfer and knock intensity on statistical basis. SAE Technical Paper 962101. 1996. https://doi.org/10.4271/962101

[12] Ferraro CV, Marzano M, Nuccio P. Knock limit measurement in high speed SI engines. SAE Technical Paper 850127. 1985. https://doi.org/10.4271/850127

[13] Franklin ML, Murphy TE. A study of knock and power loss in the automotive spark ignition engine. SAE Technical Paper 890161. 1989. https://doi.org/10.4271/890161

[14] Gis M, Gis W. The current state and prospects for hydrogenisation of motor transport in Northwestern Europe and Poland. Combustion Engines. 2022;190(3):61-71. https://doi.org/10.19206/CE-144560

[15] Heywood JB. Internal combustion engine fundamentals. 2nd ed. McGraw-Hill Education. New York 2018.

[16] Horner TG. Knock detection using spectral analysis techniques on a Texas Instrument TMS320 DSP. SAE Technical Paper 960614. 1996. https://doi.org/10.4271/960614

[17] Karim G. Hydrogen as a spark ignition engine fuel. Int J Hydrogen Energ. 2003;28(5):569-577. https://doi.org/10.1016/S0360-3199(02)00150-7

[18] Koch DT, Sousa A, Bertram D. H2-engine operation with EGR achieving high power and high efficiency emission-free combustion. SAE Technical Paper 2019-01-2178. 2019. https://doi.org/10.4271/2019-01-2178

[19] Konig G, Sheppard CGW. End gas autoignition and knock in a spark ignition engine. SAE Technical Paper 902135. 1990. https://doi.org/10.4271/902135

[20] Korn T, Ebert T, Vonnoe M, Tala H, Lang M. Hydrogen engines strong case – new performance benchmarks with hydrogen direct injection. 43rd International Vienna Motor Symposium. Vienna 2022.

[21] Lasocki J. Engine knock detection and evaluation: a review (in Polish). Zeszyty Naukowe Instytutu Pojazdów. 2016;109:41-50.

[22] Leppard WR. Individual-cylinder knock occurrence and intensity in multi-cylinder engines. SAE Technical Paper 820074. 1982. https://doi.org/10.4271/820074

[23] MAHLE Jet Ignition. https://www.mahle-powertrain.com/en/experience/mahle-jet-ignition/ (accessed on 10 April 2024)

[24] Nagalingam B, Dübel M, Schmillen K. Performance of the supercharged spark ignition hydrogen engine. SAE Technical Paper 831688. 1983. https://doi.org/10.4271/831688

[25] Natkin RJ, Tang X, Boyer B, Oltmans B, Denlinger A, Heffel JW. Hydrogen IC engine boosting performance and NO_x study. SAE Technical Paper 2003-01-0631. 2003. https://doi.org/10.4271/2003-01-0631

[26] Pielecha I, Szwajca F, Skobiej K. Experimental investigation on knock characteristics from pre-chamber gas engine fueled by hydrogen. Energies. 2024;17(4):937. https://doi.org/10.3390/en17040937

[27] Qiang Y, Ji C, Wang S, Xin G, Hong C, Wang Z, Shen J. Study on the effect of variable valve timing and spark timing on the performance of the hydrogen-fueled engine with passive pre-chamber ignition under partial load conditions. Energ Convers Manage. 2024;302:118104. https://doi.org/10.1016/j.enconman.2024.118104

[28] Siano D, Panzam MA, D'Agostino D. Knock detection based on MAPO analysis, AR model and discrete wavelet transform applied to the in-cylinder pressure data: results and comparison. SAE Int J Engines. 2014;8(1):1-13. https://doi.org/10.4271/2014-01-2547

[29] Stępień Z. Analysis of the prospects for hydrogen-fuelled internal combustion engines. Combustion Engines. 2023. https://doi.org/10.19206/CE-174794

[30] Sun J, Zhang X, Tang Q, Wang Y, Li Y. Knock recognition of knock sensor signal based on wavelet transform and variational mode decomposition algorithm. Energ Convers Manage. 2023;287:117062. https://doi.org/10.1016/j.enconman.2023.117062

[31] Szwaja S, Bhandary K, Naber J. Comparisons of hydrogen and gasoline combustion knock in a spark ignition engine. Int J Hydrogen Energ. 2007;32(18):5076-5087. https://doi.org/10.1016/j.ijhydene.2007.07.063

[32] Szwaja S, Naber JD. Dual nature of hydrogen combustion knock. Int J Hydrogen Energ. 2013;38(28):12489-12496. https://doi.org/10.1016/j.ijhydene.2013.07.036

[33] Verhelst S, Sierens R, Verstraeten S. A critical review of experimental research on hydrogen fueled SI engines. SAE Technical Paper 2006-01-0430. 2006. https://doi.org/10.4271/2006-01-0430

[34] Wang K, Zhang Z, Sun B Zhang S, Lai F, Ma N et al. Experimental investigation of the working boundary limited by abnormal combustion and the combustion characteristics of a turbocharged direct injection hydrogen engine. Energ Convers Manage. 2024;299:117861. https://doi.org/10.1016/j.enconman.2023.117861

[35] White C, Steeper R, Lutz A. The hydrogen-fueled internal combustion engine: a technical review. Int J Hydrogen Energ. 2006;31(10):1292-1305. https://doi.org/10.1016/j.ijhydene.2005.12.001

[36] Yip HL, Srna A, Yuen ACY, Kook S, Taylor RA, Yeoh GH et al. A review of hydrogen direct injection for internal combustion engines: towards carbon-free combustion. Appl Sci. 2019;9(22):4842. https://doi.org/10.3390/app9224842

Filip Szwajca, MEng. – Faculty of Civil and Transport Engineering, Poznan University of Technology, Poland.
e-mail: *filip.szwajca@put.poznan.pl*

Cezary Gawrysiak, MEng. – Faculty of Civil and Transport Engineering, Poznan University of Technology, Poland.
e-mail: *cezary.gaw@gmail.com*

Prof. Ireneusz Pielecha, DSc., DEng. – Faculty of Civil and Transport Engineering, Poznan University of Technology, Poland.
e-mail: *ireneusz.pielecha@put.poznan.pl*

Article citation info:
Smolec R, Karpiuk W, Bajerlein M, Waligórski M, Kril P. The use of dimethyl ether (DME) solution in compression ignition engine. Combustion Engines. 2024;198(3):123-128. https://doi.org/10.19206/CE-188832

Rafał SMOLEC
Wojciech KARPIUK
Maciej BAJERLEIN
Marek WALIGÓRSKI
Paweł KRIL

Combustion Engines
Polish Scientific Society of Combustion Engines

The use of dimethyl ether (DME) solution in compression ignition engine

ARTICLE INFO

Received: 16 January 2024
Revised: 8 March 2024
Accepted: 17 May 2024
Available online: 27 May 2024

The development of compression ignition combustion engines is focused on meeting many challenges, mainly related to growing ecological requirements. Currently, however, due to technological barriers, meeting them is very difficult and requires the use of additional exhaust gas treatment systems. The use of injection of a diesel and gas solution seems to be very promising. The article presents the results of engine tests involving the use of a solution of diesel fuel and dimethyl ether. The tests were performed on a single-cylinder research engine equipped with a common rail fuel system. The obtained results suggest that the use of the solution has a positive effect on the process of creating the fuel-air mixture, resulting in a reduction in the concentration of HC and CO while increasing the share of NO_x, suggesting an improvement in the combustion process, as evidenced by the limiting injection dose.

Key words: *dimethyl ether, diesel solutions, exhaust emissions, ecology, alternative fuels*

1. Introduction

Since its introduction to the market in the 1930s, diesel engines have gained wide recognition in the automotive world. Their growing popularity resulted not only from their high efficiency but also from their ability to generate a significant amount of torque at low rpm, which affects fuel economy and their durability. These engines played a key role in passenger cars, heavy-duty vehicles, buses, and even locomotives or ships, despite the fast evolution of electric motors and battery technology [14].

Initially, diesel engines were the most popular in the commercial vehicle sector due to their excellent economic properties [17]. However, over time, the technology has found a widespread use in passenger cars, since drivers expect engine efficacy balanced with fuel efficiency. As a result, for many years, diesel engines dominated the automotive market, gaining loyal supporters around the world.

With the rising popularity, diesel engines also gained some opponents. In recent years, especially in the context of growing environmental awareness and concern for the environment, these engines have come under fire due to the emission of harmful substances such as nitrogen oxides (NO_x) and particulate matter (PM) [11, 12]. More and more stringent requirements were set for exhaust emission standards, which forced the use of technologically advanced exhaust gas cleaning systems based on particulate filters, multi-level exhaust gas recirculation systems, or selective catalytic reduction (SCR) systems[15, 16].

One of the most effective ways to reduce exhaust emissions is to improve the fuel atomization process, which results in a more homogeneous fuel-air mixture and allows for better control of the combustion process. The currently used injection systems generate a fuel pressure of up to 2500 bar, which allows the atomization of the injection dose into up to 8 parts. Further, atomization by increasing the pressure of the injected fuel is becoming more and more difficult to achieve due to technological limitations and the strength of the materials.

One way to improve fuel atomization may be to create a solution of gas in the fuel. The concept involves supplying a certain amount of gas to the fuel, which is then dissolved in it; the pressure generated by the high-pressure pump causes the fuel in the reservoir and injection lines to remain in equilibrium. During the next stage occurring when the injector is opened, an effect is observed that accompanies the release of dissolved gas from the liquid fuel during injection into the combustion chamber (desorption effect), which occurs due to a strong imbalance. This phenomenon is due to the characteristics of this solution – when the pressure is lowered, the excess gas dissolved in the liquid is spontaneously released simultaneously from the entire volume. The decrease in pressure is accompanied by a decrease in the equilibrium thermodynamic potential. Thus, the negative pressure gradient is the thermodynamic stimulus that causes the release of gas from the solution. The rate of gas release is related to the rate of change of the stimulus. The goal of the proposed concept is to achieve better fuel injection, at least qualitatively, compared to that obtained in high-pressure systems while maintaining relatively low injection pressures.

Most gases dissolve poorly in liquids, and the amount of gas dissolved strongly depends on the pressure and temperature at which dissolution occurs. Gas atoms (or molecules) in the solution state are uniformly dispersed throughout the liquid volume. Releasing simultaneously throughout the volume, the molecules form dispersed microbubbles, expand, and tend to merge. As a result, the volume is divided into two parts: one – is occupied by solution and the other – by gas. However, if the pressure drop occurs dynamically, then the microbubbles will not manage to merge into a single volume. A factor that promotes the intensification of the effect of desorption of gas from the solution is, therefore, the speed of the process. This is beneficial for the engine. There is a significant pressure difference between the atomizer from which the fuel flows and the combustion chamber through which the fuel passes. The fuel flows out

over a short distance (the length of the atomizer channels) and in a very short time. The simultaneous combination of these factors means a very high rate of pressure change during injection and, thus, a very large thermodynamic potential gradient. Thus, if a fuel-gas solution is injected into the injector, we note that during the outflow of fuel through the atomizer orifices, there is a dynamic release of gas in the fuel due to a rapid drop in the thermodynamic potential in the outlet path. This mechanism causes the fuel droplets to burst from the center. Thus, it will be an additional factor supporting the existing fuel atomization mechanism.

According to the concept presented, in the high-pressure part of the injection system (from the high-pressure pump up to the atomizer ports), the pressure should be maintained at such a level that the gas cannot escape from the solution. In this part of the system, the fuel with gas should form a homogeneous solution. Gas release coupled with expansion should take place only outside the atomizer to help break up droplets along the fuel outlet. This process is qualitatively illustrated in Fig. 1 [4].

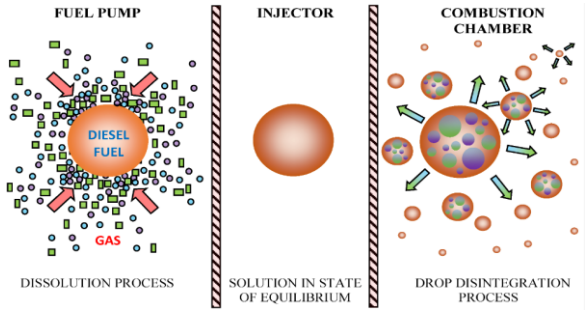

Fig. 1. Spray mechanism of gas dissolved from fuel

Various gases dissolved in diesel fuel have been studied so far, but dimethyl ether seems to be one of the most very promising. Owing to its properties (very good solubility and high cetane number), it is also suitable for diesel engines as a stand-alone fuel [10].

The use of dimethyl ether as a fuel to power compression ignition engines has many benefits. DME has physicochemical parameters similar to conventional diesel fuel. A comparison of the most important parameters is presented in Table 1.

A very important aspect supporting the wider use of dimethyl ether as a fuel is the fact that it belongs to the group of second-generation alternative fuels. DME production technology is based, among others, on biomass gasification, which makes it possible to increase independence from fossil fuels [2].

The basic parameters that determine whether the fuel is suitable for powering compression ignition engines include the self-ignition temperature and the cetane number. In both cases, the alternative fuel is characterized by more favorable values. The self-ignition temperature is lower by 15 degrees Celsius, thanks to which the fuel allows for easier starting of the engine at lower temperatures, while the cetane number is, on average, several points higher than in the case of conventional diesel fuel. Both of these parameters make the DME in the compression ignition engine ignite more easily than in the case of conventional diesel fuel. Another preferred parameter is a low boiling point, which is 25 degrees Celsius. DME occurs in atmospheric conditions in the gaseous form. Therefore, it has to be stored in the liquefied form. Its density is lower than that of conventional diesel fuel. In addition, it has an oxygen atom in its molecule, which means that its calorific value is lower than that of conventional diesel fuel. This requires the use of larger tanks to ensure the same operating time as for the conventional diesel fuel motor power supply [18, 19].

Table 1. Comparison of dimethyl ether and diesel characteristics [5, 7, 13]

Parameter	Unit	Dimethyl ether	Diesel oil
Critical pressure	MPa	5.37	3.00
Lower calorific value	MJ/kg	27.6	39.5
Lower explosion limit	% vol.	3.2	0.6
Liquid density	kg/m^3	667	842.5
Upper explosion limit	% vol.	18	7
Kinematic viscosity of liquid	cSt	< 0.1	3
Cetane index		57	51
Molar mass	g/mol	46	170
Surface tension	N/m	0.012	0.027
Vapor pressure	kPa	530	<< 10
C/H ratio		0.337	0.516
Stoichiometric ratio of air/fuel		9	14.6
Chemical structure		CH_3–O–CH_3	–
Critical temperature	°C	126	434
Self-ignition temperature	°C	234	249
Boiling point at 1atm	°C	–25	176–370
Oxygen content	% mass	34.8	0
Carbon content	% mass	52.2	86,5
Hydrogen content	% mass	13	13.4

The challenge in the widespread use of dimethyl ether as the main fuel for powering diesel engines is its low lubricity and viscosity. These parameters have a significant impact on the operation of injection systems, as they are responsible for creating a lubricating film that prevents from the wear of engine parts. Due to their low value, the production of insufficient thickness of the lubricating film leads to faster wear of engine parts. These properties disqualify the use of pure DME. The problem of low lubricity can be solved by using additives to increase lubricity. DME dissolves very well in conventional diesel fuel therefore it is very promising as an additive to conventional diesel fuel. Thanks to DME physical properties, it can be used to create a solution, and thus obtain a release effect.

A very important issue from the point of view of environmental impact is that dimethyl ether can be produced from renewable substances. One of the methods of obtaining DME is the gasification of biomass such as wood, agricultural waste, or biological residues. The biomass is subjected to a pyrolysis process, which produces synthesis gas. Then, using appropriate catalysts based on copper and zinc compounds, methanol is synthesized, which is then transformed into dimethyl ether in the next step. Producing DME from renewable raw materials is undoubtedly the most ecological, but due to the economic aspects and efficiency of the process, it is currently most often produced from natural gas rich in methane in the steam reforming

process. Due to the fact that the combustion of DME in a compression ignition engine results in a reduction in emissions of toxic compounds contained in the fuel [8], it is reasonable to examine the impact of DME as a fuel additive with its release effect on engine operating parameters and emissions.

2. Preparation of the test stand

Due to the fact that dimethyl ether is a gaseous fuel, it is necessary to prepare a suitable system for storing it and supplying it to the high-pressure pump [3].

Preparing an injection system that allows gases to dissolve is a big challenge due to the differences in compressibility of both components and the presence of different phases of concentration. For this purpose, a high-pressure pump equipped with a special pumping section (Fig. 2) was used, which allows gas to be supplied and mixed with fuel during stacking.

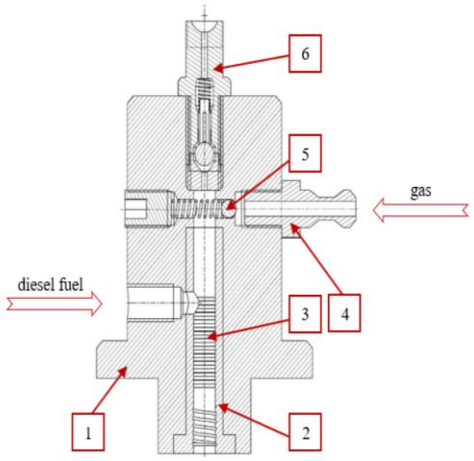

Fig. 2. Delivery section of pump: 1 – body of the delivery section, 2 – cylinder, 3 – section labyrinth seal, 4 – gas stub pipe, 5 – one-way gas valve, 6 – one-way outlet valve [4, 6]

The fuel pump is driven by an independent system consisting of an electric motor controlled by an inverter. The rotational speed is adjusted in such a way as to ensure adequate pressure and output of the pumped fuel while it is overheating since it may affect the measurement results.

Diesel fuel is supplied to the pump at a pressure of 5 bar generated by the initial fuel pump, while gaseous fuel, due to the fact that it is stored in a pressurized cylinder, is supplied to the system directly using a conditioning system equipped with a filter unit and a pressure regulator to control the amount of dissolved gas. For the first series of measurements, standard Bosch CP3 high-pressure fuel pump was used. During the second measurement series, where the solution was created, a special pump was used to dissolve the gas in place of the standard CR pump.

The concentration of dissolved gas in the fuel obtained in this way is difficult to determine precisely; however, under fixed operating conditions of the engine (i.e. constant rotational speed and constant load) it remains at an even level, depending on the pressure at which it is supplied to the high-pressure pump.

The tests were carried out on a motor dynamometer equipped with a single-cylinder SB3.1 test engine coupled with an electric swirl brake. The basic parameters of the test engine are presented in Table 2.

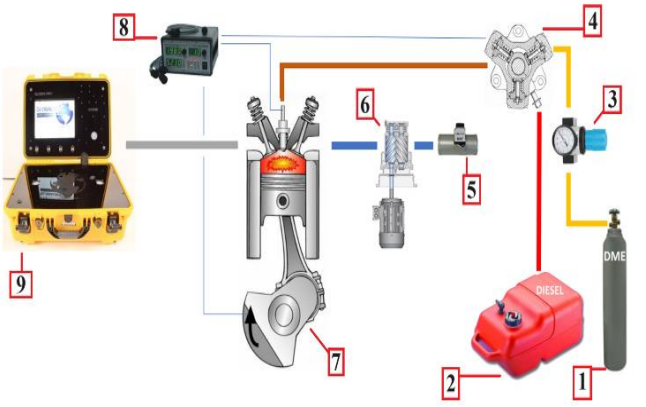

Fig. 3. Engine test bench: 1 – DME tank, 2 – diesel tank, 3 – filtration block with pressure regulator, 4 – fuel pump/modified fuel pump, 5 – mass air flow meter, 6 – inlet air compressor, 7 – SB 3.1 engine, 8 – injection controller, 9 – exhaust gases analyzer

Table 2. Tested engine parameters

Cylinder diameter	127 mm
Stroke	146 mm
Displacement	1.850 dm^3
Compression ratio	15.75
Crank ratio	0.263
Connecting rod length	277 mm
Inlet valve opening angle	4° before TDC
Inlet valve closing angle	57° after BDC
Exhaust valve opening angle	42° before BDC
Exhaust valve closing angle	24° after TDC

3. Methods

The measuring devices and test equipment mentioned in the previous section were selected to carry out the tests due to the scope of work adequate to the expected results. Exhaust gases for the Axion analyzer were collected directly from the exhaust system using dedicated, leakless holes. In accordance with current engine testing practices, measurements began after the engine warm-up phase, when the temperature of the coolant and oil had stabilized.

Tests were planned to be carried out for 900 rpm. Characteristics were performed covering 6 measurement points in the load range from 0 to 50 nm. The tests began with no-load operation, then the brake torque was increased by 10 nm and the injection time was adjusted to achieve the selected operating points.

The start of the injection angle was set up by a dedicated controller that triggered a signal controlling the power amplifier supplying the injector coil. The controller uses a signal from an absolute encoder with a resolution of 8 bits, which, due to limited availability, was mounted on the camshaft. The mounting method and resolution of the encoder allow the injection angle to be adjusted by exactly 2.8125 degrees. Adjustment of the injection time was carried out with an accuracy of 0.1 ms.

During the research, three measurement series were performed. The first for a conventional injection system equipped with a standard Bosch CP3 pump, which serves as

a reference point for further measurements. The next two tests were carried out using a dedicated high-pressure pump, enabling the dissolution of gases. Dimethyl ether was fed to a high-pressure pump equipped with a modified pumping section, enabling the dissolution of gases at pressures of 3 and 5 bar. The DME supply pressure was changed using a pressure regulator block and was controlled before the start of each series of measurements. Adjusting the dimethyl ether supply pressure allows you to control the amount of gas dissolved in the diesel fuel. Increasing the DME supply pressure changes the amount of gas in the solution. Therefore, in order to determine the impact on the concentration of harmful exhaust gas components, tests were carried out for two values of DME supply pressure (3 bar and 5 bar).

The fuel pressure during the measurements was regulated by an external controller based on the reading from the pressure sensor in the CR tank and regulating the operation of the electronic fuel dose valve on the pump and the pressure regulator on the Common Rail tank. In order to demonstrate the favorable features of gas dissolution in the fuel, the injection pressure in each measurement series was 40 MPa.

4. Results

Measurements of the concentration of gaseous components of exhaust gases were carried out after the engine reached the nominal operating temperature. The achievement of this state was determined on the basis of the temperature of the oil and the cooling liquid. The effects of using a mixture of diesel oil and dimethyl ether to power the test engine could already be observed in the case of idling, which manifested itself in the need to reduce the injection time in order to achieve the same rotational speed as the common rail. The trend shown in Fig. 4 is also noticeable for other load values.

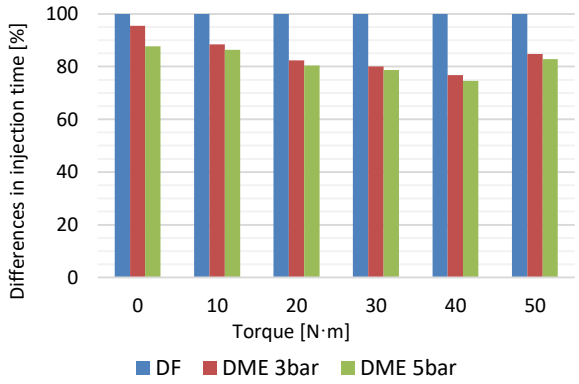

Fig. 4. Comparison of injection time for diesel and DME solutions

The comparison of carbon monoxide concentration as the percentage proportion is shown in Fig. 5. The gas-fuel solution reduces the concentration compared to conventional fuel. The share of DME in the solution can be increased by increasing the pressure of delivering it to the pump. The higher the DME share in the solution, the more noticeable the reduction of carbon monoxide concentration is.

Figure 6 shows a comparison of hydrocarbon concentrations. A significant reduction in the concentration of toxic compounds is already observed at idling speed. At the analyzed engine operating point, the use of the solution reduces hydrocarbon concentration by about 60%. As the load increases, the difference in hydrocarbon concentration becomes even more apparent. At the maximum load, the HC concentration in the case of the gas-fuel solution (for 5 bar DME) is only 10% of the concentration that was measured when feeding the engine purely with conventional fuel.

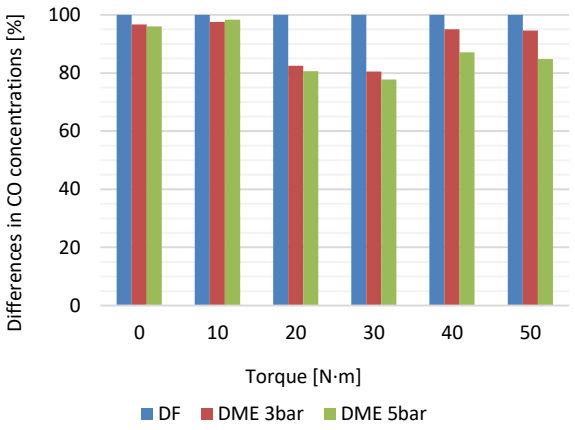

Fig. 5. Comparison of CO concentration for diesel and DME solutions

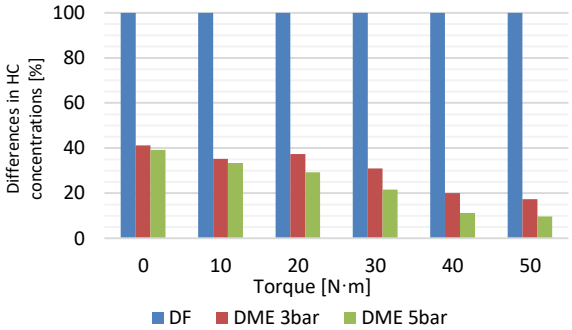

Fig. 6. Comparison of HC concentration for diesel and DME solutions

Should the improvement of the atomization structure be solely accounted for the reduction in PM and HC when the engine was supplied with a solution, an increase in NO_x concentration is exhaust gases is predicted. The results of NO_x measurements presented in Fig. 7. clearly confirm this prediction. An increase in NO_x concentration was noted at almost all measurement points. The NO_x emissions significantly increase together with the increasing amount of dissolved air, especially within the range of low engine speed.

5. Summary

Dimethyl ether, due to its properties similar to diesel fuel, is an ideal fuel for powering compression-ignition engines. However, as of today, technological problems resulting from its low lubricity, viscosity, and energy value remain to be solved. Therefore, the use of DME as an independent fuel is difficult to implement.

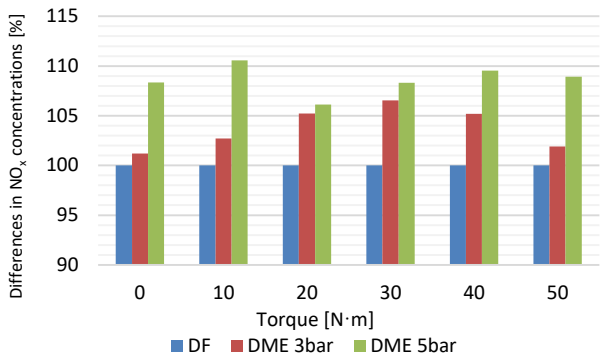

Fig. 7. Comparison of NO_x concentration for diesel and DME solutions

Dissolving the gas in the diesel fuel creates an equilibrium mixture by maintaining high pressure. At the moment of injection, when the pressure drops, gas molecules are released from the solution. The obtained research results indicate that the occurrence of this phenomenon significantly affects the combustion process and the concentration of harmful compounds in the exhaust gases. Although the use of DME as a fuel in a diesel engine is characterized by a reduction in NO_x emissions (mainly as a result of lowering the maximum combustion temperature), by using a solution of a small amount of gas and its release at the time of injection, an increase in the concentration of these compounds is observed due to the improvement of the atomization mechanism and the combustion process.

Feeding the engine with the solution has a significant impact on reducing the concentration of hydrocarbons in exhaust gases. The observed results prove the improvement of the fuel evaporation process and the improvement of the process of creating the fuel-air mixture, which becomes more homogeneous throughout the entire volume of the combustion chamber.

These studies also show that in order to perform measurements at the same engine operating points (constant rotational speed and load), it is necessary to shorten the injector opening time when fueled with a gas and diesel solution. It should be noted that all tests were performed at the same injection pressure of 40 MPa. It is worth emphasizing that the indicated fuel pressure value is too low to ensure sufficient fuel atomization in the case of diesel fuel.

The dissolution of DME in diesel fuel, enabled by the use of a specially designed fuel pump, improves the process of creating the fuel-air mixture despite maintaining the same relatively low injection pressure. This mixture has a positive effect on the combustion process from an environmental and useful perspective by increasing the generated torque.

The presented test results and their analysis show that adding dimethyl ether to diesel in a high-pressure pump equipped with a special forcing section allows for the creation of a solution that remains in a state of equilibrium until it flows out of the atomizer when the dose is injected into the cylinder. Therefore, there is a phenomenon of dynamic release of DME bubbles from the solution, which causes the fuel droplets to burst from the inside.

We can also observe that increasing the gas pressure supplied to the pump, thereby increasing the concentration of dimethyl ether in the solution, results in an even greater reduction in the concentration of HC and CO and an increase in the NO_x concentration. It can therefore be concluded that the higher the gas concentration in the solution, the more intense the desorption phenomenon occurs, significantly improving atomization.

Taking into account that currently, in order to meet increasingly stringent exhaust emission standards, it is necessary to use injection systems generating pressure exceeding 250 MPa, the use of a solution of dimethyl ether and diesel oil may be an interesting alternative to further increasing the pressure, which creates more and more technological problems, negatively affecting on the durability and reliability of engines.

It should be expected that the improvement of fuel atomization, the effects of which are observed in the presented results of concentrations of gaseous components of exhaust gases, will also affect the mass and number of generated particulate matter. Therefore, further directions of research will include determining the impact of the use of a solution of dimethyl ether with diesel fuel on the amount and mass, and size distribution of particle matter.

Nomenclature

BDC	bottom death center
CO	carbon oxide
CR	common rail
DF	diesel fuel
DME	dimethyl ether
HC	hydrocarbons
NDIR	nondispersive infrared
NO_x	nitro oxides
PM	particulate matter
SCR	selective catalytic reduction
TDC	top death center

Bibliography

[1] Arcoumanis C, Bae C, Crookes R, Kinoshita E. The potential of di-methyl ether (DME) as an alternative fuel for compression-ignition engines: a review. Fuel. 2007;87(7):1014-1030. https;//doi.org/10.1016/j.fuel.2007.06.007

[2] Azizi Z, Rezaeimaneshb M, Tohidiana T, Rahimpour MR, Dimethyl ether: a review of technologies and production challenges. Chem Eng Process. 2014;82:150-172. https://doi.org/10.1016/j.cep.2014.06.007

[3] Bajerlein M, Bor M, Karpiuk W, Smolec R, Spadło M. Strength analysis of critical components of high-pressure fuel pump with hypocycloid drive. Bull Pol Acad Sci-Te. 2020;68:1341-1350. https://doi.org/10.24425/bpasts.2020.135380

[4] Bajerlein M, Karpiuk W, Smolec R. Use of gas desorption effect in injection systems of diesel engines. Energies. 2021; 14:244. https://doi.org/10.3390/en14010244

[5] Bhide S, Morris D, Leroux J, Wain KS, Perez JM, Boehman AL. Characterization of the viscosity of blends of dimethyl ether with various fuels and additives. Energy&Fuels. 2003; 17(5):1126-1132. https://doi.org/10.1021/ef030055x
[6] Bor M, Borowczyk T, Karpiuk W, Smolec R, Spadło M. Concept of a pump for diesel engines fuel supply using hypocycloid drive. IOP Conf Ser: Mater Sci Eng. 2018;421: 042034. https://doi.org/10.1088/1757-899X/421/4/042034
[7] Lee D, Lee CS. Effects of DME-isobutane blended fuels on combustion and emissions reduction in a passenger car diesel engine. J Energ Eng. 2017;143(4). https://doi.org/10.1061/(ASCE)EY.1943-7897.0000428
[8] Karpiuk W, Smolec R, Idzior M. DME use in self-ignition engines equipped with common rail injection systems. 2016 International Conference on Sustainable Energy, Environment and Information Engineering (SEEIE 2016). 2016:37-43. https://doi.org/10.12783/dteees/seeie2016/4494
[9] Kozak M. Exhaust emissions from a diesel passenger car fuelled with a diesel fuel-butanol blend. SAE Technical Paper 2011-28-0017. 2011. https://doi.org/10.4271/2011-28-0017
[10] Kozak M, Merkisz J. Oxygenated diesel fuels and their effect on PM emissions. Appl Sci. 2022;12(15):7709. https://doi.org/10.3390/app12157709
[11] Jaworski A, Mądziel M, Kuszewski H, Lejda K, Jaremcio M, Balawender K et al. The impact of driving resistances on the emission of exhaust pollutants from vehicles with the spark ignition engine fuelled with petrol and LPG. SAE Technical Paper 2020-01-2206. 2020. https://doi.org/10.4271/2020-01-2206
[12] Jedliński Ł, Caban J, Krzywonos L, Wierzbicki S, Brumerčík F. Application of the vibration signal in the diagnosis of the valve clearance of an internal combustion engine. J Vibroeng. 2015;17(1):175-187. https://www.extrica.com/article/15446
[13] Paliwa do pojazdów samochodowych. Oleje napędowe. Wymagania i metody badań. PN-EN 590:2022-08 (in Polish).
[14] Pigłowska M, Kurc B, Galiński M, Fuć P, Kamińska M, Szymlet M et al. Challanges of safe electrolytes applied in lithium-ion cells – a review. Materials. 2021;14(22):6783. https://doi.org/10.3390/ma14226783
[15] Rymaniak Ł, Kamińska M, Szymlet N, Grzeszczyk R. Analysis of harmful exhaust gas concentrations in cloud behind a vehicle with a spark ignition engine. Energies. 2021;14(6): 1769. https://doi.org/10.3390/en14061769
[16] Rymaniak Ł, Merkisz J, Szymlet N, Kamińska M, Weymann S. Use of emission indicators related to CO_2 emissions in the ecological assessment of an agricultural tractor. Eksploat Niezawodn. 2021;23(4):605-611. https://doi.org/10.17531/ein.2021.4.2
[17] Sawczuk W, Merkisz-Guranowska A, Rilo Cañás AM, Kołodziejski S. New approach to brake pad wear modelling based on test stand friction-mechanical investigations Eksploat Niezawodn. 2022;24(3):419-426. https://doi.org/10.17531/ein.2022.3.3
[18] Smolec R, Idzior M, Karpiuk W, Kozak M. Assessment of the potential of dimethyl ether as an alternative fuel for compression ignition engines, Combustion Engines. 2017;169(2):181-186. https://doi.org/10.19206/CE-2017-232
[19] Thomas G, Feng B, Veeraragavan A, Cleary MJ, Drinnan N. Emissions from DME combustion in diesel engines and their implications on meeting future emission norms – a review. Fuel Process Technol. 2014;119:286-304. https://doi.org/10.1016/j.fuproc.2013.10.018

Rafał Smolec, MEng. – Faculty of Civil and Transport Engineering, Poznan University of Technology, Poland.
e-mail: *rafal.smolec@put.poznan.pl*

Maciej Bajerlein, DSc., DEng. – Faculty of Civil and Transport Engineering, Poznan University of Technology, Poland.
e-mail: *maciej.bejerlein@put.poznan.pl*

Wojciech Karpiuk, DSc., DEng. – Faculty of Civil and Transport Engineering, Poznan University of Technology, Poland.
e-mail: *wojciech.karpiuk@put.poznan.pl*

Prof. Marek Waligórski, DSc., DEng. – Faculty of Civil and Transport Engineering, Poznan University of Technology, Poland.
e-mail: *marek.waligórski@put.poznan.pl*

Paweł Kril, MEng. – ENVIBRA Sp. z o.o., Poznan, Poland.
e-mail: *pawel.kril@wp.pl*

PTNSS

Silesian University of Technology

XI INTERNATIONAL

CONGRESS ON COMBUSTION ENGINES

POWERTRAINS TECHNOLOGIES AND ALTERNATIVE FUELS

POLISH SCIENTIFIC SOCIETY
OF COMBUSTION ENGINES

23rd-25th June 2025

congress.ptnss.pl

Silesian University of Technology
Faculty of Transport and Aviation Engineering
Zygmunta Krasinskiego str. 8, 40-019 Katowice, Poland

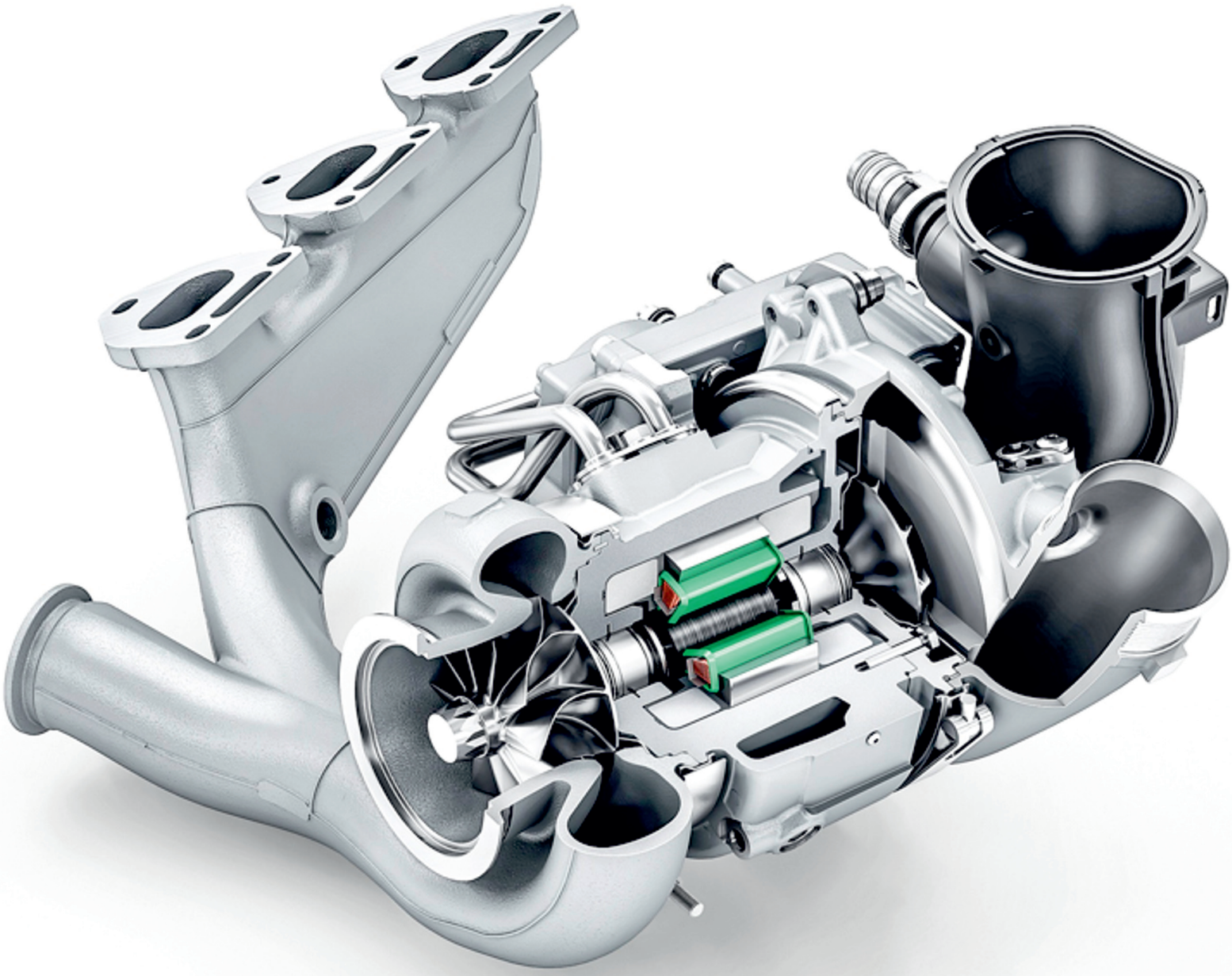

Publisher:

Polish Scientific Society of Combustion Engines

ISSN: 2300-9896
eISSN: 2658-1442

Combustion Engines

Polskie Towarzystwo Naukowe Silników Spalinowych

www.combustion-engines.eu